CAPABILITY OF SILICON CARBIDE SCHOTTKY DIODES AS RADIATION DETECTOR AND FOR X-RAY PHOTON ENERGY HARVESTING

NURUL SYAZWINA BINTI MOHAMED

NEWCASTLE UNIVERSITY

CAPABILITY OF SILICON CARBIDE SCHOTTKY DIODES AS RADIATION DETECTOR AND FOR X-RAY PHOTON ENERGY HARVESTING

NURUL SYAZWINA BINTI MOHAMED



A thesis submitted to the Faculty of Science, Agriculture and Engineering for the degree of Doctor of Philosophy

NEWCASTLE UNIVERSITY
SCHOOL OF ENGINEERING

JUNE 2018

ABSTRACT

Silicon carbide (SiC) offers a response that is closer to human tissue in comparison to high atomic number semiconductor materials and is highly radiation tolerant in a wide range of applications including space exploration, nuclear decommissioning and medical applications. Investigations to the radiation performance of SiC have been reported by a number of research groups aspiring to invent new detectors with a view to monitoring dose rates across a wide dose rate range, but few have reported low dose rate measurements that are suitable for medical applications. Accurate knowledge of the dose rate is imperative in medical treatment, which involves both imaging and radiotherapy, where a wide range of dose rates and energies are used, primarily comprising photonic radiation. Therefore, this project investigated the suitability of 4H–SiC Schottky diodes as radiation detectors for medical applications, which involved low and high dose rate range, as well as the first demonstration of an X–ray photon energy harvester capable of powering a wireless sensor node.

The initial phase of the study involved optimization of the fabrication and parametric characterisation of Schottky diode based on Ni₂Si. Current–voltage (I–V) characteristics utilising forward and reverse bias voltages were used to determine the specific on resistance, R_{on} , ideality factor, n, barrier height, Φ_b and leakage current. The diodes showed outstanding characteristics in terms of the extracted ideality factor and barrier height at room temperature and these showed minimal variation with temperature for measurements below 100 °C, indicating the formation of a high–quality metal–semiconductor interface.

Valuable insights on the capability of the fabricated Schottky diodes to exposure to low dose rate X-ray photons in terms of the linearity and dose rate sensitivity at room and elevated temperatures have been presented. Detectors were exposed to X-ray photons from a tungsten tube operating with an accelerating bias of 35 kV using a Phywe Xpert4 system operating with tube currents between 0.2 and 1.0 mA. The generated current signal was linearly dependent on the volume of the space charge region formed under the Schottky contact and revealed a sensitivity which is a factor of 10^6 higher than that reported in the literature. The temperature dependence of the characteristics indicated that SiC Schottky diode-based detectors offer a performance suitable for medical applications at temperatures below $100\,^{\circ}\text{C}$ without the need for external cooling.

The correlation of diode electrical characteristics with the spectroscopic response when exposed to a 241 Am alpha source and the performance capabilities as an X–ray photon energy harvester was investigated. Spectroscopic characterisation revealed detector D5 with the highest energy resolution in the range of 0.084 % and 0.133 % for bias voltages between 0 and -40 V, in comparison to the other two detectors. Additionally, the leakage current of detector D5 which was < 1nA/cm^2 for biases below -50 V, that demonstrated a significantly lower noise spectral density, with a current dependence $\beta = 3.16$, was demonstrated to be the most suitable for use as a X–ray photon energy harvester. This confirms the possibility of scavenging energy from an X–ray beam and the capability of developing a self–powered system using silicon carbide technology for deployment in extreme environments.

The final phase of this project involved the response of the selected detector (D2) to high energy (6 MV) photon irradiation as a function of cumulative dose to a maximum of 1000 Gy. The realization of a vertical detector structure, coupled with the high quality of epitaxial layers, has resulted in a high dose sensitivity of the detector that is highly linear for all bias voltages used in the study. In addition, the effect on the characteristics properties and performance capabilities in terms of X–ray photon energy harvester before and after the high–energy irradiation was analysed. The specific on resistance, ideality factor and barrier height demonstrated insignificant changes after exposure to a cumulative dose of 1000 Gy, whilst the dopant concentration and depletion width based on the C–V measurements were observed to decrease by approximately 11% and 17% (at typically -30 V), respectively.

In summary, the realization of dosimeters with enhanced sensitivity for a wide range of incident dose rates is feasible with silicon carbide technology, opening up the possibility of radiation monitoring for long periods in extreme environments. Furthermore, it is possible to power a wireless sensor node, comprising the power converter, signal conditioning and sensor manufactured from silicon carbide, from incident radiation with a dose rate comparable to that found in conventional medical systems.

Dedicated to baba and mama my sibling

DECLARATION

I certify that all materials in this thesis, which is not my own work has been identified and that no material has previously been submitted and approved for the award of a degree by this or any other university.

Nurul Syazwina binti Mohamed

June 2018

ACKNOWLEDGEMENTS

I would like to express my utmost gratitude and appreciation to those who had extended their help and support throughout my studies and towards the completion of this thesis in the past 3 years.

First and foremost, I would like to thank my supervisor; Dr. Alton Horsfall for inspire and motivate me to explore the field of semiconductor materials and devices, apart from my field of background previously. Thank you for your patience, guidance and supports in both my professional and personal development. I would also like to thank my co–supervisor; Prof. Nick Wright for sharing knowledge and expertise with me, providing invaluable support and useful discussions over the course of my PhD.

I am grateful for the technical guide and assistance during fabrication process, electrical characterisation and experimental measurements giving by Konstantin Vasilevskiy, Hua Kee Chan, and Andrea Dawson (Department of Physics). Not to be forgotten, special thanks to Mr. Steve Locks (Consultant Clinical Scientist–Radiotherapy Physics) and his colleague, Rob Dacey for giving me permission to use their LINAC facility in Northern Centre for Cancer Care, Freeman Hospital. I am really appreciate your guidance and assistance during the high energy photon irradiation.

I am thankful to my colleagues, Marzaini Rashid, Srinivas Ganti, Chloe Peaker, Oras Al–Ani, Fatimah Bahrani, Hind Alsnani, Sandip Roy, Neal Wood, Idzdihar Idris, Faiz Arith, Tiago Marinheiro, Luke Bradley, Johan Gausden, Amy Peters, Ryan Siddall, and many more who have contributed and make my years in pursuing PhD interesting.

I am indebted to both Universiti Sultan Zainal Abidin and the the Ministry of Higher Education (MOHE) Malaysia for sponsoring my study through the SLAI (academic staff training scheme) scholarship.

My special thanks to my beloved parent and my sibling for their great patience and support. Not to be forgotten, my other family members and close friends, for their continuous moral support. Their support and understanding on a daily basis has been determinant for the successful completion of my PhD.

LIST OF PUBLICATIONS

- 1. N. S. Mohamed, N. G. Wright and A. B. Horsfall, 'Self-powered X-Ray sensors for extreme environments', *Conf. Proc. IEEE SENSORS 2017*, pp. 1 3, 2017.
- N. S. Mohamed, N. G. Wright and A. B. Horsfall, 'Dose Rate Linearity in 4H–SiC Schottky Diode–Based Detectors at Elevated Temperatures, *IEEE Trans. Nucl. Sci.*, vol. 64, no. 7, pp. 1912 – 1919, 2017.
- 3. N. S. Mohamed, M. I. Idris, N. G. Wright and A. B. Horsfall, 'Silicon Carbide Radiation Detectors for Medical Applications', *Mater. Sci. Forum*, vol. 897, pp. 626 629, 2017.
- 4. N. S. Mohamed, N. G. Wright and A. B. Horsfall, 'High linearity silicon carbide detectors for medical applications', *Conf. Proc. IEEE Nuclear Science Symposium, Medical Imaging Conference and Room–Temperature Semiconductor Detector Workshop (NSS/MIC/RTSD)* 2016, pp. 1 5, 2016.

Contents

1	Intr	oduction	1
	1.1	Background	1
	1.2	Motivation	3
	1.3	Scope of thesis	3
	1.4	Key contribution	6
2	Lite	rature Review	7
	2.1	Introduction	7
	2.2	Physical Properties of Silicon Carbide (SiC)	7
		2.2.1 Background and Crystal Structure	7
		2.2.2 SiC characteristics	10
		2.2.3 Advantages of SiC over other semiconductor materials	11
	2.3	SiC Schottky diode	14
		2.3.1 Principles of Schottky diode	14
		2.3.2 Current transport process in Schottky diode	16
	2.4	Radiation interaction detection properties	17
		2.4.1 Detection properties	17
		2.4.2 Radiation interaction with matter	20
	2.5	Semiconductor radiation detector	24
		2.5.1 Principle of radiation detector	24

		2.5.2	SiC as a semiconductor radiation detector	25
	2.6	Alpha	spectroscopy measurements with ²⁴¹ Am	28
		2.6.1	Spectroscopic detection system	28
		2.6.2	Alpha particle detection properties	29
	2.7	Energy	scavenging in radiation environments	31
		2.7.1	Principles of X-ray photon energy harvester	31
		2.7.2	Factors affecting the performance of X -ray photon energy harvester	32
	2.8	Low fr	equency noise (LFN)	36
		2.8.1	Low frequency noise models	36
		2.8.2	Factors influencing the low frequency noise	37
	2.9	4H–Si	C Schottky diode as an X–ray photon dosimeter	38
		2.9.1	Beam line monitoring system	38
		2.9.2	Trap-recombination and radiation damage due to extreme environments	40
	2.10	Summ	ary	44
3			n on Fabrication and Characterisation of 4H–SiC Schottky Diode	44 45
3		imisatio		
3	Opti	imisatio Introdu	n on Fabrication and Characterisation of 4H–SiC Schottky Diode	45
3	Opti	imisatio Introdu 3.1.1	n on Fabrication and Characterisation of 4H–SiC Schottky Diode	45 45 46
3	Opti	imisatio Introdu 3.1.1	n on Fabrication and Characterisation of 4H–SiC Schottky Diode	45 45 46 47
3	Opti	Introdu 3.1.1 Device	n on Fabrication and Characterisation of 4H–SiC Schottky Diode action	45 45 46 47 51
3	Opti	Introdu 3.1.1 Device 3.2.1 3.2.2	n on Fabrication and Characterisation of 4H–SiC Schottky Diode action	45 45 46 47 51 53
3	Opti 3.1 3.2	Introdu 3.1.1 Device 3.2.1 3.2.2	n on Fabrication and Characterisation of 4H–SiC Schottky Diode action	45 45 46 47 51 53 57
3	Opti 3.1 3.2	Introdu 3.1.1 Device 3.2.1 3.2.2 Electri	n on Fabrication and Characterisation of 4H–SiC Schottky Diode action	45 45 46 47 51 53 57
3	Opti 3.1 3.2	Introdu 3.1.1 Device 3.2.1 3.2.2 Electri 3.3.1	n on Fabrication and Characterisation of 4H–SiC Schottky Diode action	45 45 46 47 51 53 57 57 58
3	Opti 3.1 3.2	Introdu 3.1.1 Device 3.2.1 3.2.2 Electri 3.3.1 3.3.2	n on Fabrication and Characterisation of 4H–SiC Schottky Diode action	45 45 46 47 51 53 57 57 58 60

		3.3.6	Leakage current density, J_L	65
	3.4	C–V m	neasurements at room temperature	68
		3.4.1	Doping concentration, N_D	68
		3.4.2	Flat–band barrier height, ϕ_B	69
		3.4.3	Depletion width, W_d	71
	3.5	Conclu	ısion	72
4	Tem	peratur	re Independence of 4H–SiC Schottky Diode Radiation Detector at Elevate	d
	Tem	- peratur	res	74
	4.1	Introdu	action	74
		4.1.1	Overview of SiC as a radiation detector	75
		4.1.2	Highlight of the chapter	76
	4.2	Experi	mental set up	76
	4.3	Electri	cal characterisation at elevated temperatures up to 100 °C	78
		4.3.1	Specific on resistance, $\Omega.cm^2$	80
		4.3.2	Ideality factor, n and Schottky barrier height, Φ_b	83
	4.4	Low do	ose rate radiation response at room and elevated temperatures up to 100 $^{\circ}\text{C}~$	86
		4.4.1	Experimental procedure	87
		4.4.2	Dose rate linearity: Room temperature measurements	87
		4.4.3	Dose rate linearity: Elevated temperature measurements	91
		4.4.4	Dose Sensitivity: Room temperature measurements	95
		4.4.5	Dose Sensitivity: Elevated temperature measurements	100
	4.5	Conclu	ision	104
5	Ene	rgy Scav	venging in X–ray Environment and The Correlation with The Electrical and	d
	Spec	ctroscop	oic Characterisation of 4H–SiC Schottky Diode	106
	5 1	Introdu	action	106

	5.1.1	Overview of the SiC as a X-ray photon energy harvester and the correlation	
	3.1.1	with spectroscopic properties using ^{241}Am	107
		, and appearance properties down	10,
	5.1.2	Highlights of the chapter	109
5.2	Spectr	oscopic properties of 4H–SiC Schottky diode irradiated with $^{241}\mathrm{Am}$	109
	5.2.1	Experimental set up	110
	5.2.2	Channel peak position	113
	5.2.3	Full width at half maximum (FWHM) and energy resolution	117
	5.2.4	Charge collection efficiency	120
5.3	Low fi	requency noise (LFN) measurements	122
	5.3.1	Dependance of noise spectral density with frequency	123
	5.3.2	Dependance of noise spectral density with current	124
	5.3.3	Normalised noise spectral density	126
5.4	Perfor	mance characteristics of 4H-SiC Schottky diode as X-ray photon energy	
	harves	ter	126
	5.4.1	Short circuit current density, J_{SC}	131
	5.4.2	Open circuit voltage, V _{OC}	132
	5.4.3	Peak power density, P _{OUT}	135
	5.4.4	Fill factor, FF	136
5.5	Potent	ial Applications	138
	5.5.1	Self-powered X-ray sensors for extreme environments	138
5.6	Conclu	usion	141
Rad	iation [Folerance of 4H–SiC Schottky Diode Radiation Detector in High–Energ	y
Pho	ton Env	vironments	143
6.1	Introd	uction	143
	6.1.1	Overview of the SiC as high dose rate radiation detector	144
	612	Highlights of the chanter	146

6

	6.2	Cnarac	cterisation with high dose rate photon irradiation	140
		6.2.1	Experimental set up	147
		6.2.2	High dose rate response	149
	6.3	Effect	of high-energy photon irradiation on the electrical characteristics	155
		6.3.1	Specific on resistance, R_{on}	155
		6.3.2	Ideality factor, n and Schottky barrier height, Φ_b	157
		6.3.3	C–V measurements at room temperature	159
	6.4	Radiat	ion tolerance of X-ray photon energy harvester in high radiation dose	
			nments	161
		6.4.1	Short circuit current density, J_{SC}	162
		6.4.2	Open circuit voltage, V_{OC}	163
		6.4.3	Peak power density, P _{OUT}	165
		6.4.4	Fill factor, FF	165
	6.5	Low fr	requency noise (LFN) before and after irradiation at elevated temperatures up	
		to 100	°C	166
		6.5.1	Dependance of noise spectral density with frequency	167
		6.5.2	Dependance of noise spectral density with current	169
	6.6	Conclu	asion	171
7	Con	clusions	s and Future works	173
	7.1	Summ	ary	173
	7.2	Future	work	176

List of Figures

2.1	Schematic structures of common SiC polytypes; 3C–SiC, 4H–SiC and 6H–SiC.	
	Open and closed circle denote Si and C atoms, respectively	8
2.2	Absorption efficiency of different semiconductor detectors as a function of radiation	
	energy	13
2.3	Schematic diagram of energy band structure of the metal-semiconductor	15
2.4	Schematic diagram of five basic transport processes under forward bias which are (1)	
	thermionic emission, (2) tunneling, (3) recombination, (4) diffusion of electrons, and	
	(5) diffusion of holes	16
2.5	Conduction mechanism for low, intermediate and high dopant concentration of $n-$	
	type substrate	18
2.6	Ionization produce by a radiation electron within the medium	19
2.7	The relative contribution of the different mechanisms of radiation interaction in SiC,	
	which contribute to photoelectric effect, Compton scatter and pair production	21
2.8	Schematic illustration of the photoelectric effect in a free atom. The electron from	
	higher energy level will fill the gap if the K-shell electron is knocked of by the	
	incident photon. The energy of emitted photon will be equal to the different of the	
	two energy levels	21
2.9	Schematic illustration of the Compton scattering of a photon having energy $E_{\gamma 0}$ =	
	hc/λ_0 from a bound electron. Some of the energy of the incident photon goes into	
	knocking the orbital electron out of its orbit	23
2.10	Schematic diagram of radiation interaction inside the depletion region which leads	
	to creation of electron-hole pairs. The collection of the charges created operated by	
	the electric field applied	25

2.11	excitation process	26
2.12	Plots of the forward and reverse bias of the I–V characteristics when radiation incident on the detecting medium. Electrical current can be observed to generate in the reverse direction by the application of reverse bias	26
2.13	The signal processing of the detection system of alpha spectroscopy	29
2.14	Alpha particle interaction while pass through the detector medium. It has a linear trajectory through matter and loses energy through Coulomb collisions with electrons in the cloud. These electrons are energetic and can undergo secondary, tertiary and high order interactions as they lose energy	31
2.15	Simulation of the ionization produced in dry air by 5.4 MeV alpha particle using SRIM2011 model software depicted the Bragg curve at the end of the range	32
2.16	Schematic diagram of the collection of electron–hole pairs during X–ray scavenging inside SiC Schottky diode	33
2.17	Schematic diagram of the electron and hole movement inside the depletion region of a Schottky diode	33
2.18	Plot of energy deposition of 63 Ni emitting β -particles of 17.4 keV as a function of effective absorption thickness of GaN Schottky betavoltaic cell for (a) with and (b) without the influence of dead layers	35
2.19	Plots of relationship between depletion layer width, built–in potential, and doping concentration of <i>n</i> –type substrate of GaN	35
2.20	μ_{ch} for H ₂ SiC MOSFETs and result reported for Si MOSFETs as a function of absorbed dose are also plotted. The value of the channel mobility is normalized by the initial value	41
2.21	Shift of the breakdown voltage from the initial value for SiC SITs (squares), Si MOSFETs (triangles) and Si IGBT (upside–down triangles) as a function of absorbed dose. The blocking characteristics for SiC SITs and Si ones (IGBTs and MOSFETs) were measured under V_G at 10 V and 0V, respectively	41
2.22	Schematic cross section of band–recombination with subsequent emission of an Auger electron	42

2.23	photons	43
2.24	Schematic electron band diagram for a semiconductor with deep–level impurities	43
3.1	Mask layout design of the Schottky diode 10mm × 10mm die with different Schottky contact areas	52
3.2	Schematic cross section of Schottky diode with mesa structure	55
3.3	Schematic cross section of the standard processing condition of the Schottky diode .	56
3.4	Schematic cross section of Schottky diode with silicon nitride (Si_3N_4) as a passivation layer	56
3.5	Top view of the detector die after fabrication. The overall die dimensions are 10 mm \times 10 mm $$	56
3.6	Specific on resistance for all fabricated diodes as a function of diameter size. The error bars represent the absolute minimum and maximum of the data	59
3.7	Ideality factor for all fabricated diodes as a function of diameter size. The error bars represent the absolute minimum and maximum of the data	60
3.8	Barrier height for all fabricated diodes as a function of diameter size. The error bars represent the absolute minimum and maximum of the data	62
3.9	Barrier height plotted against ideality factor for all fabricated diodes as a function of diameter size. The error bars represent the absolute minimum and maximum of the data	64
3.10	Leakage current density for all diodes with increasing detector's diameter, DC2 – purple, DC4 – green, DC5 – orange, DC7 – red, and DC8 – blue (× – 200 μ m, \triangle – 300 μ m, \circ – 500 μ m, \Box – 1 mm, \diamond – 2 mm)	67
3.11	$1/C^2$ plotted against bias voltage for all diodes, slope from the graph was used to extracted doping concentration, N_D values for all fabricated diodes	68
3.12	Depletion width, W_d plotted against bias voltage for all diodes	
4.1	Optical micrograph of fabricated diodes mounted on the specially designed PCB	76

4.2	Circuit box with a fabricated diode mounted on top of the Peltier cooler. The	
	Peltier cooler and Pt_{1000} sensor were used to regulate the temperature applied during	
	measurement	77
4.3	Experimental set up for low dose rate response. Circuit box with a 1.5 cm diameter	
	hole in the middle was aligned with the incident X–ray beam	78
4.4	Current–voltage (I–V) characteristics with increasing temperature up to 100 $^{\circ}\mathrm{C}$ for	
	detector D2. Increasing the measurement temperatures resulted in the I–V plots to	
	be shifted towards the low bias voltage	80
4.5	Specific on resistance; $R_1(\diamond)$ and R_2 (\square) for D1 (light blue), D2 (red), D3 (green),	
	D4 (grey) and D5 (purple) at room and elevated temperatures up to 100 $^{\circ}$ C	81
4.6	Electron Hall mobility of 4H-SiC at different doping concentrations and	
	crystallographic orientations.1: high quality , unintentionally doped, 2: $N_d\cong 1.2$	
	$ imes$ $10^{17}~{ m cm}^{-3}$ electric field $F\ c$, 3: ${ m N}_d\cong 1.2 imes 10^{17}~{ m cm}^{-3}$ electric field $F\perp c$	82
4.7	Ideality factor, IF (⋄) and barrier height, BH (□) for detectors D1, D2, D3, D4 and	
	D5. Electrical characteristics for all detectors exhibited temperature independence at	
	room temperature and up to 100 °C. The error bars represent the absolute minimum	
	and maximum of the data	84
4.8	Barrier height against ideality factor as a function of temperature for detectors D1,	
	D2, D3, D4 and D5. Variation of the barrier height against ideality factor exhibited	
	a linear relationship, where the deduced straight line of the least squares fit to the	
	experimental data expressed as Φ_b (T) = (m.n + c) eV. The error bars represent the	
	absolute minimum and maximum of the data	85
4.9	The relative contribution of the different mechanisms of radiation interaction which	
	contribute to photoelectric effect, Compton scattering and pair production	86
4.10	Calibration curve in terms of dose rate (mGy/min) and current signal density	
	(nA/mm²) plotted against tube current which obtained from RMS 30 and BPW34	
	Si photodiode, respectively	88
4.11	Current signal density plotted against dose rate for detectors D1, D2 and D3 at room	
	temperature.	89

4.12	Current signal density against depletion width for D1, D2 and D3 at room temperature and dose rate ranging from 0.105 mGy/min to 0.185 mGy/min. Linear	
	fitted lines for all detectors at all dose rates give R^2 between 0.94 and 1	90
4.13	Dose rate linearity as a function of bias voltage applied at room temperatures for D1, D2 and D3. The data demonstrate slight increase in the dose rate linearity with increasing bias voltage. The error bar which represent the standard deviation of the dose rate linearity is smaller than bullet data point.	92
4.14	Current signal density against leakage current density at temperature up to 100 °C and bias voltage from -40 V till -120 V for detector D2. Current signal density values plotted were subtracted with the dark current values before measurements were performed	93
4.15	Intrinsic carrier concentration against measurement temperature for 3C, 4H and 6H–SiC	93
4.16	Dose rate linearity as a function of bias voltage applied at operated temperatures up to 100 °C for D2. With the exception at 100 °C, the dose rate linearity at all measurement temperates were almost consistent at all bias voltage. The error bar which represent the standard deviation of the dose rate linearity is smaller than bullet data point	96
4.17	Current response for detector D2 as a function of exposure time for -80 V reverse bias at room temperature after background subtraction. Current signal is stable and reproducible at typically 3.25 nA	97
4.18	Leakage current density for detectors D1 and D2 as a function of exposure time at room temperature and bias voltages between -80 V and -180 V	98
4.19	Collected charge per unit area as a function absorbed dose during irradiation to 0.185 mGy/min at different bias voltages and room temperature for D1 (with dashed line) and D2 (with solid line). The error bars represent the fractional standard deviation attributed from the random fluctuation of the signal response	99
4.20	Signal-to-noise ratio (SNR) as a function of bias voltage for D1 and D2. High leakage current and high random fluctuation may attributed to a low SNR value especially at high bias voltage.	100
	COLOCIALLY ALTHER MAN WHATE,	// /

4.21	Dose sensitivity as a function of bias voltage applied at room temperature for D1 and
	D2. Increasing the bias voltage has increased the dose sensitivity for both D1 and
	D2 detectors. The error bar which represent the root mean standard error of the dose
	sensitivity is smaller than bullet data point
4.22	Photon detection efficiencies between 100 eV and 30 keV for silicon carbide or
	silicon detectors with active regions of 50, 100, 300, and 500 μm
4.23	Response against leakage current density at room temperature and elevated
	temperatures up to 100 °C and bias voltage from -80 V to -150 V for D2. $\dots \dots 102$
4.24	Dose sensitivity as a function of bias voltage applied at room temperature and
	elevated temperatures up to 100 $^{\circ}\mathrm{C}$ for D2. The data demonstrate consistent dose
	sensitivity for a variation of bias voltage and measurement temperature and the error
	bar which represent the root mean standard error of the dose sensitivity is smaller
	than the bullet data point
5.1	Decay scheme of ²⁴¹ Am
5.2	Simulated target depth of the alpha particle; ²⁴¹ Am inside the fabricated detector for
	(a) Ni ₂ Si and (b) Ni Schottky contacts. Both contacts demonstrate almost similar
	energy loss with increasing target depth (μ m)
5.3	Experimental set up of the spectroscopy measurement on the fabricated detector 112
5.4	Spectra responses of detector D2 by exposure to ²⁴¹ Am at different bias voltages
	before gaussian fitting
5.5	Typical spectra response from exposure to ²⁴¹ Am which depicted two peaks from
	two energies of 5.486 MeV (84.8%) and 5.443 MeV (13.1%)
5.6	Pulse height spectra for (a) D2, (b) D4 and (c) D5 with increasing bias voltages after
	Gaussian fitting
5.7	Channel peak position for detectors D2, D4 and D5 as a function of bias voltage
	applied
5.8	Channel peak position for detectors D2, D4 and D5 as a function of leakage current
	density at different applied bias voltages
5.9	Definition of the full-width at half maximum (FWHM) and energy resolution 117
5.10	Illustration of the response functions for detectors with good and poor resolution 118

5.11	Full-width at half maximum (FWHM) for detectors D2, D4 and D5 as a function of
	bias voltage applied
5.12	Energy resolution for detectors D2, D4 and D5 as a function of bias voltage applied 120
5.13	Charge collection efficiency (CCE) for detectors D2, D4 and D5 with increasing bias
	voltage applied
5.14	Schematic block diagram of the low frequency noise measurement system 122
5.15	Current-voltage characteristics for detectors D2, D4 and D5 before measurement of
	low noise frequency
5.16	Frequency dependance of noise power spectral density, S_I at different currents for
	(a) D2 and (b) D4 (c) D5 detectors at room temperature
5.17	Noise power spectral density, S_I for detectors D2, D4 and D5 with increasing current
	at $f = 10 \text{ Hz.} \dots 126$
5.18	Normalised noise power spectral density, S_I/I^2 for detectors D2, D4 and D5 with
	increasing current at $f = 10$ Hz
5.19	Typical trend of current-voltage characteristics of X-ray photon energy harvester
	depicting the maximum power (P_{max}) (described as peak power density (P_{OUT}) for
	the case in this section), short circuit current (I_{SC}) and open circuit voltage (V_{OC}) 129
5.20	Current-voltage characteristics of detector D2, D4 and D5 after illumination with 35
	kV X-ray and increasing tube current between 0.2 and 1 mA
5.21	Current-voltage characteristics of BPW34 Si photodiode after illumination with 35
	kV X-ray and increasing tube current between 0.2 and 1 mA
5.22	Short circuit current density (J_{SC}) for all detectors as a function of dose rate. The
	error bars represent the standard deviation of the data
5.23	Open circuit voltage $(V_{\it OC})$ for all detectors as a function of dose rate. The error bars
	represent the standard deviation of the data
5.24	Peak power density (P_{OUT}) for all detectors as a function of dose rate. The error bars
	represent the standard deviation of the data
5.25	Fill factor (FF) for all detectors as a function of dose rate. The error bars represent
	the standard deviation of the data

5.26	Schematic representation of a self-powered sensor node for deployment in extreme	
	environments	139
5.27	Circuit schematic for a self starting boost converter suitable for converting the 0.7 V output to 14 V	140
6.1	Experimental set up of the 6 MV photon irradiation	148
6.2	Current signal generated from irradiation between 17.6 to 52.9 Gy/min of 6 MV photons with increasing bias voltages	149
6.3	Current signal generated as a function of depletion width (W_d) from irradiation between 17.6 to 52.9 Gy/min of 6 MV photons	150
6.4	Leakage current density from irradiation between 47.6 to 1000 Gy cumulative dose of 6 MV photons with increasing bias voltages	152
6.5	Leakage current density with increasing cumulative dose from 47.6 up to 1000 Gy of 6 MV photons at bias voltages between -100 V to -200 V	152
6.6	Dose rate linearity from low and high dose rate irradiation respectively between 0.020 to 0.185 mGy/min of 35 kV X-ray and 8.8 to 52.9 Gy/min of 6 MV photons at different bias voltages	153
6.7	Plots of the calculated quantum detection efficiencies of the $0.06~\text{mm}^2~\text{SiC}$ photodiode based on two different thicknesses of active layer (2.69 μ m, dashed line; 34.5 μ m, solid line) as a function of X–ray energy. The discontinuity at 1.8 keV is the Si K absorption edge	154
6.8	Current–voltage (I–V) characteristics of detector D2 before and after each irradiation of cumulative dose between 47.6 to 1000 Gy.	156
6.9	Specific on resistances $(\Omega.cm^2)$; R_1 and R_2 for detector D2 before and after exposure to cumulative dose between 47.6 to 1000 Gy. The error bars which represent the standard deviation of the data are smaller than the bullet points	156
6.10	Ideality factor and barrier height (eV) for detector D2 before and after each exposure to cumulative dose between 47.6 to 1000 Gy. The error bars which represent the standard deviation of the data are smaller than the bullet points	158

6.11	1/C ² plotted against bias voltage for detector D2, slope from the graph was used
	to extracted doping concentration, N_D values before and after irradiation to 6 MV
	photons with 1000 Gy maximum cumulative dose
6.12	Depletion width, W_d plotted against bias voltage before and after irradiation to 6 MV
	photons with 1000 Gy maximum cumulative dose
6.13	Current-voltage characteristics of detector D2 after illumination with 35 kV X-ray
	and increasing dose rate between 0.043 and 0.185 mGy/min for before and after
	irradiation to 1000 Gy cumulative dose
6.14	Short circuit current density (J_{SC}) for detector D2 as a function of dose rate before
	and after irradiation to 6 MV photon. The error bars represent the standard deviation
	of the data
6.15	Open circuit voltage (V_{OC}) for detector D2 as a function of dose rate before and after
	irradiation to 6 MV photon. The error bars represent the standard deviation of the data.164
6.16	Peak power density (P_{OUT}) for detector D2 as a function of dose rate before and
	after irradiation to 6 MV photon. The error bars represent the standard deviation of
	the data
6.17	Fill factor (FF) for detector D2 as a function of dose rate before and after irradiation
	to 6 MV photon. The error bars represent the standard deviation of the data 167
6.18	Current dependance of noise spectral density, S_I at $f = 10$ Hz for (a) before and (b)
	after irradiation with 6 MV photon
6.19	Frequency dependance of noise power spectral density, S_I at different currents for
	(a) before and (b) after irradiation with 6 MV photon at room temperature 168
6.20	Current dependance of noise spectral density, S_I at $f = 10$ Hz and (a) 27 °C, (b) 50 °C,
	(c) 75 $^{\circ}\text{C}$ and (d) 100 $^{\circ}\text{C}$ measurement temperatures for before and after irradiation
	with 6 MV photons
6.21	Current dependance of noise spectral density, S_I as a function of measurement
	temperatures for before and after irradiation with 6 MV photons

List of Tables

2.1	Table of physical properties for 3C, 4H and 6H at 300 K	9
2.2	Table of material properties of major semiconductor for use as ionising radiation detectors	12
3.1	Table of metal work–function, predicted ϕ_B (eV) and actual ϕ_B (eV) of few possible metals for Schottky contacts	50
3.2	Table of different treatment control on fabricated Schottky diode designated as DC 2, DC 4, DC 5, DC 7 and DC 8	54
3.3	Table of flat–band barrier height for DC 2, DC 4, DC 5, DC 7 and DC 8 for 2 mm device size	70
4.1	Table of different treatment control on Schottky diode designated as Detector 1 (D1), 2 (D2), 3(D3), 4(D4) and 5(D5)	77
4.2	Table of comparison on the dosimetric sensitivity of detector D2 with previously reported data	103
5.1	Table of material properties; Schottky contact, ideality factor, barrier height and current saturation density for detectors D2, D4, and D5	128
6.1	Table of different exposure performed during irradiation to 6 MV photon that expressed in monitor unit (MU), dose rate (Gy/min), dose (Gy) and cumulative dose (Gy); 1 MU is equivalent to 0.022 Gy	148

ABBREVIATION

ALARP as low as reasonably practicable

CCE charge collection efficiency

CdTe cadmium telluride

CdZn(Te) cadmium zinc telluride

C-V capacitance-voltage

CVD chemical vapour deposited

DLTS deep level transient spectroscopy

FPGA field-programmable gate array

FWHM full width at half maximum

GaAs gallium arsenide

GaN gallium nitride

Ge germanium

G–R generation–recombination

HgI₂ mercury iodide

ICRP International Commission of Radiation Protection

I-T current-temperature

I-V current-voltage

JFETs junction field effect transistors

JTE junction termination extension

kerma kinetic energy release per unit mass

KOH potassium hydroxide

LET linear energy transfer

LFN low noise frequency

LINAC linear accelerator

MCA multi-channel analyser

MOSFETs metal oxide semiconductor field effect transistors

MU monitor units

NPSD noise spectral density

NNPSD normalised noise spectral density

PCB printed circuit board

P-C photocurrent

plasma enhanced chemical vapour deposition **PECVD**

PVD physical vapour deposition

RCA Radio Corporation of America

RIE reactive ion etching

SBH Schottky barrier height

Si silicon

SNR

SiC silicon carbide

silicon nitride $Si_3N_4 \\$

signal-to-noise ratio SRIM stopping and range of ions in matter

STSSD semitransparent SiC Schottky diode

TlBr thallium bromide

TPR tissue phantom ratio

Chapter 1

Introduction

1.1 Background

The use of radiation in space exploration, nuclear environments, industrial and medical applications has required significant advances in the technology for the fabrication and characterisation of new detector materials for a range of applications. In the field of medical applications, the International Commission of Radiation Protection (ICRP) proposed the main radiation protection principles in conjunction with the use of radiation, which include justification where no use of radiation is permitted, unless the advantages outweigh the disadvantages, limitation of the maximum dose experienced by individuals shall not exceed the dosage limits recommended for the appropriate circumstances by the Commission and optimization where in all cases the radiation doses should be kept as low as reasonably practicable (ALARP) [1]. The commission actively requires that it is not sufficient to just remain under the radiation dose limits, but the actual radiation dose should be significantly lower than the permitted limit and kept as low as reasonably practicable.

Therefore, precise control of the beam target bombardment (known as beam line monitoring) is imperative in medical applications, particularly during radiotherapy treatment [2], in order to assure correct dose delivery to the patient [3]. The outcome of treatments is highly dependent on the radiation dose, which needs high levels of traceability, accuracy and consistency of radiation dosimetry measurements [4]. However, the use of different types of radiation such as gamma rays, alpha particles, beta particles, electrons, neutrons and protons provide different values of stopping power and average distance travelled in the detector medium. High energy radiation and low mass charged particles such as gamma rays, electrons and neutrons will travel longer distances where they produce ionization along the track and deposit the majority of their energy at higher path length. The stopping power is higher for heavy charged particles in comparison to low charged particles. Hence, the development of accurate, vigorous and reliable instruments coupled with a large response for

beam line monitoring is essential as there is often an inadequate number of detectors due to their cost, size and complexity [5].

In recent years, technological advances in the development of radiation detectors have resulted in significant interest at a research level in the exploration of new radiation hard detector materials that are highly radiation tolerant to a wide range of radiation types and energies. The development of the semiconductor materials and devices has been a strong driving force for a variety of revolutionary changes and innovations in modern society. High energy radiation commonly produces a low signal–to–noise ratio due to the high depth of penetration and the formation of defects in the detector material that will affect the measurement [6]. In view of those circumstances, radiation detectors with high radiation resistance, sensitivity and accuracy are highly desirable for an efficient and safe dose delivery during treatment. Nava *et al.* defined radiation resistance as the condition where the parameters of the semiconductor detector do not vary with exposure to nuclear radiation; the higher radiation dose corresponding to the onset of the detection parameters' degradation, the higher the radiation resistance [6].

Concurrently, recent technological advances have increasingly become of interest in the ability of electronic devices to operate in high power, high voltage applications and often in high temperatures. Wide bandgap semiconductors have the ability to withstand high radiation flux for a prolong period with reduced charge trapping and polarization effects, resulting in resilient electronics that can operate within environments that are not possible with conventional semiconductor radiation detectors (Si and Ge). The feasibility of wide bandgap semiconductors as an alternative solutions to the deployment of conventional radiation detectors, has opened up the possibility to tailor the needs of the detector with those of the beam monitoring system. Barry *et al.* suggested that silicon carbide is more resistant to lifetime degradation by displacement damage by more than three orders of magnitude in comparison to gallium arsenide (GaAs) at high voltage for electron energies above approximately 500 keV [7]. This is due to the wide bandgap of SiC that results in the high breakdown electric field, high carrier mobility and high electron saturation drift velocity. Thus, wide bandgap semiconductors are suitable for the realisation of dosimeters in medical applications by virtue of their high radiation tolerance in harsh environments and a response that is closer to human tissue in comparison to high atomic number semiconductor materials.

1.2 Motivation

There has been significant progress in the development of SiC detectors by a number of research groups with interest in measuring alpha, beta, heavy ions, neutrons, gamma and X-rays. However, not all of the detectors are able to operate in real-time applications and measure the variety of particles produced from beam generation. Whilst, a significant amount of research has been devoted to investigate the response of intermediate and high atomic number (Z) materials in range of applications because they offer a higher stopping power than the low atomic number materials that are commonly used. Detectors fabricated from tissue equivalence materials (Z=6) offer similar detection properties and stopping power as in human tissue. Therefore, by taking advantage of the material having a response that is closer to human tissue in comparison to other high atomic number (Z) semiconductor materials, there is a possibility to develop a silicon carbide as radiation detector for beam line monitoring system in medical applications.

The majority of present detectors are restricted by temperature constraints and poor resistance to radiation damage [8], due to low bandgap and displacement threshold energy of these materials. Nevertheless, a significant challenge remains in the development of an ideal radiation detector for operation in high dose rate applications at elevated temperatures that is responsive to a range of ionising radiation with a high signal amplitude and is able to operate for a prolonged lifetime. The superlative material properties of silicon carbide (that is an order of magnitude more radiation hard than silicon) has enabled it to be demonstrated in a range of detector structures for deployment in extreme environments. The proficiency of silicon carbide to operate in high radiation flux and temperature environments, which are relevant to the control of nuclear plants and guidance systems for satellites and shuttles is due to its high displacement threshold energy [6]. In correlation with the increasing demand of power sources that are able to sustain the operation of electronic circuits, there is possibility to develop silicon carbide detector systems as X–ray sensors in extreme environments, which are capable of prolonged life time with reduced radiation damage.

1.3 Scope of thesis

The aims of this thesis are to determine the capability of 4H–SiC Schottky diodes to act as radiation detectors for both low and high dose rate X–ray photon irradiation and identify the possibility of energy scavenging in X–ray environments. The realisation of 4H–SiC Schottky diode radiation detectors involves the optimisation of the fabrication process, electrical characterisation and the experimental measurements of the sensitivity to low and high dose rate response and energy

scavenging in X-ray environments. Therefore, this study is divided into four specific objectives that have been fulfilled in achieving the aims as described in Chapters 3, 4, 5 and 6.

Chapter 2: Literature Review

This chapter presents a detailed overview on the crystal structure, physical properties, characteristics, applications and advances in the field of silicon carbide (SiC) for the realisation of radiation detectors and X-ray photon energy harvesters. A brief explanation on the comparison between different wide bandgap materials highlights the superlative characteristics of 4H–SiC in the specified applications. Different interactions between the radiation and the detection medium are described in order to obtain a better understanding of the parameters affecting the performance of the radiation detector. To gain a better understanding in characterising the diodes in relevant applications, details of the basic principles and working procedures of the detector involved during this study are also discussed. Additionally, an overview of the temperature dependance, behaviour of the noise density with both frequency and current dependance and the possibility for long terms exposure of silicon carbide have been emphasised.

Chapter 3: Optimisation on Fabrication and Characterisation of 4H-SiC Schottky Diode

The initial phase of the study involves the optimisation and fabrication process of Schottky diodes for the realisation of radiation detectors. This chapter describes the forward and reversed bias I–V characteristics to extract series resistance, R_s , ideality factor, n, barrier height, Φ_b and leakage current. C–V characteristics were performed to investigate the dopant concentration, N_D and depletion width, W_d of the fabricated Schottky diode. Results obtained demonstrate outstanding characteristics of the fabricated diodes in terms of ideality factor and barrier height at room temperature, along with almost constant characteristics with elevated temperatures indicative of a high quality Schottky diode has been fabricated.

Chapter 4: Temperature Independence of 4H–SiC Schottky Diode Radiation Detector at Elevated Temperatures

The capability of fabricated Schottky diode to respond to low dose rate X-rays at room and elevated temperatures is reported. The dose rate linearity and dose sensitivity of selected Schottky diodes based on the results presented in Chapter 3 have been measured to study the current response and collected charge to low dose rate radiation. The 4H–SiC Schottky diode detectors were exposed to X-ray photons with incident energies of 35 keV using a Phywe Xpert4 system operating with tube currents between 0.2 and 1.0 mA. Linearity and sensitivity measurements were performed at different bias voltages and elevated temperatures to study the temperature dependance and the effect

of different bias voltages, which lead to variation in the depletion width. The realisation of a vertical detector structure, coupled with the reduction in defect concentration in epitaxial layers, has resulted in an enhanced linearity and sensitivity of the detector than those published previously for moderate dose rate testing. Additionally, measurements performed below 75 °C, show a negligible temperature dependance indicating a highly stable performance of the fabricated detectors.

Chapter 5: Energy Scavenging in X-ray Environment and The Correlation with The Electrical and Spectroscopic Characterisation of 4H-SiC Schottky Diode

This chapter presents the energy scavenging performance in extreme environments of the 4H–SiC Schottky diode radiation detector. The correlation of the diode characteristics in terms of spectroscopic properties and performance capabilities of the X–ray photon energy harvester were studied. This part focused more on the spectroscopic properties of the fabricated diodes to Americium-241 (241 Am) in terms of channel peak position, full width at half maximum (FWHM), and charge collection efficiency (CCE) and its capabilities as an X–ray photon energy harvester in terms of short circuit current density, J_{SC} , open circuit voltage, V_{OC} , power output, P_{OUT} and fill factor, FF for dose rates between 0.043 to 0.185 mGy/min. A direct comparison of the performance with the commercial silicon PIN photodiode BPW34 was made.

Chapter 6: Radiation Tolerance of 4H–SiC Schottky Diode Radiation Detector in High-energy Photon Environments

The last phase of this project emphasises the responsivity of 4H–SiC Schottky diode detector to high-energy photon irradiation and the effects on the electrical characteristics and performance as an X–ray photon energy harvester in comparison to the non–irradiated detectors. The radiation response and hardness of the detector to high–energy photon irradiation and the effect on the forward and reverse I–V and C–V characteristics were determined to a maximum cumulative dose of 1000 Gy. Moreover, the effect of high–energy photons on low frequency noise and the performance of the X–ray photon energy harvester was investigated due to its high radiation tolerance and insensitivity to radiation induced damage.

Chapter 7: Conclusions and Future work

The final chapter summarises and concludes the research. Suggestions and recommendations for future work are also included.

1.4 Key contribution

The experimental procedure and measurements that carried out throughout the completion of this thesis presented several key contribution as added knowledge to the research community;

- i. Analysis of the I–V and C–V characteristics of the fabricated Schottky diode at elevated temperature for the realisation of radiation detector.
- ii. Experimental investigation on the low dose rate response of fabricated 4H–SiC Schottky diode to 0.043 to 0.185 mGy/min X–ray at room and elevated temperatures.
- iii. Experimental measurement of the spectroscopic properties on the fabricated detector using alpha emitted source (²⁴¹Am).
- iv. Comparison of the measured characteristics of energy scavenging in X-ray environments with the silicon PIN photodiode BPW34 in terms of short circuit current density, J_{SC} , open circuit voltage, V_{OC} , power output, P_{OUT} and fill factor, FF.
- v. Analysis on the correlation between the performance of 4H–SiC Schottky diode detector as X–ray photon energy harvester with the spectroscopic properties and low noise frequency measurement.
- vi. A comparison of the radiation response to high dose rate photon irradiation between 8.8 to 52.9 Gy/min with the low dose rate response was made.
- vii. Experimental investigation on the radiation tolerant of the 4H–SiC Schottky diode in highenergy photon environments by observing the changes in the I–V, C–V and low noise frequency characteristics.

Chapter 2

Literature Review

2.1 Introduction

This chapter will described the crystal structure, physical properties, characteristics, applications and advances in the field of silicon carbide (SiC) as a material suitable for the realisation of radiation detectors and X–ray photon energy harvesters.

2.2 Physical Properties of Silicon Carbide (SiC)

2.2.1 Background and Crystal Structure

Silicon carbide, which is a IV–IV compound material with the chemical formula SiC, has been identified as the preferred semiconductor for the fabrication of the Schottky diode based detectors fabricated in this study. SiC, which is also known as carborundum is a stoichiometric compound containing equal amounts of silicon and carbon. Each atom is bonded to four atoms of the opposite type in a tetrahedral configuration. The strong chemical bonding between Si and C atoms gives this material very high hardness, chemical inertness, and high thermal conductivity [9]. SiC occurs in nature as the extremely rare mineral "Moissanite", which was first artificially synthesized in 1891 by Edward Acheson and later discovered in its natural form by Henri Moissan in 1905 [10]. Artificial SiC was discovered as small black crystals in an electrically heated melt of carbon and alumina [11]. However, there are no large naturally occurring deposits of SiC found in nature and all of the SiC used today is synthetic [10]. Silicon carbide can be doped with atoms from group V in the periodic table such as nitrogen or phosphorus to become a n–type, while it becomes a p–type when doped with atoms from group III in the periodic table such as aluminium or boron.

Silicon carbide exists in about 250 crystalline forms and the polymorphism of SiC is categorised by a huge family of similar crystalline structures known as polytypes [12]. Different types of silicon carbide polytypes which are cubic, hexagonal and rhombohedral structures can be formed based on the different unique stacking sequence in a layered of the crystal structure as illustrated by the schematic structures shown in Figure 2.1. The stacking sequence of the tetrahedrally bonded SiC bilayers govern the polytype of SiC through the overall symmetry of the crystal, which is determined by the stacking periodicity [13]. A, B, or C are the three possible positions of tetrahedral SiC bilayer with respect to the lattice. Stacking order of the bonding between Si and C atoms in adjacent bilayer planes can be either zinc—blende (which results in a cubic lattice), which is 60° with respect to nearest neighbours or wurtzite (hexagonal) in nature, which are mirror images [13].

The different polytypes of SiC demonstrate an extensive range of physical properties, including crystal structure, bandgap, carrier mobilities, and thermal conductivity as presented in Table 2.1. The bandgaps show a significant difference between the polytypes which is linked to the wurtzite component, where the higher the wurtzite component in the crystal structure the larger the bandgap [13]. The bandgap for the common polytypes ranges from 2.36 eV for 3C–SiC to 3.23 eV for 4H–SiC [9]. The physical properties are the main essential features that require careful consideration prior to detector fabrication, in order to result in the fabrication of detectors with high quality electrical properties [14]. In this study, 4H–SiC has been chosen as the polytype for the fabrication and characterisation of radiation detectors, primarily because of the wide bandgap which results in a lower intrinsic carrier concentration.

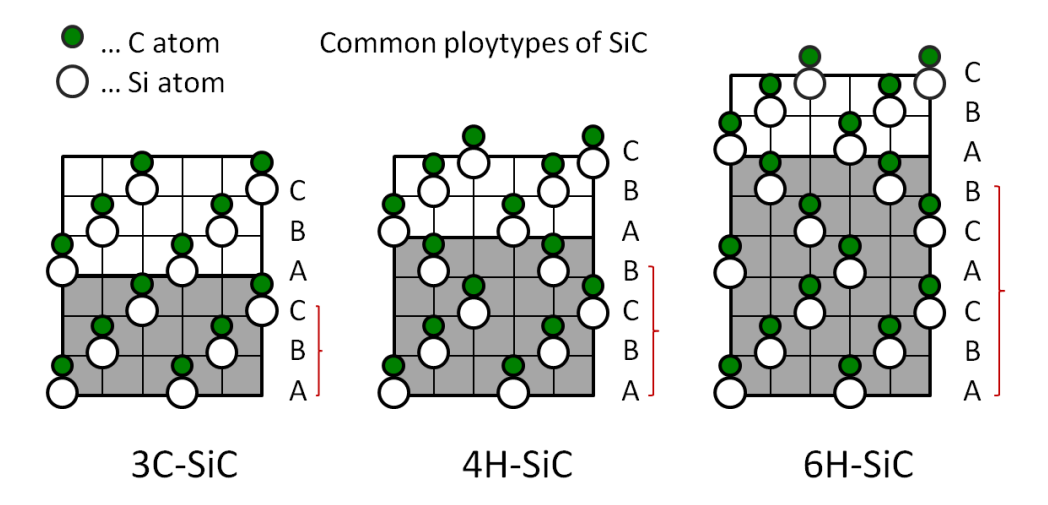


Figure 2.1: Schematic structures of common SiC polytypes; 3C–SiC, 4H–SiC and 6H–SiC. Open and closed circle denote Si and C atoms, respectively.^[15]

Polytypes	3C	4H	6Н
Crystal structure	Zinc blende (cubic)	Hexagonal	Hexagonal
Density (g/cm ³)	3.21	3.21	3.21
Dielectric constant static	9.72	The value of 6H	9.66 (⊥c axis)
		is usually used	10.03 (c axis)
Bandgap (eV)	2.36	3.23	3.0
Breakdown field (Vcm ⁻¹)	$\sim 10^6$	$(3 \div 5) \times 10^6$	$(3 \div 5) \times 10^6$
Mobility (cm ² V ⁻¹ s ⁻¹)			
• electrons	1000	1000 (⊥c axis)	450 (⊥c axis)
	1000	1200 (c axis)	100 (c axis)
• holes	50	120	100
Diffusion coefficient (cm ² s ⁻¹)			
• electrons	≤20	≤22	≤10
• holes	≤8	≤3	≤2
Thermal velocity (ms ⁻¹)			
• electrons	$2 imes 10^5$	1.9×10^{5}	1.5×10^{5}
• holes	1.5×10^5	1.2×10^{5}	1.2×10^{5}
Thermal conductivity	3.6	3.7	4.9
$(\text{Wcm}^{-1}{}^{\circ}\text{C}^{-1})$			
Thermal diffusivity (cm ² s ⁻¹)	1.6	1.7	2.2
Effective electron mass			
(in units of m ₀)			
• longitudinal m _l /m ₀	0.68	0.29	2.0
• transverse m _t /m ₀	0.25	0.42	0.42
Effective hole masses	0.6	~1	~1
(in units of m ₀)			

Table 2.1: Table of physical properties for 3C, 4H and 6H at 300 K.^[9, 16]

Although 6H has been the most easily prepared and studied of the SiC polytypes, contemporary research has focussed on the 3C and 4H polytypes, because they offer better material properties [13]. The reduction in phonon scattering which occurs as a result of the higher crystal symmetry results in the highest electron mobility and saturation velocity of 3C–SiC [13]. However, the bandgap is substantially lower than that of the hexagonal polytypes and this results in the maximum operating

temperatures of devices on 3C being lower and the devices suffering from higher leakage currents. The superior material properties of 4H–SiC, includes the high critical electric field and it exhibits an on–axis mobility nearly ten times that of 6H–SiC [17], make it the most commonly used in power electronic devices [13]. Furthermore, 4H–SiC has been the most suitable polytype for high temperature and high power device applications due to its larger bandgap, a higher and nearly isotropic electron mobility [18], high breakdown electric fields ($> 2 \times 10^6$ V/cm), high carrier mobilities, and relative maturity in wafer quality [19]. Further discussion on their characteristics will be described in the following section.

2.2.2 SiC characteristics

Development in SiC technology has initiated significant advances in the wafer growth technology, materials processing, electronic devices, and sensors due to its remarkable material properties [17]. The outstanding material characteristics of silicon carbide has led to it becoming one of the commonly used materials in a range of industrial engineering applications including aerospace, electronics, industrial furnaces and wear–resistant mechanical parts among others. It is increasingly recognised as a superior semiconductor in comparison to traditional semiconductor materials such as silicon and germanium due to its wide bandgap, high displacement threshold energy, high radiation hardness, low leakage current and low temperature sensitivity [20–24].

The attractive characteristics of silicon carbide detectors in terms of electrical and mechanical properties make it possible to be used in applications involving high temperature and harsh environments [17, 20, 21, 25]. High breakdown electric field; $2-4 \times 10^6 \text{ Vcm}^{-1}$, high saturation electron velocity; $2 \times 10^7 \text{ cms}^{-1}$, and high thermal conductivity; 3.6 to 4.9 W/cm K of SiC make it an ideal material for high–power device operation [13, 26]. Additionally, it is being used as a substitute for silicon in high performance electronic devices, due to its wider bandgap with acceptable bulk mobility [27]. The wide bandgap and low intrinsic carrier concentration make it possible to maintain their performance at high junction temperatures [6, 24] and consequently overcome the restrictions imposed by silicon in terms of elevated temperatures [6, 23] and high voltage blocking (approaching 10 kV) [22, 28]. The high thermal conductivity of SiC permits dissipated heat to be removed from the device more effectively than in other wide bandgap semiconductors, such as gallium nitride (GaN), whereas, high breakdown voltage make it possible to manufacture devices with thinner and more highly doped blocking layers in power devices [27].

The ultra low leakage current densities observed in SiC detectors makes them ideal for dosimeter development [21] and because of the wide bandgap, they do not require any external cooling systems to operate in high temperature ambients or to minimise the electronic noise [29, 30]. Furthermore, the material properties of silicon carbide make it a suitable material for operation in high dose and high dose rate radiation fields due to its high displacement threshold energy [6]. This is an important consideration for dosimeters in radiotherapy applications, as these often involve wide range of dose rates and hence radiation induced damage within the detector material become a crucial aspect for a precise measurements and long detector lifetimes. By taking advantage of these characteristics, 4H–SiC had emerged as a preferred detector material for the fabrication of Schottky diode radiation detectors and opens up the possibility of operating as an X–ray photon energy harvester.

2.2.3 Advantages of SiC over other semiconductor materials

Evolution of radiation detectors within the semiconductor industry began after the rapid development of germanium (Ge) and silicon (Si) radiation detectors in 1960s [31]. The early research showed that semiconductor detectors provide the same overall detection efficiency of a gas detector which has a volume that is \sim 1000 times greater, due to the increased density. For instance, the density of silicon is 2.3 g.cm⁻³ whereas the density of air is 1.3×10^{-3} g.cm⁻³ [32]. Moreover, semiconductor detectors require a lower average energy to create a electron-hole pair in comparison to ionization chambers, resulting in a higher signal-to-noise ratio [32]. Major improvements in the growth of high quality semiconductors was a major factor in obtaining high performance detectors. By the end of the 1950s, synthesis of large crystals of cadmium telluride (CdTe) had resulted in the interest in the utilisation of other compound semiconductors [31], including silicon carbide (SiC), cadmium zinc telluride (CdZn(Te)), gallium nitride (GaN) and gallium arsenide (GaAs). CdTe and CdZn(Te) have become dominant in the development of radiation detectors for X-ray and gamma ray imaging due to their high density (high carrier mobilities) and atomic number (Z) (see Table 2.2), which results in high detection efficiency at high photon energies [33]. However, due to susceptibility to polarization effects in CdTe, its usage has been widely replaced with CdZn(Te) which has higher bandgap, increased energy of defect formation and removal of polarization effect that results in a reduction in the dislocation density and hence leakage current during operation [31].

Property	Diamond	Silicon	4H–SiC	6H-SiC	GaN	GaAs	Ge	CdZn(Te)	TIBr	HgI ₂
Z number	9	14	14/6	14/6	31/7	31/33	32	48/52	81/35	80/53
Density	3.5	2.3	3.2		6.2	5.3	5.33	5.9 – 6.0	7.5	6.4
(g/cm ³)										
Band gap (E_g)	5.5	1.12	3.3	3.03	3.39	1.4	0.67	1.4 - 1.6	2.7	2.1
Electron mobility	1800 –	1450	-008	370	1000	= 8500	3900	1000	40	100
(cm^2/Vs)	2200		1000							
Hole mobility	1200-	450	-05	50	30	= 400	1900		12	4
(cm^2/Vs)	1600		115							
Saturated electron	2.7×10^7	1.0×10^7	2.0×10^7	2.0×10^7		1.2×10^7				
drift velocity (cm/s)										
e–h pair	13	3.6	7.8		8.9	4.3	2.96	4.4 – 4.7	5.9	4.2
creation (eV)										
Displacement	43	13 - 20	21.8		Ga - 20	10	30			
(eV)					N-10					
Breakdown voltage	10	0.5	4	2.4		~ 0.4				
(MV/cm)										

Table 2.2: Table of material properties of major semiconductor for use as ionising radiation detectors. [33]

Intermediate Z-materials such as GaN and GaAs have photon absorption efficiency that lie between between Si and CdTe/CdZn(Te) as shown by the plots in Figure 2.2, due to their Z-number between Si and CdZn(Te) which are 31/7 and 31/33, respectively (refer Table 2.2). GaAs has the potential to enable devices with integrated microelectronics [34]. Whilst, GaN can be considered to be particularly ideal for high temperature operation for applications that include radiation hard particle and X-ray detectors, due to its relatively wide bandgap, high atomic density, large displacement energy, and thermal stability as shown by the data in Table 2.2. Nevertheless, the limited availability of bulk substrates and the challenge of growing high quality material on non-lattice matched substrates, results in it being limited to thin layers at the present time [31]. Of the other commonly used materials, diamond has the advantage for medical imaging applications that the atomic number is closer to human tissue (Z = 6) than other semiconductors, which make it more suitable for clinical dosimetry applications [35, 36]. However, the Chemical Vapour Deposited (CVD) process used in the growth of the layers contributes to the presence of bulk defects and high concentrations of deep levels, which can give rise to priming effects, which in turn degrade the stability, reproducibility and velocity of response of the current and charge signal [35, 36].

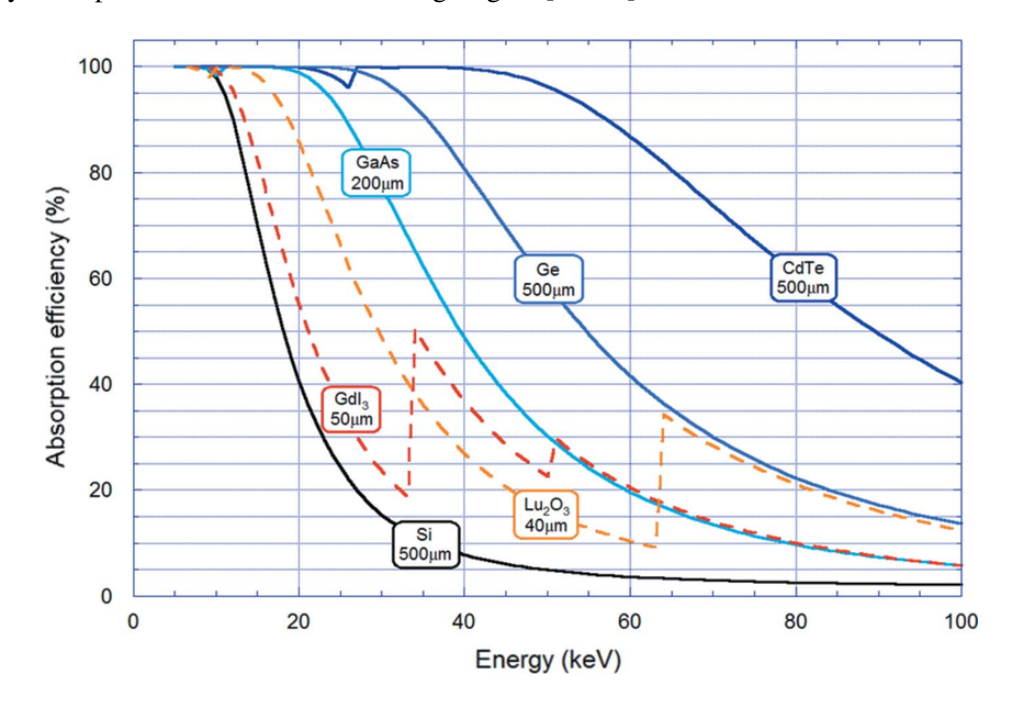


Figure 2.2: Absorption efficiency of different semiconductor detectors as a function of radiation energy.^[37]

Semiconductor detectors based on SiC are well suited for use for radiation detection, due to the outstanding material properties, including the wide bandgap (3.26 eV) that is larger than that of the conventional semiconductor detectors such as Si (1.12 eV) or Ge (0.77 eV), which results in the high radiation tolerance, low leakage current, and a capability to realize electronic devices that can

operate at temperatures significantly beyond room temperature [6]. Despite the focus on intermediate and high atomic number (Z) materials in the development of radiation detectors, silicon carbide based—diode detectors [38, 39] demonstrate excellent characteristics regarding radiation response, in terms of low leakage current, high long term stability [40] and higher resolution detection of low mass charged particle and low energy photonic radiation [41], at room and elevated temperatures as explained in section 2.2.2. Silicon carbide also offers a response ($Z \approx 10$) that is closer to human tissue than the high atomic number materials. However, a significant challenge remains for SiC, which is in the development of an ideal radiation detector for operation in low dose rate applications, such as those that are found in medical imaging and require a high signal amplitude and charge response with the incident radiation. The low–Z number of SiC results in a lower photon absorption coefficient, where the dominant mechanism is through photoelectric absorption, which is determined by the Z-number. Further discussion on the radiation interaction with the detector material will be described in the following section.

2.3 SiC Schottky diode

2.3.1 Principles of Schottky diode

Discovery of the electrical characteristics of the metal–semiconductor contact was made in 1874 by Braun, who observed behaviour of the electrical resistance which was influenced by the magnitude and polarity of the applied voltage when metal sulphides were contacted by metal points [31]. He also investigated the phenomena of a thin interface layer of extremely high resistance [31]. In the 1930s, Schottky developed the first acceptable theory to describe the behaviour of metal–semiconductor devices, which are subsequently referred to as Schottky barrier devices. This represents the use of these devices as rectifiers with noticeably nonlinear current–voltage characteristics [42]. Later in 1938, Schottky and Mott found that direction of rectification can be described in terms of electrons having to pass over a potential barrier formed by the metal–semiconductor junction and then following the normal process of drift and diffusion through the semiconductor.

A metal–semiconductor diode or Schottky barrier diode is created when a metal layer is brought into intimate contact with a semiconductor material. The metals that commonly used to form Schottky barriers on n–type silicon are molybdenum, platinum, chromium or tungsten. The choice of the combination of the metal and semiconductor determines the forward voltage of the diode only if the surface is not pinned. The condition of Fermi level pinning will be discussed in detail in section 3.2. The metal side acts as the anode and n–type semiconductor acts as the cathode of the diode,

which is produced by a junction formed at the surface of the semiconductor [43]. Referring to Figure 2.3, the Fermi levels in the metal and semiconductor will equalize when the surfaces of a metal and semiconductor come into intimate contact as a consequence of the valence and conduction bands bending as a result of charge equalisation at the junction [31] as illustrated in Figure 2.3 (b). The metal and the dopant atoms on the n-side of the depletion region become negatively and positively charged ions, respectively. This effect generates a potential, known as the built-in-potential, $\phi_{bi} = \phi_m - (\chi + \phi_n)$ in the depletion region which acts as a barrier to the diffusion of holes and electrons. This barrier allows holes to flow from the metal to the semiconductor, but not electrons [31].

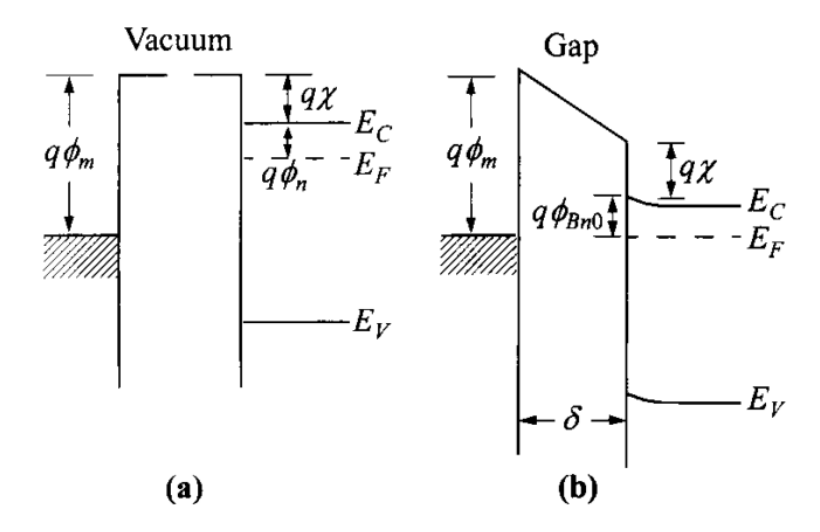


Figure 2.3: Schematic diagram of energy band structure of the metal-semiconductor. [44]

As a result, a work function whose height is defined as the energy difference between the Fermi level, E_F and the respective majority carrier band–edge at the interface, that is the valence–band maximum, E_V for p–type or conduction–band minimum, E_C for n–type semiconductors [31, 44]. It can be denoted by $q\phi_m$ for the metal and equal to $q(\chi + \phi_n)$ in the semiconductor, where $q\chi$ is the electron affinity measured from the bottom of the conduction band E_C to the vacuum level, and $q\phi_n$ is the energy difference between E_C and the Fermi level [44]. The barrier height can be expressed as the difference between the metal work function and the electron affinity of the semiconductor, $q\phi_{Bn0} = q(\phi_m - \chi)$. However, this equation cannot be realised experimentally due to the sensitivity of the metal work function $q\phi_m$ on surface contamination [44]. Additionally, the barrier height can be affected by the presence of interfacial layers and interface states which lead to deviation of the experimental barrier height from the ideal condition [44].

2.3.2 Current transport process in Schottky diode

The generation of current inside the depletion region of a semiconductor depends on a number of factors. The fundamental current transport mechanism is due to majority carriers inside the depletion region. The current transport processes that occur under forward bias are (1) emission of electrons from the semiconductor over the potential barrier into the metal which is the dominant process for Schottky diode with moderately doped semiconductors operated at moderate temperature, (2) quantum mechanical tunneling of electrons through the barrier which is related to heavily doped semiconductor and responsible for the formation of Ohmic contacts, (3) recombination in the space charge region, (4) diffusion of electrons in the depletion region and (5) holes injected from the metal into the semiconductor [44]. The illustration of all the current transport processes are shown schematically in Figure 2.4.

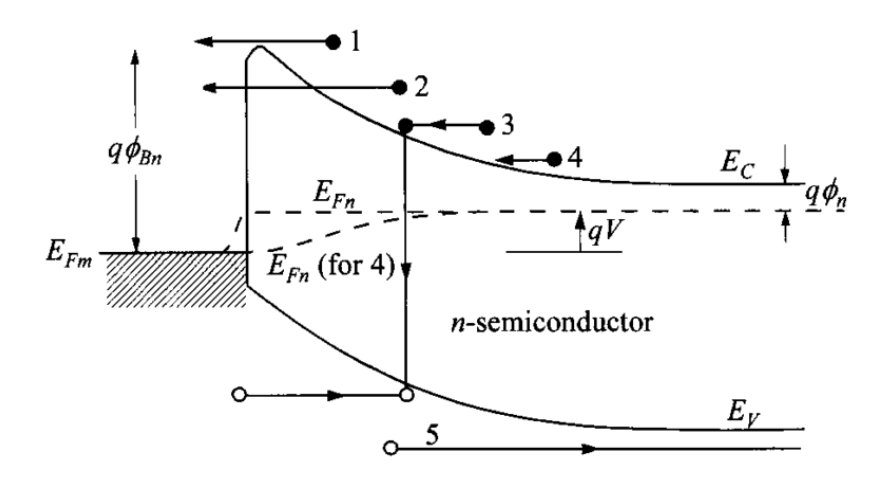


Figure 2.4: Schematic diagram of five basic transport processes under forward bias which are (1) thermionic emission, (2) tunneling, (3) recombination, (4) diffusion of electrons, and (5) diffusion of holes.^[44]

Since the epilayer used in this work has a low dopant concentration ($N_D = 1.00 \times 10^{15}$ cm⁻³), thermionic–emission theory is the dominant current transport process of the fabricated diodes. During conduction, the current flows as a result of the electrons that are thermally excited over the barrier. Following Bethe, thermionic emission theory can be derived based on the assumption that a) the barrier height $q\phi_{Bn}$ is much larger than kT, b) thermal equilibrium is established at the plane that determines emission and c) the existence of a net current flow does not effect the equilibrium so that one can superimpose two current fluxes – one from metal to semiconductor, the other from semiconductor to metal, each with different quasi Fermi level [44, 45]. By neglecting series and shunt resistance, the thermionic current–voltage (I–V) relationship of a Schottky barrier diode can be expressed as

$$I = I_0 \left(\exp\left(\frac{qV}{nkT}\right) - 1 \right) \tag{2.1}$$

and

$$I_0 = AA^*T^2 \exp\left(\frac{-q\Phi_B}{kT}\right) \tag{2.2}$$

where I_0 is the saturation current, n is the ideality factor, k is the Boltzmann's constant, Φ_B is the barrier height, A is the diode area and A^* is the Richadson's constant $(A^* = 4\pi q k^2 m^*/h^3)$.

The ideality factor takes into account the effects which contribute to nonideal devices [42]. A nonuniform Schottky diode over the contact area results in barrier height imhomogeneities, which lead to n > 1 [42]. The value of n decreases with temperature and the variation with reverse bias can also be explained by this condition [42]. Further discussions of the I–V characteristics at room and elevated temperatures will be described in details in following chapters; Chapters 3 and 4.

Based on the relationship of the space charge region width, W_d and dopant concentration ($W_d \propto N_D^{-1/2}$), high dopant concentration will result in the formation of a narrow space charge region that results in electron tunneling from the metal to the semiconductor and from the semiconductor to the metal [42]. The tunnelling of the electron comprises contributions from thermionic–field emission and field emission which are the dominant conduction mechanisms for the intermediate and high doping densities, respectively [42]. Thermionic–field emission occurs when the carriers are thermally excited to an energy where the barrier is sufficiently narrow for tunnelling to take place, whilst, field emission occur when the barrier is sufficiently narrow at or near the bottom of the conduction band for the electrons to tunnel directly [42], as shown in Figures 2.5 (b) and (c), respectively.

2.4 Radiation interaction detection properties

2.4.1 Detection properties

In order to detect the radiation, it has to interact with the medium that forms the detector. Electronic detectors act as a detection medium which are capable of detecting radiation, and hence generate a measurable signal through a small number of interaction mechanisms [43]. The generated electrical signal can be used to characterize the radiation and its properties. Knowledge of the dominant mechanism by which radiation interacts and hence loses energy in matter is a prerequisite to

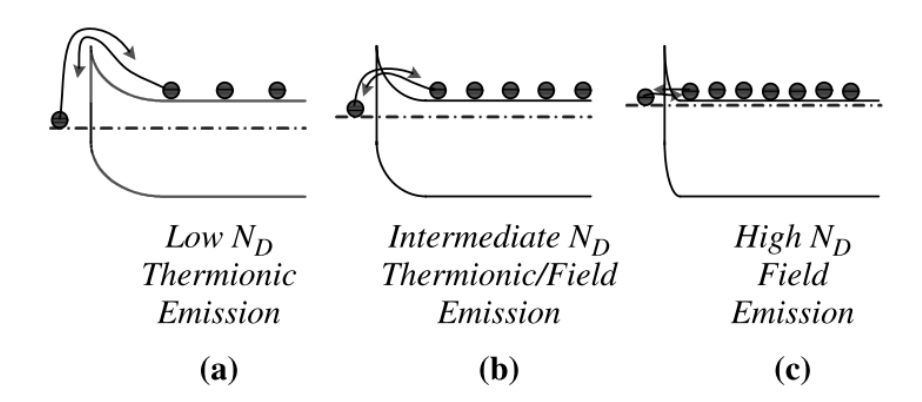


Figure 2.5: Conduction mechanism for low, intermediate and high dopant concentration of n-type substrate.^[42]

understand the response of a specific type of detector [46]. Different types of radiation particularly charged particles and photonic (uncharged) will have a different mechanisms of interaction with matter. The dominant interactions include linear energy transfer (LET), which can be described in terms of range and the linear attenuation coefficient. When an X–ray beam passes through any medium or detector, there are three possible interactions that dominate the energy loss [47]:

- 1. penetrate without interacting,
- 2. interact with the medium and be completely absorbed by depositing its energy and
- 3. interact and be scattered or deflected from its original direction and deposit part of its energy.

There are two different mechanisms through which photons deposit their energy which are photoelectric absorption (where the photon loses all its energy to the lattice) and Compton scattering, where the incident photons lose a portion of their energy to the lattice, and the remaining energy is transferred to other carriers. The removal of energy from the incident photons through either photoelectric or Compton scatter interaction is known as attenuation. There is probability to eject an electron and ionize the matterial if the energy of the incoming photons exceeds the binding energy of the electrons in the material through which the radiation is passing. There are two factors that determine the penetration ability of the incident photon, which are the initial energy and the density of the material [47]. The lower the energy of the incident X–ray photons, the lower the penetration ability in comparison to those higher–energy radiation (which is often labelled as hard radiation) [47]. Therefore, the different incident energies of the radiation that are typically found in medical applications will lead to different penetrating ability, which result from the different absorption mechanisms that occur in the semiconductor and these have to be considered in the design of new detector or dosimeter structures [43].

The mechanism which transfers the photon energy to the medium generates free (conduction) electron—hole pairs, which have kinetic energy ranging from relatively low value to values slightly lower than the energy of the incident photons [47]. The electron will pass through and interact with the material by transferring this energy, which can potentially cause ionization of other electrons or an excitation in the material as illustrated in Figure 2.6. The energy losses as the electrons pass through the medium can be related to the linear energy transfer (LET), which may be defined as the amount of energy locally transferred to the medium per unit of distance travelled ($keV/\mu m$) [48]. Therefore, the rate at which the electron transfers the energy to the material depends on the the kinetic energy (velocity) of the electron and it is normally inversely related to the electron velocity [47]. The velocity decrease as the electron passes through the medium and loses energy until all of its energy is dissipated. The value of the LET will increase as the electron velocity reduces, before it is loses its excess energy. Therefore, the effectiveness of a particular radiation type in producing biological damage is often described in terms of the LET of the radiation and this is commonly used in dosimetry [43, 47]. High LET radiation such as proton and heavy charged particles will cause more damage to the medium that they pass through in comparison to low LET such X–ray and γ –rays.

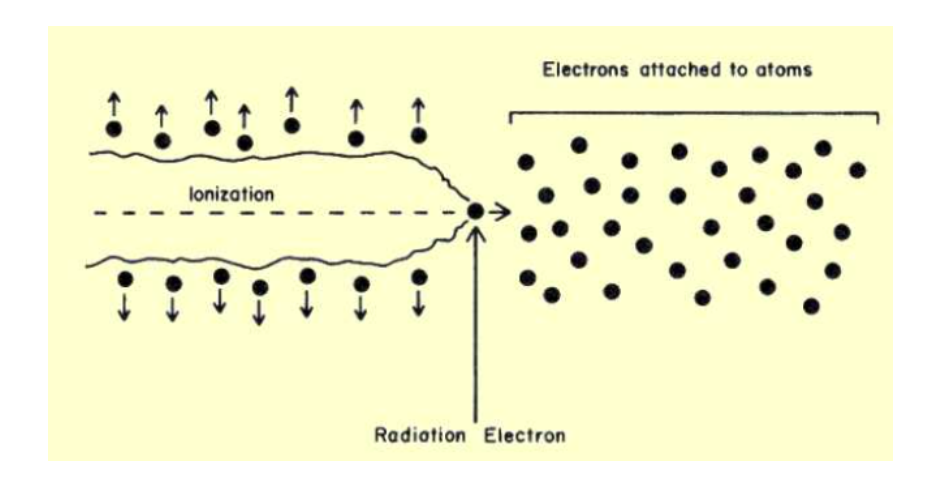


Figure 2.6: Ionization produce by a radiation electron within the medium.^[47]

The medium with which the photon interacts can also be described by the linear attenuation coefficient (μ) and this describes the fraction of photons interacting per unit thickness of the detector material [47]. When incoming photon beam pass through any medium, it will lose part of its energy due to attenuation. The relationship of energy loss in the medium can be explained by the Beer–Lambert law as expressed in Equation 2.3, where I is the remaining intensity of the beam after interaction in thickness, x of a medium, I_0 is the initial incoming beam intensity and μ is the linear attenuation coefficient [49]. The rate of the photon attenuation by the material depends on the atomic number, atomic mass and density of the material [48]. Otherwise, the linear attenuation coefficient

is directly related to density, ρ and the mass attenuation coefficient (μ_m), where $\mu = \mu_m \rho$. The mass attenuation coefficient (μ_m) increases with increase in the atomic number of a medium.

$$I = I_0 \exp\left(-\mu x\right) \tag{2.3}$$

The total distance that the photon can travel in the medium before losing all of its energy is defined as the path length and it is inversely proportional to the LET and linear attenuation coefficient. The total attenuation rate of any medium is related to the photoelectric and Compton interactions which can be expressed as [47]:

$$\mu \text{ (total)} = \mu \text{ (photoelectric)} + \mu \text{ (Compton)} + \mu \text{ (pair production)}$$
 (2.4)

The probability of the different interactions occurring within the material depends on the density of the material and in general [47]

- 1. Photoelectric interactions occur most frequently when the electron binding energy is slightly less than the photon energy.
- 2. Compton interactions occur most frequently with electrons with relatively low binding energies.

2.4.2 Radiation interaction with matter

There are two main interactions mechanisms which will determine the distance travelled by the incident radiation that are relevant to the energies used in this study, namely the photoelectric effect and Compton scattering. The relative contribution of the different mechanisms that are involved when radiation interacts with the detector material and hence contribute to the total attenuation can be observed from Figure 2.7. Whenever a beam of photons of sufficient energy passes through a material, not all of the photons in the beam undertake the same type of interaction [43]. Different materials will have different threshold energy and regions of high cross–sections which results in that mechanism dominating the characteristics [43]. Both processes lead to the partial or complete transfer of the photon energy to the electron, which results in the incident photon undergoing scatter over a range of angles or being completely absorbed [46].

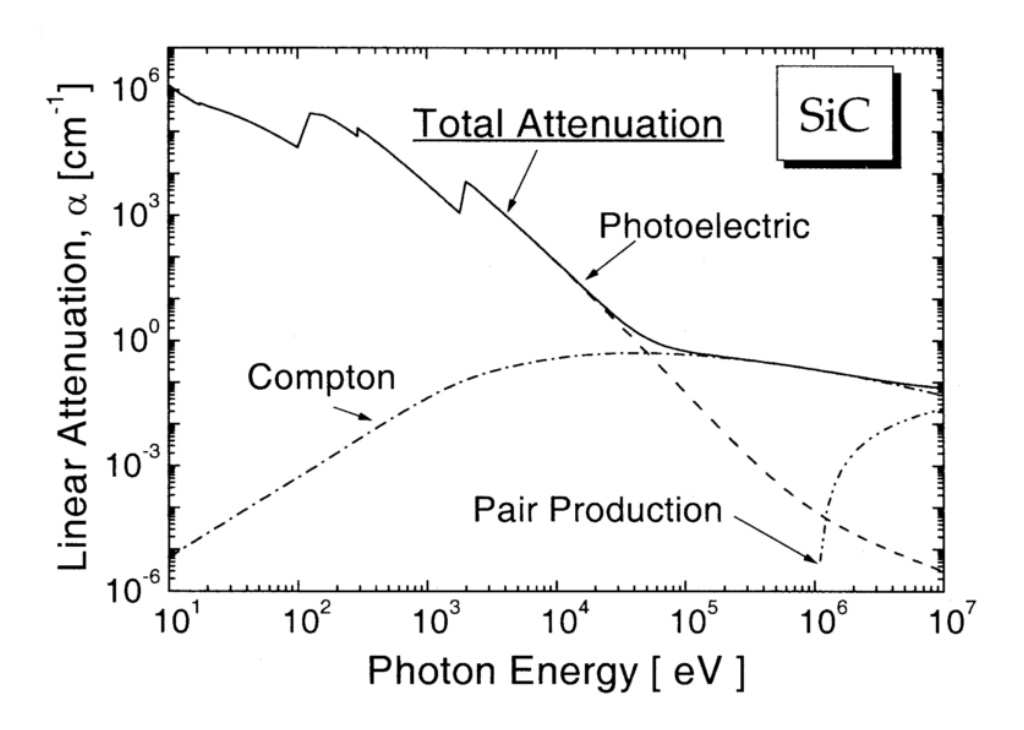


Figure 2.7: The relative contribution of the different mechanisms of radiation interaction in SiC, which contribute to photoelectric effect, Compton scatter and pair production.^[50]

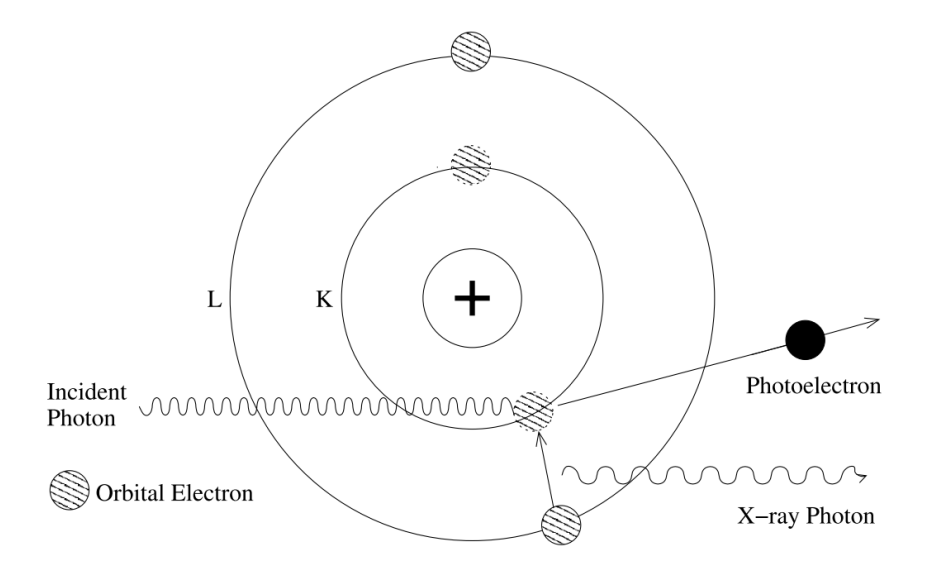


Figure 2.8: Schematic illustration of the photoelectric effect in a free atom. The electron from higher energy level will fill the gap if the K–shell electron is knocked of by the incident photon. The energy of emitted photon will be equal to the different of the two energy levels.^[43]

In the photoelectric absorption process, the incident photon transfers all of its energy to the absorber atom, resulting in the photon being completely absorbed. The result of this interaction is the generation of an energetic, free photoelectron, which is ejected by the atom from one of its bound shells as can be observed in Figure 2.8. The most probable origin of the photoelectron is the most

tightly bound or K-shell of the atom [46]. This interaction is possible only when the photon has sufficient energy to overcome the binding energy and remove the electron from the atom [43]. After the interaction, the photoelectron will have energy, E_e given by [46]

$$E_e = hv - E_b \tag{2.5}$$

where E_b represents the binding energy of the photoelectron in its original shell.

The ionisation of the electron creates a vacancy in the bound shells and this hole will be rapidly filled through capture of a free electron from the adjacent shell (probably the L or M shells). The outcome from this reaction is that one or more characteristic X–ray photons will be generated. The cross section for this reaction has a strong Z dependence, that is the probability of photoelectric effect increases rapidly with the atomic number of the target atom. In addition, the mechanism also shows a strong inverse relationship with energy of the incident photon. The predominant interaction of low energy gamma rays can be observed from the data in Figure 2.7. Specifically, these dependences can be expressed as [43]

$$\sigma_{pe} \propto \frac{Z^n}{E_{\gamma}^{3.5}} \tag{2.6}$$

where n lies between 4 and 5.

The strong dependance of the photoelectric effect on the Z number, resulted in the intense research into the possibility of high–Z being developed for low energy dosimeter applications. However, the main disadvantage of high–Z number materials is that they cannot be considered as tissue equivalent material, because their Z number is significantly higher than that of human tissue (Z = 6). This is imperative in dosimetry response from the detector should be mimicking the interactions occur in the human body to precisely estimate the radiation dose for each procedure. The relationship also suggests that the probability of the photoelectric effect to occur decreases sharply with increasing incident photon energies. For high energy photons, Compton scattering becomes the dominant absorption mechanism, as can be observed by the plot in Figure 2.7.

Compton scattering which was first discovered and studied by Compton in 1923 is an inelastic scattering of photons from free or loosely bound electrons which are at rest [43]. It is more probable than photoelectric effect described previously, if the energy of the incident photon is higher than the binding energy of the innermost electron in the target atom. During the interaction, the incoming photon will be deflected through an angle θ with respect to its original direction and transfer a portion of its energy to the scattered electron (which is assumed to be initially at rest) which is commonly

known as a recoil electron [46]. This is shown by the schematic illustration in Figure 2.9. The relationship in Equation 2.7 shows that the Compton interaction not only depends on the energy of the incoming photon ($E_{\gamma 0}$) but also the scattering angle, since there is a possibility at all angles of scattering [43, 46]. This can be expressed by the conservation of energy and momentum given by

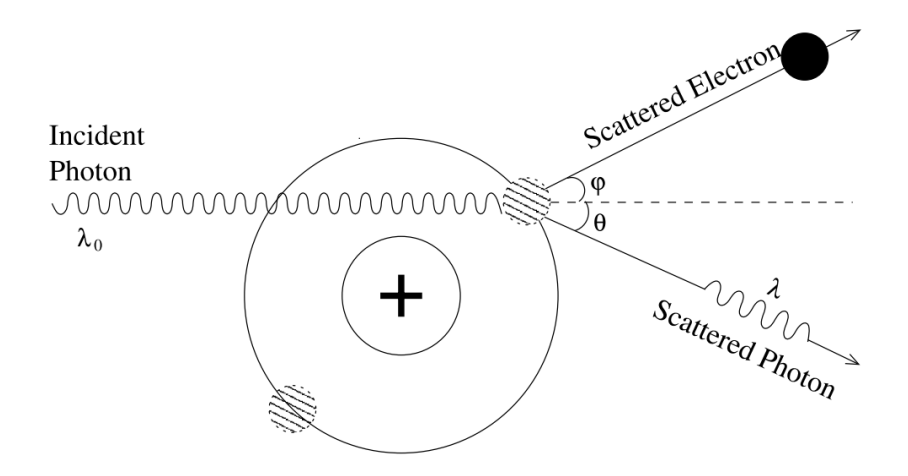


Figure 2.9: Schematic illustration of the Compton scattering of a photon having energy $E_{\gamma 0} = hc/\lambda_0$ from a bound electron. Some of the energy of the incident photon goes into knocking the orbital electron out of its orbit.^[43]

$$E_{\gamma} = E_{\gamma 0} \left[1 + \frac{E_{\gamma 0}}{m_0 c^2} (1 - \cos \theta) \right]^{-1}$$
 (2.7)

where $(E_{\gamma 0})$ is the energy of the incoming photon and m_0c^2 is the rest–mass energy of the electron (0.511 MeV).

The probability of Compton scattering per atom of the absorber depends on the number of available electrons as scattering targets and therefore increases linearly with Z. The angular distribution of scattered gamma rays is predicted by the Klein–Nishina formula for the differential scattering cross section $d\sigma/d\Omega$ [46]:

$$\frac{d\sigma}{d\Omega} = Zr_0^2 \left(\frac{1}{1 + \alpha(1 - \cos\theta)} \right)^2 \left(\frac{1 + \cos^2\theta}{2} \right) \left(1 + \frac{\alpha^2(1 - \cos\theta)^2}{(1 + \cos^2\theta)[1 + \alpha(1 - \cos\theta)]} \right)$$
(2.8)

where Z is the atomic number of the medium, $\alpha \equiv hv/m_0c^2$ and r_0 is the classical electron radius.

Due to the change in the photon direction after the interaction with the electron, Compton scattering results in a portion of the incident radiation 'bouncing off' or being fully scattered by the material [47]. Therefore, material within the primary X–ray beam which includes the detector itself becomes the actual source of scattered radiation [47]. This condition contributes to an undesirable consequence that results in an increase in the detector noise (unwanted additional signal from the secondary radiation) and hence degrades signal—to—noise ratio of the detector's performance.

2.5 Semiconductor radiation detector

2.5.1 Principle of radiation detector

In semiconductor detectors, the charge carriers are electrons and holes and the generation process is similar to that observed in the ionization process in gases. The number of electron-hole pairs is determined by the average energy required to produce a single electron-hole pair in the detector [46]. The sensitivity of semiconductor detector is typically about 10⁴ higher than the gas filled detector [48], which in part can be attributed to the lower energy needed to produce an electron-hole pair, which is typically 4 to 8 times lower [43] than the ionisation energy in gases. In addition, the higher density of semiconductors in comparison to air (typically three orders of magnitude higher) leads to significantly higher number of charge carries produced than in gases and this facilitates the miniaturization of radiation monitoring instrumentation [48]. Therefore, semiconductors are considered to be superior to gaseous detectors in terms of resolution and sensitivity [43].

Incident radiation creates electron hole pairs when it interacts within the depletion region of the radiation detector as illustrated in the schematic diagram of radiation incident inside the detector material shown in Figure 2.10. The generation of electron–hole pairs is depicted schematically in Figure 2.11. The electrons in the valence band will jump to the conduction band when the electron in the material receive sufficient energy from collisions with the photon. If the incoming photons had more than enough energy, few electrons may even jump from the deeper bands, which are below the valence band. Both processes will leave holes in the valence and deeper bands and this results in an increased number of electrons in the conduction band. Whilst, de–excitation steps occur when electrons move to the bottom of the conduction and holes move to the top of the valence band [51]. This condition cause an additional electron–hole pairs to be generated and there is also some energy imparted to the crystal lattice structure due to the conservation of momentum that generates phonons [51].

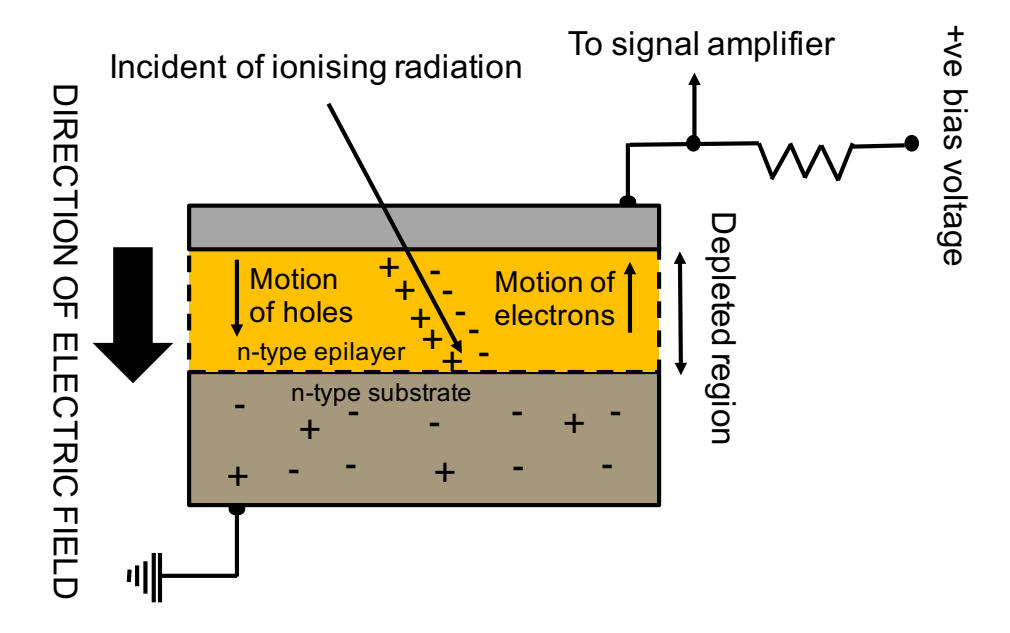


Figure 2.10: Schematic diagram of radiation interaction inside the depletion region which leads to creation of electron–hole pairs. The collection of the charges created operated by the electric field applied.

A small leakage current flows in the depletion region in the absence of radiation, due to the low concentration of free charge carriers present, particularly at room temperature and below. The application of a high electric field to the Schottky contact ensures that the charge is separated after generation and this allows the detection of a current at the external terminals of the detector. Hence, the application of a reverse bias across the junction results in charge (electrons and holes) flow in opposite directions and constitutes an electrical current generated in the reverse direction in the diode as can be observed by the I–V characteristics shown within the reverse bias voltage range in Figure 2.12. The magnitude of this current can be described in terms of the energy deposited by the incident radiation within the depletion region. Increasing the incident radiation flux (or dose rate) will increase the number of electron–hole pairs generated in the depletion region and therefore increase the generated current.

2.5.2 SiC as a semiconductor radiation detector

Substantial advantages of semiconductor radiation detectors over other types of detectors had led to the exploration and development of silicon carbide radiation detector for over a decade in a range of applications, including space exploration, nuclear reactor monitoring or medical diagnostic and radiotherapy. The detectors have shown a response to a range of radiation types, including X–rays,

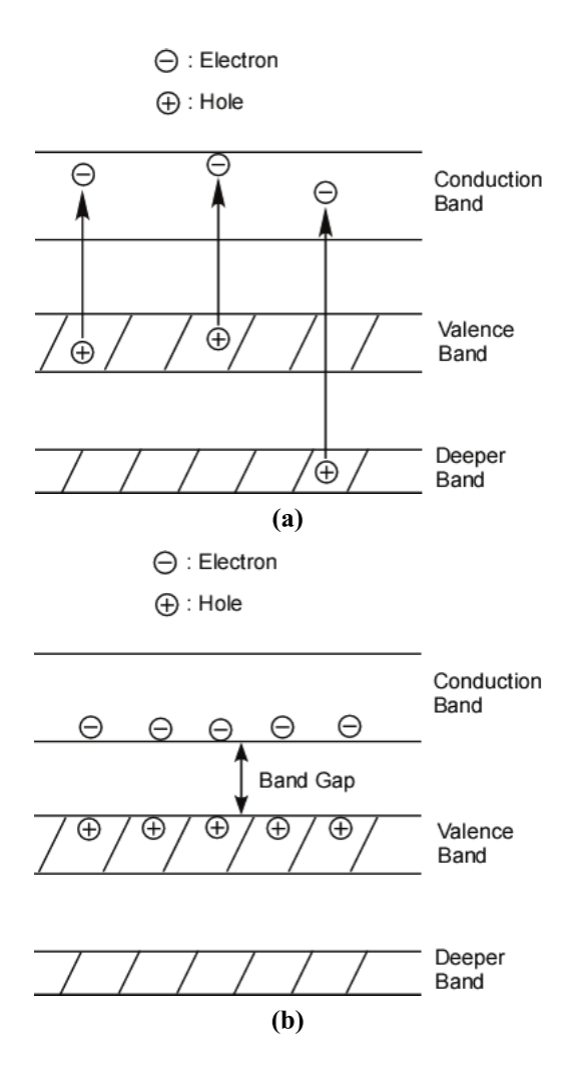


Figure 2.11: Schematic diagram of generation of electron hole pairs by (a) excitation and (b) de-excitation process.^[51]

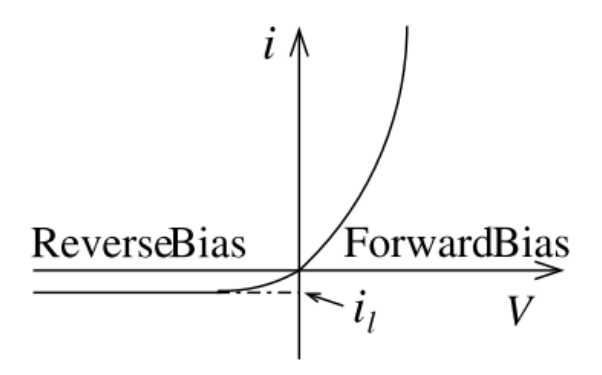


Figure 2.12: Plots of the forward and reverse bias of the I–V characteristics when radiation incident on the detecting medium. Electrical current can be observed to generate in the reverse direction by the application of reverse bias.^[43]

gamma rays, alpha [52, 53], beta [54], protons [55, 56] and neutrons [55, 57, 58]. Additionally, solid state detectors are suitable for a wide range of applications, because it is possible to grow semiconducting materials with a wide range of physical and electronic properties such as bandgap, atomic number, and density to tailor the detectors to the specific radiation type to be measured [59]. The potential to develop bespoke detectors for a given application that involves high radiation dose based on wide bandgap semiconductors can leverage the advances in SiC fabrication techniques that have been developed to realise high quality SiC microelectronic devices for use in power electronic circuits, including thick, lightly doped epitaxial layers [8].

The interest in radiation detectors operating at room temperature and beyond [60, 61] has contributed to the significant development of compound semiconductor detectors with wide bandgaps [59]. Revolution of the radiation detector development started over fifty years ago where Babcock had investigated the use of SiC solid–state diodes for the detection of neutrons and alpha particles [8]. Their findings found that diodes were responsive to alpha particles at temperatures up to 700 °C. Detection at temperatures lower than 700 °C did not show a strong temperature dependence, however the data showed that the pulse height of the alpha–induced signal increases with increasing temperature [8].

In addition, Ruddy et al. also reported that a strong signal was observed when both Schottky and p-n junction diodes were exposed to alpha radiation without an external bias voltage [8]. The current generated by the detector gave a linear response as a function of dose rates over the range of 700 to 40 000 rad-Si h^{-1} . This was attributed to the high quality of the 4H-SiC epitaxial layers when used in high temperature and radiation fields [8]. Their finding demonstrates the possibility of SiC detectors to be used in applications of elevated temperatures and/or high radiation fields [8]. These findings are supported by the work of Seshdari et al. who studied the possibility of SiC-based nuclear particle detectors in the same high radiation environment but focused more on the evolution of the electrical characteristics of the diode [20]. They found that neutron damage prevented the self-biased operation observed in the alpha detection work of Ruddy et al. after exposure to high fluences and this was caused by the degradation of the charge collection efficiency [8, 20]. However, no shift in the energy resolution, detector efficiency and noise characteristics were observed in the data [20]. Whilst, R. R. Ferber and G. N. Hamilton examined the possibility of using SiC p-n junction diodes to monitor the behaviour of a low-power nuclear reactor, with a focus on the neutron response. They found that diodes coated with ²³⁵U showed a good level of agreement between the neutron flux profile measurement with that performed using conventional gold foil activation techniques [8, 62]. The neutron flux determined from the diode showed a highly linear response with the reactor power range between 0.1 W to 1 kW [62].

In the 21st century, Bertuccio and Bruzzi have determined the advantages of SiC detectors in medical applications, particularly in the field of radiation dosimetry. Response of their fabricated detectors have been tested in terms of both linearity and sensitivity. In addition, Bertuccio et al. studied the behaviour of pixellated detectors and the resulting noise characteristics of the detectors at elevated temperatures. In contrast, Lees et al. investigated the potential of SiC for the development of X–ray detectors [23, 25, 63, 64] that focused on low energy radiation. One notable finding is that there is no increase in leakage current observed between pre and post proton irradiated devices of semi–transparent SiC Schottky diode (STSSD), however, there is marked increase of leakage current after a subsequent irradiation of 10¹³ protons cm⁻² [25]. C–V measurements taken before and after irradiation showed unchanged barrier height, while the ideality factor slightly decreases after exposure [25]. X–ray measurements on the STSSD showed that second irradiation of X–ray caused the spectral peak become less distinct, affected by the degradation of spectral performance and increase in low level noise [25].

Meanwhile in 2011, Bertuccio *et al.* found that current density of a SiC pixel X–ray detector increases with the temperature for two different bias voltages [30]. The energy spectrum acquired was unaffected by the changes in the range of temperature [30]. They suggested that preamplifier noise and stray capacitances need to be reduced in order to improve the system performance [30]. Conversely, three years later Bertuccio *et al.* studied the electrical and dosimetric properties of SiC for photon beam applications [21]. They investigated and compared the characteristics of a SiC dosimeter prototype with three commercial silicon dosimeters [21]. They found that leakage currents of SiC diodes are negligible within the temperature range of interest for dosimetry in radiotherapy and the increase after irradiation is extremely low value for a semiconductor diode operating at room temperature [21].

2.6 Alpha spectroscopy measurements with ²⁴¹Am

2.6.1 Spectroscopic detection system

Alpha spectroscopy measurements have been performed in order to study the detection properties of the fabricated Schottky diode. The results are presented in section 5.2. The spectroscopic detection system that was used during the measurement will be discussed in this section. The crucial part in extracting useful information from a detector is the signal processing where signal obtained from the channel in a detector array must be amplified and processed for storage and analysis [65]. The important information with respect to detection and measurement of radiation are the amplitude

and the timing of the output pulse [43]. However, only the amplitude of the output pulse will be considered in this study. The amplitude information allows the determination of the energy deposited by the incoming radiation, which is generally known as energy spectroscopy. In this detection system, the height of the output pulse is proportional to the energy delivered by the incident radiation, and the energy spectrum of the radiation can be determined by counting pulses of different amplitudes [46]. The detection system utilised in this study includes the preamplifier and multi–channel analyser (MCA) as as shown schematically in Figure 2.13. Signals from the radiation incident on the detector can not be directly digitized or even counted, due to the narrow width and lower amplitude of the analog signal pulse produced [43]. Hence, a preamplifier is required to amplify the signal before it is passed to the MCA. The two main purposes of the preamplifier is to amplify the low level signal as it comes out of the detector and to match the detector and external circuit impedances [43].



Figure 2.13: The signal processing of the detection system of alpha spectroscopy. [43]

A multi-channel analyser was used to count all the pulses incident inside the detector medium and then convert them into the total radiation intensity [46]. A MCA consists of an array of single channel analyzers with adjacent windows and has either 512 or 1024 channels each, which corresponds to a specific range of pulse heights [43]. The number of channels will determine the energy resolution of the spectrum obtained. The spectrum commonly referred to as pulse height spectrum obtained corresponds to the energy spectrum of the radiation, since the pulse height is proportional to the energy deposited by the incident radiation. Most multi-channel analyzers can be operated in two different modes and one of the mode is the pulses are counted with respect to some other parameter. The process starts with a logic pulse that starts incrementing the counts in the first memory location and it continue until another logic pulse arrives and move the counting to the next memory location [43]. The logic pulses can correspond to any parameter of interest, and for the case of alpha spectroscopy it measures the total intensity which corresponds to the height of the amplitude.

2.6.2 Alpha particle detection properties

The alpha-emitting radioisotope; ²⁴¹Am has been used to measure the spectroscopic performance of the fabricated Schottky diodes. An alpha particle interacts with the electron cloud in the detector

through Coulomb interactions. Coulomb scattering also known as Rutherford scattering, can be described in terms of the Coulomb force between the incident particle and the target nucleus. It was first discovered by Lord Rutherford which explain the elastic scattering of a heavy charged particle from a nucleus [43]. The discovery initiated after he observed that the majority of α -particles passed through gold foil undeflected while very few deflected at very large angles from their original direction of motion [43].

When passing through a medium, an alpha particle will excite an energetic electron from its bound state and the energetic electron goes on to create further ionization as illustrated in Figure 2.14 [66]. The interaction may lead to secondary and tertiary interactions, where the secondary electron defines the length of the track for the alpha particle ionization can take place and cause further ionization [66]. The ionization produced by an alpha particle along the track in a medium causes greater amount of ionization in its path until it reaches the highest point as depicted in Figure 2.15 (described by a Bragg curve). The particles will lose almost all of their energy after that point and quickly become neutralized by attracting electrons from their surroundings [43]. The interaction of alpha particle within the medium are governed by the Bethe Bloch stopping power equation which can be expressed as [43]

$$\left[-\frac{dE}{dx} \right]_{\text{Bethe-Bloch}} = \frac{4\pi N_A r_e^2 m_e c^2 \rho Z q^2}{A\beta^2} \left[\ln \left(\frac{W_{\text{max}}}{I} \right) - \beta^2 \right]$$
 (2.9)

where N_A is the Avogadro's number ($N_A = 6.022 \times 10^{23} \text{ mole}^{-1}$), r_e is the classical radius of electron ($r_e = 2.818 \times 10^{-15} \text{ m}$), m_e is the rest mass of the electron ($m_e = 9.109 \times 10^{-31} \text{ kg}$), Z is the atomic number of the medium, ρ is the density of the medium, q is the electrical charge of the ion, A is the mass number of the medium, I is the ionization potential of the medium, β is the relativistic factor and W_{max} is the maximum energy transferred in the encounter, $W_{max} = 2m_e c^2 \beta^2/(1-\beta^2)$.

The range of the alpha particle is determined by the energy loss along the track known as linear stopping power. Linear stopping power depends on the electron density of the stopping material, where materials with lower density provide a lower stopping power than higher density materials [66]. To eliminate the dependence of the linear stopping power on the density, mass stopping power was introduced which is the linear stopping power divided by the density of the absorbing medium [48]. The mass stopping power is similar for similar Z materials [48]. The units for the linear and mass stopping powers are MeV/cm and MeVcm²/g, respectively. There are two types of stopping power which are known as collision (ionization); resulting from interactions of charged particles with atomic orbital electrons and radiative; resulting from interactions of charged particles with atomic nuclei [48].

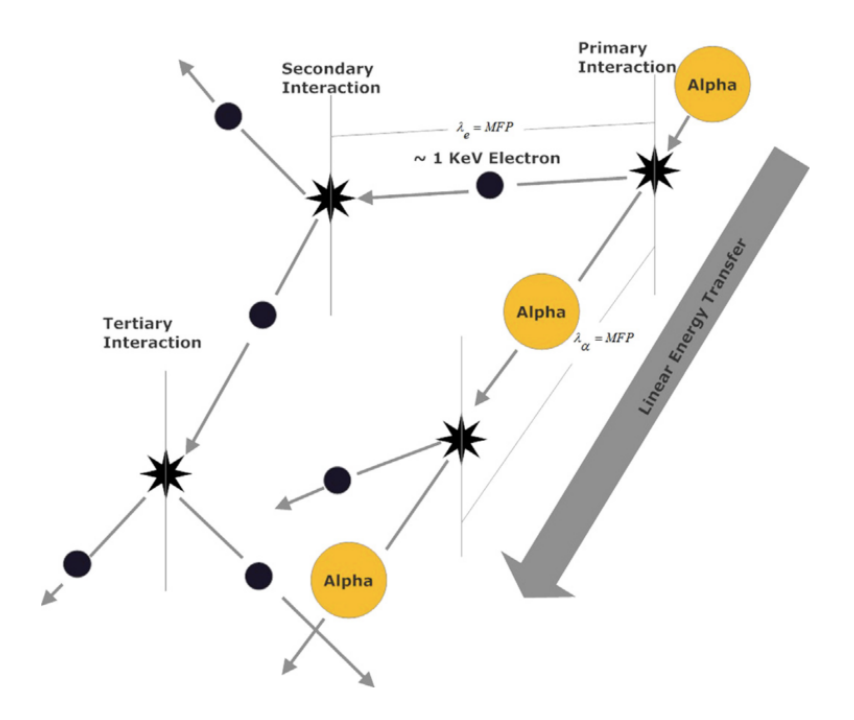


Figure 2.14: Alpha particle interaction while pass through the detector medium. It has a linear trajectory through matter and loses energy through Coulomb collisions with electrons in the cloud. These electrons are energetic and can undergo secondary, tertiary and high order interactions as they lose energy.^[66]

2.7 Energy scavenging in radiation environments

2.7.1 Principles of X-ray photon energy harvester

The principle operation of energy scavenging in X–ray environments is similar to that of the radiation detector. Direct energy conversion systems generally use the ion pairs generated in the material to generate current. The electron–hole pairs generated inside the detecting medium can be observed in the schematic diagram in Figure 2.16. The incident X–rays will penetrate through the Schottky contact and reach the depletion region, creating electron–hole pairs through collisions, excitations and ionization as explained in section 2.4.1. It is important to maximize the separation of the generated electron–hole pair to minimise recombination because recombination of the electron–hole pair will lead to a reduction of the maximum power that can be generated by the energy harvester [51].

To increase the collection efficiency of the electron-hole pairs created in the depletion region, the majority of the incident radiation needs to be absorbed within the depletion region, as opposed to beyond it. However, the energy of the generated carriers may also lost due to collisions with other electrons or due to lattice vibrations resulting in a temperature increase [51]. The electron-hole pairs

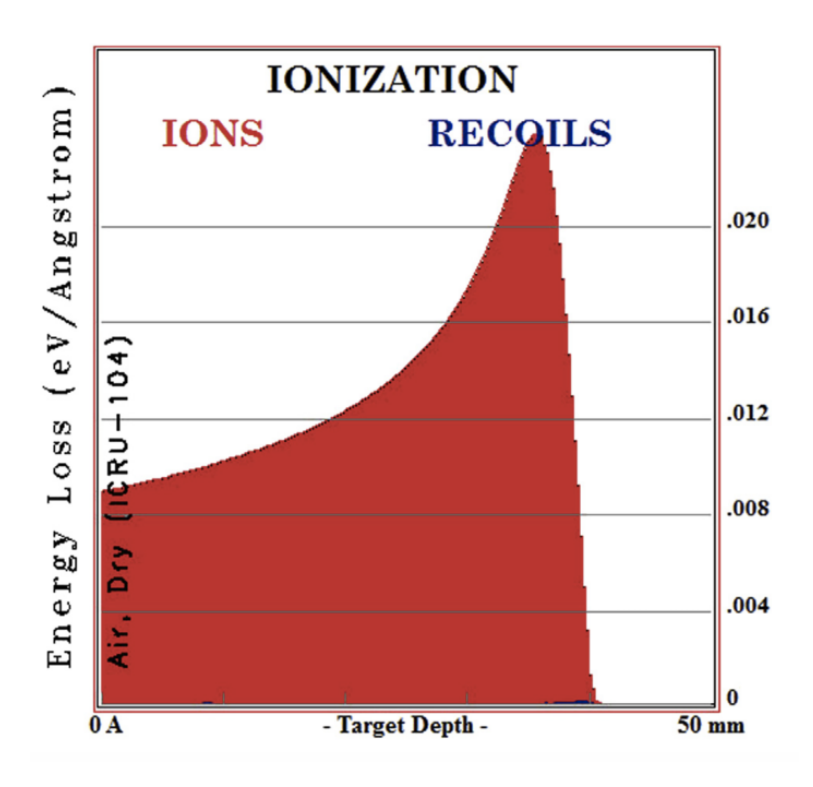


Figure 2.15: Simulation of the ionization produced in dry air by 5.4 MeV alpha particle using SRIM2011 model software depicted the Bragg curve at the end of the range.^[66, 67]

created in the depletion region will be swept across to each side of opposite polarity as shown in Figure 2.17. This can be driven by the built–in potential in the space charge region, which acts as barrier for diffusion of the holes and electrons. The electric field in the depletion region will result in the electrons moving to the cathode (*n*–type region) and the holes to the anode side (metal contact). The movement of charge generates a current, which is similar to the operating principle of a conventional photovoltaic cell.

2.7.2 Factors affecting the performance of X-ray photon energy harvester.

The capability of the fabricated Schottky diodes to operate as X–ray photovoltaic cells was tested and the data analysis is presented in Chapter 5. The characteristics of an X–ray photon energy harvester depends on a number of parameters that can be optimised during the fabrication process. The main parameters to increase the efficiency of the energy conversion from incident photon to electricity is the charge collection efficiency. Charge collection efficiency can be improved by increasing the depletion width, the wider the depletion region, the higher the number of electron–hole pairs that are generated [51]. The charge collection efficiency depends on the drift length of the charge carrier,

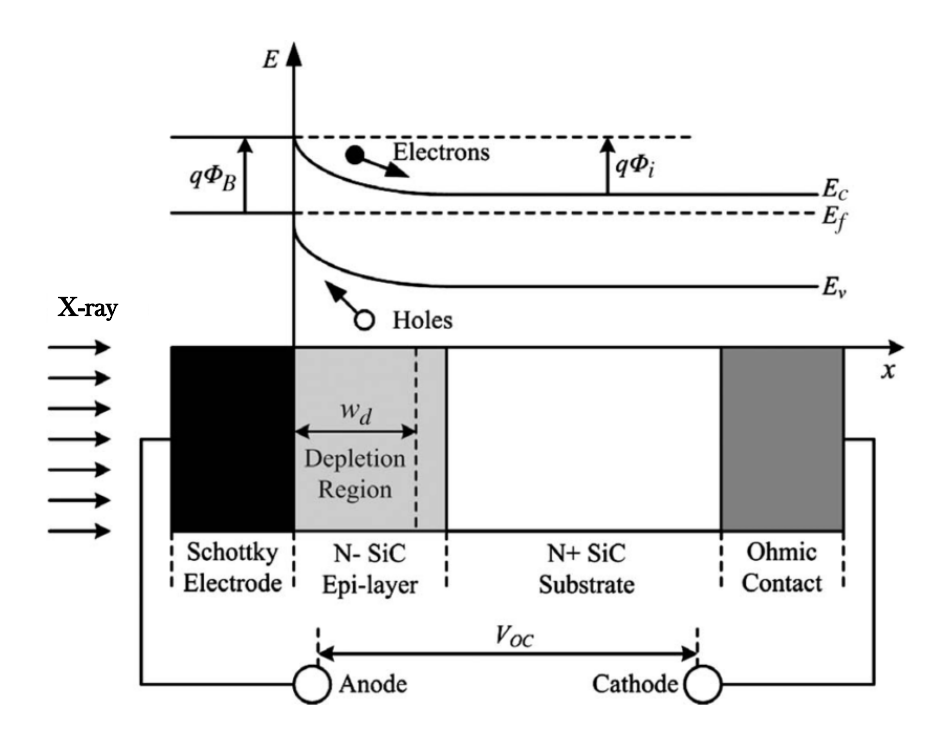


Figure 2.16: Schematic diagram of the collection of electron–hole pairs during X–ray scavenging inside SiC Schottky diode. [68]

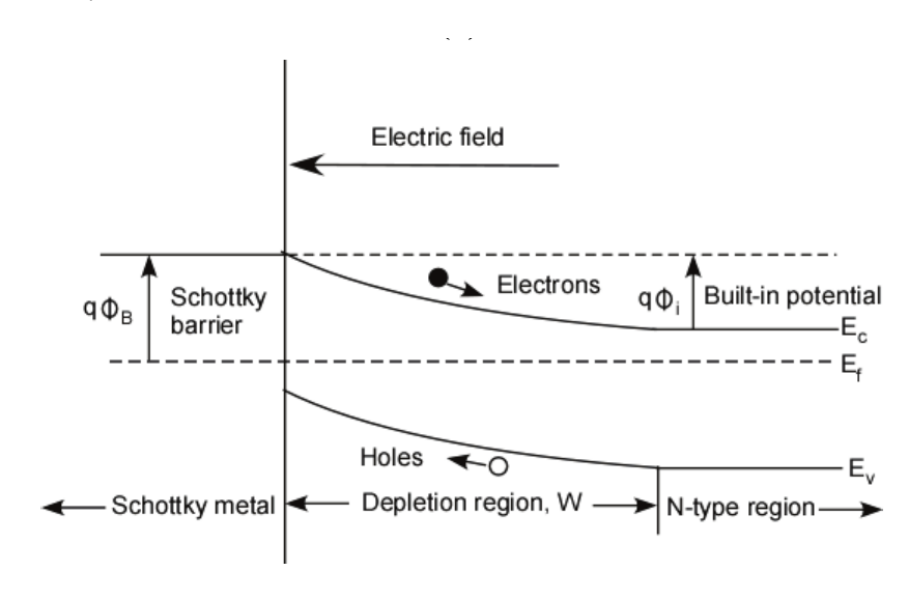


Figure 2.17: Schematic diagram of the electron and hole movement inside the depletion region of a Schottky diode.^[51]

which is related to carrier mobility, electric field strength, and the carrier lifetime [69]. Improvement in the material quality of semiconductor films by minimizing the dislocation density has led to significant increases in the charge collection efficiency [69]. This indicates that the junction depth and the width of the depletion region need to be adjusted according to the penetration depth of the X–

ray photons. The penetration ability and the average distance travelled by the photon beam depends on the energy of the photon beam as described in section 2.4.1. Therefore, the path length of the incident photon energies need to be optimised so that maximum number of electron—hole pairs are generated in the depletion region [70]. The collection efficiency of the electron—hole pairs generated outside the depletion region, depends on the distance the are generated from the edge of the depletion region. The charge collection is degraded if the minority carrier diffusion lengths are smaller than the width of the depletion region.

In order, to ensure that a large fraction of the incident photon beam reaches the depletion region, the properties of the metal layer used to form the Schottky contact should be optimised. The Schottky contact can acts as a dead layer to the photon beam [51]. Thick Schottky contacts will lead to higher absorption and attenuation of the beam before the photons reach the depletion region and hence a smaller fraction of incident energy will be deposited in the space charge region [71]. Other than that, the high–Z number and density of the Schottky contact will cause higher attenuation by the strong dependance on Z of the photoelectric absorption as explained in section 2.4.2. Alam *et al.* suggested the use of low–Z materials for the Schottky contact, such Al to overcome the loss of energy in the incident beam [51]. The effect of a dead layer on the absorption properties of GaN Schottky betavoltaics cell was calculated using stopping and range of ions in matter (SRIM) software [69]. The energy deposition for devices with and without the inclusion of dead layers (including the Schottky contact layer which comprised 25 nm Ni/25 nm Au) and a 1 mm gap air can be observed from the data in Figure 2.18. The relationship between the energy deposition of 17.4 keV 63 Ni emitting β –particles and the effective absorption thickness of the cell in air gave a 20% difference in the energy deposited in the active region of the device [69].

The dopant concentration also plays an important role in designing a photovoltaic cell, including the influence on the depletion width, short circuit current and open circuit voltage [70]. Lower dopant concentrations result in high short circuit current of a photovoltaic battery, however, it will lead to decrease in the open circuit voltage [51]. By decreasing the dopant concentration also results in a wider depletion region of a specified bias and minority carrier diffusion length, which in turn increases the charge collection efficiency. This condition can lead to an increase in the collection efficiency of electron–hole pairs, and hence the short–circuit current of the photovoltaic battery. However, the built–in potential decreases with lower dopant concentration as shown by the data for GaN semiconductor in Figure 2.19 and resulted in lower value of the open circuit voltage [51, 70]. However, in SiC technology, although the moderate–to–high resistivity substrates are desirable for high–voltage devices, 4H–SiC epilayers with dopant concentration less than 10^{13} cm⁻³ are not commercially available [17]. Typically devices are fabricated on homo–epitaxial layers, which are

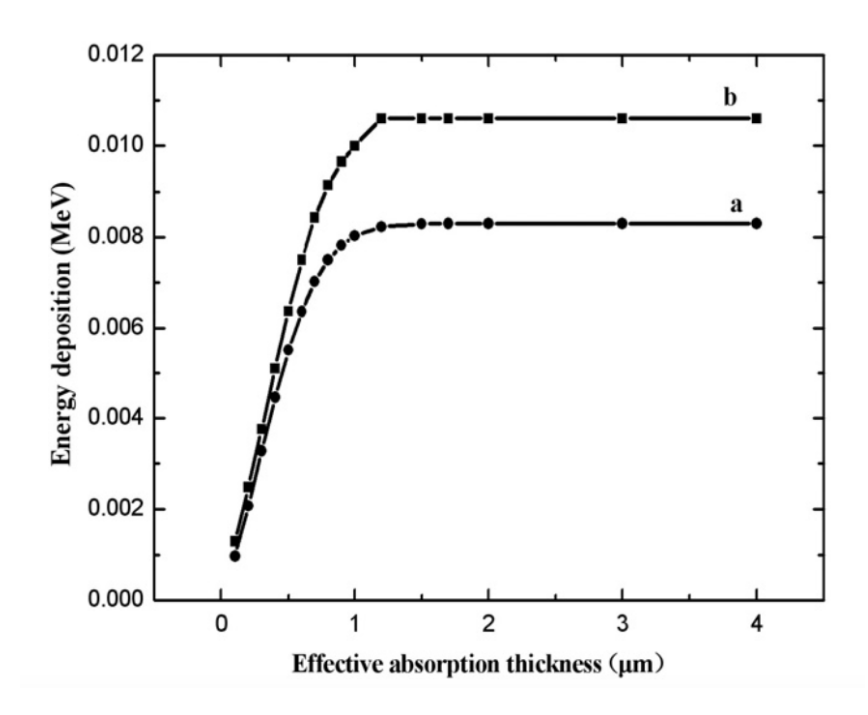


Figure 2.18: Plot of energy deposition of 63 Ni emitting β -particles of 17.4 keV as a function of effective absorption thickness of GaN Schottky betavoltaic cell for (a) with and (b) without the influence of dead layers. $^{[69]}$

routinely grown to thicknesses of over 100 μ m with doping densities as low as 10^{14} cm⁻³ using hot wall chemical vapor deposition (CVD) [17, 72]. Therefore, to obtain the optimum performance of the battery and maximize the output power, an optimised dopant concentration needs to be identified.

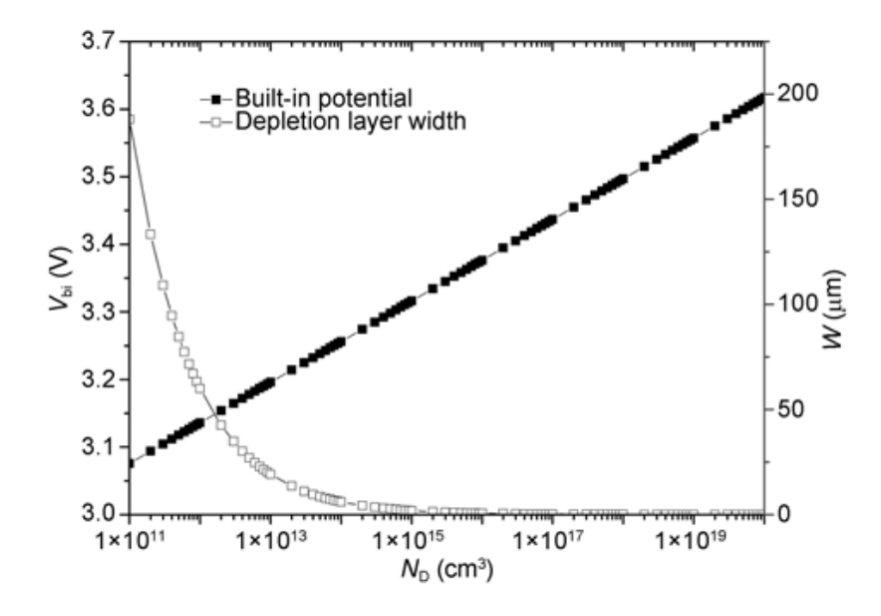


Figure 2.19: Plots of relationship between depletion layer width, built–in potential, and doping concentration of n–type substrate of GaN.^[70]

Since, the parameters of a Schottky diode depend on the temperature, therefore the electrical performance of an energy harvester is also dependent on the operating temperature [73]. Results published by Wang $et\ al$. reported the decrease in the open circuit voltage, power output and power conversion efficiency with increasing temperature in silicon p-n diode [73]. This may attributed to the smaller bandgap of the silicon in comparison to the SiC that was used throughout this study as explained previously in section 2.2.2. However, the short circuit current is almost constant with increasing temperature and the fill factor showed a minor decrease [73]. Additionally, Alam $et\ al$. suggested the performance of the energy harvesters suffers from degradation of the semiconductor materials when exposed to high doses of radiation [51]. This will lead to deterioration in the power output and promptly causes failure of the battery and circuit that is connected to it. Therefore, the usage of the energy harvesting system need to take into account the operating temperature and radiation hardness of the semiconductor in order to obtain a high performance system that can operate in these extreme environments.

2.8 Low frequency noise (LFN)

2.8.1 Low frequency noise models

Low frequency noise analysis provides a significant insight into device performance, along with valuable information on the physical properties of the SiC material [74]. Rumyantsev *et al.* suggested that important information on the location and nature of noise sources can be obtained from the noise properties of forward biased Schottky diodes [75]. Low frequency noise (1/f) or flicker noise was first introduced by S. Hsu. He proposed that low frequency excess noise in a metal–semiconductor Schottky barrier diode is dominated by the fluctuations of the potential barrier height [76]. This is due to the random occupancy of trap states or generation–recombination centers in the space charge region immediately under the contact. The multistep tunnelling current flowing through the diode causes fluctuations in the occupancy of the trap states, and hence results in the generation of low frequency noise in the diode. However, Kleinpenning had rejected the hypothesis of Hsu's model by identifying that 1/f noise originates from fluctuations in the mobility of the free carriers and not to fluctuations in their number [77].

The argument made by Kleinpenning was supported by work by Luo, who argued the 1/f noise originates from the mobility and diffusivity fluctuations of the carriers within the space charge region [78]. Later, Güttler and Werner presented their work on the the spatial inhomogeneities at the metal–semiconductor interface on metal–silicide/Si Schottky diodes, which can be used to describe the

increase in noise with reductions in temperature [79]. The decrease in the noise behaviour with increasing temperature was also predicted by the Jäntsch model, which relates it to the random walk model in explaining the 1/f noise in Schottky barrier diodes [80]. It was suggested that the spatial inhomogeneities at the metal—semiconductor interface arises from surface defects, threading dislocations, surface treatment, and the metal deposition process [79]. This will indirectly affect the current transport and noise properties, that may result in characteristics that can be described in terms of a local distribution of Schottky barrier heights. Otherwise, the mobility fluctuations were correlated with statistical scattering processes within the space charge region and analyzed based on the framework of Handel's theory of infraquanta emission [79].

2.8.2 Factors influencing the low frequency noise

Factors that are commonly used to describe the origin of 1/f noise in Schottky diode includes barrier inhomogeneity, temperature and the characteristics of defects that act as a trapping centers. Barrier inhomogeneities are generally sensitive to inhomogeneities of semiconductor structures [81] due to any small variation in Schottky barrier height, which lead to a significant shift in the current [82]. Both Hsu's and Luo's models assumed that the metal-semiconductor interface is spatially homogeneous [76, 78, 82], whilst Güttler and Werne proposed an analytical potential fluctuation model using Schottky barrier inhomogeneities to describe the electrical transport properties of Schottky contacts [79]. This can be explained form the distribution of patches with low and high Schottky barrier height which resulted in the inhomogeneous Schottky contact [82]. Current dependance of the noise spectral density, SI(I) depends on the barrier inhomogeneity, which results in a different behaviour when it passes through lower-barrier patches embedded in the matrix with a homogeneously high barrier [81]. This become more prominent in small current value that will resulted in large noise density in the high-barrier region and other part of the diode, which attributed to a barrier height distribution over contact area of SiC Schottky barrier diode [81]. Shabunina et al. presented data, which show that the nature of the barrier fluctuations in the nano-patches embedded in the higher barrier matrix differs significantly from the nature of the barrier fluctuations in the homogeneous part of the diode [81].

According to Hsu, 1/f noise is predicted to be temperature independent [76], however, according to Luo's model, increasing the temperature leads to an increase in the magnitude of the 1/f noise [78]. Other reports on the temperature dependence of 1/f noise for Ir/p–Si and Pd/n–GaAs were not in agreement with the predictions of Hsu's model [83–85]. Luo's model and spatial inhomogeneities model may be used for explaining the observed temperature dependence of the current noise spectral

density in the diode [82]. Kumar *et al.* who investigated the temperature dependance on the noise fluctuation found that noise decreases with increasing temperature in the range between 80 K to 300 K [82]. This can be explained by the inclusion of barrier inhomogeneities at the metal–semiconductor interface, where the majority of the current flows through the patches of lower barrier height at low temperature [82]. However, by increasing the temperature, carriers have sufficient energy to surmount the barrier in the region of high barrier height and take part in the conduction process [82].

On the other hand, the 1/f noise behaviour described by Hsu's model is based on the assumption that trapping states are uniformly distributed in space as well as in energy, whilst Luo's model does not consider the role of the interface trap states [76, 78, 82]. Hsu explained that a small number of thermally activated electrons are able to tunnel through the potential barrier by way of trapping states, although the current flow through a Schottky diode is dominated by thermionic emission, which is only true if n = 1 [76]. This results in the prediction that the flicker noise is linearly proportional to the trap density and proportional to the square of the dc diode current [76]. The occupation of the effective trap states from the two–step tunneling process is vulnerable to fluctuation and suggests that the distribution of the trap states is very broad [76]. Kumar *et al.* hypothesised that trapping states at the interface need to be considered due to the presence of deep level centres which act to provide a wide distribution of time constants and hence affect the traps that result in the generation of noise which are non–uniformly distributed in space as well as in energy [82].

2.9 4H–SiC Schottky diode as an X–ray photon dosimeter

2.9.1 Beam line monitoring system

A radiation detector with an accurate, wide dose measurement range and preferably a real-time dosimetry response is imperative for both quality assurance and patient dosimetry [32]. Quality assurance is an essential part of the patient irradiation procedure, which enable verification of the treatment planning and measurement of the actual dose deposited into the patient body for an efficient and safe dose delivery during treatment [86]. The quality assurance of a treatment requires a stable, linear, and sensitive radiation detector with high spatial resolution and radiation hardness [87]. Ideally, the photon beam needs to be monitored in real-time, without suffering from long term degradation to enable precise and accurate measurement. A number of types of detector, including ionization chambers, silicon and germanium solid-state detectors have been built and characterized [86]. However, the majority of them show significant levels of degradation during beam exposure [86]. The detector itself is a source of multiple Coulomb scattering and as a result the beam penumbra

expands, which contributes to the risk for surrounding healthy tissues [88]. Thus, the effort to identify and implement a suitable detector for a photon beam online monitoring system is imperative to support patient treatment.

Ionization chambers which need long data acquisition time during exposure and the requirement to analyse off-line images acquired by the GAF-chromic films make both techniques sub-optimal [89]. The disadvantage of the ionization chambers in comparison to semiconductor detectors is the larger ionization energy need, which is between 10 and 25 eV for the least tightly bound electron shells in most gases of interest for radiation detectors [46]. The larger ionization energy leading to lower signal generated for equivalent energy deposition, and hence contribute to the low energy resolution of the detector system. Silicon semiconductor detectors have been utilised in a wide range of applications in radiation oncology in the last few decades, as a valid alternative to both radiochromic films and ionization chambers. These offer significant advantages, particularly in applications with high counting rates in the pulse mode of operation, because of the faster charge-collection times and the ability to measure the intensity gradient profiles over relatively small distances due to their compact size [8]. Their sensitivity to radiation at zero bias voltage and good mechanical stability has enabled them to become the primary semiconductor devices for use in in-vivo dosimeters [21]. However, they are restricted by operational temperature constraints and show poor resistance to radiation damage [8] due to the low band gap and displacement threshold energy [7]. Furthermore, due to the low radiation hardness and a strong dependence on accumulated dose results in the need for preirradiation before use and frequent recalibration [21, 90]. Bertuccio et al. reported the sensitivity of 4H-SiC dosimeters, which are comparable to those of commercial silicon dosimeters [21]. The possibility to use 4H–SiC as in–vivo dosimeters during radiotherapy treatments is supported by the high reproducibility of the output charge during repeated measurements at constant irradiation and the disappearance of priming effects or degradation after exposure to X–rays [21].

Otherwise, recent advances in semiconductor fabrication has lead to use of Metal Oxide Semiconductor Field Effect Transistors (MOSFETs) in dosimetry applications [43, 48]. The prominent advantages over the conventional ion chamber and silicon diodes are related to the very small size, with typical dimensions of less than a millimeter which offer excellent spatial resolution, the axial anisotropy of $\pm 2\%$ for 4π , large dynamic range which can be used in very low to very high radiation environments, and sensitivity to different types of radiation including photon, electron, and proton dosimetry [43]. However, MOSFETs present disadvantages that need to be considered, they are very sensitive to any drift in bias voltage and therefore require highly stable power supplies and are highly susceptible to the damage caused by the radiation, as well as showing a strong temperature dependance [43].

2.9.2 Trap-recombination and radiation damage due to extreme environments

Absorbed dose is the amount of energy deposited by ionizing radiation in a medium per unit mass of the medium [46]. The SI unit for absorbed dose is J/kg, however the unit of gray (Gy) has been introduced, where 1 Gy = 1 J/kg. The severity of damage depends on the amount of radiation absorbed by the material [43]. The type and energy of radiation and the type of material determine the type of damage likely to occur inside the medium. The resistance to high radiation dose can be predicted by the knowledge of the value of atomic displacement energy. The atomic displacement energy can be defined as a measure of the minimum kinetic energy required to displace an individual atom from its regular crystal lattice site to a defect position [51]. Radiation–induced defects result in the released atom diffusing inside the material.

Numerous studies have been performed on the radiation tolerance of silicon detectors and it is reported that the present form of silicon detectors need to be replaced after being exposed to high radiation fields every two years to continue the measurements [43]. Ohshima et al. reported the comparison of radiation hardness between silicon and silicon carbide in terms of channel mobility and shift of the breakdown voltage [91]. The change in the channel mobility was observed with increasing absorbed dose (kGy) as the μ_{ch} for Si MOSFETs is known to decrease with increasing absorbed dose [91]. Their finding presented by the data in Figure 2.20 shows that the μ_{ch} for H₂ SiC MOSFETs does not change up to 20 kGy and the values decreases with increasing absorbed dose above 60 kGy, which then reduces to be 50 % of the initial value at 530 kGy [91]. μ_{ch} for the Si MOSFETs decreases with increasing absorbed dose and becomes 50 % of the initial value by irradiation at 10 kGy [91]. Whilst, data on the shift of breakdown voltage as a function of absorbed dose for SiC SITs, Si MOSFETs and Si IGBT can be observed in Figure 2.21. Ohshima et al. studied the shift in the breakdown voltage by irradiating SiC SITs and two Si power devices; Si MOSFET (17N80C3) and Si IGBT (5J301) with gamma rays at similar current and voltage ratings. Results demonstrated that there is no significant shift in the breakdown voltage observed up to 10⁷ Gy for the SiC SITs and the Si IGBT [91]. However, above 4×10^5 Gy, the shift of the breakdown voltage increases with absorbed dose for the Si MOSFETs and large shift can be observed at 10⁷ Gy [91]. Therefore, their finding suggested that the radiation hardness of SiC MOSFETs is higher in comparison to Si MOSFETs.

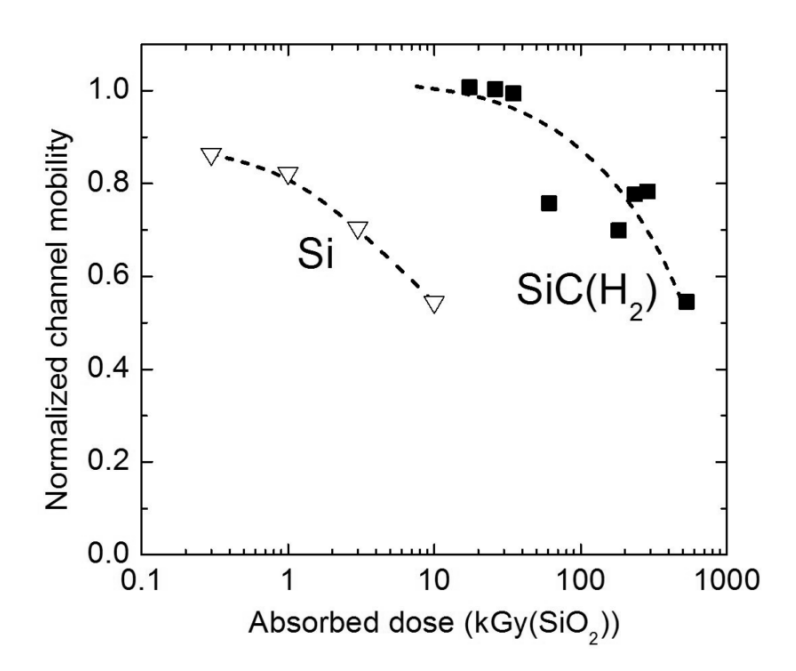


Figure 2.20: μ_{ch} for H₂ SiC MOSFETs and result reported for Si MOSFETs as a function of absorbed dose are also plotted. The value of the channel mobility is normalized by the initial value.^[91]

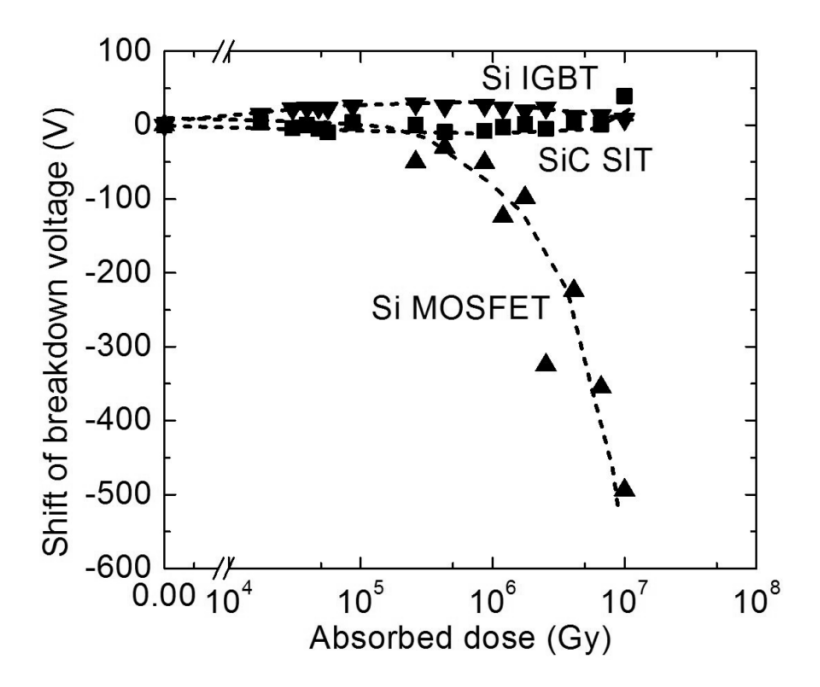


Figure 2.21: Shift of the breakdown voltage from the initial value for SiC SITs (squares), Si MOSFETs (triangles) and Si IGBT (upside–down triangles) as a function of absorbed dose. The blocking characteristics for SiC SITs and Si ones (IGBTs and MOSFETs) were measured under V_G at 10 V and 0V, respectively.^[91]

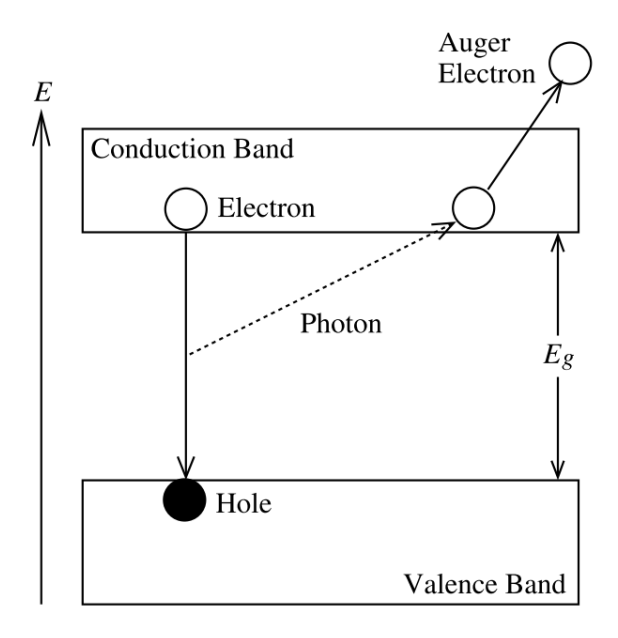


Figure 2.22: Schematic cross section of band–recombination with subsequent emission of an Auger electron. [43]

Carrier recombination occurs when electrons and holes recombine through an intermediate energy state created by crystal imperfection or impurity inside the material [43]. Two types of possible recombination that can occur in the detectors which are band–recombination and trap–recombination [43]. Band–recombination occur when an electron in the conduction band falls into the valence band to recombine with a hole without an intermediate as illustrated in Figure 2.22. The difference in the energy of the electron in the two states is then emitted as a photon, which has the ability to eject another electron in the conduction band with the promotion of an electron to a higher energy level, that is generally known as Auger recombination. The excess energy also results in the increase in the lattice vibrations of the crystal, which travel through the crystal in the form of phonons [43].

Trap assisted recombination is mediated by the existence of energy levels within the band gap formed by crystal defects and impurities as shown in Figure 2.23. These energy levels act as a metastable electron trap, where an electron falling into that energy level and remains there for some time before falling into the valence band [43]. This causes a delay in the signal in comparison to the band to band recombination process. This process which is also known as generation–recombination (G–R), results in the removal of a charge pair from the free carrier population [42, 43]. There are a few potential capture and emission processes that may be attributed to the existence of deep–levels as shown by the schematic band diagram in Figure 2.24 [42]. The initial process starts when the trap captures an electron from the conduction band as shown in Figure 2.24(a). This process can be characterised by the capture coefficient described by c_n . Two possible events which can

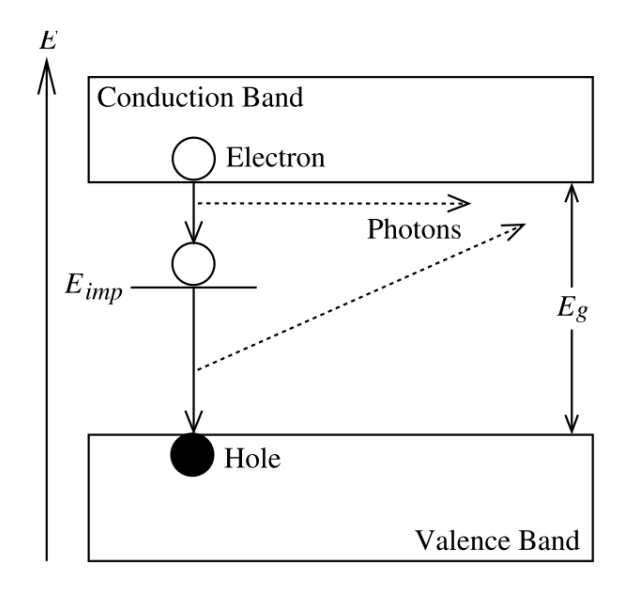


Figure 2.23: Schematic cross section of trap–recombination with sub–sequent emission of two photons.^[43]

occur after trapping are either electron emission back to the conduction band, which is described as electron emission, e_n (Figure 2.24(b)) or capture of a hole from the valence band described by c_p (Figure 2.24(c)) [42]. After occupation by a hole, the trap can either emit the hole back to the valence band, described by e_p as shown in Figure 2.24(d) or captures an electron [42]. These processes are labelled as a recombination event if (a) occurs followed by (c). In contrast, it is called generation when event (b) occurs followed by (d). Trapping events occur when (a) is followed by either (b) or (c), and subsequently by (d) [42]. In either case, a captured carrier will subsequently emitted back to the band where it is originated [42].

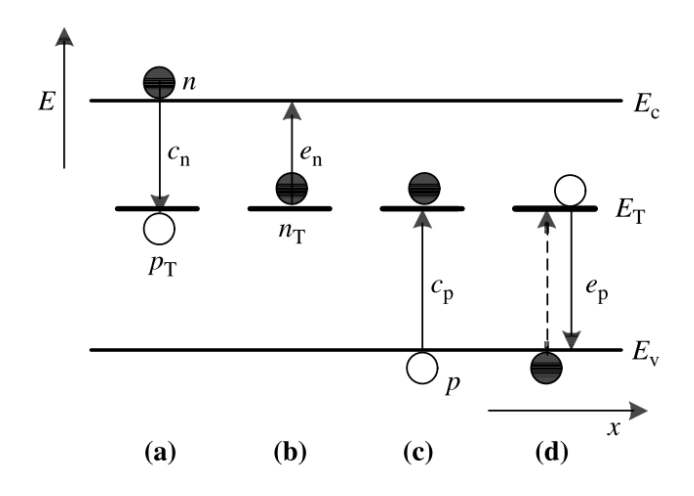


Figure 2.24: Schematic electron band diagram for a semiconductor with deep-level impurities.^[42]

2.10 Summary

This chapter presents the material properties and electronic structure of 4H–SiC that has been used throughout this study. Comparison between this and other wide bandgap materials that were commonly investigated previously, provides an appreciation of the superlative material characteristics of 4H–SiC in a wide range of applications. The performance of SiC detectors can be related to the different interactions that occur within the active region of the detector, which depend on different properties of the semiconductor materials and incident radiation. Knowledge of factors that determine the possible interactions that occur during exposure to radiation flux are imperative in ensuring optimum performance of the fabricated detector. Details of the basic principles and working procedures of the detector during the experimental measurements and data collection methods used throughout this study were discussed, to enable a better understanding of the technical procedures in related applications.

Additionally, the possibility of this material to operate at high temperature and radiation dose have been discussed. The electrical and mechanical properties of SiC with wide bandgap energy and low intrinsic carrier concentration, make it possible to maintain their performance at high junction temperatures and enable to overcome the restrictions imposed by silicon in terms of elevated temperatures and high voltage blocking. Due to the ultra low leakage current densities, SiC is proposed to be an ideal candidate for dosimeter development. Those outstanding properties also resulted in no external cooling systems are required to operate in high temperature ambients or to minimise the electronic noise.

Consideration of the optimum dosimeters for radiotherapy applications is a crucial aspect for a precise measurements and prolong the detector lifetimes, as the treatment procedure often involve wide range of dose rates. Therefore, the correlation of the ability to withstand radiation induced damage within the detector material are imperative to be considered in the development of dosimeters. The high displacement threshold energy of silicon carbide presents the capability to be operated in high dose and high dose rate radiation fields. The methods or techniques that are capable to observe and investigate the damage occur after exposure to high energy radiation such as low noise frequency measurement also has been emphasised in this chapter.

Chapter 3

Optimisation on Fabrication and Characterisation of 4H–SiC Schottky Diode

Part of the methodology in the chapter was published in N. S. Mohamed *et al.*, *IEEE Trans. Nucl. Sci.*, vol. 64, no. 7, pp. 1912-1919, 2017.

3.1 Introduction

The use of radiation in space exploration, nuclear environments, industrial and medical applications requires the development of detectors with high radiation resistance, which are both sensitive and accurate to enable precise radiation detection, coupled with a large response. In recent years, technology advances in the development of radiation detectors have resulted in significant interest at a research level in the exploration of new radiation hard detector materials. Development of these radiation hard detector materials that are highly tolerant to a wide range of radiation types and energies has attracted a large number of researchers. Whilst these different radiation types have different values of average distance travelled within the detector material, development of radiation detectors for deployment in environments with a high dose or dose rate is very challenging. This is a particular challenge when dealing with a high-energy radiation and low-charged particles which have a longer distance travelled in the detector material. The operation of detectors for these particles is based on the need for a thick depletion region, hence high bias voltages are required to maximise the depletion region width and enable full charge collection. To detect the full energy spectrum of the incident radiation, the active thickness of the semiconductor device should be greater than the average distance travelled by the particles [46]. Therefore, the average distance travelled by each of the radiation interacts in the detector material must be precisely known [92] before the design and fabrication of new detectors can be undertaken.

3.1.1 Overview of the radiation detector material

As outlined in section 2.4.1, the choice of detector material is one of the main considerations prior to detector fabrication and depends critically on the application. Radiation detectors that are manufactured from materials with properties that are insensitive to radiation damage (often described as having high radiation hardness) are capable to reduce the influence of charge trapping and polarization effects on the detector characteristics [93]. Consequently, the material ultimately contributes to the suitability of the detector for the specified application. Suitable materials for the development of radiation detectors are;

- i. a large bandgap and a high atomic displacement threshold energy, which increases the radiation hardness [94] and the capability to withstand both high radiation dose and high dose rate [24, 95],
- ii. high electron and hole mobility, which leads to fast signal collection [94] and high signal stability [95],
- iii. high linearity with both dose and dose rate,
- iv. wide dynamic range [95],
- v. a low dielectric constant, which lowers the capacitance and therefore the noise [95]
- vi. monocrystalline, which gives a high $\mu\tau$ product, resulting in a high charge collection efficiency [95], and
- vii. high thermal conductivity, to have good cooling properties when the detector is operated under high bias conditions for long periods [24, 94].

Numerous studies have described the suitability of silicon carbide as a radiation detection material for a range of monitoring applications, including particle detection [38, 96, 97], radiation dosimetry [21, 95], X-ray detection [30] and photovoltaic detection [98]. Silicon carbide has advantages over other traditionally used semiconductors (such as silicon) in terms of the low leakage current, high breakdown electric field and high radiation hardness, as described in sections 2.2.2 and 2.2.3. These attractive characteristics of silicon carbide detectors in terms of electrical and mechanical properties make it possible to be used in an extensive range of devices and sensors, especially in applications involving high temperatures and harsh environments [17, 20, 21, 25]. Throughout this study, silicon carbide has been chosen as the detector material for the development of radiation detectors and photovoltaic cells that will described in detail in the subsequent chapters.

In addition to the choice of material, device design and subsequent fabrication process also exert a significant influence on the electrical and mechanical properties of an ideal radiation detector. Schoen *et al.* [99] has reviewed the relationship of the key performance parameters between the device physics and geometry in the design and fabrication of power Schottky diode rectifiers. The key performance parameters that need to be considered during the design of an optimal high-performance SiC Schottky diode for power electronics applications are the breakdown voltage, forward voltage drop, reverse leakage current, power dissipation, and switching time [99]. In contrast, the performance characteristics of the SiC X–ray detector has been outlined by Wright and Horsfall [24], which include high critical field, low defect density, a low intrinsic carrier concentration, low surface leakage current (by means of an optimised edge termination scheme) and high barrier height device (to ensure low noise performance) [24]. The Schottky diode characteristics including the Schottky contact metal work function, epilayer doping, and epilayer and Schottky contact thickness were optimised during the fabrication process and the resulting characteristics are reported in the following section.

In this chapter, a mask layout and process flow were designed for the development of 4H–SiC Schottky based radiation detectors. Subsequently, the forward and reverse bias current–voltage (I–V) characteristics have been determined using a low voltage system to extract the specific on resistance (R_{on}), barrier height (Φ_b), ideality factor (n) and reverse bias leakage current. Additionally, capacitance–voltage (C–V) measurements were performed on selective diodes to extract the flat–band barrier height (ϕ_B), doping concentration (N_D), which allowed the determination of the depletion width (W_d). The ideality factor of the diodes were used as the critical metric to identify fully functional devices which were suitable to be wire–bonded and subsequently tested as radiation detectors and photovoltaic cells. All the parametric measurements reported in this thesis have been performed using a Cascade 12000 Summit Series probing station and Keithley 4200 parameter analyser at room temperature.

3.2 Device physics geometry and detector fabrication

n-type 4H–SiC Schottky diodes were fabricated from commercial wafers produced by Dow Corning with 35.3 μ m thick epitaxial layers with a nitrogen dopant concentration of 1.00×10^{15} cm⁻³ and a substrate resistivity of 0.019 Ω .cm. The choice of an epitaxial layer with low doping concentration is to enable the formation of a large depletion width at moderate reverse bias, to increase the active volume of the detector. The maximum applied voltage strongly depends on the critical electric field at the surface of the semiconductor, as well as the bulk material value. High voltage devices often

utilise edge termination techniques [99]. The realisation of high voltage devices also requires the fabrication of devices on sections of the wafer that are free from defects in the semiconductor. Wahab *et al.* reported that macroscopic defects such as micropipes and domain boundaries that exist within the active area of the device will cause the breakdown voltage to be deteriorated [26]. The correlation between the dopant concentration, N_D and the breakdown voltage, V_B can be expressed as [100]

$$N_D = \frac{K_s E_{CR}^2}{2qV_B} \tag{3.1}$$

where K_s is the semiconductor dielectric constant, E_{CR} is the semiconductor critical field and q is the electron charge. From Equation 3.1, the breakdown voltage can be estimated based on the epilayer doping that is selected prior to fabrication process. The maximum breakdown voltage can be sustained depends on the epilayer doping. Therefore, in order to attain a high breakdown voltage, lightly doped wafers are required. The wide bandgap of silicon carbide results in an additional advantage as the critical electric field is an order of magnitude higher than silicon, resulting in devices with a high voltage capability [22].

Carrier mobility is one of the characteristics that is critical to result in high performance devices, particularly in terms of the maximum operating frequency or time response [42]. High carrier mobility results in a reduced transit time for carriers in the depletion region leading to a higher frequency response [42]. This indirectly results in higher currents that charge capacitances more rapidly, generating a higher frequency response [42]. The relatively high carrier mobility of the wide bandgap semiconductors including 4H–SiC that is used in this study, make them suitable for the realisation of high performance radiation detection. The high carrier mobility also results in a high charge collection efficiency, which is linked to the diffusion length, L, of the charge carrier [51]. A lightly doped epilayer results in an increased depletion region width and high minority carrier diffusion length, which also increases the charge collection efficiency [51]. Electron and hole mobilities are affected by the doping concentration levels, as well as the high field saturation, as described by the empirical Masetti model, as shown in Equation 3.2, which relates the dependancy of the dopant concentration to the mobility [42].

$$\mu = \mu_{min} + \frac{\mu_0}{1 + (\frac{N}{N_{ref}})^{\alpha}}$$
 (3.2)

where the electron or hole mobility, μ is inversely related to the donor or acceptor doping density, N. Lightly doped semiconductors have lower recombination rates, and higher diffusion length. Following L = $\sqrt{D\tau}$, where D is expressed in Equation 3.3, semiconductors with long diffusion

lengths also have long carrier lifetimes. In contrast, high recombination rates, k_r occur in highly doped semiconductors and the lifetime is limited by the high density of defects present. Highly doped material results in an increase in the concentration of defects present, which in turn contribute to the high recombination rate and shorter diffusion length $\left(\tau = \frac{1}{k_r}\right)$ [43].

$$D = \mu \frac{k_B T}{e} \tag{3.3}$$

The predicted depletion width W_d can be determined from the knowledge of the epilayer doping concentration used, according to

$$W_d = \sqrt{\frac{2K_s\varepsilon_0 V}{qN_D}} \tag{3.4}$$

where K_s is the semiconductor dielectric constant, ε_0 is the permittivity of free space, q is the electronic charge and N_D is the doping concentration. Based on Equation 3.4, W_d is inversely proportional to $\sqrt{N_D}$, hence an epitaxial layer with low doping concentration results in an increased depletion width in comparison to a highly doped epilayer. Knowing the thickness of the epilayer ($t_{epi} = 35.5~\mu m$) and dopant concentration ($N_D = 1.00 \times 10^{15}~cm^{-3}$) it is possible to determine that a reverse bias of 1.2 kV needs to be applied in order to fully deplete the epilayer, resulting in a maximum detection efficiency.

The corresponding epilayer thickness is the reverse bias depletion width at the breakdown voltage [99]. The relationship between minimum epilayer thickness, t_{epi} , the critical field, E_{CR} and the breakdown voltage, V_B denoted as [100]

$$t_{epi} = \frac{2V_B}{E_{CR}} \tag{3.5}$$

Based on those factors and criteria that briefly explain in this section, optimisation and considerations have been taken prior to mask layout design and fabrication process that will be described in detail in the subsequent subsection.

Other than the aforementioned factors, the structure of the detector itself also plays an important role in the development of an ideal device. According to Schottky–Mott equation, as expressed in Equation 3.6, SiC Schottky diodes have been shown to have a strong dependence of metal–semiconductor barrier height, ϕ_{Bn0} on metal work function, ϕ_m and electron affinity of the semiconductor, χ [44].

$$\phi_{Bn0} = \phi_m - \chi \tag{3.6}$$

This relationship implies that the choice of metal for the Schottky contact would determine the resulting barrier height value. However, for practical diodes, it is experimentally observed that the barrier height is weakly dependant on the work function of the metal [42]. Bardeen described the empirical deviation from the Schottky–Mott limit in terms of the existence of surface states, rather than the difference in the work function [101]. This can be explained in terms of the Fermi level pinning, where the Fermi level in the semiconductor is pinned at a given energy in the band gap. This results in the formation of a depletion region [42], which contributes to the relative constancy of the barrier height with different metals and hence control over the barrier height becomes irrelevant [102]. The complete independence of the metal work function on the resulting barrier height, as observed by Bardeen can be described by the density of surface states being extremely high (comparable to the surface atomic density), which results in a barrier height that is independent of the choice of metal contact [101]. However, Porter and Davis claimed that the actual relationship between barrier height and metal work function usually falls somewhere between the Schottky Mott limit and Bardeen limit [102], and hence the surface can be described as semi–pinned.

Element	ϕ_m (eV)	Predicted ϕ_B (eV)	Actual ϕ_B (eV)
Al	4.28	1.01	1.30
Au	5.10	1.68	1.40
Cu	4.65	1.38	1.30
Mo	4.6	1.33	1.30
Ni	5.15	1.63	1.40
Pt	5.65	2.08	1.70
Ti	4.33	1.06	1.10
W	4.55	1.28	1.10

Table 3.1: Table of metal work–function ^[103], predicted ϕ_B (eV) ^[104] and actual ϕ_B (eV) ^[44] of few possible metals for Schottky contacts.

Itoh *et al.* suggested that in order to achieve a high current density at much lower forward bias voltage, it is necessary to employ Schottky metals with barrier heights lower than that of Au [105]. Therefore, metals with large work functions should be chosen as the Schottky metal in producing device with high Schottky barrier. The high metal work function of nickel; 5.15 eV in comparison to the other metals listed in Table 3.1 [103] coupled with the ease of processing, has resulted in it being

chosen as a Schottky contact material with a potential barrier height (1.40 eV) [44] when it brought to intimate contact with the SiC surface.

The considerable increase in reverse leakage current with temperature is a potential drawback for detectors manufactured from conventional semiconductors due to the inherent low barrier heights formed at metal–semiconductor contacts [99]. A significant advantage of SiC over both Si and GaAs is the higher barrier height which enables the development of detectors with low leakage current under high reverse bias conditions and high temperature measurements without the need for an external cooling system. The wide bandgap and resulting low intrinsic carrier concentration, makes it possible for SiC based detectors to maintain their performance at high temperatures [6, 24] and thus overcome the restrictions imposed by silicon in terms of both temperature [24, 25] and voltage blocking [22].

The thickness of the Schottky contact requires optimisation in order to avoid parasitic absorption of the incident radiation prior to it reaching the depletion region in the epitaxy layer [43]. Thinner Schottky contacts have a significantly lower absorption, which results in higher detection efficiencies [63] especially for low energy radiation and heavy charged particles, such as alpha and beta particles. However, reducing the thickness of the Schottky contact can decrease the barrier height of the diodes, and so a trade—off between the low energy detection threshold and the noise in the detector is essential [63]. This situation is a significant challenge for radiation detectors which are fabricated for the detection of both low and high energy radiation in a single device. Therefore, a compromise between the different factors affecting diode characteristics need to be considered for each radiation type of interest.

3.2.1 Mask layout design

Prior to fabrication of the radiation detector, it is necessary to design the device structure and mask layout for the Schottky diode. The contact shape, contact area, and distance between adjacent contact areas are critical factors that need to be considered during the design of the mask layout. The devices were designed using LASI software and fabricated on $10 \text{ mm} \times 10 \text{ mm}$ die as shown in Figure 3.1 and the devices of different contact areas can be individually diced out for wire bonding purposes. Annular enforcement layers, $35 \mu \text{m}$ wide with a $105 \mu \text{m}$ quadrant were designed at the left upper corner of the device to act as the electrical contact during on–wafer probing and subsequent wire bonding. The annular contact was designed to have a $5 \mu \text{m}$ gap from the edge of the contact area to remove the possibility of mask misalignment that may occur during the photolithography procedure.

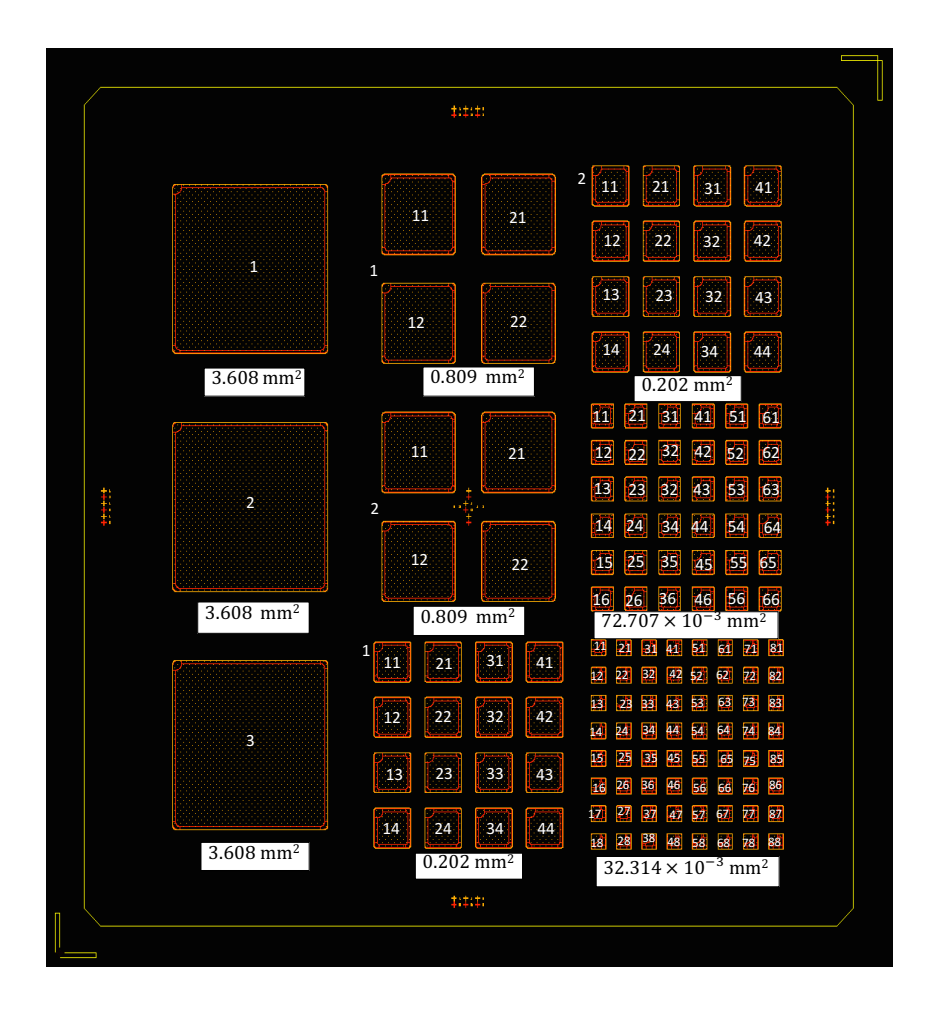


Figure 3.1: Mask layout design of the Schottky diode $10\text{mm} \times 10\text{mm}$ die with different Schottky contact areas.

Amatalo *et al.* investigated the effect of metal–semiconductor contact geometry on I–V characteristics of the Al/ZnSe Schottky contact with the ideality factor used as the critical metric [106]. They found that large metal contacts $(2.04 \times 10^{-4} \text{ and } 2.50 \times 10^{-5} \text{ m}^2 \text{ respectively}$ for circular and rectangular contact areas) and shorter electrode spacing of the Schottky devices produce better diode ideality factor and electrical properties due to lower series and contact resistance [106]. In this study, square Schottky contacts with five different area have been designed with rounded corners to avoid field crowding under reverse bias. The active areas of the detectors are 3.608 mm², 0.809 mm², 0.202 mm², 72.707 \times 10⁻³ mm² and 32.314 \times 10⁻³ mm². The different contact areas are comparable to those reported in previous studies [21, 55, 107–109]. According to the literature, 5 mm² Schottky contact areas have been developed by both Bertuccio *et al.* [21] and Ruddy *et al.* for high energy photon and alpha particles detection. The effect of proton and neutron irradiation were measured using detectors with Schottky contact areas of 3.96 mm² [55], while Nava *et al.* [107, 108] fabricated Schottky diodes with smaller contact areas, (1.767 mm² and 3.142 mm²) for the detection of alpha particles.

The distance between adjacent contact areas had been varied with the smallest distance between adjacent pixels being 110 μ m length for the contacts with 200 μ m and 300 μ m edge length, 120 μ m for the 500 μ m devices and 220 μ m for the 1 mm devices. The maximum blocking voltage of the device is limited by charge crowding at the edges of Schottky active region, and edge termination is necessary to relieve the electric field [99]. The lack of the edge termination in the devices used here resulted in high peripheral leakage and breakdown voltages that were lower than expected due to the increased field crowding at the edge of the devices [110]. However, the majority of edge termination schemes, such as guard rings and implanted junction termination extension (JTE) structures contribute to a significantly higher leakage current at moderate reverse bias, resulting in a deterioration of the signal to noise ratio in the detector [110, 111]. In comparison to guard rings that require deep diffusion of regions with a high dopant concentration in order to achieve sufficiently large cylindrical junctions to minimize field crowding, JTE structures are more preferable due to nearly ideal breakdown voltage and ease of fabrication because of the lower dopant concentration required [112]. Guard ring technology is not very suitable in SiC technology due to the very low diffusivity of dopants in the material [112] and ion implantation techniques are required. In-Ho et al. assert that the ion implantation process results in the increase in surface leakage due to the surface diffusion of ions [111] and the creation of defects that are not removed during the postimplantation anneal process. Breakdown voltages exceeding 1200 V were observed in [110] in nonedge terminated device structures for diodes similar to those fabricated in this study. Coupled with the increased signal-to-noise ratio in unterminated diodes, it was decided that this breakdown voltage was sufficient for the studies being undertaken, as it would result in a depletion region width of 35 μ m.

3.2.2 Detector fabrication

Five samples were processed for the development of the SiC Schottky diode radiation detectors used throughout this study. Three different processes were used to examine the variation in the detector characteristics, as summarised in Table 3.2. Three samples (DC 2, 7, 8) followed the standard fabrication process as outlined below. One sample (DC 4) had an additional etch step prior to the Schottky contact formation to form mesa structures, to examine the effect on the breakdown voltage. Sample (DC 5) had a silicon nitride (Si_3N_4) layer deposited as a passivation layer on the silicon carbide surface. The Schottky contact was deposited on four samples using electron beam deposition and one sample (DC2) deposited using physical vapour deposition (PVD).

Sample number	Schottky contact	Annealing	Passivation	Additional
		temperature		process
DC 2	Ni PVD	700 °C	No	-
DC 4	Ti/Ni e-beam	660 °C	No	$2.2~\mu\mathrm{m}$ etched SiC
DC 5	Ti/Ni e-beam	700 °C	$0.5~\mu\mathrm{m~Si}_3\mathrm{N}_4$	-
DC 7	Ti/Ni e-beam	700 °C	No	-
DC 8	Ti/Ni e-beam	660 °C	No	-

Table 3.2: Table of different treatment control on fabricated Schottky diode designated as DC 2, DC 4, DC 5, DC 7 and DC 8.

All wafers were initially cleaned in organic solvents, followed by piranha and standard Radio Corporation of America (RCA) cleans to remove surface contaminants. Formation of low–resistance Ohmic contacts on the back of the wafers were achieved by the deposition of chromium (5 nm) and nickel (80 nm) films, followed by annealing for five minutes at 1040 °C [113] under high vacuum using Edwards 306 with TECTRA ceramic resistive heater. The Schottky contacts were patterned using standard photolithography and AZ–5214E photoresist. Lift–off process has been used to pattern the Schottky contacts using the mask layout design described in the previous section. Prior to metal deposition, the samples were immersed in 10% BHF (NH₄F (36%)/ HF (6%)/ H₂O (58%)) for 3 minutes at room temperature to remove the native oxide followed by blow drying in dry nitrogen.

The formation of the nickel silicide or mono–silicide (Ni₂Si/NiSi) Schottky contact was performed based on the process described fully elsewhere [61, 114]. In summary, 4H–SiC Schottky diodes fabricated in this study comprise the deposition of Ti/Ni (5/80 nm) using electron beam deposition or Ni (80 nm) using PVD and annealing for a period of 25 minutes at 660 °C (DC 2, 4, 8) or 700 °C (DC 5, 7) in high vacuum. These process conditions have been demonstrated to result in a highly stable Schottky barrier, with greater thermal stability than pure Ni [113]. Previously published data indicates that the current voltage characteristics for this process show almost ideal forward and reverse bias electrical characteristics [61]. Immediately after annealing process of the Schottky contacts, sample DC 5 was covered with 500 nm of plasma enhanced chemical vapour deposition (PECVD) silicon nitride to act as a passivation layer.

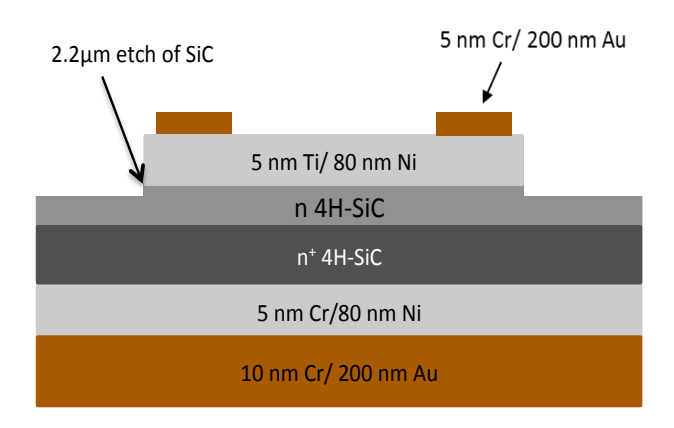


Figure 3.2: Schematic cross section of Schottky diode with mesa structure.

Just before annealing the Schottky contact to form Ni₂Si, one of the samples designated as DC 4 was etched to form a mesa structure using the reactive ion etching (RIE) as illustrated in a schematic cross section in Figure 3.2. Lazar *et al.* has suggested the high current handling capability in diodes with a mesa structure may be correlated to the improvement in the breakdown voltages [115]. However, the RIE process also leaves a carbon rich polymer layer on the surface of the mesa, depending on the fluorine/carbon (F/C) ratio in the gas composition, which can increase the leakage current in the etched samples [116]. High leakage currents in non–etched device is often attributed to the presence of thin interfacial SiO₂ layer under the Schottky contact, which reduces the barrier height under reverse bias [116] and increases the ideality factor in the forward direction [117].

Subsequently, annular enforcement layers were realised using electron beam deposited chromium/gold (5/200 nm). A schematic cross section of the final devices fabricated using the standard process (DC 2, 7, 8) are illustrated in Figure 3.3. The Si_3N_4 passivation layer on sample DC 5 was etched using reactive ion etching (RIE) immediately prior to deposition of the enforcement layer. Electron beam deposition using aluminium was used as the mask on top of silicon nitride. During the lift–off process using potassium hydroxide (KOH), aluminium along with the gold layer on top of aluminium were brushed away, leaving the gold layer to form the enforcement part as illustrated in Figure 3.4. An optical micrograph of the final fabricated Schottky diode from top view for all samples can be seen in Figure 3.5.

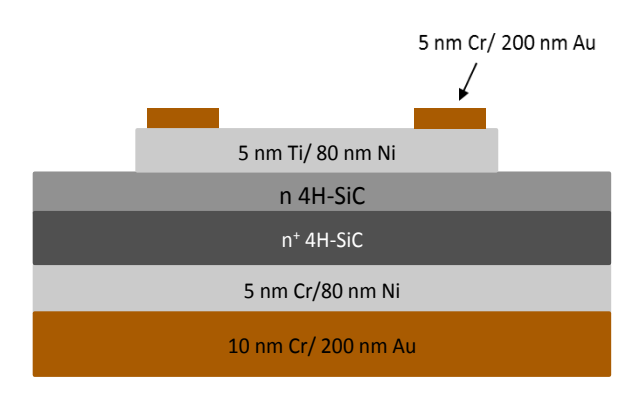


Figure 3.3: Schematic cross section of the standard processing condition of the Schottky diode

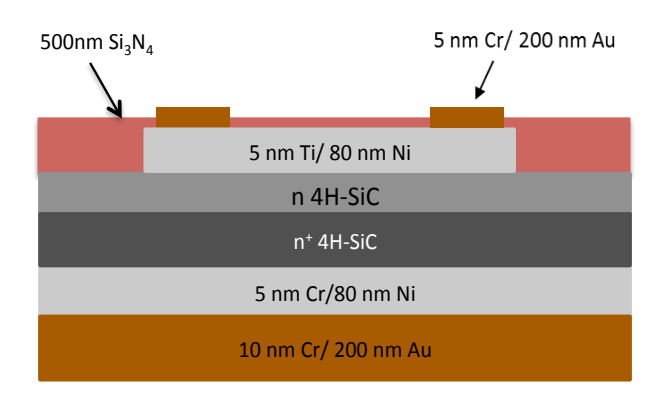


Figure 3.4: Schematic cross section of Schottky diode with silicon nitride (Si_3N_4) as a passivation layer

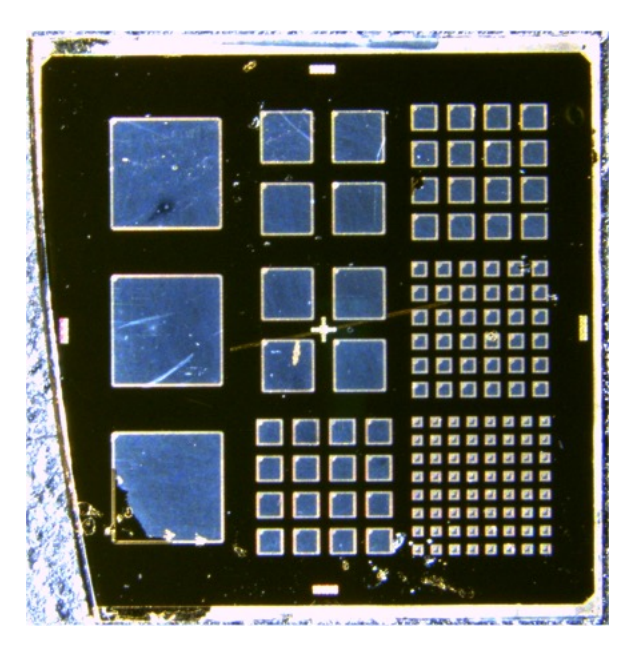


Figure 3.5: Top view of the detector die after fabrication. The overall die dimensions are 10 mm \times 10 mm

3.3 Electrical characterisation at room temperature

Prior to wire bonding, the forward and reverse bias I–V and C–V characteristics have been measured using a parametric analyser to extract series resistance (R_s), barrier height (Φ_b), ideality factor (n), reverse bias leakage current, and doping concentration (N_D). These parameters will give useful information related to the nature of the device and device performance, stability and reliability [118]. Device performance, stability and reliability are the important criteria for radiation detectors in order to realise a high performance detector that is able to give precise signal response and withstand high dose radiation in harsh environment over an extended period. Measurements on electronic properties of all samples have been performed using a Cascade 12000 Summit Series probing station and Keithley 4200 parameter analyser at room temperature. This preliminary screening of the detectors phase was used to identify those with ideal characteristics that were then selected for wire bonding and subsequent analysis as a high performance radiation detector.

3.3.1 Forward and reversed bias I-V characteristics

The specific on resistance (R_s) , barrier height (Φ_b) and ideality factor (n) were extracted using Cheung's method described in [119] to account for the high series resistance of the thick, lightly doped epilayer. Cheung's method uses plots of auxiliary functions to calculate the diode parameters, resulting in higher accuracy than the conventional thermionic emission model and is significantly simpler to implement than the Norde function method [120]. Under large forward bias conditions, the series resistance (R_s) of the diode causes the forward bias I–V characteristics of the Schottky diode to deviate from that predicted by the thermionic emission model [121] and this reduces the accuracy of the extracted barrier height (Φ_b) and ideality factor (n) [122] when the simple extraction method is utilised. The Norde method typically results in the overestimation of the series resistance (R_s) because of the assumption that the ideality factor is very close to unity, which is not always true for a real diode and the barrier height extraction is based on a single point in the I–V characteristics [120].

Cheung's functions can be expressed as [119]:

$$\frac{dV}{d(\ln I)} = IR_s + n\frac{kT}{q} \tag{3.7}$$

$$H(I) = V - n \left(\frac{kT}{q}\right) ln \left(\frac{I}{AA^*T^2}\right)$$
(3.8)

$$H(I) = IR_s + n\Phi_b \tag{3.9}$$

where n is the ideality factor, A the Schottky contact area, A^* the Richardson constant and Φ_b the barrier height extracted from the lower-voltage region of the forward I-V characteristics. A plot of dV/d(lnI) as a function of I is a straight line, where the slope gives the series resistance, R_s and the ideality factor, n can be extracted from the y-axis intercept (n kT/q). A plot of H(I) versus I will also give a straight line for a second determination of R_s and Φ_b can be extracted from the y-axis intercept ($n\Phi_b$) using the value of the ideality factor determined from Equation 3.7. The second determination of R_s can be used to check the accuracy of the values extracted from the first plot [119]. The specific on resistance (R_{on}) values can be obtained from the multiplication of the series resistance extracted from Equations 3.7 and 3.9 with the Schottky contact area, in the unit of Ohm.cm² (Ω .cm²). As discussed previously, samples which had different process conditions during fabrication were characterised to study the variation of their electrical characteristics, with an emphasis on the specific on resistance, R_{on} , ideality factor, n and barrier height, Φ_b .

3.3.2 Specific on resistance, R_{on}

Series resistance in a packaged device is the total resistance of bulk of the semiconductor, contact wires and Ohmic contacts [123]. The series resistance depends on the bulk wafer resistivity, the resistivity of the epilayer and on the contact resistances [42]. The data in Figure 3.6 show the calculated specific on resistances extracted from the I–V characteristics for all fabricated samples as a function of Schottky contact dimension. The values of R_{on} extracted from the two different steps in Cheung's method are shown in Figure 3.6 for the different samples fabricated and the values obtained demonstrate an agreement within 5.5% for each of the Schottky contact areas considered here. The data also show an increase in specific on resistance with Schottky contact dimension in the range of 2.5×10^{-2} to $4.0 \times 10^{-1} \Omega.\text{cm}^2$, where it produced higher specific on resistance for bigger diodes. Moreover, high values of specific on resistance, R_{on} of the fabricated Schottky diode are similar to those observed by Kimoto et al. [124], where they attributed the high resistivity to the use of highly resistive epilayers.

Since all the samples were fabricated from the same wafer, that has the same manufacturer specified dopant concentration and epilayer thickness, it is expected that equivalent Schottky contact areas should provide the same specific on resistance. However, the slight deviation of the trend in the specific on resistance data between big diodes (diameters of 2 mm and 1 mm) and the smaller diodes (diameters below 500 μ m) can be explained by differences in the phase of nickel silicide formed during the annealing process, and the surface roughness resulting from the metal deposition [125]. In fact, the specific on resistance of all fabricated wafers were in the same range within 0.035 \pm 0.019

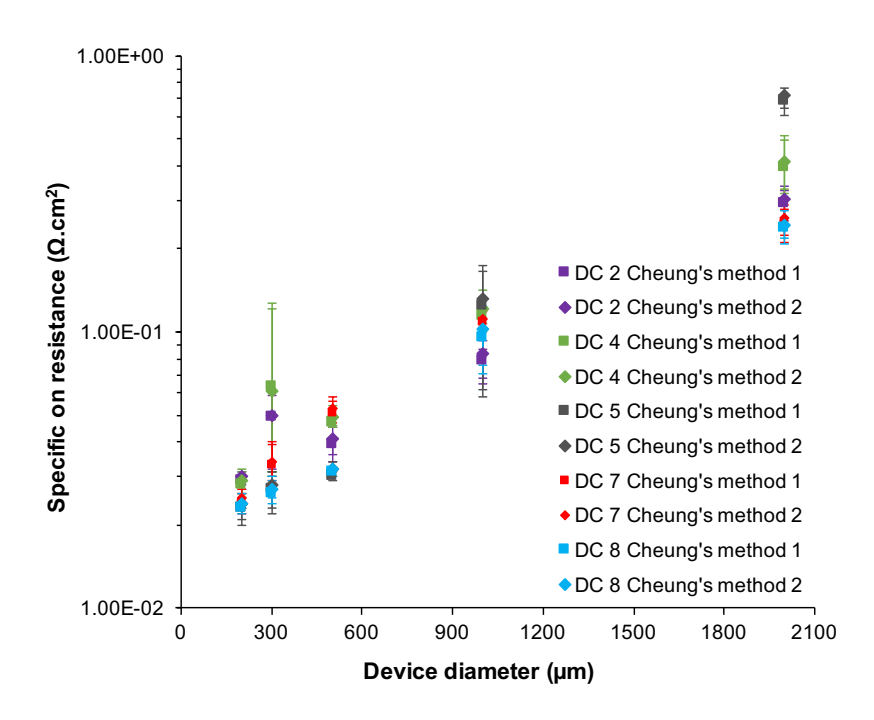


Figure 3.6: Specific on resistance for all fabricated diodes as a function of diameter size. The error bars represent the absolute minimum and maximum of the data.

 Ω .cm² for detector diameters up to 500 μ m. Slight deviations from these values can be observed in the specific on resistance for detectors with diameters of 1 mm and 2 mm, for all fabricated diodes. The increase in the specific on resistance for the larger diodes is thought to be linked to a higher number of semiconductor defects located under the Schottky contact. This hypothesis is matched by the data in [42], which identified that imperfections at the semiconductor surface play an important role during contact formation.

Despite the size dependence of the extracted specific on resistance, it is expected that the contact resistivity should decrease when higher annealing temperatures are used for the formation of Schottky contact [126]. Based on the annealing temperature used for the Schottky contacts in this fabrication step (summarised in Table 3.2), diodes on wafers DC 4 and DC 8 (660 °C) would be expected to show a higher specific on resistance in comparison to those on sample DC 7 (700 °C). However, the variation in the data is not statistically significant for all Schottky contact areas on these wafers, as can be observed by the data in Figure 3.6. This situation may result from the relatively small difference between the high and low annealing temperatures used to form the Schottky contact, resulting in the formation of the same phase of NiSi $_x$ in the Schottky contact and will have an insignificant effect on the specific on resistance in comparison to the variation that is likely to arise from the dopant concentration and thickness variations in the epilayer, which are often specified as $\pm 10\%$ in both cases.

3.3.3 Ideality factor, n

Ideality factor, n, is a parameter used to describe the deviation of ideal diodes from those described by the thermionic emission model [123]. The ideality factor of a diode should be in the range between 1 and 2, depending on the dominant current mechanism [127]. There are many factors that influence the ideality factor; the ideality factor will be more than 1 if the current is dominated by generation current mechanisms [127]. Moloi and McPherson suggested that the presence of an interface layer between the metal and the semiconductor, temperature and the generation or recombination of charge carriers in the energy gap has a significant effect on the extracted ideality factor values [127]. Ideality factors values were extracted using Equation 3.7 for all fabricated diodes and shown in Figure 3.7 as a function of detector dimension.

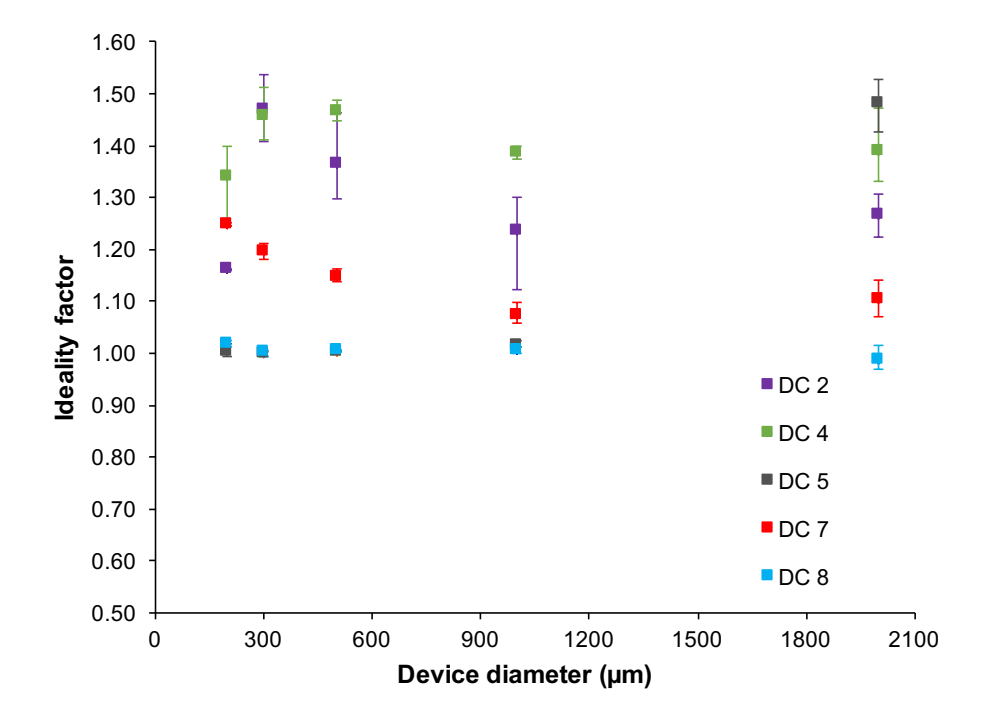


Figure 3.7: Ideality factor for all fabricated diodes as a function of diameter size. The error bars represent the absolute minimum and maximum of the data.

The observed variation in the ideality factor of all the diodes investigated here is minor, with all values being comparable to that of an ideal diode (n = 1.0), except for the diodes fabricated on wafers DC 2 and DC 4. The deviation of the ideality factor for these diodes from that of an ideal device is especially noticeable for devices with 300 and 500 μ m sides. As shown by the data in Figure 3.7, the values of ideality factor are less than 1.30 ± 0.08 for all samples investigated (except for DC 2 and DC 4) and agree well with values published in the literature for n-type 4H-SiC nickel silicide barriers [113]. From the data, it can be observed that the ideality factors for samples DC

2 and DC 4 at all detector diameters, are in the range of 1.25 to 1.50. DC 4 where the silicon carbide was etched slightly at the edge of the contact presented a significant increase in ideality factor (n) in range between 1.34 ± 0.12 and 1.50 ± 0.09 , which is significantly higher than the ideality factor of the planar devices. This finding is supported Khemka et al. [116], which reported that dry etching had produced damage created in the near-surface region of the semiconductor as a result of bombardment by energetic ions. The high ideality factor values observed in DC 2 may arise from the different deposition method used to deposit the metal for the Schottky contact. The location of the PVD machine which is not in the same room as the other cleanroom facilities, resulted in a larger time between etching and metal deposition, which is expected to allow an oxide layer to build up between the surface of the epilayer and the metal-contact. Whilst, an annealing process is used to form the nickel silicide Schottky by consuming the top surface of the SiC led to the existence of an oxide layer that will significantly change the diffusion of the nickel to the solid state reaction, resulting in different chemistry. However, ideality factor values increase slightly for 300 μ m to 200 μ m sized devices. This increase may be due to the small pixel effect where the separation between devices (110 μ m) is comparable to three times the epilayer thickness (105.9 μ m). The unterminated design for the Schottky contacts results in a greater pixel effect for the smaller devices, resulting in the observed increase in ideality factor.

3.3.4 Schottky barrier height, Φ_b

A potential barrier is formed at the metal–semiconductor interface when a metal is in intimate contact with a semiconductor [44]. The electrical behaviour of an Schottky or Ohmic contact in terms of the current characteristics, as well as its capacitance behaviour [44] can be determined from the Schottky barrier height (SBH) [102]. In order to minimise the current under reverse bias conditions (increasing the signal–to–noise ratio when used as a radiation detector), it is necessary to have a high SBH to form a good Schottky contact. Otherwise, a low SBH is required for a good Ohmic contact [102]. The Schottky barrier height can be determined using a number of techniques, including I–V, C–V, current–temperature (I–T) and photocurrent (P–C) measurements. The ideal barrier height, ϕ_{B0} can be acquired only when then the diode is under high forward bias, where the excited electrons can easily pass through the barrier [42]. Owing to image barrier lowering, the barrier height, Φ_b extracted from the I–V characteristics is lower than the ideal value [42]. I–V and C–V measurements are more sensitive to spatial inhomogeneities, the existence of insulating layers between the metal and the semiconductor, doping inhomogeneities, surface damage, and tunneling [42]. In addition, for I–V measurements, accurate knowledge of the Richardson constant (A*) is crucial for the determination

of Φ_b . The value of A* is known to vary significantly with processing conditions and hence will produce different values of barrier height [42]. In this section, A* = $4\pi m^* q k^2/h^3 = 146 \text{ A}(\text{cmK})^{-2}$ [44] has been used in the analysis, following the work of Nikitina *et al.* [114] and is identical to the theoretical expression given in [128] using the electron effective masses for 4H–SiC taken from the literature.

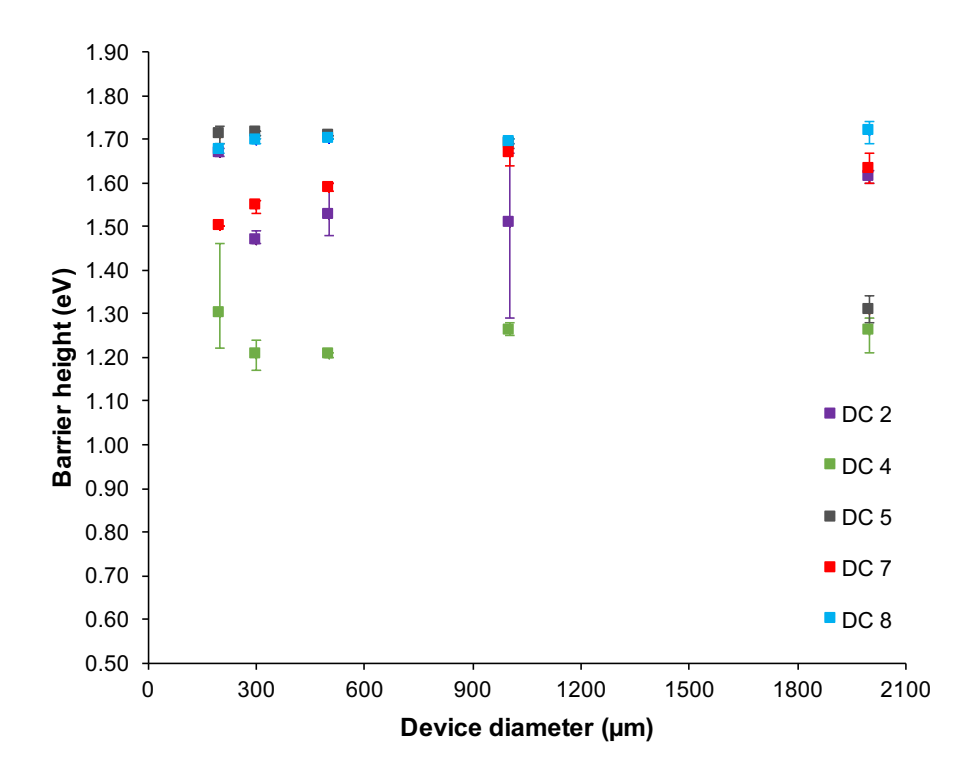


Figure 3.8: Barrier height for all fabricated diodes as a function of diameter size. The error bars represent the absolute minimum and maximum of the data.

The data in Figure 3.8 show the Schottky barrier heights extracted from the forward bias I–V data using Equation 3.9. The data show that the Schottky barrier heights show negligible variation with detector diameter. However, DC 8 which had a Schottky annealing temperature of 660 °C has the highest barrier of 1.72 ± 0.03 eV and 1.69 ± 0.01 eV for 2 mm and 1mm detectors, respectively. In contrast, DC 4 demonstrates the lowest barrier heights for all detector diameters with values in the range of $(1.21 - 1.30) \pm 0.04$ eV, which is related to the increased ideality factor caused by the etching of the sidewall to form the mesa structure. The etching process used to form the side wall results in increased roughness and the ion bombardment creates defects in the semiconductor, that act as carrier generation/recombination sites [115]. This finding was supported by the study performed by Khemka *et al.*, where they claimed that the observed increase in the effective surface state density and hence reduction in the effective barrier height in the etched samples is correlated with the creation of donor–like traps on the surface of the semiconductor [116]. Bardeen has pointed out the importance

of surface states in determining the barrier height, where it can result in the formation of chemically unsatisfied (dangling) bonds at the surface [42].

With the exception of DC 4, the experimental barrier height values obtained are higher than those reported in [25, 113] which is in the range of $(1.40 - 1.70) \pm 0.06$ eV. The enhanced barrier heights may be caused by quality of the epilayer used for the diode fabrication and a reduction in the interface roughness under the Schottky contact [129], which can be minimised by careful cleaning of the substrate before nickel deposition [125]. Otherwise, the two different annealing temperatures; 660 °C and 700 °C did not significantly affect the barrier height with both samples (DC 8 and DC 5) having barrier heights of 1.70 ± 0.01 eV. This appears to contradict to the findings reported by Badila *et al.* [130] and Nikitina *et al.* [114] which observed that, increasing the annealing temperature will decrease the Schottky barrier height. The data presented here indicates that the slight increase in the annealing temperature does not affect which phase of nickel silicide is formed and hence, the barrier height values.

3.3.5 Schottky barrier height, Φ_b against ideality factor, n

The relationship between the Schottky barrier height and ideality factor as a function of Schottky diode diameter size at room temperature can be observed from the data in Figure 3.9. The data exhibit a linear relationship between the Schottky barrier height and ideality factor, where the line of best fit to the experimental data can be deduced. Referring to the figure, the data for DC 5, DC 7 and DC 8 can be described by a single line of best fit with slopes of 0.84, 0.97 and 1.38, respectively. The quality of the line of best fit is significantly lower for DC2 (0.54), which is due in part to the significant uncertainty in the barrier height and ideality factors extracted from the I–V data, which can be linked to the poor electrical properties of the diodes.

Both the barrier height and ideality factor for diodes DC 5 and DC 8 were observed to lie within the same range, despite the different processing conditions used during fabrication; DC 5 was passivated with a Si₃N₄ layer and DC 8 was unpassivated. This observation contradicts that presented by Nguyen *et al.*, where they report that devices passivated with Si₃Ni₄ exhibit ideality factors approaching unity and unpassivated devices gave higher ideality factor values [131]. This phenomenon was attributed to the reduction in the concentration of defect levels in the passivated device [131]. Defects are expected to behave as recombination centers or as intermediate states for trap–assisted tunnel currents, increasing the ideality factor [42]. The electrical performance in terms of the ideality factor and barrier height in SiC Schottky diodes, is reported to be degraded by the

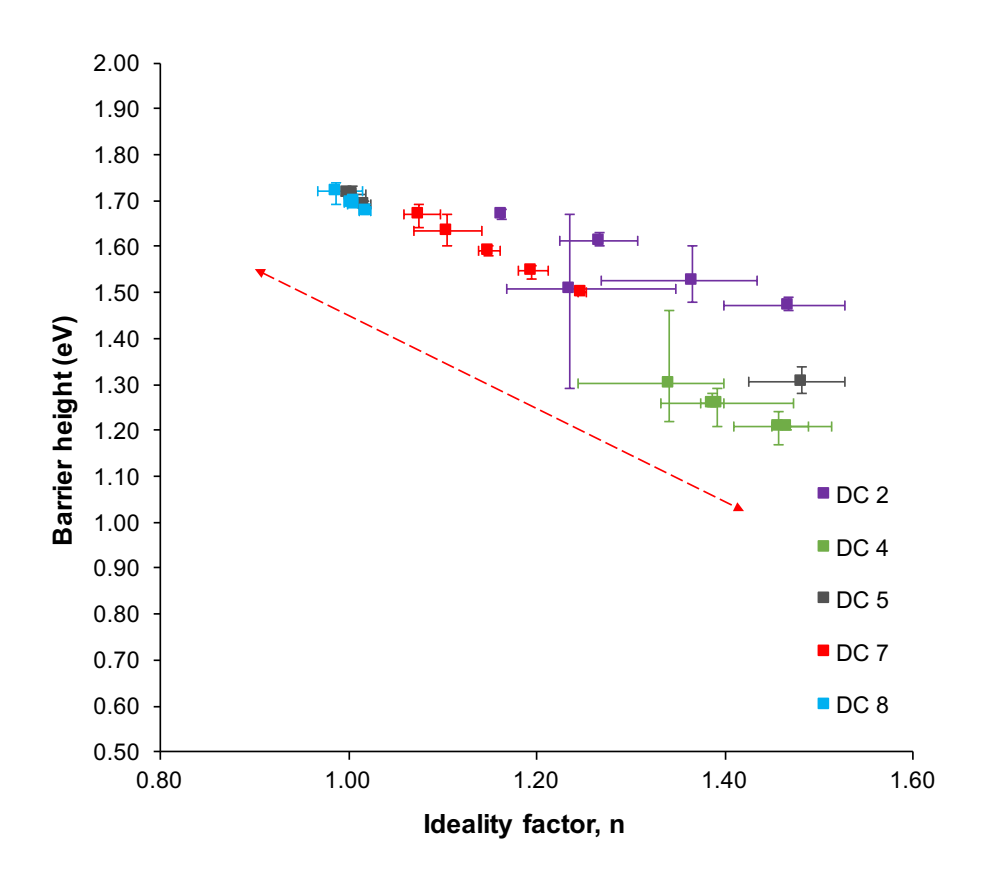


Figure 3.9: Barrier height plotted against ideality factor for all fabricated diodes as a function of diameter size. The error bars represent the absolute minimum and maximum of the data.

presence of surface traps, owing to higher ideality factor and lower barrier height values [42], which resulting in a significant increase in reverse leakage current and reduction in blocking voltage [44].

It should be noted that the use of the Cheung's model in this work results in a barrier height that is higher than that calculated using conventional thermionic emission theory [132] or the Norde function [61] because the values are not influenced by the high series resistance of the thick, lightly doped epitaxial layer. Since diodes are very sensitive to SiC surface preparation before metal deposition, Rhoderick and Williams [117] suggested that the presence of an interface layer between the metal and the silicon carbide, such as an unintentionally grown silicon dioxide film affects both the ideality factor and barrier height. Hence, there will be considerable variation in those values obtained for the same metal as investigated by different authors. This is because the chemically clean and atomically ordered surface of device is critically important to the resulting contact properties and proven to be crucial problem in SiC [102, 117].

3.3.6 Leakage current density, J_L

According to Knoll, an ideal radiation detector should have a leakage current that does not exceed 10^{-9} A to avoid significant resolution degradation [46]. This is critically important in fabricating high breakdown voltage diodes, as it will affect the reverse voltage that can be applied, limiting carrier drift velocities and charge collection efficiency [133]. Schoen *et al.* proposed a mechanism responsible for the reverse leakage current which depends on the Schottky barrier height, temperature, and applied bias [99]. The reverse bias characteristics of a Schottky diode can be approximated using thermionic emission theory, which enables it to be expressed in terms of the Schottky barrier height and the temperature [99].

The relationship between reverse leakage current density, J_L and Schottky barrier height, Φ_b is [44]

$$J_L = A^* T^2 e^{\left(\frac{-\Phi_b}{kT}\right)} \left[e^{\left(\frac{qV}{nkT}\right)} - 1 \right]$$
(3.10)

$$=J_S[e^{(\frac{qV}{nkT})}-1] \approx -J_S \tag{3.11}$$

where J_L is the reverse leakage current density, and J_S is the reverse saturation current density. In general, the leakage current in a practical diode is higher than the saturation current predicted by simple thermionic emission theory and shows a bias dependence. The inclusion of an image–force barrier height lowering term, where the barrier height is decreased by the influence of the electric field at the metal–semiconductor interface [99]. The image–force barrier height lowering is [44]

$$\triangle \Phi_B = \sqrt{\frac{qE_M}{4\pi K_s}} \tag{3.12}$$

where $\triangle \Phi_B$ is the image–force barrier height lowering, and E_M is the electric field at the metal–semiconductor interface.

The thermionic emission reverse leakage current density, accounting for image–force barrier height lowering may be written as [99]

$$J_L \approx -A^* T^2 e^{\left(\frac{-\Phi_B}{kT}\right)} e^{\left(\frac{\Delta\Phi_B}{kT}\right)} = -J_S e^{\left(\frac{\Delta\Phi_B}{kT}\right)}$$
(3.13)

by the insertion of Equation 3.12 into Equation 3.13, the relationship between J and E_M can be identified as

$$J_L = -J_S e^{\left(\frac{(qE_M)^{1/2}}{2(\pi K_S)^{1/2}kT}\right)}$$
(3.14)

From equation 3.12, high values of electric field at the metal–semiconductor interface decrease the barrier height at the semiconductor–metal interface by increasing the image–force barrier height lowering, and this results in the observed increase in the reverse leakage current density (as described by Equations 3.13 and 3.14). As can be expected from Equation 3.13, the measurement temperature also affects the leakage current density, where high temperatures produce high leakage current densities and this suggests that detectors have a maximum operating temperature that is limited by the leakage current exceeding the 1nA requirement specified at the beginning of the section. The data reported in this subsection were taken at room temperature and the variation of leakage current with measurement temperatures is reported in Chapter 4.

To investigate the leakage current for all fabricated Schottky diodes, all samples were reverse biased at voltages up to -200 V. As shown by the data in Figure 3.10, the majority of the Schottky contacts measured exhibit low reverse leakage current densities typically 0.20 ± 0.05 nA/cm² for reverse bias of -200 V, which is lower than the results reported by both Kimoto *et al.* [124] and Ma *et al.*[134] and comparable to those reported by Bertuccio *et al.* [135]. A few diodes from samples DC 4 and DC 5 demonstrated significantly higher leakage current densities (the highest being around 100 ± 0.112 μ A/cm² at -200 V) that may be due to different processing conditions and surface treatment during fabrication [125] or the inclusion of defects within the active area of the devices.

The lower barrier height (1.0 - 1.2 eV) of the sample DC 4 correlates to the higher leakage current, which is dominated by the enhanced tunnelling mechanism due to image forces [136]. A by product of the reaction between SiC and Ni during high–temperature annealing that is used to form the NiSi $_x$ region of the Schottky contact is the creation of carbon vacancies in the near–interface region of SiC [129]. These vacancies have a positive charge and act as donors, causing a reduction of the effective depletion width formed under the Schottky barrier and increasing the electron tunnelling probability [129]. These effects also result in a higher ideality factor under forward bias conditions. Furthermore, the existence of these donor–like traps are likely to be the reason for the higher leakage current in sample DC 5, where the Si $_3$ Ni $_4$ passivation was etched to open the window for the Schottky contact. Si $_3$ Ni $_4$ deposited on sample DC 5 as a passivation layer is expected to reduce the leakage current density by minimising the contribution arising from surface recombination, with the intention that this would lead to an increase in the signal–to–noise ratio [131]. Nonetheless, for our case, the ideality factor of DC 5 is close to unity, which indicates that the excess leakage current is not related to the recombination at the silicon carbide surface.

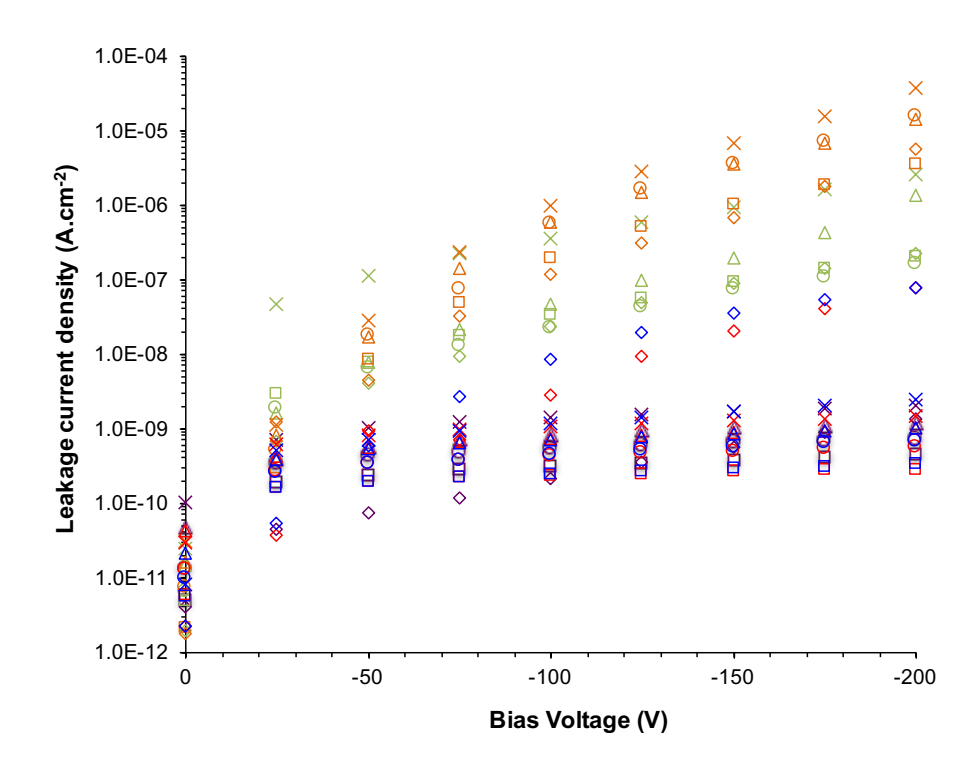


Figure 3.10: Leakage current density for all diodes with increasing detector's diameter, DC2 – purple, DC4 – green, DC5 – orange, DC7 – red, and DC8 – blue (× – 200 μ m, \triangle – 300 μ m, \circ – 500 μ m, \Box – 1 mm, \diamond – 2 mm)

The leakage current density for all the samples investigated here is shown in Figure 3.10. The data show an insignificant variation with detector diameter (except for samples DC 4 and DC 5) and does not show a strong dependence on the bias voltage, indicating that the electric field at the SiC-metal interface is low. The data show that the leakage current density does not vary with the diode area and this indicates that the current flow in the diodes is areal (i.e. through the whole of the detector) rather than peripheral (where it flows predominantly through the periphery). This indicates that despite the lack of an edge termination structure, the diodes do not suffer from significant field crowding under the edge of the Schottky contacts for the bias conditions examined here. Based on the characteristics shown, diodes on wafers DC 2, DC 7 and DC 8 meet the requirement for an ideal detector outlined at the beginning of this section and they have been considered in more detail for use as a radiation detector.

3.4 C-V measurements at room temperature

3.4.1 Doping concentration, N_D

The doping of the epilayer was extracted from completed detectors using C–V measurements and subsequently compared to the specifications provided by the vendor at the time of purchase. The capacitance, C, of a reversed biased junction and the dopant concentration can be expressed as [42]

$$C = \frac{K_s \varepsilon_0 A}{W_d} \tag{3.15}$$

$$N_D(W) = \frac{C^3}{qK_s\varepsilon_0 A^2 dC/dV} = \frac{2}{qK_s\varepsilon_0 A^2 d(1/C^2)/dV}$$
(3.16)

where K_s is semiconductor dielectric constant, ε_0 is the permittivity of free space, A is the Schottky contact area, and W_d is the depletion width. The dopant concentration, N_D is extracted from the slope of the straight line obtained from a plot of the reciprocal of the squared capacitance $(1/C^2)$ as a function of the bias voltage. This gradient can be expressed as $d(1/C^2)/dV$ in Equation 3.16.

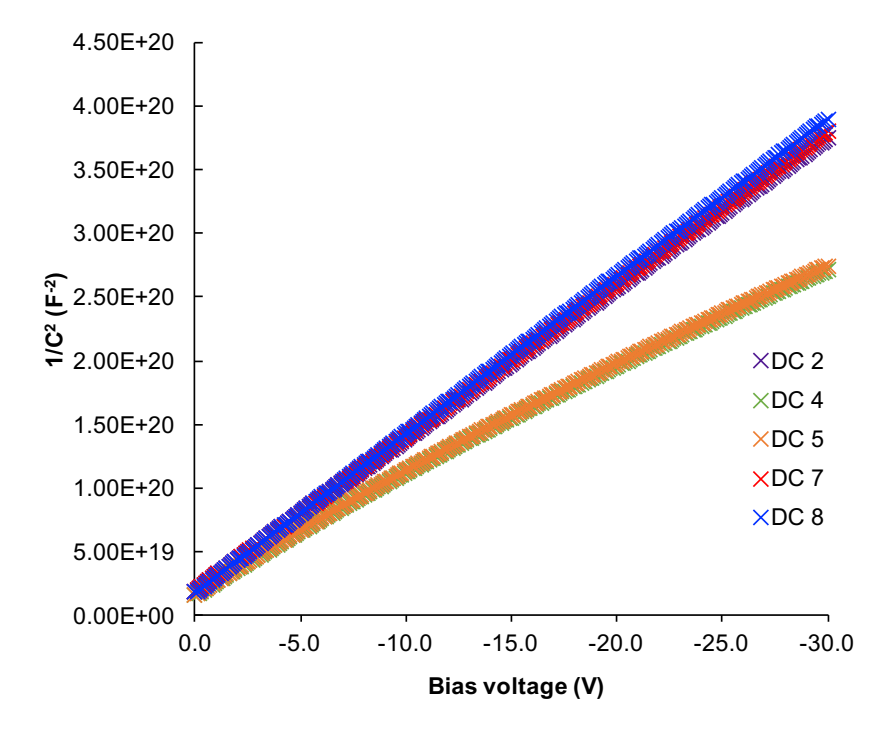


Figure 3.11: $1/C^2$ plotted against bias voltage for all diodes, slope from the graph was used to extracted doping concentration, N_D values for all fabricated diodes

Figure 3.11 shows a linear trend between the reciprocal of the squared capacitance and bias, along with the fitted line of best fit over the voltage range 0 – -30 V for the 2 mm diameter diodes studied here. The data demonstrate the expected reciprocal relationship between the capacitance and bias voltage, where the capacitance decreases with increasing reverse bias voltage. Following Equations 3.15 and 3.16, the application of a higher bias voltage results in lower detector capacitance, because of the increased in the depletion width. The dopant concentration for all of the fabricated samples was extracted from the data shown in Figure 3.11 and directly compared with the value given by the vendor of $N_D = 1.00 \times 10^{15} \text{ cm}^{-3}$. At typically low bias voltage (less than -10 V), the slope of the graph gives a dopant concentration of $N_D(W) = 1.12 \times 10^{15} \text{ cm}^{-3}$. Deviation of the calculated doping concentration from the actual value given by the wafer vendor has a discrepancy of approximately 9%. Nonetheless, at high bias voltage, a shift in the capacitance and hence Xintercept were observed between two devices from samples DC 4 and DC 5, which relate to a dopant concentration of $1.40 \times 10^{15} \text{ cm}^{-3}$ and $1.24 \times 10^{15} \text{ cm}^{-3}$, respectively. The cause for the increase in the calculated dopant concentration of approximately 37% and 21 % for samples DC 4 and DC 5, respectively can be explained from the processing conditions discussed in aforementioned section. In addition, due to high value of ideality factor and lower barrier height value as presented in preceding section, may be associated with a fairly thick interfacial layer that may have a significant effect on the capacitance attributed from the potential drop in the layer [44].

3.4.2 *Flat-band barrier height,* ϕ_B

Other than extraction of the barrier height from the I–V characteristics, C–V techniques have also been used to extract the flat–band barrier height of the fabricated diodes. The C–V data were extrapolated to $1/C^2 = 0$ corresponding to the flat–band condition in the semiconductor and this enables the extraction of the barrier height without influence of any barrier height lowering mechanisms [42]. The Schottky barrier height can then be deduced from the relationship with the built–in potential, V_{bi} , where the intercept on the voltage axis enables the built in potential to be determined [42]

$$\phi_B = V_{bi} + V_0 \tag{3.17}$$

where $V_0 = (kT/q) \ln(N_C/N_D)$, N_C is the effective density of states in the conduction band. A plot of $1/(C^2)$ as a function of bias (V) gives a fitted line with the slope of $2/[qK_S\varepsilon_0(N_A - N_D)]$ and the

intercept on the x-axis, $V_i = V_{bi} + kT/q$. The barrier height is extracted from the intercept voltage by [42]

$$\phi_B = -V_i + V_0 + \frac{kT}{q} (3.18)$$

Sample number	$(\phi_B \pm 0.10) \text{ (eV)}$	
DC 2	1.88	
DC 4	1.88	
DC 5	1.90	
DC 7	1.83	
DC 8	1.73	

Table 3.3: Table of flat-band barrier height for DC 2, DC 4, DC 5, DC 7 and DC 8 for 2 mm device size.

In the presence of an interfacial layer, the value of the barrier height obtained from C–V measurements is equal to the 'flat–band' barrier height which occurs under the application of a forward bias sufficient to eliminate the band–bending in the semiconductor [44]. The barrier height obtained under the flat–band condition is considered to be real fundamental quantity due to the fact that the electrical field in semiconductor is zero under the flat–band condition [137]. This condition eliminates the effects observed in the I–V characteristics and removes the influence of lateral inhomogeneity, owing to the effect from the image force lowering [137]. Aydin *et al.* suggested that homogenous barrier height values extracted from I–V measurements can be associated with the value of Schottky barrier height determined from C–V measurements and both values should be equal and a significant discrepancy can be linked to imperfections at the Schottky interface [138].

Table 3.3 summarises the extracted flat-band barrier heights for the fabricated diodes, with 2 mm diameters contact. In comparison to the barrier height (Φ_b) obtained from I–V measurements described in Section 3.3, samples DC 4 and DC 5 demonstrated a difference of approximately 60% with the values obtained using C–V techniques. Otherwise, the barrier heights for samples DC 2, DC 7 and DC 8 extracted using the two techniques are in close agreement. Any discrepancy between the barrier heights measured by the C–V and I–V methods may attributed to existence of a thick interfacial layer [44]. Barrier inhomogeneities contribute to deviations in the barrier height determined using the I–V methods in comparison to the values extracted using C–V methods [137, 138]. Song *et al.* suggested that inhomogeneities in the interfacial oxide layer composition,

non-uniformity of the interfacial charges, and interfacial oxide layer thickness are the main parameters that contribute to the barrier inhomogeneities [139]. The additional processing steps experienced by samples DC 4 and DC 5 may result in the formation of a thicker interfacial layer, which is supported by the observed I–V characteristics in terms of the ideality factor and barrier height, as described in previous section.

3.4.3 Depletion width, W_d

The depletion region is related to the capacitance of a Schottky barrier, which is often represented as a parallel plate capacitor where the separation between those plates is the depletion region and so can be increased by the application of a reverse bias [44]. Based on Equation 3.15, measurement of the capacitance characteristics of a diode allows the calculation of the depletion width, where the capacitance is inversely related to depletion width. From the C–V measurement, increasing the reversed bias will lower the capacitance and increase the depletion width. The extracted depletion width of 2 mm diameter size diodes on all samples were determined using Equation 3.15 and plotted as a function of bias voltage in Figure 3.12. Based on the calculated dopant concentration, the depletion width on all wafers was comparable for all the wafers for bias voltages less than -10 V, which are within the range 1.304 ± 0.056 to $3.524 \pm 0.209~\mu m$. Otherwise, the increase in the $d(1/C^2)/dV$ value and hence dopant concentration for samples DC 4 and DC 5 at bias voltages more negative than -10 V resulted in a 1.5% decrease in the depletion width. As can be observed from the data in the figure, the depletion width increased following the expected square root behaviour at bias voltages below -10 V. However, at higher bias voltages, the depletion width showed a linear trend for depletion region widths up to 6 μm , which occurred at typically -30 V.

Estimation of the depletion width is a critical step in the prediction of the detection efficiency of a radiation detector. In general, the detection efficiency is assumed to increase with increasing depletion width. In order to achieve a high quantum efficiency, the detector needs a wide depletion region where 100% of the incident energy is stopped, however this depends on the number of electron hole–pairs generated per incident photon [44]. However, thicker depletion regions are not always the most suitable solution as there are significant disadvantages in systems that require high speed operation. In this situation, a thinner depletion region is required in order to reduce the carrier transit time and hence increase the frequency response, whilst sacrificing some of the signal–to–noise ratio [44]. Hence, the trade–off between the speed of the response and quantum efficiency need to be considered in development of high performance systems [44].

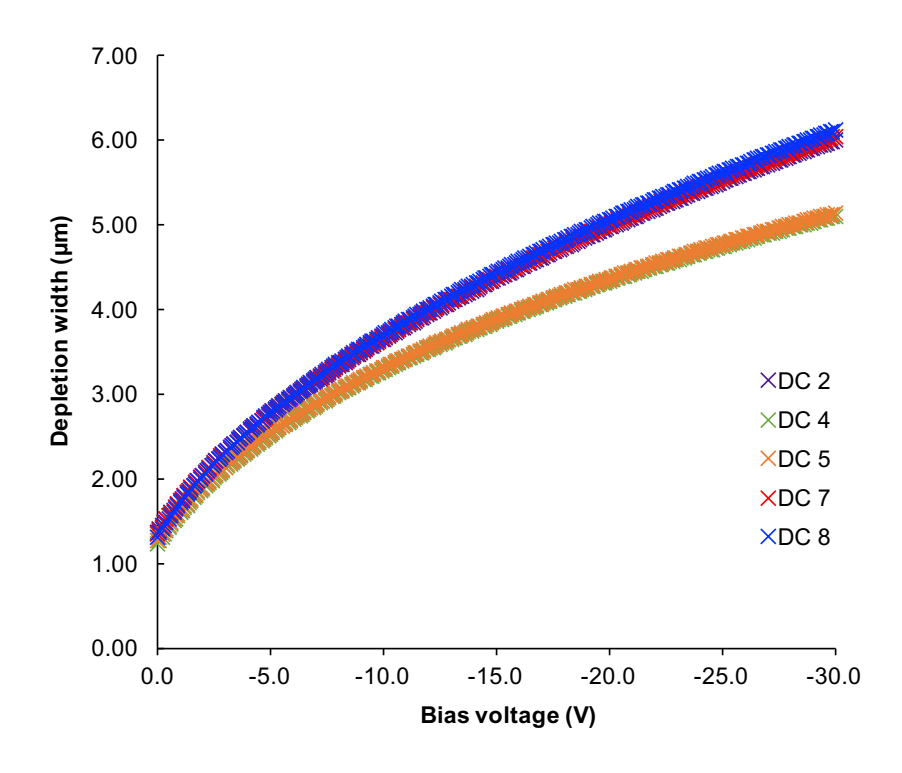


Figure 3.12: Depletion width, W_d plotted against bias voltage for all diodes

3.5 Conclusion

Details of the process used during device fabrication, layout design and subsequent fabrication process have been discussed. Parameters used during designing the mask layout and fabrication process were chosen based on the relationship of several factors which were explained theoretically. Additionally, the I-V and C-V characteristics were measured for all fabricated diodes. A comparison between the extracted parameters in terms of the specific on resistance, R_{on} , ideality factor, n, barrier height, Φ_b , reverse leakage current and depletion width, W_d have been investigated. Device characteristics with different detector diameters demonstrate almost constant ideality factor and barrier height values, however, there were slight deviations in specific on resistance and reverse leakage current for 2 mm diameter diodes. The different processing conditions used during the fabrication were observed to exert a significant influence on the diode characteristics. The dry etch process used during the fabrication of sample DC 4 was found to increase the ideality factor and reverse leakage current density, resulting in a reduction in the extracted barrier height values. In fact, passivation process accomplished through dry etching after deposition of Si₃Ni₄ layer on the surface of DC 5 sample, resulted in a significant surface leakage, resulting in deteriorating leakage current density. Meanwhile, two different annealing temperature; 660 and 700 °C used for the formation of $NiSi_x$ applied on all diodes did not result in a significant influence on either the ideality factor or barrier height values extracted.

Through C–V characteristics measurements, the dopant concentration, flat–band barrier height and depletion width were determined for 2 mm diameter devices for all wafers. Extraction of the dopant concentration on all fabricated diodes from the capacitance measurement showed a 9 % deviation from the value given by the vendor, which demonstrates the high quality of devices that were fabricated. Whilst, slight differences in the value of barrier height extracted from two different measurements; I–V and C–V on DC 4 and DC 5 samples, indicate an interfacial layer, mostly likely formed from a sub–stoichiometric SiO₂ layer, has been formed, which can be attributed to the additional processing condition on those samples.

In summary, based on the extracted characteristics and analysed performed on all fabricated diodes, DC 2, DC 7 and DC 8 wafers were chosen to be wire bonded and tested as a radiation detector due to its ideal characteristics, where they demonstrated a high quality metal—semiconductor interface. Their characteristics after wire bonded at elevated temperatures will be presented in Chapter 4 and compared with the data obtained in this chapter along with the signal response as a radiation detector.

Chapter 4

Temperature Independence of 4H–SiC Schottky Diode Radiation Detector at Elevated Temperatures

Part of the data and analysis in the chapter was published in N. S. Mohamed *et al.*, *IEEE Trans. Nucl. Sci.*, vol. 64, no. 7, pp. 1912-1919, 2017.

4.1 Introduction

Major improvements in material growth performance has resulted in enhanced detector performance from the materials used for semiconductor radiation detectors, including SiC, GaN, GaAs, CdZn(Te) and CdTe. Nevertheless, a significant amount of research has been devoted to intermediate and high atomic number (Z) materials, including CdZn(Te) and CdTe as they offer a higher stopping power, than the low atomic number materials that are commonly used. Silicon carbide based diode detectors have demonstrated excellent characteristics in regard to the radiation response [38, 39], in terms of low leakage current, high stability for long term deployment [40] and higher resolution detection for low mass charged particles and low energy photonic radiation [41], both at room and elevated temperatures. The outstanding material properties make silicon carbide an order of magnitude more radiation hard than silicon and this ability has enabled it to be demonstrated in a range of detector structures for deployment in extreme environments, including those where the ability to tolerate high radiation dose is imperative. This includes applications in space and nuclear environments, where the ability to detect highly energetic radiation is important. In contrast, detectors used in medical treatment, such as imaging and radiotherapy, use a range of radiation dose rates and energies for both particulate and photonic radiation often at relatively low energies.

4.1.1 Overview of SiC as a radiation detector

Semiconductor detectors based on silicon carbide (SiC) are well suited for use as radiation detectors due to the outstanding material properties, including the wide bandgap, which results in the high radiation tolerance, low leakage current, and a capability to realise electronic devices that can operate at temperatures significantly beyond room temperature [6, 20, 63]. There is a possibility to develop a silicon carbide based medical radiation detector for detection of low energy X–rays by taking advantage of the material having a response that is closer to human tissue in comparison to high atomic number (Z) materials. This tissue equivalence results in the detector having the same stopping power as human tissue. A significant challenge remains in the development of an ideal radiation detector for operation in low dose rate applications at elevated temperatures that is responsive to a range of ionising radiation whilst maintaining a high signal amplitude and charge response.

Previous reports in the literature describe the characterisation of silicon carbide devices for radiation detection and monitoring applications, reporting a response to X–rays, gamma rays, alpha and beta particles, protons and neutrons [24]. However, these investigations concentrated on the measurement of noise, full width at half maximum (FWHM), and charge collection efficiency (CCE) based on spectroscopic measurements [8, 21, 25, 30]. In addition, the high radiation tolerance of SiC has led to testing in high radiation flux at temperatures significantly beyond room temperature. Ruddy *et al.* studied the response of SiC Schottky and p–n junction diodes to alpha, neutron and gamma radiation and their findings demonstrate the potential of SiC detectors for use in applications where elevated temperatures and/or high radiation fields are encountered [8]. This finding was supported by Bertuccio *et al.* who observed that the current density of a SiC pixel X–ray detector increases with temperature, whereas the resolution of the energy spectrum are deteriorate slightly due to small changes in leakage current for measurement temperature up to $100 \, ^{\circ}$ C [30].

The linearity and sensitivity of SiC to high dose rate X–ray exposure has only been determined in a limited number of reported studies, all of which were performed by the same group of researchers, which observed that the diode characteristics are stable and show no evidence of carrier trapping or de–trapping [36, 96, 140]. Moreover, the charge and current responses of the detector were observed to be linear with the dose, dose rate and the sensitivity increasing linearly with the reverse bias applied to the detector [36, 140]. These results are consistent with those of standard silicon based dosimeters [36, 140]. However, the measurements reported were limited to the low bias regime (with data typically reported for a single applied bias) or at room temperature.

4.1.2 Highlight of the chapter

In this chapter, 4H–SiC Schottky diodes were selected to be wire–bonded and characterised prior to and during low dose rate X–ray irradiation. They were selected to be tested as radiation detectors based on their electrical characteristics presented in Chapter 3. Electrical characteristics in terms of forward and reverse bias I–V characteristics have been performed at room temperature prior to X–ray irradiation to ensure there are no changes in the electrical characteristics as a result of the wire bonding process. Subsequently, their performance as a radiation detector has been determined based on the dose rate linearity and dose sensitivity using a Phywe Xpert4 tabletop X–ray generator operated with an acceleration voltage of 35 kV and tube currents between 0.2 and 1.0 mA. The variation in the signal response and collected charge as a function of applied bias and measurement temperature were studied.

4.2 Experimental set up

Based on the electrical characterisation discussed in section 3.3, the selected diodes with superior electrical characteristics were wire—bonded using the small bonding pad area incorporated within the annular contact. Five representative detectors designated as detector 1 (D1) to detector 5 (D5) were selected from wafers DC 2, DC 7 and DC 8 and were thoroughly analysed as radiation detectors. The different treatment control on these designated detectors which have different Schottky contact areas and processing conditions during fabrication process are summarised in Table 4.1. Prior to the electrical characterisation and irradiation procedure, the selected diodes were mounted on a printed circuit board (PCB) which was designed to enable high voltage biasing of the detectors. The detector was grounded on the Ohmic contact side by means of a via through to the backside of the PCB. An optical micrograph of the fabricated diode mounted on the specifically designed PCB can be seen in Figure 4.1.

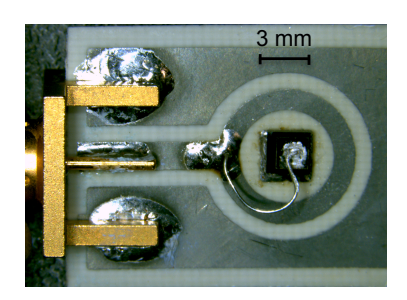


Figure 4.1: Optical micrograph of fabricated diodes mounted on the specially designed PCB.

Detector	Schottky contact	Annealing temperature (°C)	Schottky contact area (cm ²)
D1	Ti/Ni e-beam	660	0.81×10^{-2}
D2	Ti/Ni e-beam	700	3.61×10^{-2}
D3	Ti/Ni e-beam	700	0.81×10^{-2}
D4	Ti/Ni e-beam	660	3.61×10^{-2}
D5	Ni PVD	700	3.61×10^{-2}

Table 4.1: Table of different treatment control on Schottky diode designated as Detector 1 (D1), 2 (D2), 3(D3), 4(D4) and 5(D5).

The diodes were mounted in a die–cast enclosure and were electrically connected by means of low leakage BNC connectors as illustrated in Figure 4.2. A hole with a diameter of 1.5 cm was drilled in the middle on the top cover of the circuit box to avoid attenuation of the radiation incident on the diode, which was mounted on a Peltier cooler. To allow the evaluation of the temperature of the detector, a Pt₁₀₀₀ sensor was mounted on the Peltier cooler. The experimental setup used for dose rate linearity and dose sensitivity is schematically shown in Figure 4.3. The circuit box with fabricated diode was aligned with the X–ray beam emitted from the tube, which was operated without the use of a collimator in order to maximise the dose rate. During the measurements, the light in the X–ray unit was turn off and the unit was covered to ensure all measurements were measured in dark conditions.

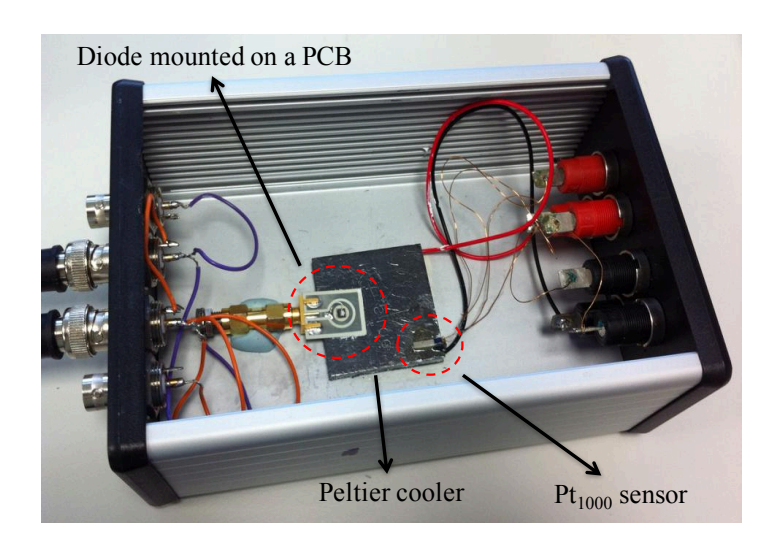


Figure 4.2: Circuit box with a fabricated diode mounted on top of the Peltier cooler. The Peltier cooler and Pt_{1000} sensor were used to regulate the temperature applied during measurement.

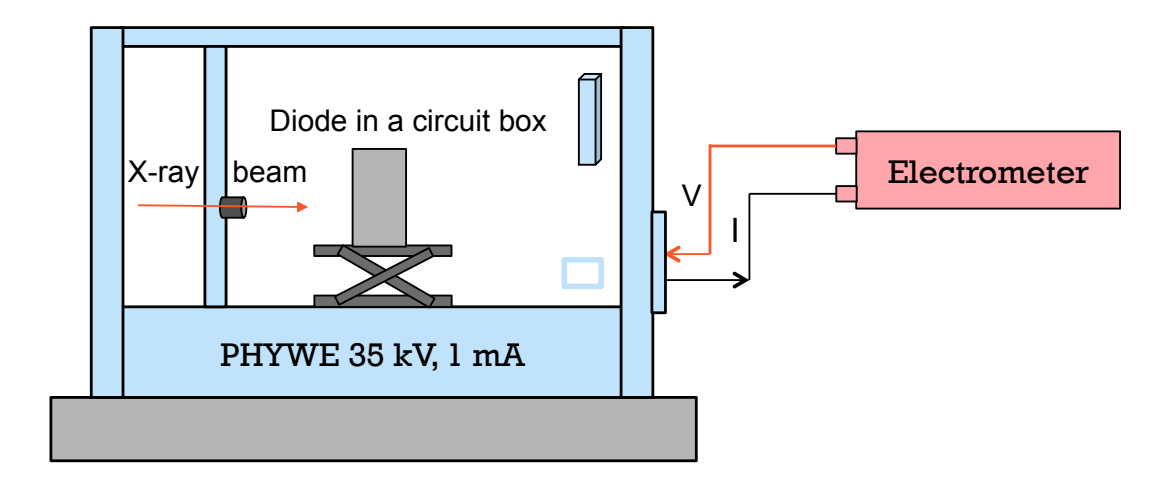


Figure 4.3: Experimental set up for low dose rate response. Circuit box with a 1.5 cm diameter hole in the middle was aligned with the incident X–ray beam.

4.3 Electrical characterisation at elevated temperatures up to 100 $^{\circ}\text{C}$

Temperature insensitivity for a radiation detector is very crucial for the response, particularly if it is to be used over a wide temperature range, as it can be one of the limiting factors in the determination of an accurate and precise dose measurement. Since the electrical characteristics show a temperature dependance, any changes in the characteristics will indirectly affect the detector response and detection properties. Aydin *et al.* reported that the temperature dependence of the I–V characteristics allowed them to investigate the different aspects of the conduction mechanism [138] through the Schottky contact. They also highlight that the detailed information about the conduction process or the nature of barrier formed at the metal–semiconductor interface cannot be extracted from the analysis of the I–V characteristics of the Schottky barrier diode at room temperature itself [138].

Whilst, wide bandgap semiconductors, including silicon carbide that has been used in this study, have a negligible sensitivity to temperature changes [141], the characteristics are not completely temperature independent. The high thermal conductivity of SiC permits dissipated heat to be removed from the device more effectively than in other traditional and wide bandgap semiconductors, such as silicon, cadmium zinc telluride (CdZn(Te)) and gallium nitride (GaN) [27]. The wide bandgap of the SiC observed to result in ultra low leakage current densities, which makes them ideal for dosimeter development [21]. They also do not require any external cooling systems to be operated in high temperature ambients and the electronic noise can be minimised for prolong operation especially in radiotherapy treatment, which use a high operational dose rate that may rise the temperature of the detector and electronics circuits [29, 30].

Parametric testing of the detectors using a Keithley 6517B electrometer were used to identify suitable diodes for radiation testing. These measurements are important to observe any changes in the electrical characteristics of those selected diodes before and after the wire–bonding process. Measurements at elevated temperature were performed using a Keithley 2200–32–3 power supply and Keithley 2110 51/2 Digit Multimeter to respectively supply power to the Peltier cooler and monitor the temperature experienced by the diode. The specific on resistance, R_{on} , ideality factor, n and barrier height, Φ_b were extracted using Cheung's method, which was described in detail in section 3.3.1, based on low voltage measurements at room and elevated temperatures, up to 100 °C. These parameters were used for screening suitable diodes for the radiation testing, based on their characteristics with the ideality factor used as the critical metric, which will be described in more detail in the next section.

In terms of the characteristics for radiation detection, the existence of an interfacial layer results in an increased leakage current at low reverse bias and a soft breakdown, meaning that the detector cannot be operated in the high bias regime. This severely limits the detector volume that can be depleted [93], limiting the active volume contributed to the narrow depletion region and low minority carrier diffusion length ($\mu\tau$ product), which in turn decreases the charge collection efficiency. This is due to the lower carrier mobility that indirectly relates to the low charge collection efficiency, which is governed by the $\mu\tau$ product as described in section 3.2 [51]. Therefore, the existence of an interfacial layer is detrimental to the carrier transport across the interface, which decreases the $\mu\tau$ product and is therefore expected to severely degrade the charge detection efficiency of the detector [93].

Plots of the current–voltage characteristics at room and elevated temperatures for detector D2 are shown in Figure 4.4. These characteristics are representative of the behaviour of all the detectors studied here. The current–voltage characteristics can be observed to be shifted towards the low bias region as the measurement temperature increases. Referring to the data plotted in Figure 4.4, high temperatures cause the diode to conduct at a lower bias voltage and this can be described by the explicit temperature dependence in Equations 4.1 and 4.2

$$I = AA^*T^2 \exp\frac{-q\Phi_b}{kT} \left(\exp\frac{qV}{nkT} - 1\right) = I_0 \left(\exp\frac{qV}{nkT} - 1\right)$$
(4.1)

$$I = I_0 \exp \frac{qV}{nkT} \tag{4.2}$$

where A is the Schottky contact area, A^* is the Richardson constant, Φ_b is the barrier height, T is the measurement temperature and I_0 is the saturation current.

Electrons are released by breaking the bonds with neighbouring atoms when thermal energy is absorbed by the semiconductor lattice, allowing them to move freely in the crystal structure [51]. This mechanism results in a greater concentration of electrons that are able to conduct as the temperature increases. Hence, the detector will conduct at a lower voltage in comparison to room temperature measurement. At high forward voltages, the I–V characteristics are linear and dominated by the series resistance of the drift region as shown by the data in Figure 4.4. This has a minor effect on the three main diode parameters, including the specific on resistance (R_{on}), ideality factor (n), and barrier height (Φ_b), which will be discussed in the following section.

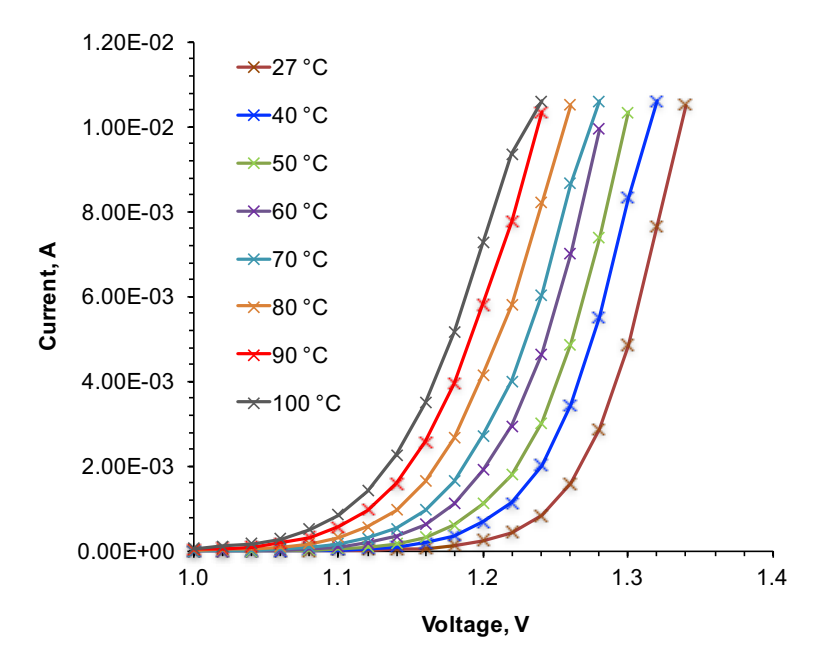


Figure 4.4: Current–voltage (I–V) characteristics with increasing temperature up to 100 °C for detector D2. Increasing the measurement temperatures resulted in the I–V plots to be shifted towards the low bias voltage.

4.3.1 Specific on resistance, Ω .cm²

Both plots of the specific on resistance as a function of temperature were extracted from the two different steps using Cheung's method as explained in section 3.3.1. The values of R_{on} extracted using dV/d(lnI) against I (R_1) and H(I) against I (R_2) are both shown in Figure 4.5. The values obtained for both plots demonstrate an agreement within 3% for the detectors at all temperatures considered here, where R_2 are typically higher than R_1 . The origin of this discrepancy arises from the calculation of H(I) used to extract the value of R_2 . The calculation is based on the ideality factor (n),

which is obtained from the extraction of the first plot (dV/d(lnI) against I) and so any uncertainties or systematic error in the ideality factor will have an influence on the extracted specific on–state resistance calculated. As can be observed from the data, the extracted values of R_{on} increases with increasing temperature, where it is more prominent for detectors D2, D4 and D5. These have larger Schottky contact areas in comparison to detectors D1 and D3 which exhibit almost constant value of R_{on} . This constant behaviour with variation in temperature is more noticeable for detector D3. The observed range of the specific on resistance as a function of reciprocal temperature demonstrate by the D2, D4 and D5, lie within the range of $0.3 - 0.7 \Omega.cm^2$, whilst, D1 and D3 exhibit a smaller range of the specific on resistance which are within the range of $0.1 - 0.25 \Omega.cm^2$.

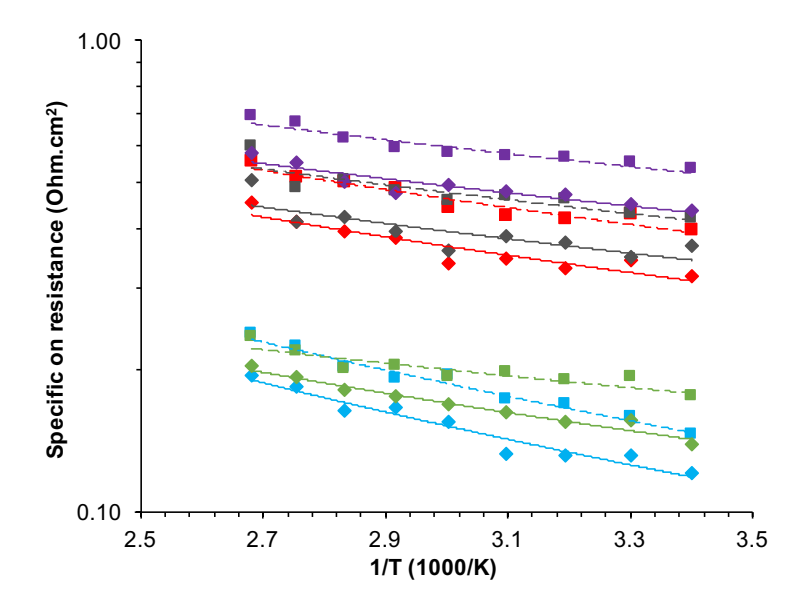


Figure 4.5: Specific on resistance; $R_1(\diamond)$ and R_2 (\square) for D1 (light blue), D2 (red), D3 (green), D4 (grey) and D5 (purple) at room and elevated temperatures up to 100 °C.

The solid and dash fitted lines in Figure 4.5 correspond to linear regression fits to the plots of R_1 and R_2 , respectively. From the plots, the power of the fitted line of all detectors indicates a power law dependance with temperature (T^P), which relates to the restriction of the carrier mobility with increasing temperature as shown in Figure 4.6. For lower impurity concentrations, the mobility (μ_l) at temperatures above 200 K is limited by optical phonon scattering and it decreases with temperature by $T^{-3/2}$ at lower temperatures [44]. At lower temperatures, carriers are scattered by ionised impurities and in general this is more of an issue for more highly doped semiconductors. For the temperature range of interest in this work, the carrier mobility is limited to the the optical phonon regime and so the specific on–resistance is expected to be approximated by $T^{-1.5}$. Values in the literature are typically in the range of $T^{-2.1}$ [105] and $T^{-1.6}$ [142] for 4H–SiC Schottky diode. In fact, the similar trend of temperature dependence has been observed experimentally by a number

of groups [40, 122]. Tekeli *et al.* reported that the observed temperature dependance is due to the different behaviour of the free charge carriers at low and high temperatures [122]. This is linked to the lack of free carriers at low temperatures (significantly below 200 K) and in the temperature region where there is no carrier freeze out, the specific on–resistance is dominated by the scattering mechanisms [44, 122].

Thus, this can be related to the specific on–resistance of the detectors, where R_{on} is proportional to $\frac{1}{\sigma}$ and $\sigma \propto n_e \mu_n$. Therefore, $R_{on} \propto \frac{1}{\mu_n}$. The data shown in Figure 4.5 demonstrate the power law of temperature dependance (P values) that fall within 0.9 to 2.0 for the variation in both R_1 and R_2 . Meanwhile, the fits to the data for detectors D1 and D2 both indicate that the specific on–resistance is dominated by optical phonon scattering with the P values of 1.9 - 2.0 and 1.32 - 1.35, respectively, that are close to the values observed by Itoh *et al.* [105].

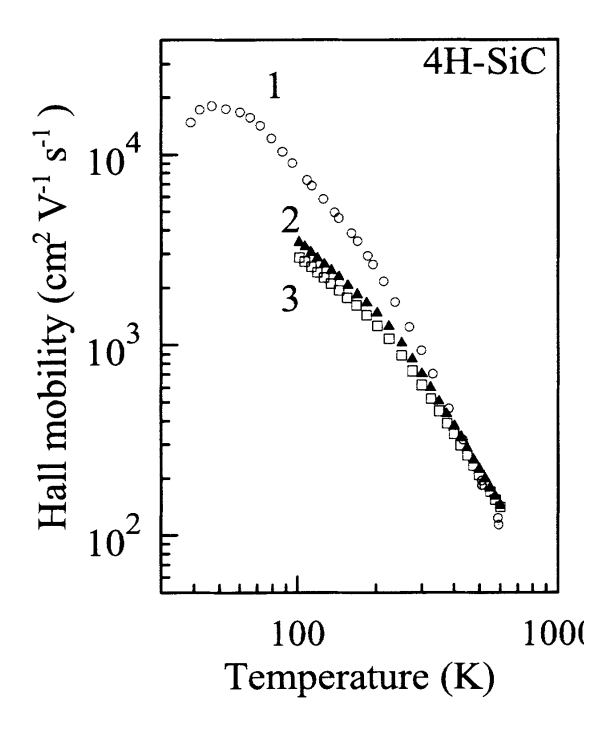


Figure 4.6: Electron Hall mobility of 4H–SiC at different doping concentrations and crystallographic orientations.1: high quality , unintentionally doped, 2: $N_d\cong 1.2\times 10^{17}~{\rm cm}^{-3}$ electric field $F\|c$, 3: $N_d\cong 1.2\times 10^{17}~{\rm cm}^{-3}$ electric field $F\perp c$. [9]

4.3.2 *Ideality factor, n and Schottky barrier height,* Φ_b

Extracted values for the ideality factor (n) and Schottky barrier height (Φ_b) as a function of measurement temperature for all wire-bonded diodes are shown by the data in Figure 4.7. The data show that the characteristics of the detectors are stable over the temperature range of 27 °C – 100 °C, with only minor variation. The exception to this is detector D4 where the values of ideality factor and barrier height as a function of temperature show significant shifts, which indicate that the additional process step during the fabrication results in a significant deterioration of the electrical characteristics. The stability of the extracted ideality factors and barrier height values with increasing temperature for detectors D1, D2, D3 and D5 are consistent with the data reported in [61, 132] and confirm the hypothesis that these detectors comprise a high quality metal-semiconductor interface. Detectors D1, D2 and D3 have ideality factors below 1.20 and the value for D5 is only slightly higher than this, with a value of 1.27 ± 0.06 . This hypothesis is strongly supported by the observation that detectors D1, D2 and D3 show an insignificant deviation of ideality factor values from that of an ideal diode (n = 1), where detector D1 has a value of 1.00 ± 0.04 across the temperature range studied. Whilst, detectors D2 and D3 have ideality factors of 1.10 ± 0.04 and 1.03 ± 0.04 , respectively. These values are comparable to the data reported previously for both X-ray detectors [63] and power diodes [61] in silicon carbide.

The extracted values for the barrier height for all detectors studied here are slightly higher than those published in the literature for Ni₂Si Schottky contacts on 4H–SiC [61, 114]. It should be noted that the Schottky contact for detector D5, which was fabricated using PVD for the deposition of Ni is within the same range as the other detectors described here, where the barrier height values obtained for all detectors are in the range of 1.54 - 1.74 eV. Detector D2 exhibits the highest barrier height with the value of 1.74 ± 0.06 eV, whilst detector D4 has the lowest barrier height of 1.54 ± 0.08 eV. Some of the discrepancy is thought to arise from the influence of the series resistance on the extracted barrier height and thickness of the interfacial layer [132]. However, this is minimised by the use of the Cheung analysis to perform the parameter extraction and the diodes revealed highly stable electrical characteristics in terms both the barrier heights and ideality factors. In addition, the values described here demonstrate only a minor variation in the electrical characteristics in comparison to the data measured at room temperature using probing station as described in section 3.3. This finding suggests that wire—bonding process did not significantly change the electrical characteristics of detectors under investigation.

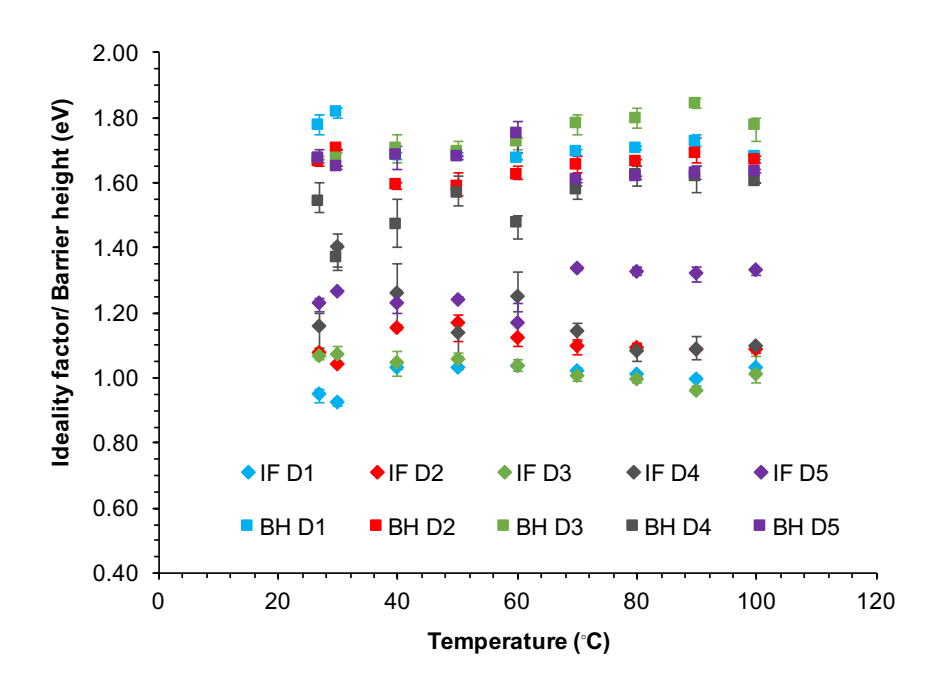


Figure 4.7: Ideality factor, IF (\diamond) and barrier height, BH (\Box) for detectors D1, D2, D3, D4 and D5. Electrical characteristics for all detectors exhibited temperature independence at room temperature and up to 100 °C. The error bars represent the absolute minimum and maximum of the data.

To observe the influence of the measurement temperature on the relationship between the Schottky barrier height and ideality factor, the extracted Schottky barrier heights were plotted as a function of ideality factor as shown by the data in Figure 4.8. The data exhibit a linear relationship between the Schottky barrier height and ideality factor, where the straight line of the least squares fit can be expressed as Φ_b (T) = (m.n + c) eV, where m and c are respectively the slope and intercept of the line. The observed variation in the linear relationship between the Schottky barrier height and the ideality factor of the Schottky contacts with temperatures were consistent with data previously published for a range of Schottky contacts, including Ni/4H-nSiC [138] and Al/p-Si [137]. This trend is similar to that observed by Schmitsdorf et al., who observed that the linear correlation between the experimental zero bias barrier height (Φ_b) and the ideality factors of the Schottky contact can be explained by the inclusion of lateral barrier height inhomogeneities in the Schottky diodes [143]. Based on the data, it can be observed that detectors D1 and D2 have a relationship which close to unity and can be expressed using Φ_b (T) = (2.971 -1.254 n) eV and Φ_b (T) = (2.755 -1.005 n) eV, respectively. In contrast, the data for detector D3 demonstrate a higher gradient of the fitted line $(\Phi_b (T) = (3.349 - 1.566 n) \text{ eV})$ due to the slight reduction in the barrier height with decreasing measurement temperature as exhibited by the data in Figure 4.7. Dokme et al. [137] and Tung et al. [144] observed that the significant decrease in the barrier height and corresponding increase in the ideality factor, especially for the low temperatures investigated, were caused by barrier height

inhomogeneities. Meanwhile, the increased variation in the ideality factor and Schottky barrier height over the range of measurement temperatures for detectors D4 and D5 were as a result of the lower value of the slope extracted from the fitted line.

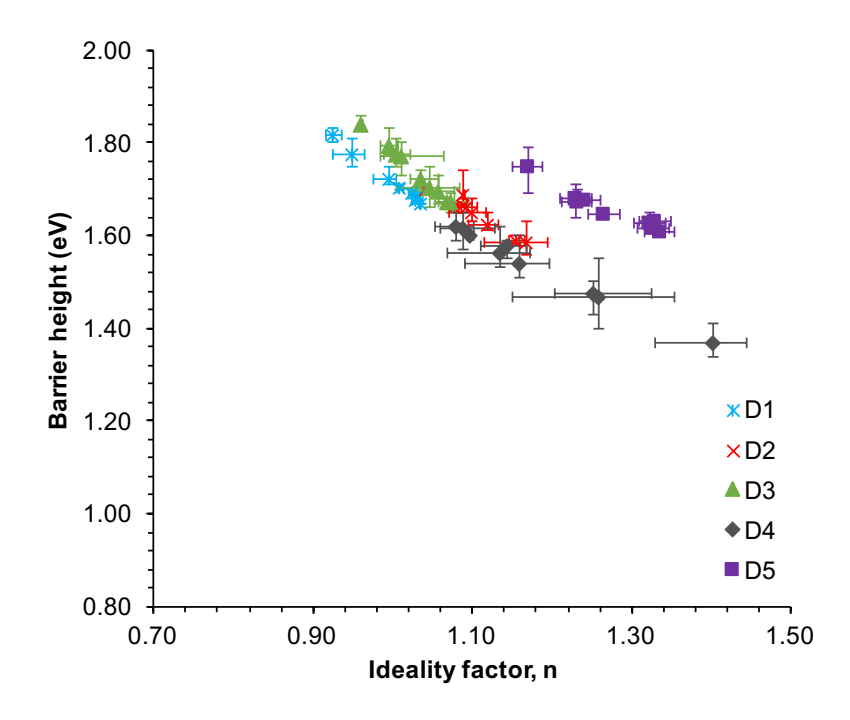


Figure 4.8: Barrier height against ideality factor as a function of temperature for detectors D1, D2, D3, D4 and D5. Variation of the barrier height against ideality factor exhibited a linear relationship, where the deduced straight line of the least squares fit to the experimental data expressed as Φ_b (T) = (m.n + c) eV. The error bars represent the absolute minimum and maximum of the data.

As mentioned in section 3.3.1, it should be noted that the use of the Cheung model in this work results in a barrier height that is higher than that calculated using conventional thermionic emission theory [132] or the Norde Function [61] because the values are not influenced by the high series resistance of the thick, lightly doped epitaxial layer. Additionally, inhomogeneities and/or residual processing induced contamination in the interfacial region are commonly the reason for deviations from the ideal behaviour in the electrical characteristics of Schottky contacts [138]. The extracted barrier heights of 1.71 ± 0.05 eV for D1 and 1.65 ± 0.04 eV for D2, coupled with the low ideality factors indicate their suitability for high performance radiation detection. The temperature dependence of the characteristics presented in this section indicates that silicon carbide Schottky diode—based detectors offer a performance suitable for medical applications at temperatures below 100 °C without the need for external cooling.

4.4 Low dose rate radiation response at room and elevated temperatures up to 100 °C

The dominant interaction mechanism for photon energies below 50 keV is the photoelectric effect, whereas the Compton scattering begins to be relevant above 50 keV as illustrated schematically in Figure 4.9. The photoelectric effect produced an electrical current as a result of the interaction of the low energy photons in the intrinsic layer of the detector, formed by the depletion region. The low Z number of silicon carbide ($Z_{\rm eff}\approx 10$ [21]) decreases the possibility of a photoelectric effect within the detector material, where it is the dominant mechanism that contribute to a high detection efficiency (i.e high current signal). Detection of the low energy photons, particularly for low dose rate radiation is a significant challenge. However, the incorporation of carbon as a significant portion of the SiC detecting medium provide a significant advantage in comparison to Si detectors, as it is more tissue—equivalent for dosimetry applications [141]. This is important for dosimetric systems in medical imaging applications, where low dose diagnostic procedures are routinely used. Romei *et al.* emphasis that both quality assurance and patient dosimetry which is accurate and easy to use with a wide dose range and preferably a real—time response are required to support a range of medical procedures [32].

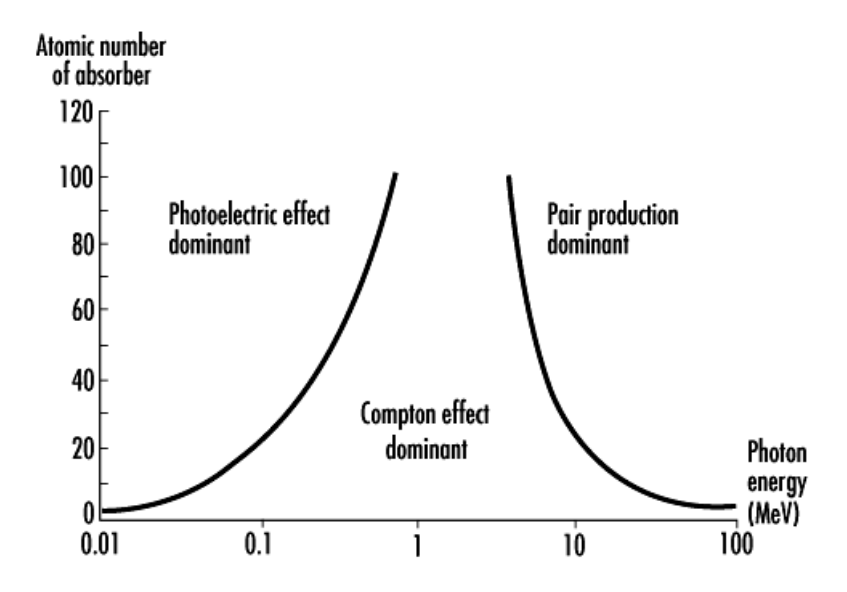


Figure 4.9: The relative contribution of the different mechanisms of radiation interaction which contribute to photoelectric effect, Compton scattering and pair production.^[145]

In this study, the low dose rate response has been evaluated in terms of dose rate linearity and dose sensitivity for the detectors that showed good electrical characteristics. Dose rate linearity and dose sensitivity in radiation detection are define as the ratio of the current detected in the detector from exposure to increasing dose rate and the collected charge generated by the radiation with increasing absorbed dose, respectively. Increasing the dose sensitivity and response to low—

energy X-ray photons enables the use of lower doses in imaging applications, which has significant benefit for patients and radiographers. Increases in both characteristics are linked to the more efficient generation of electron-hole pairs created in the space charge region, that determine the electrical signal generated by the detector. To investigate the response of the fabricated detectors when exposed to ionising radiation, they were exposed to increasing dose rates at different bias voltages and measurement temperatures as described in the following subsection.

4.4.1 Experimental procedure

Dose rate linearity measurements were performed on detectors D1, D2, and D3, before D1 and D2 were selected for dose sensitivity measurements as a function of reverse bias at room temperature due to their superior electrical characteristics. Following this characterisation, the characteristics of D2 were determined as a function of both bias voltage and temperature up to 100 °C in order to gain a greater understanding of the mechanisms responsible for the radiation detection behaviour. The dose rate linearity and dose sensitivity of all detectors were determined from the exposure to X-ray photons generated from a tungsten target (W) with an acceleration voltage of 35 kV, operating at tube currents between 0.1 and 1.0 mA. The variation of the dose rate incident on the detectors as a function of tube current was determined using Vishay BPW34 Si photodiode [146] and validated using an RMS 30 from John Caunt Scientific [147], which is specifically calibrated to the energy range of interest (30 keV). Following the study performed by Oliveira et al., the BPW34 photodiode offers the highest sensitivity and response with the best repeatability and reproducibility in comparison to other commercially available photodiodes, including the SFH205, SFH206 and BPX90F [148]. The output from both the BPW34 and RMS30 as shown in Figure 4.10 indicate that, the current signal density and dose rate generated increase linearly with the tube current, as has been demonstrated previously by means of direct comparison to air kerma (kinetic energy release per unit mass) measurements [148].

4.4.2 Dose rate linearity: Room temperature measurements

The current generated during the exposure to the incident radiation, highlighting the variation with increasing dose rate is shown in Figure 4.11 as a function of bias voltage at room temperature for detectors D1, D2 and D3. The data show the expected linear correlation between the current density generated in the 4H–SiC Schottky diode and the incident dose rate. This can be directly

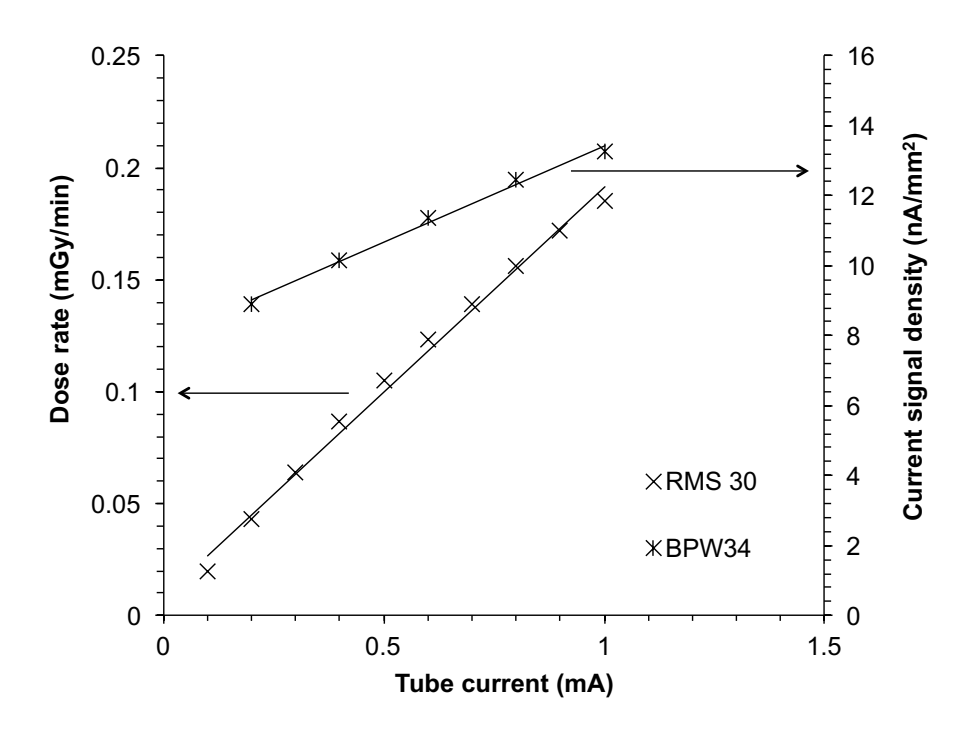


Figure 4.10: Calibration curve in terms of dose rate (mGy/min) and current signal density (nA/mm²) plotted against tube current which obtained from RMS 30 and BPW34 Si photodiode, respectively.

correlated to the tube current in the X-ray generator and hence the photonic flux incident on the detector [148], allowing the conclusion that the current detected in the detector is linearly related to the incident dose rate. From the data it is possible to determine the sensitivity of detectors D1 and D2 (in nA.min/Gy) is 20% of that measured using the BPW34 Si photodiode detector. The similarity in the current levels generated indicate that the silicon carbide detectors have a sensitivity that is comparable to conventional silicon based detectors, such as SFH206 and BPX90 [148]. The difference in the electron-hole pair creation energy in 4H–SiC (7.8 eV), which is almost double the equivalent value in Si (3.62 eV) [50] is expected to influence the generated current level in the detector. This is due to the average number of carriers generated in the detector by an X-ray photon is inversely proportional to the electron-hole pair generation energy [50] for an equal Fano factor. The lower average energy required by the silicon detector to create a pair of charge carriers, resulting in the formation of a greater number of charge carriers, resulting in a higher signal-to-noise ratio [32].

In addition, the data in Figure 4.11 show that the current signal density increases with the magnitude of the reverse bias for the dose rates studied here. The observed increase in response correlates with the increased volume of the depletion region with increasing reverse bias [36, 149]. However, the majority of the incident photon energy is not lost within the depletion region of the detector, because

the stopping range of the photons are significantly greater than the thickness of the epitaxial region used for the fabrication of the detector. The detection efficiency of a SiC detector with a depletion region thickness of 14.5 μ m can be estimated to be 0.5% for an incident photon energy of 30 keV [63]. This low efficiency is because the majority of the electron-hole pairs are generated in the highly doped substrate region beyond the depletion region where the carriers recombine before they can be pulled apart by the electric field and hence do not contribute to the signal.

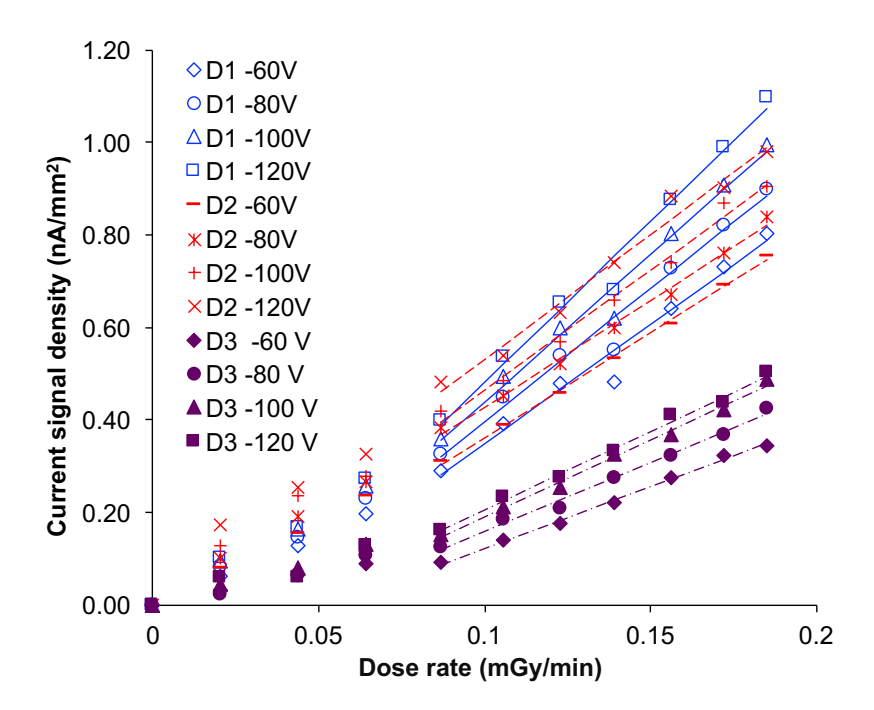


Figure 4.11: Current signal density plotted against dose rate for detectors D1, D2 and D3 at room temperature.

The data show that the current signal density generated on exposure to the X-ray photons is approximately 50% lower for detector D3 in comparison to D1 and D2, despite the ideal electrical characteristics (in terms of ideality factor and barrier height) over the range of temperatures as shown by the data in Figure 4.7. Otherwise, the similarity in the current signal density for detectors D1 and D2 under identical conditions indicates that diode area effects are dominating the response, supporting the hypothesis that the diodes are well suited to operating as radiation detectors. The detected current signal density at a reverse bias of -100 V extracted from the data in Figure 4.11 for detectors D1 and D2 at 0.18 mGy/min, is almost 25 times greater than the value of 40 pA/mm² reported in the literature [36], for a silicon carbide Schottky diode irradiated with 60 Co gamma irradiation at dose rate of 0.3 Gy/min. This can be related to the different range of radiation energies that were used during this study (35 kV X-ray) and in the previous published data (1.17 and 1.33 MeV γ -ray). The differences in the dominant radiation interaction mechanisms for X-ray and γ -ray,

resulted in different values of absorption efficiency between these detectors as described previously in sections 2.2.3 and 2.4. The radiation response from high energy and high dose rate produced by exposure to 6 MV photons will be discussed in section 6.2, Chapter 6.

In order to more fully understand the mechanism responsible for the current generation, the variation in the measured current as a function of depletion region width was determined, as shown by the data in Figure 4.12. However, the data were plotted only from the linear fitted region of the medium and high dose rate data (0.087 to 0.185 mGy/min) as shown in Figure 4.11, due to the linear fitting for the very low dose rate data (0.020 to 0.064 mGy/min) show a slight deviation from linear behaviour when the dose rate data is extrapolated back to zero. This deviation originates from the increase in the leakage current, which becomes comparable to the current generated by the incident radiation and hence reduces the signal—to—noise ratio. The dose rate data for the region of the linear fitted line show the expected linear correlation between the current density and the depletion width, which corresponds to the active volume of the detector. Linear regression fitting confirms that the generated current signal density falls to zero as the depletion region width is reduced to zero, which is consistent with the model that the origin of the current is the generation of electron—hole pairs in the depletion region.

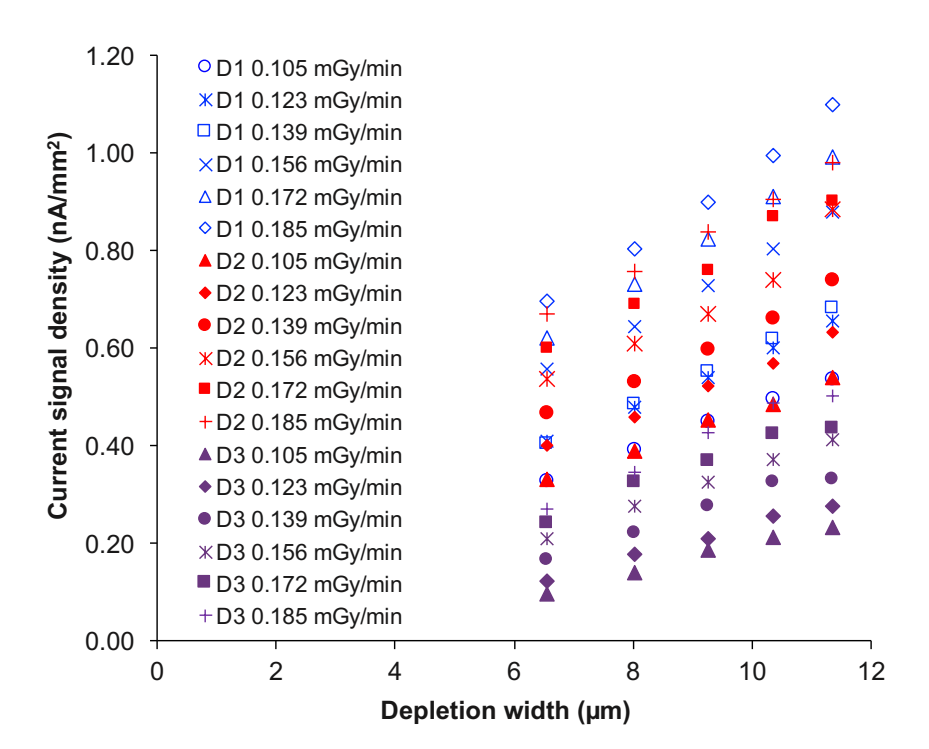


Figure 4.12: Current signal density against depletion width for D1, D2 and D3 at room temperature and dose rate ranging from 0.105 mGy/min to 0.185 mGy/min. Linear fitted lines for all detectors at all dose rates give R² between 0.94 and 1.

Moreover, with the exception of detector D3, the current signal at 0.185 mGy/min for a depletion width of 10.36 μ m, which is generated by the application of a -100 V bias, is approximately 50 times higher than the value reported previously in the literature [140], using a dose rate of 0.19 Gy/min 60 Co source that is 10^3 times greater than the one used in these measurements. Because the generated current is expected to be linear with dose rate, the response of both detectors D1 and D2 to incident X-ray photons are greater than those published previously with a current signal density of 0.995 ± 0.003 nA/mm² and 0.905 ± 0.0002 nA/mm², respectively. This enhancement is linked to the improvements in the quality of silicon carbide epitaxy, in particular the decrease in the concentration of carbon vacancies, that led to the increase in carrier lifetime from μ s to ms [150, 151]. Storasta et al. suggested that the $Z_{1/2}$ and $EH_{6/7}$ defects in the epilayer can be created by primary displacement of carbon atoms and it is related to different charge states of either V_C or C_i defects [150]. Deep level transient spectroscopy (DLTS) measurements have shown a strong correlation between the reduction in the $Z_{1/2}$ concentration, which coincides with improvements of the carrier lifetime [150]. This increase in the carrier lifetime increases the carrier mobility, which results in an increase in the diffusion length following equation $L = \sqrt{D\tau}$ and in turn increases the detection efficiency as described in section 4.3.

Dose rate linearity values can be extracted from the slope of the current signal density as a function of the incident dose rate data , as shown by the fitted lines at the linear region in Figure 4.11 and are expressed in μ A.min/Gy.mm². The value of dose rate linearity was normalised to the Schottky contact areas in order to compare the variation of their response between detectors D1, D2 and D3. The contact areas of the different detectors are summarised in Table 4.1. The data in Figure 4.13 show a linear correlation between the extracted dose rate linearity and bias voltage for all detectors characterised in this study. All detectors demonstrate an increase in dose rate linearity with increasing bias voltage, which can be explained by the generation of a wider depletion region with the application of a high bias voltage, resulting in an increase in the detection efficiency. Despite the variation in the Schottky contact areas for detectors D1 and D2, both detectors exhibit almost similar dose rate linearity. In contrast, detector D3 shows a value which is 50% lower at the range of bias voltages studied here. In fact, the data show that the detector response to the incident dose rate is within the range of (4.5 - 70) \pm 9.5E-05 μ A.min/Gy.mm² for detectors D1 and D2.

4.4.3 Dose rate linearity: Elevated temperature measurements

The performance of detector D2 has been determined at temperatures up to 100 °C under identical exposure conditions to those used to generate the data in Figures 4.11 and 4.12. Prior to the

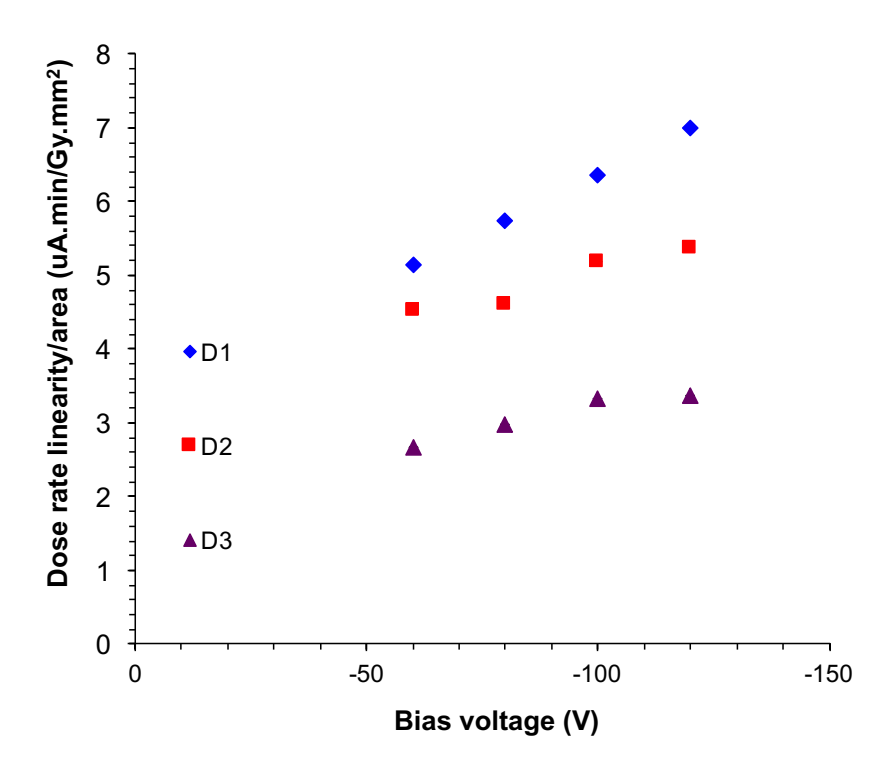


Figure 4.13: Dose rate linearity as a function of bias voltage applied at room temperatures for D1, D2 and D3. The data demonstrate slight increase in the dose rate linearity with increasing bias voltage. The error bar which represent the standard deviation of the dose rate linearity is smaller than bullet data point.

exposure, the leakage current for D2 has been determined as a function of bias voltage for the range of temperatures of interest, as shown by the data in Figure 4.14. The data show the variation in the current density generated on exposure to an X-ray dose rate of 0.185 mGy/min as a function of the leakage current when the beam was switched off. The individual data points relate to different applied bias levels, where the direction indicated by the arrow indicate increasing (more negative) bias points. The minimum and maximum leakage current densities for the detector D2 are 9.7×10^{-3} and 6.4×10^{-2} nA/mm², respectively. Increasing the temperature up to 100 °C leads to an increase in the diode leakage current as may be predicted by the thermionic emission reverse leakage current density, using Equation 3.13, as described in section 3.3.6.

However, the leakage current density taken at 27 °C was shown to be slightly higher at high bias voltages in comparison to other measurement temperatures. This odd trend of the leakage current density is consistent with the finding by Saxena *et al.* [142], and they related this behaviour with the 'annealing effect', which is commonly observed in SiC Schottky diodes and a potential improvement of the metal–SiC interface with increasing temperature, linked to reduction of the barrier inhomogenities within the contact area [142]. The temperature dependence of the leakage

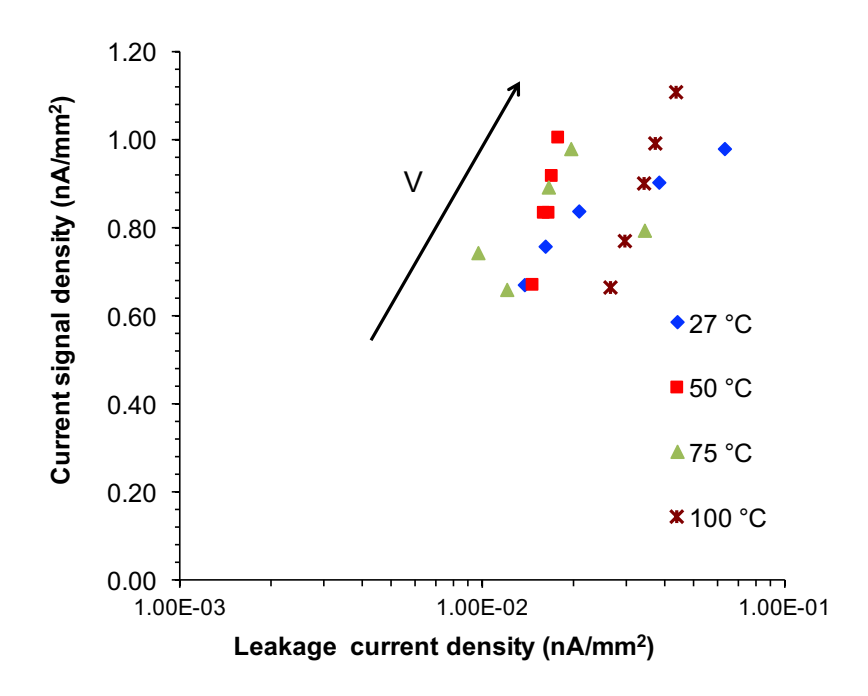


Figure 4.14: Current signal density against leakage current density at temperature up to $100\,^{\circ}$ C and bias voltage from -40 V till -120 V for detector D2. Current signal density values plotted were subtracted with the dark current values before measurements were performed.

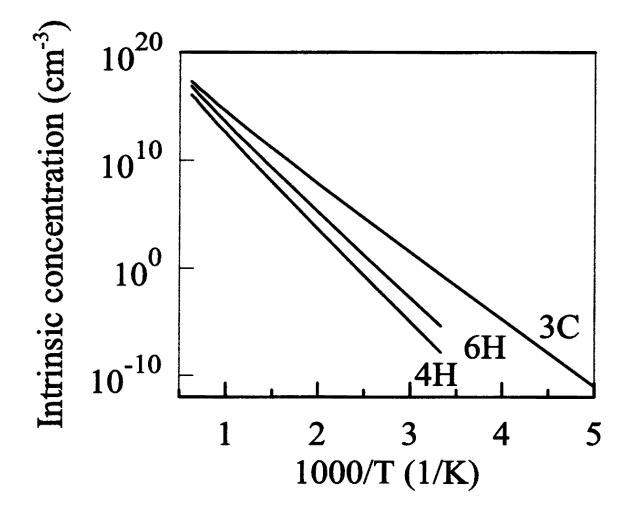


Figure 4.15: Intrinsic carrier concentration against measurement temperature for 3C, 4H and 6H-SiC.^[9]

current through the diode is very low for temperatures of 75 °C and below, whilst the 100 °C data indicates a factor of two increase over that observed at 75 °C. Theoretically, increasing the measurement temperature results in an increase in the intrinsic carrier concentration (n_i) as shown by the data in Figure 4.15. The relationship between the intrinsic carrier concentration (n_i) and measurement temperature (T) is given below [44]

$$n_i = \sqrt{N_C(T)N_V(T)} \exp\left(-\frac{E_G(T)q}{2kT}\right)$$
(4.3)

where E_G is the band gap and $N_C(T)$ and $N_V(T)$ are the effective densities of states in the conduction and valence band, respectively expressed as

$$N_C(T) = 2\left(\frac{2m_e^*kT}{h^2}\right)^{\frac{3}{2}} = \left(\frac{T}{300}\right)^{\frac{3}{2}} N_C(300) \tag{4.4}$$

and

$$N_V(T) = 2\left(\frac{2m_h^*kT}{h^2}\right)^{\frac{3}{2}} = \left(\frac{T}{300}\right)^{\frac{3}{2}} N_V(300) \tag{4.5}$$

where m_e^* and m_h^* are respectively the effective mass of electron and hole, and h is the Planck's constant.

In addition, the reverse leakage current that originates from generation–recombination mechanisms in the depletion region depend on the intrinsic carrier concentration and the volume of the depletion region. The relationship for the generation–recombination leakage current under reverse bias conditions ($J_L \propto n_i$) may be expressed as [117]

$$J_L = \frac{qn_iW_d}{2\tau_r} \tag{4.6}$$

where n_i is the intrinsic carrier concentration, W_d is the width of the depletion region, and τ_r is the lifetime within the depletion region.

The generated reverse leakage current in a radiation detector operating under high reverse bias can be substantial, but can be minimised through the use of a wide bandgap semiconductor, which reduces the intrinsic carrier concentration. For example, the intrinsic carrier concentration in silicon carbide is approximately 16 orders of magnitude lower than in silicon at 300 K [152]. The insignificant increment in the leakage current density (J_L) with increasing bias voltage that can be observed from the data shown in Figure 4.14 supports the hypothesis that carrier generation in the depletion region is not the dominant mechanism responsible for the reverse leakage current. Whilst the leakage currents are still small, typically 2 nA/cm² at -100 V, the rapid increase in reverse leakage current observed when the measurement temperature is increased from 50 °C to 75 °C. This condition is indicates of an upper operating temperature for high sensitivity measurements [40]. The data in the figure also

show that the increase in the leakage current through the detector correlates strongly with the increase in the signal current (detected signal) and the level of this correlation decreases significantly between 75 and 100 °C. This observation also indicates a practical limit on the upper operating temperature of the detector. Similar trends in increasing leakage current at operating temperatures of 100 °C have been observed previously in both 4H–SiC and 6H–SiC [30, 94] and this indicates that 100 °C is a fundamental limit for high performance radiation detection using silicon carbide.

The dose rate linearity (μ A.min/Gy) as a function of applied bias for detector D2 for a range of temperatures up to 100 °C is presented in Figure 4.16. The data show that the dose rate linearities do not show a significant variation with temperature below 100 °C but show an increase with applied bias up to -120 V (this equates to a depletion width of 11.35 μ m). Increasing the applied bias leads to an increase in the dose rate linearity as predicted from the dose rate linearity measurement at room temperature and described in section 4.4.2. The average dose rate linearity at temperatures below 75 °C for bias voltages between -60 V to -120 V are within $(14.83 - 19) \pm 0.46 \mu$ A.min/Gy. The temperature stability is due to the extremely low intrinsic carrier concentration in SiC, which arises from the wide bandgap, in comparison to conventional lower bandgap semiconductor materials such as silicon or gallium arsenide [94]. This is the material property of SiC that makes it capable of operating in high temperature applications without the requirements of external cooling. Nonetheless, the observed slight deviation in the linearity at 100 °C can be considered to be the practical temperature limit for the detector, supporting the observations drawn from the leakage current data described previously.

4.4.4 *Dose Sensitivity: Room temperature measurements*

The low $Z_{1/2}$ concentration of the epitaxial layer not only produces detectors with optimum electrical characteristics, but is also one of the factors that results in a highly reproducible and stable signal on exposure to the incident X-ray flux. Thus, to study the response of the fabricated detectors in terms of dose sensitivity, the X-ray beam has been switched on and off five times over a period of 30 minutes, with a constant applied reverse bias of -80 V, as shown by the data in Figure 4.17. Bias voltages were only applied between -80 V up to -180 V to maintain and ensure a high signal–to–noise ratio obtain during the measurement. This is due to the very low signal generated when low bias voltage applied (between 0 V to -70 V) and otherwise, high bias voltage more than -180 V will contribute to high noise and hence reducing the signal–to–noise ratio for both cases. The dose rate was maintained at 0.185 mGy/min during the exposure portions of the experiment by ensuring that the tube current was held constant at 1 mA. The high signal–to–noise ratio of the detector can

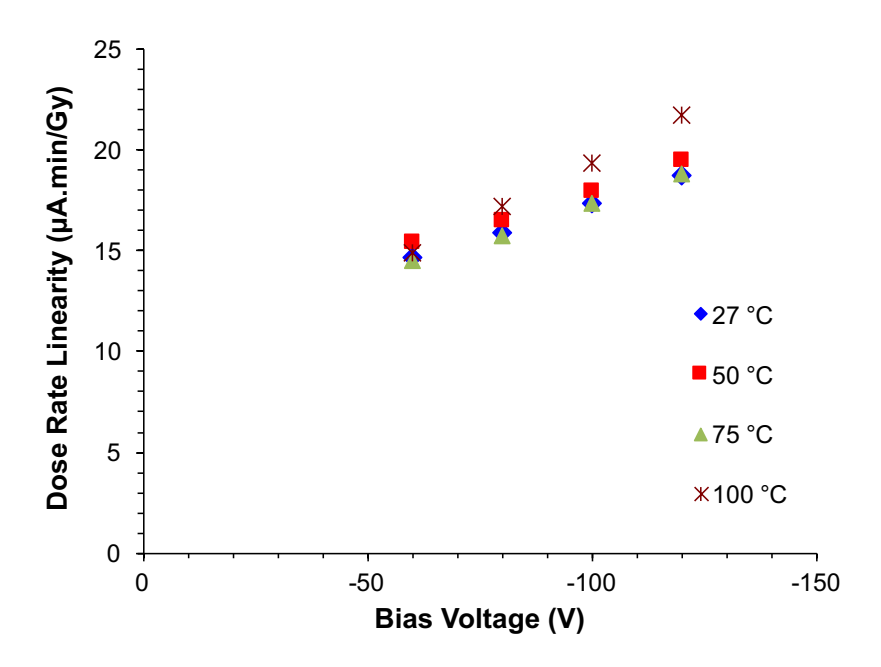


Figure 4.16: Dose rate linearity as a function of bias voltage applied at operated temperatures up to 100 °C for D2. With the exception at 100 °C, the dose rate linearity at all measurement temperates were almost consistent at all bias voltage. The error bar which represent the standard deviation of the dose rate linearity is smaller than bullet data point.

be observed from the difference between the high current portion of the data when the beam is on and the low current portion when the beam is off. The radiation–induced current is about 50 times higher than the background current. The leakage current during the beam off period is reproducible and stable with a typical value of 68.3 ± 13.3 pA corresponding to a current density of 19 nA/mm^2 , that is comparable to values reported in the literature from previous studies [36, 149]. The leakage current value during the beam off period is also consistent with the leakage current values described in section 4.4.3. As can be observed from the data, the detector takes about an average of 5 seconds to read the maximum signal after the beam is turn on. This delay is likely to be due to the X–ray tube warming up to ensure maximum emission.

The current signal response over the 30 minutes of exposure had the background leakage current from the background reading of detectors D1 and D2 at each bias voltage subtracted in order to clearly identify the current generated by the incident photons. To investigate the stability of the leakage current of both detectors over a range of time, the leakage current densities were plotted as a function of exposure time. Both detectors demonstrated stable leakage current density in a shorter exposure time at almost all bias voltages. Leakage current for detectors D1 and D2 seem to reach the stable values after 10 seconds of exposure time as can be seen from the data presented in Figure 4.18. However, it can be observed that detector D2 takes over 50 seconds to fully stabilise when operated

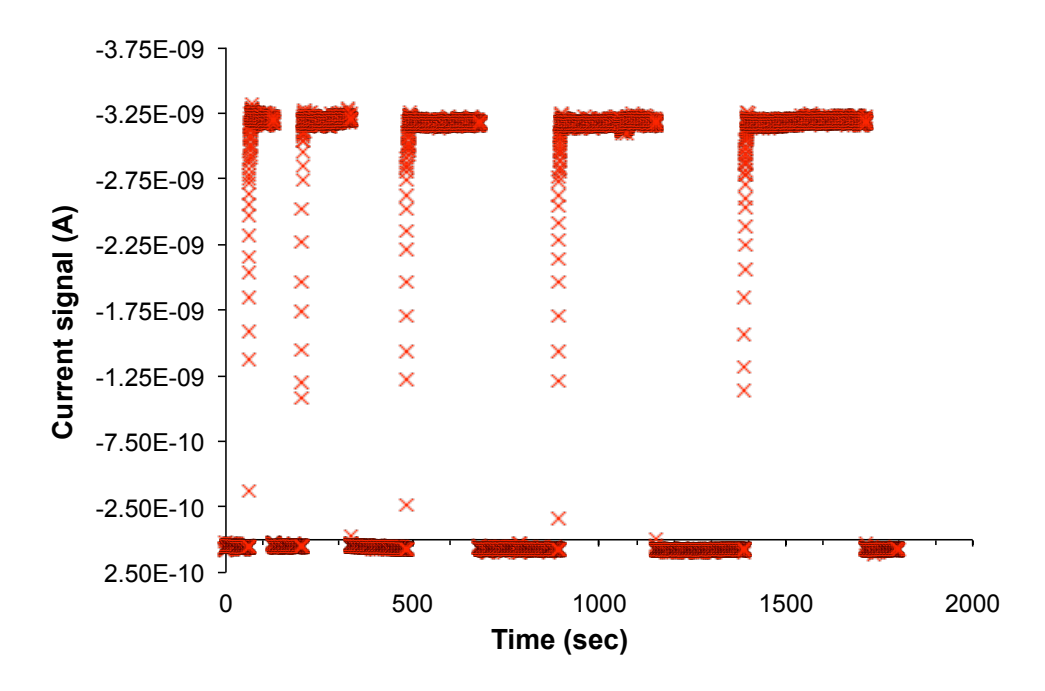


Figure 4.17: Current response for detector D2 as a function of exposure time for -80 V reverse bias at room temperature after background subtraction. Current signal is stable and reproducible at typically 3.25 nA.

at a bias of both -150 V and -180 V. This is due to the higher leakage current at both bias voltages, which is typically double that observed at bias voltages of below -120 V. The high leakage current observed in both diodes is expected to significantly influence the background signal, resulting in fluctuations in the current signal and hence a significant reduction in the signal—to—noise ratio, which will be discussed in a later section.

To compare the dose sensitivity between both detectors D1 and D2, the collected charge was calculated from the time integral of the data in Figure 4.17. The data in Figure 4.19 show the collected charge per unit area (μ C/mm²) as a function of exposure time for a detector exposed to a constant dose rate of 0.185 mGy/min. The absorbed dose is obtained by exposing the detector to the uncollimated X-ray beam for a cumulative duration from 66 seconds (1.1 minutes) up to 324 seconds (5.4 minutes), resulting in a total absorbed dose in the detector between 0.2 and 1.0 mGy. The data show that the collected charge per unit area increases linearly with exposure time and applied bias for both of the detectors, where it demonstrated a higher collected charge per unit area at high bias voltage and absorbed dose. The observed increase in the collected charge and hence dose sensitivity of the detectors at higher applied bias is due to the increased depletion width [36, 140], similar to the enhancement in the detected current described in subsection 4.4.2. Although the collected charge has been normalised to the Schottky contact area, the data show that detector D2 has a higher collected

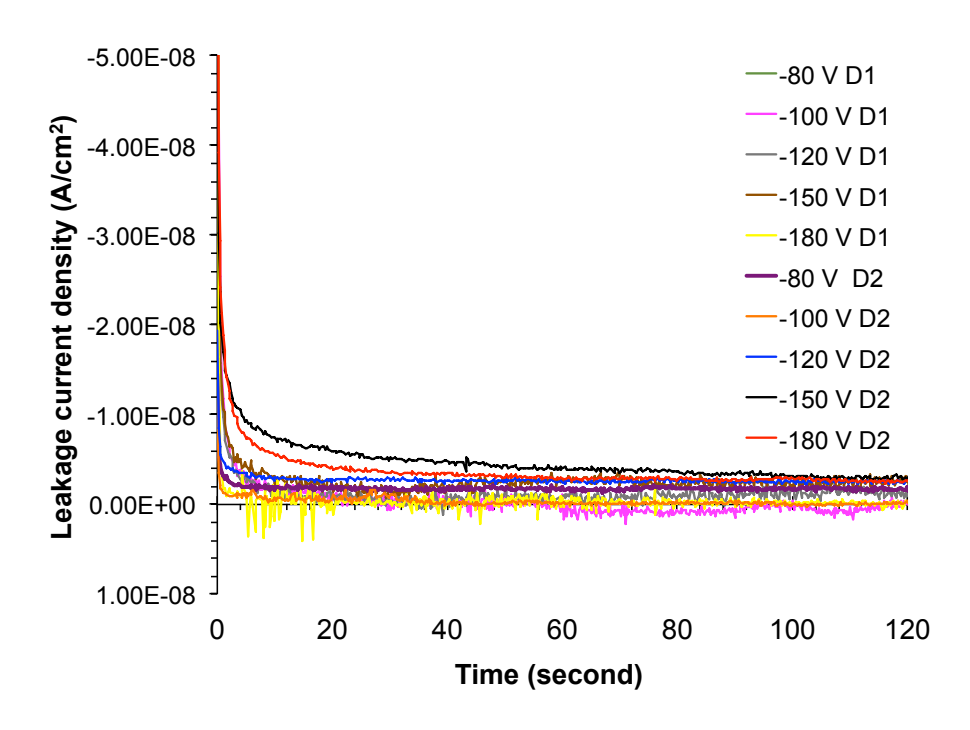


Figure 4.18: Leakage current density for detectors D1 and D2 as a function of exposure time at room temperature and bias voltages between -80 V and -180 V.

charge per unit area than detector D1. At -180 V bias voltage and 1 mGy absorbed dose, detector D2 achieved a maximum value of collected charge per unit area; $0.427 \,\mu\text{C/mm}^2$, which is almost 1.5 times higher than detector D1. This increase in the collected charge density for detector D2 is despite the ideality factor being higher and the barrier height lower than detector D1. This result indicates that the quality of the metal–semiconductor interface, as determined using conventional parametric testing techniques, does not determine the most suitable diode for the detection of low dose rate, low energy X–rays.

To further compare the characteristics of the current response from both detectors, the signal–to–noise ratio (SNR) was calculated using Equation 4.7 from the current response data shown in Figure 4.17. The SNR for detectors D1 and D2 as a function of bias voltage can be observed from the data in Figure 4.20. The data show that detector D2 has a higher SNR at bias voltages between -80 V and -120 V in comparison to D1, whereas, it was observed to have similar values of SNR once the bias voltage is increased above -150 V. It should be noted that detector D1 demonstrates an almost constant SNR over the full range of bias voltages investigated here, which is 53.4±3.7. The low SNR value of detector D2 at high bias voltages may be related to the high leakage current that can be observed from the data in Figure 4.18 and the large spread in the current response that can be observed from the error bars presented in Figure 4.19. This indicates that a detector with a smaller leakage current value, specifically at lower bias voltage will result in high SNR [94].

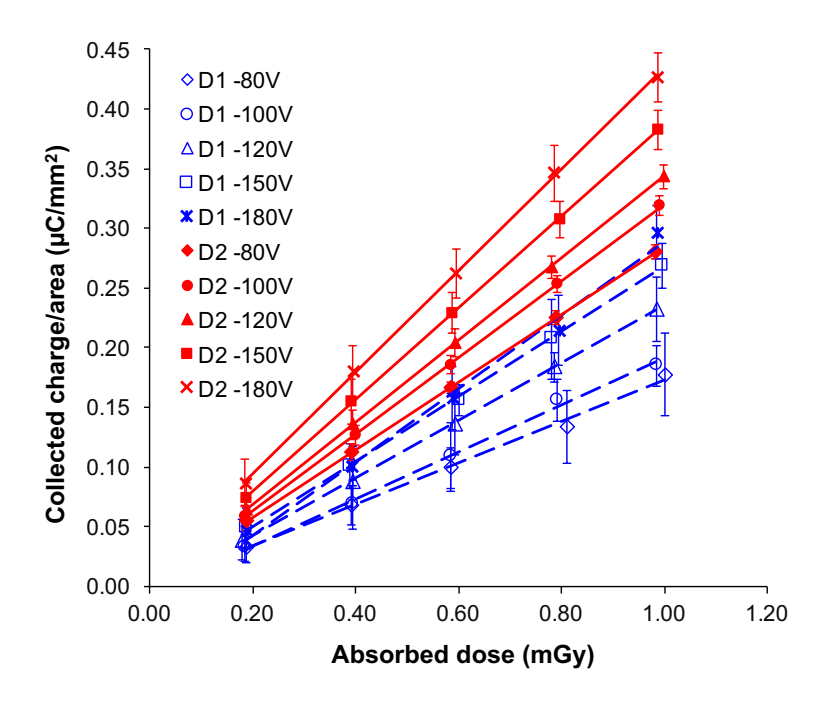


Figure 4.19: Collected charge per unit area as a function absorbed dose during irradiation to 0.185 mGy/min at different bias voltages and room temperature for D1 (with dashed line) and D2 (with solid line). The error bars represent the fractional standard deviation attributed from the random fluctuation of the signal response.

$$SNR = \frac{Average current signal}{Standard deviation of the current signal}$$
 (4.7)

The dose sensitivity of both detectors at room temperature were extracted from the slope of a linear fit to the plot of collected charge per unit area against absorbed dose (mC/Gy.mm²) in Figure 4.19. As expected from the linearity test data described in section 4.4.2, linear fitting to the data results in dose sensitivities between 0.284±8.91E-04 and 0.426±9.25E-04 mC/Gy.mm² for D2 and between 0.173±4.52E-05 to 0.307±6.24E-04 mC/Gy.mm² for D1 as shown in Figure 4.21. The data show that the dose sensitivity of D2 is higher than D1, despite the insignificant variation in the dose rate linearity for detectors D1 and D2 at room temperature. Based on the leakage current density described previously in Figure 4.18, both detectors demonstrate similar values of leakage current density. Hence, this parameter can be disregarded from the list of possible factors that contribute to the observed discrepancies in the dose sensitivity of detectors D1 and D2. Although the values of the dose sensitivity has been normalised to the areas of the Schottky contact, however, the difference in the contact areas may be one of the parameters that exert an influence in the observed discrepancies

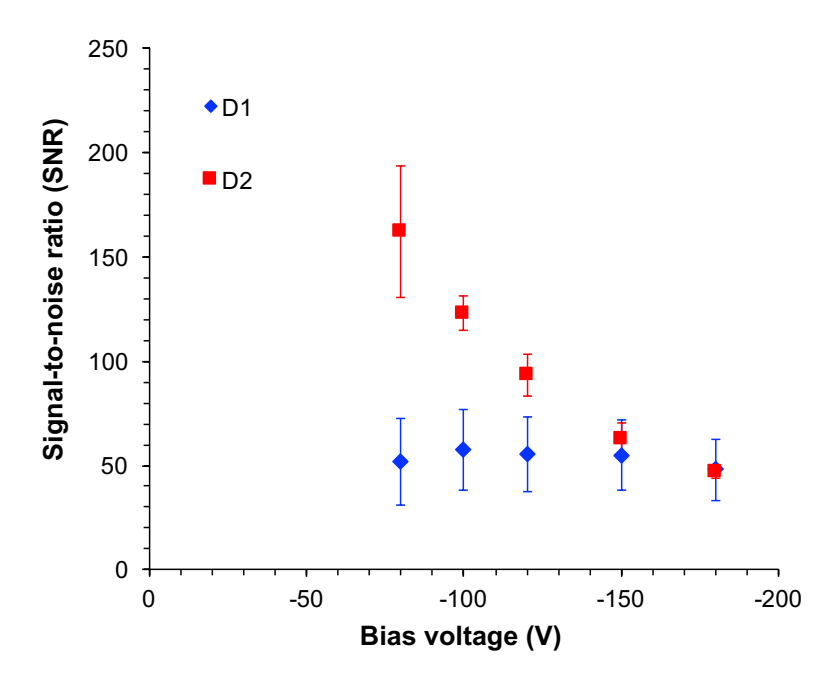


Figure 4.20: Signal-to-noise ratio (SNR) as a function of bias voltage for D1 and D2. High leakage current and high random fluctuation may attributed to a low SNR value especially at high bias voltage.

in the dose sensitivity values. The larger detection area of detector D2 in comparison to D1, resulted in a higher number of photons being absorbed in the active volume and hence detected by the detector [148]. This can be supported by the data presented in Figure 4.22, where different active regions of SiC detector have a different photon detection efficiency (η) , which is defined as percentage of the absorbed photon in the detector active region divided by the total incident photons [50].

4.4.5 Dose Sensitivity: Elevated temperature measurements

The variation in dose sensitivity of detector D2 has been determined as a function of temperature up to 100 °C. In order to determine the influence of leakage current on the response of fabricated detector at high temperatures, the response as a function of leakage current for different applied biases prior to the dose sensitivity measurement was plotted, as shown by the data in Figure 4.23. The response of the detector when exposed to the X–rays was determined using Equation 4.8.

$$Response = \frac{current \ signal - leakage \ current}{leakage \ current}$$
(4.8)

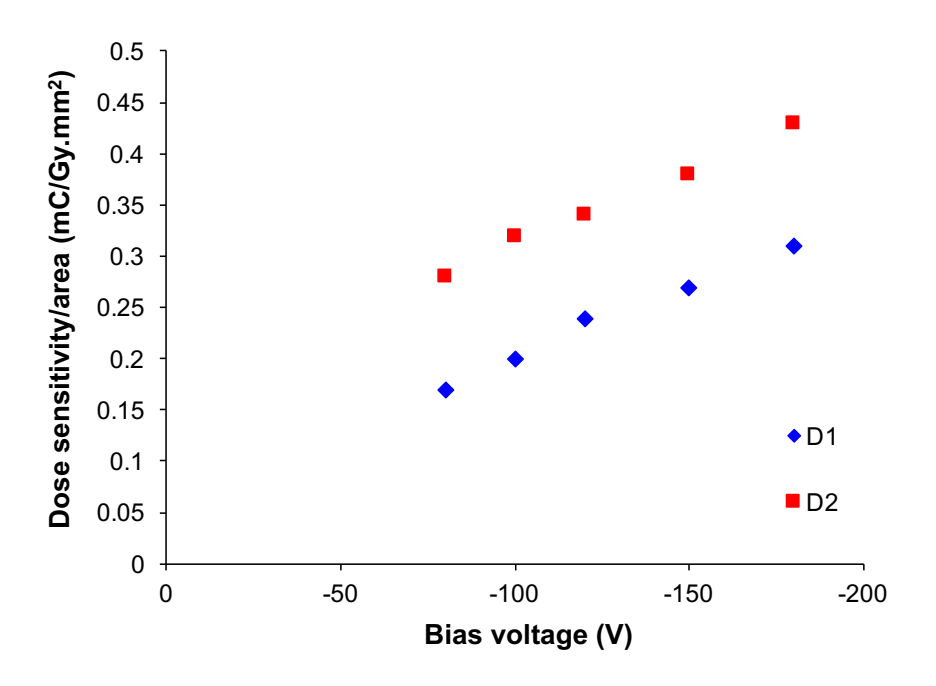


Figure 4.21: Dose sensitivity as a function of bias voltage applied at room temperature for D1 and D2. Increasing the bias voltage has increased the dose sensitivity for both D1 and D2 detectors. The error bar which represent the root mean standard error of the dose sensitivity is smaller than bullet data point.

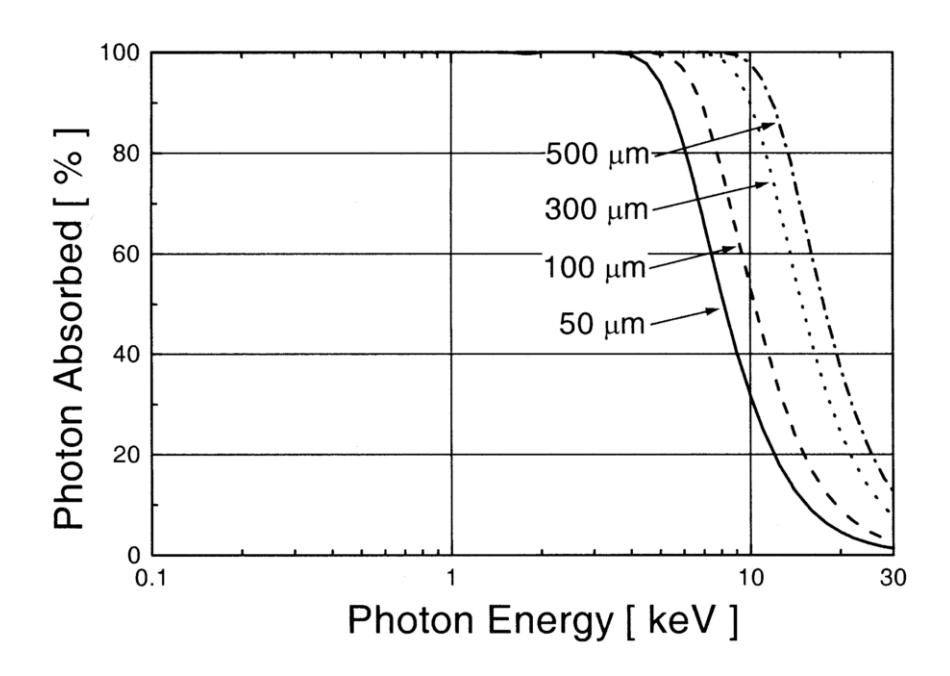


Figure 4.22: Photon detection efficiencies between 100 eV and 30 keV for silicon carbide or silicon detectors with active regions of 50, 100, 300, and 500 μ m. [50]

The data in Figure 4.23 show that in contrast to the current signal density plotted in Figure 4.14, the response of detector D2 decreases exponentially with increasing leakage current density for the range of operating temperatures and applied biases considered here. The dependance of the leakage current density on the detector response is expressed in Equation 4.8, where a detector with a higher leakage current density will result in a lower detector response. Following Equation 4.6 ($J_L \propto W_d$ as described in section 4.4.3), the increased volume of the depletion region (W_d) with increasing reverse bias results in the increased leakage current density (J_L). This observation is supported by the data shown in Figure 4.18, where a high bias voltage contributed to a high leakage current density and a low SNR as described in section 4.4.4. Hence, in contrast to the hypothesis presented in section 4.4.3, the data indicates that carrier generation in the depletion region is the dominant reverse leakage current mechanism during dose sensitivity measurements. This is supported by the high leakage current of detector D2 at room temperature, as presented by the data in Figure 4.18. This contributes to the lower response of the current signal in comparison to that measured at other temperatures. This indicates that the increased leakage current leads to a rapid deterioration in the response of the detector on exposure to X–rays.

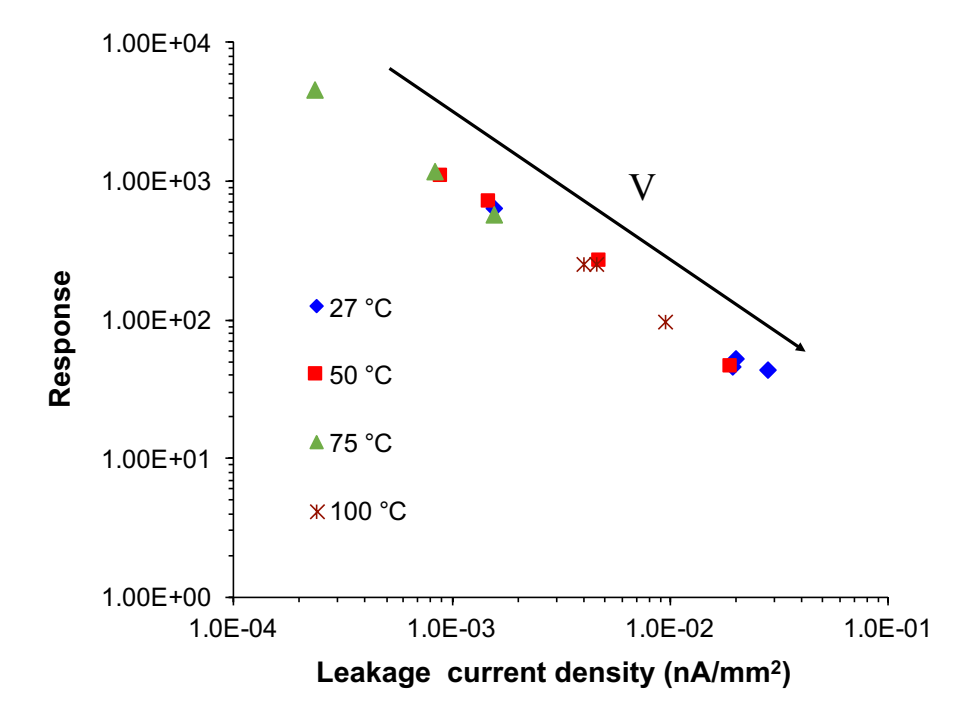


Figure 4.23: Response against leakage current density at room temperature and elevated temperatures up to $100\,^{\circ}$ C and bias voltage from -80 V to -150 V for D2.

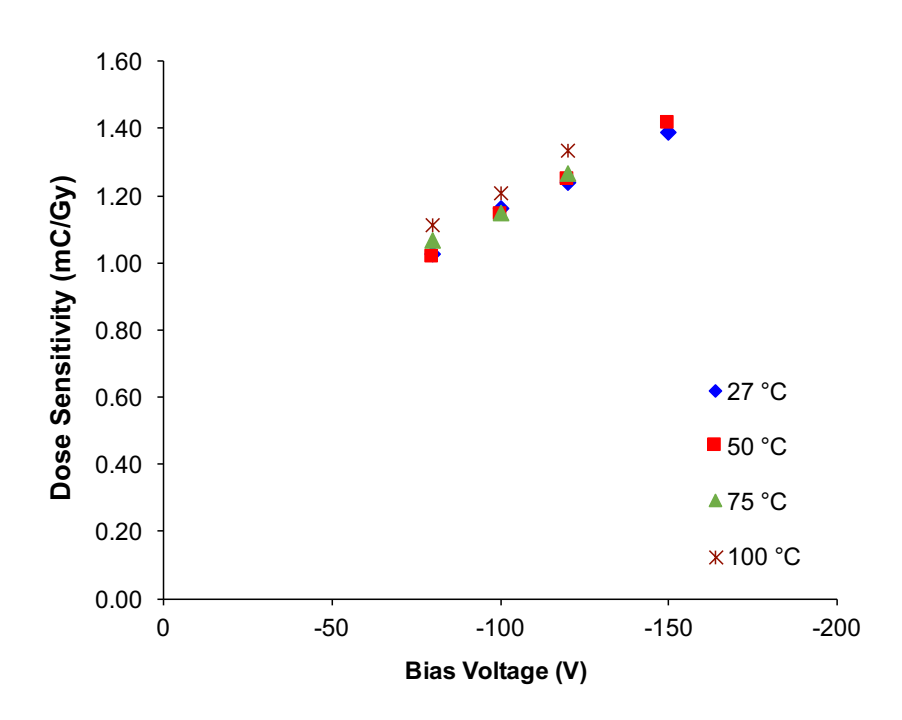


Figure 4.24: Dose sensitivity as a function of bias voltage applied at room temperature and elevated temperatures up to 100 °C for D2. The data demonstrate consistent dose sensitivity for a variation of bias voltage and measurement temperature and the error bar which represent the root mean standard error of the dose sensitivity is smaller than the bullet data point.

Device	Bias Voltage (V)	Source	Sensitivity (nC/Gy)
Epitaxial SiC diode ^[36]	-100	300.8 mGy/min 60 Co γ –source	24.53
Detector D2		0.185 mGy/min X-ray	$(1.2\pm3.3\text{E}-09)\times10^6$

Table 4.2: Table of comparison on the dosimetric sensitivity of detector D2 with previously reported data.

As can be observed from the data plotted in Figure 4.24, linear fits to the collected charge as a function of absorbed dose (calculated from the product of the incident dose rate and exposure time) allow the determination of the dose sensitivity in mC/Gy at investigated applied bias and measurement temperature. The observed trend in the data is similar to that observed in the dose rate linearity data reported in section 4.4.3, where the dose sensitivity is higher for high applied bias for all the temperatures investigated. These values range from $1.0\pm1.0\text{E}-03$ to $1.5\pm6.0\text{E}-03$ mC/Gy and show a significant improvement in sensitivity for the detectors reported here in comparison to reported previously at room temperature [36]. The data summarised in Table 4.2 show the extracted value of $1.2\pm3.3\text{E}-09$ mC/Gy at -100 V, which offer an enhancement of 5.0×10^4 over the data published in the literature [36]. This can be described by the explanation that has been

given in section 4.4.2, which considered the difference in the energies used and radiation interaction mechanisms involved during measurements of X-ray (35 kV) and 60 Co γ -source (1.17 and 1.33 MeV).

4.5 Conclusion

Prior to irradiation, the characteristics of selected 4H–SiC Schottky diodes have been tested in terms of I–V measurements including the specific on resistance, ideality factor and barrier height at temperatures up to 100 °C. Their characteristics at room temperature were compared with the measurements performed at the wafer level, prior to wire–bonding. Results show that all detectors revealed unchanged barrier heights and ideality factors, indicating that the wire bonding performed on them prior to irradiation did not produce any significant deterioration of the characteristics. Measurements up to 100 °C also demonstrate constant values of ideality factor and barrier height over the range of operated temperatures, which are respectively between 1.00 \pm 0.04 to 1.27 \pm 0.06 and from 1.54 \pm 0.08 eV to 1.74 \pm 0.06 eV .

Furthermore, the suitability of 4H–SiC Schottky diodes as radiation detectors for use in low energy, low dose rate applications has been determined for bias voltages up to -180 V and operating temperatures up to 100 °C. Linearity measurements on three detectors selected based on their low ideality factors exhibited a highly linear correlation of the current response as a function of dose rate for all applied bias voltages and temperatures investigated. The data show that the generated current originates within the depletion region of the detector and that the response is linearly dependent on the volume of the space charge region, which controlled by the bias voltage applied. This findings were consistent with the data presented in several studies performed by Bruzzi *et al.*. Despite the ideal electrical characteristics over the range of temperatures, the current signal density for detector D3 was observed to be approximately 50% lower in comparison to detectors D1 and D2.

The collected charge within the detector increased linearly with absorbed dose within the range of 0.2 to 1 mGy. The collected charge measured by one of the detectors is higher than the previously reported data, by a factor of 10^4 . The realisation of a vertical detector structure, coupled with the reduction in defect concentration in epitaxial layers, has resulted in an enhanced linearity and sensitivity of the detector than those published previously for moderate dose rate testing. Furthermore, the linearity and sensitivity are independent of temperature for measurements performed below 75 °C, indicating a highly stable performance particularly for detector D2.

In conclusion, despite the focus on silicon carbide detectors for high dose rate applications, such as those found in the nuclear industry, the data show that it is ideally suited for radiation detection in low dose rates and elevated temperatures, such as those found in medical imaging applications, where reliable operation and high sensitivity are critical.

Chapter 5

Energy Scavenging in X-ray Environment and The Correlation with The Electrical and Spectroscopic Characterisation of 4H-SiC Schottky Diode

Part of the result in the chapter was published in N. S. Mohamed et al., Proceeding of IEEE Sensors Conference, 2017.

5.1 Introduction

Abrupt growth of technological areas has resulted in the increasing demand of power sources that are able to sustain the operation of an electronic circuits to enable a prolonged life time and reduce operational cost. In high temperature environments, especially those which also have a high radiation dose rate, the selection of the power source is extremely challenging. Development of photovoltaic cells has attracted a great deal of research to invent and improve the performance of the power sources, since it affects the contribution to the renewable energy production. The majority of photovoltaic cells have been developed and characterised using silicon and germanium which are the dominant semiconductors for solar cells involving low energy (longer wavelength) photons. Unfortunately, those traditional photovoltaic cells are prone to radiation induced damage when bombarded with increased photon energies, due to their lower radiation tolerance in comparison to wide bandgap semiconductors, such as silicon carbide (SiC) [153]. This restriction limits the use of these conventional semiconductors to operation in benign environments and precludes them from a range of scientific and industrial applications, including volcanic emission monitoring, closed loop control of combustion processes and long term nuclear installation monitoring.

Recently, SiC has been demonstrated as a material for the realisation of microelectromechanical systems, which harvest energy from fields containing radiation particles including alpha, beta or gamma rays [68, 154]. These power sources are often referred to as nuclear batteries and have become a topic of active research in recent years for long term, stable supply of electricity in a range

of applications from deep space exploration to long term battery backup for field–programmable gate array (FPGA) encryption keys. Nevertheless, the harvesting of energy from X–ray fields has not been extensively discussed in the literature. This application has the potential to offer a step change in capability in space applications or nuclear power plants, where the X–ray or gamma ray flux can be converted to usable electrical power. High radiation hardness and insensitivity to radiation damage, make SiC a potential candidate for the realisation of a high–quality X-ray photon energy harvester in a high radiation environment. This opens up the possibility of developing high power X–ray photon based energy harvesters, where the dose encountered by the harvester and subsequent power conversion electronics is beyond the limitations of silicon based systems.

5.1.1 Overview of the SiC as a X-ray photon energy harvester and the correlation with spectroscopic properties using ²⁴¹Am

In the early of 20th century, interest in the development of nuclear batteries was sparked by the work of Moseley and Harling in 1913 [155]. More recent developments in the field have been driven by the emergence of microelectromechanical systems and nanotechnology that require safe, direct, long–life, stable and integrated electrical power. The significant advantages of wide bandgap semiconductors, such as the higher open circuit voltage, higher conversion efficiency and greater radiation resistance explains why these materials were initially considered for solar photovoltaic applications [51]. In addition, due to the higher internal quantum efficiency of wide bandgap semiconductors, they are often used in a wide range of applications, including as power sources to be operated at elevated temperatures and/or in harsh environments. The high radiation tolerance of semiconductors reduces the possibility of radiation damage from the integrated radioisotope or from external radiation sources [156]. However, the drawback of increasing the bandgap is the increase in the semiconductor resistivity, which results in the deterioration of the charge collection in the semiconductor [51]. This need to be optimised in terms of the materials and radioisotopes used in the creation of the nuclear battery.

Numerous experimental data have been reported detailing the characteristics of UV photovoltaic cells and nuclear batteries based on SiC detectors. However, the literature does not contain any description relating to the capability of silicon carbide to act as an X-ray photovoltaic cell. Qiao *et al.* has demonstrated that SiC is effective to transfer radioactive decay energy into electrical power when exposed to the ⁶³Ni (beta emitter – 66.945 keV) and ²⁴¹Am (alpha emitter – 5.4857 MeV) as the radiation sources with respectively 0.5% and 0.1% efficiency [68]. They proposed an improvement in the energy conversion efficiencies by an order of magnitude under illumination from

both ⁶³Ni and ²⁴¹Am by optimising the dopant concentration of the epilayer [68]. In addition, Li *et al.* showed the Schottky barrier diode to be a feasible energy converter for beta–voltaics, in comparison to both *p–n* and *p–i–n* junctions, with a maximum output power density of 4.08 nW/cm² and power conversion efficiency (g) of 1.01% [157]. Náfrádi *et al.* reported the performance of photovoltaic cells fabricated from methylammonium lead iodide (CH₃NH₃PbI₃) for X–ray energy conversion [153]. They observed that these devices demonstrates a high photon absorption coefficient and high radiation stability when exposed to X–ray flux for an extended dose range of the CH₃NH₃PbI₃ bulk crystals [153]. There are no studies presented in the literature to date that detail the correlation of the electrical and detection characteristics of 4H–SiC Schottky diodes and their capability as X–ray energy harvesters.

The capability of SiC to operate in high temperature and radiation dose environments has prompted studies on the semiconductor properties and the suitability of silicon carbide (SiC) for radiation detection. This has attracted a great deal of research to determine the spectroscopic performance of detectors manufactured from SiC. Bertuccio *et al.* proposed the possibility of SiC detectors as spectrometers for on–satellite spectrometers for X–ray Astronomy or portable systems which are very compact and low power in comparison to those based on silicon [29]. Detectors based on semiconductors have significant advantages in the vast majority of electron detection applications, in comparison to detection systems based on scintillators. Semiconductors also demonstrate a notable improvement in energy resolution, due to the relatively low energy required to produce an electronhole pair in a semiconductor in comparison to the energy needed to produce a photoelectron ejection in a scintillation/photomultiplier tube [158]. The value of the electron–hole pair creation energy in a semiconductor determines the signal–to–noise ratio (SNR) of the spectroscopic systems, where the amplitude of the signal at the output from the preamplifier is directly proportional to the number of generated electron–hole pairs [50].

In spite of the drawback related to the high energy for electron–hole pair production (7.8 eV), SiC is presently widely investigated for operation in harsh environments, where highly stable characteristics are required. This is due to wide bandgap of SiC, which results in the reverse leakage currents of the Schottky diodes at room temperature that are approximately 4 orders of magnitude lower than those of equivalent detectors manufactured from Si, GaAs and CdTe [159]. The lower leakage current of the SiC contributes to the lowest reported noise detectors operating at room temperature that are able to compensate the lower signal, which results from the increased electron–hole pair generation energy [159]. Bertuccio *et al.* suggested the possibility of wide operating temperature range of SiC detectors, with a view to achieving high energy resolution at room temperature and adequate resolutions up to 100 °C without the cooling systems which are power consuming, bulky and expensive [29].

5.1.2 Highlights of the chapter

Following the characterisation of 4H–SiC Schottky diodes to low dose rate X–ray irradiation as described in Chapter 4, the performance of selected detectors were determined when operated as photovoltaic cells during exposure to X–rays, similar to those that have recently been developed for micro battery applications. Measurements were performed using a Phywe Xpert4 tabletop X–ray generator operating with a tungsten target at an accelerating voltage of 35 keV and a tube current of 1 mA. The performance capability of 4H–SiC Schottky as an X–ray photon energy harvester were correlated with the characteristics of the diode extracted from the parametric characteristics and the spectroscopic detection capabilities. The detection properties of detectors D2, D4, and D5 were investigated using Americium (²⁴¹Am) and alpha emitter with an energy of 5.4857 MeV, in terms of the channel peak position, full–width at half maximum (FWHM), energy resolution and charge collection efficiency (CCE). Those characteristics were then correlated with the the performance capability of detectors D2, D4 and D5 as X–ray photon energy harvesters during irradiation to an X–ray dose rate of 0.185 mGy/min.

5.2 Spectroscopic properties of 4H–SiC Schottky diode irradiated with ²⁴¹Am

Knoll highlighted the critical information regarding the charge generated from the interaction of particular radiation with matter that can be deduced from the individual pulse amplitude of the pulse mode from radiation detectors [46]. Therefore, other than the electrical characteristics, spectroscopic characterisation which is based on the differential pulse height distribution is a crucial parameter for radiation detectors. The spectroscopic properties of the detector prior to and after irradiation need to be determined to identify if the detector is operating at its ultimate performance. Detectors with superior spectroscopic performance also need to be resistant to damage caused by incident high energy radiation. Hence, a better understanding of the detection performances of the detector before and after irradiation is a prerequisite [58] for high performance detectors.

Alpha spectroscopy has been used to study the detection properties of the fabricated detectors. The detector performance has been determined using alpha particles from Americium (241 Am) source in vacuum (pressure of approximately 1Pa). Decay products from 241 Am can be observed in the data shown in Figure 5.1, where the main peak located at 5.486 MeV (84.8% of the emission) can be clearly determined. The spectroscopy measurements performed on the fabricated detectors allow the deduction of the performance of the detector, including the channel peak position, full–width at half maximum (FWHM), charge collection efficiency (CCE) and energy resolution. From the

characteristics of the main peak, the detection properties and performance characteristics of different detectors can be compared and analysed in order to study the ability of the detectors to be a X-ray photon energy harvester.

To estimate the range of alpha particle produced from the 241 Am source inside the fabricated detector, a simulation of the ionization occurrence was performed. The corresponding Bragg ionisation curve inside the detector was simulated using SRIM2000 simulation software for a structure comprising both Ni₂Si and Ni Schottky contacts which are presented in Figures 5.2 (a) and (b), respectively. The Schottky contacts which are nickel silicide; formed by the deposition of Ti (5 nm) and nickel (80 nm) and nickel were taken into consideration during simulation. The shorter range of the incident radiation will result in lower numbers of electron–hole pairs created along the track, reducing the detection efficiency. The predicted range for the incident alpha particles of 18.9 μ m can be determined from the plots for both the Ni and Ni₂Si Schottky contacts, although the energy loss along the track is slightly different. From the relation of the depletion region with the reverse bias that have been described in section 3.2, a reverse voltage of -120 V is required to ensure that the depletion width exceeds the range of the incident radiation. This predicted depletion width and the required applied voltage was used in all the subsequent measurements to ensure optimum charge collection efficiency.

5.2.1 Experimental set up

The same experimental set up has been used to measure all the channel peak position, full—width at half maximum (FWHM), charge collection efficiency (CCE) and energy resolution as shown in Figure 5.3. In order to calibrate the multi—channel analyser used in the measurements, a commercial Si detector was used along with an uncovered 3.7 kBq ²⁴¹Am source. A commercial preamplifier from Phywe was used to amplify the signal, where an internal bias of -33 V was selected. The MCA is the main component for this measurements where its record the incoming incident energy in a pulse shape and the input pulses are then sorted into channels according to their amplitude. The MCA is connected by USB to a computer with "measure" software installed. A vacuum pump was used to evacuate the experimental vessel and obtain a standard vacuum pressure. When the final pressure is the tube was achieved, a pinch cock on the tube was used to isolate the pump, which was then turned off to avoid additional noise being generated in the measurements. The calibration procedure was performed until the position of the main peak could be easily determined from the background.

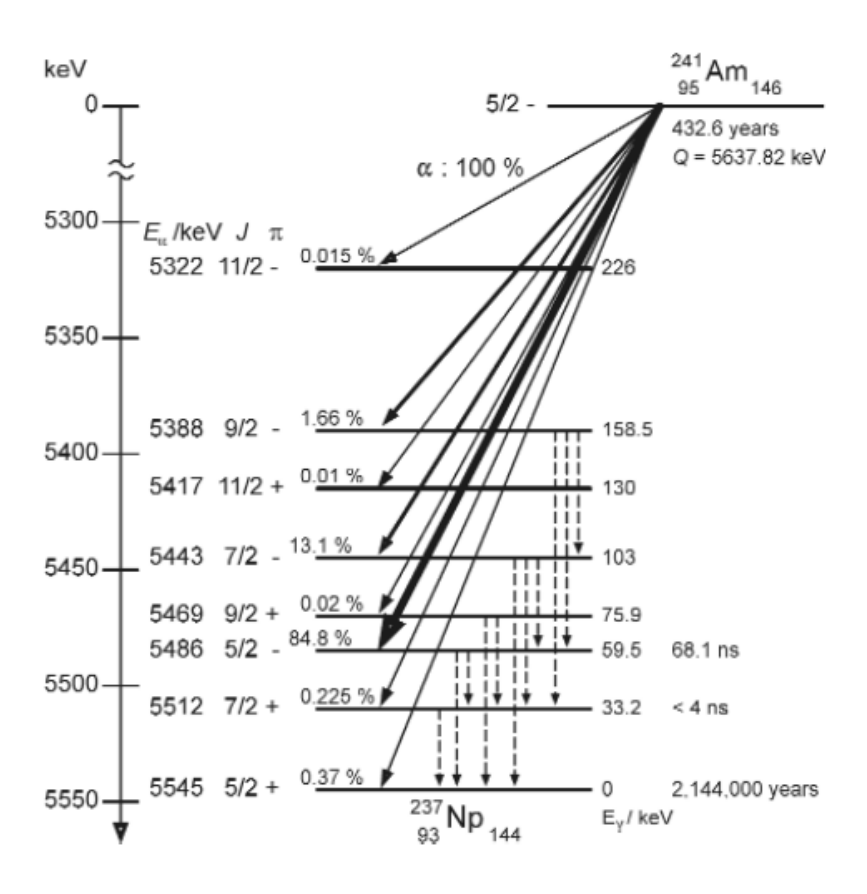


Figure 5.1: Decay scheme of ²⁴¹Am.

The initial measurements on the fabricated silicon carbide detectors were performed using the high activity source; 370 kBq ²⁴¹Am. The silicon diode was removed and replaced with the fabricated detector connected using SMA connector. The source was positioned as close as possible to the detector so that the incident alpha particles did not lose energy during transit. To allow different bias voltage applied during measurement, an external bias voltage was applied to the preamplifier using the voltage source in the Keithley 6517B electrometer. Detectors D2 and D5 were operated at reverse bias up to -150 V, whilst due to the higher leakage current of detector D4, the applied bias voltage was limited to -50 V. An exposure time of 30 minutes was used to ensure that a clear peak was obtained, so that all the parameters of the detection properties can be analysed and extracted.

The spectral response of detector D2 to the ²⁴¹Am at different bias voltages, prior to fitting to the peaks by means of Gaussians is shown in Figure 5.4. These spectral responses are representative of the behaviour of the three silicon carbide detectors studied. Based on the energy decay scheme in Figure 5.1, there are two energies; 5.486 MeV (84.8%) and 5.443 MeV (13.1%) should be clearly resolved in the spectra as depicted in Figure 5.5. However, due to the noise in the system, the lower energy peak at 5.443 MeV cannot be clearly resolved due to the overlap with the shoulder of the main peak. However, the data shown can be observed to be similar with the finding by De Napoli *et*

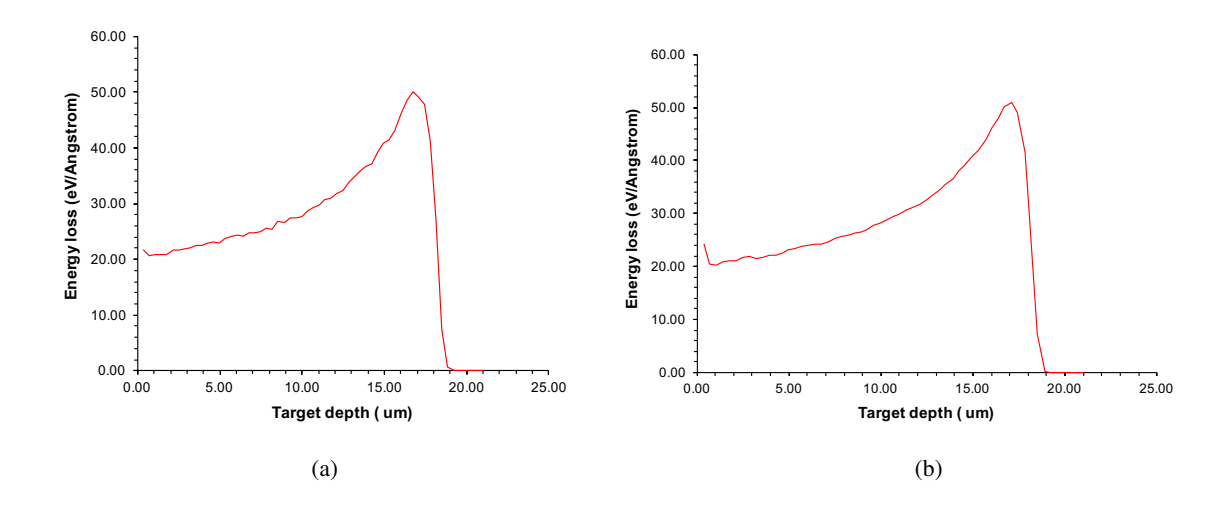


Figure 5.2: Simulated target depth of the alpha particle; 241 Am inside the fabricated detector for (a) Ni₂Si and (b) Ni Schottky contacts. Both contacts demonstrate almost similar energy loss with increasing target depth (μ m).

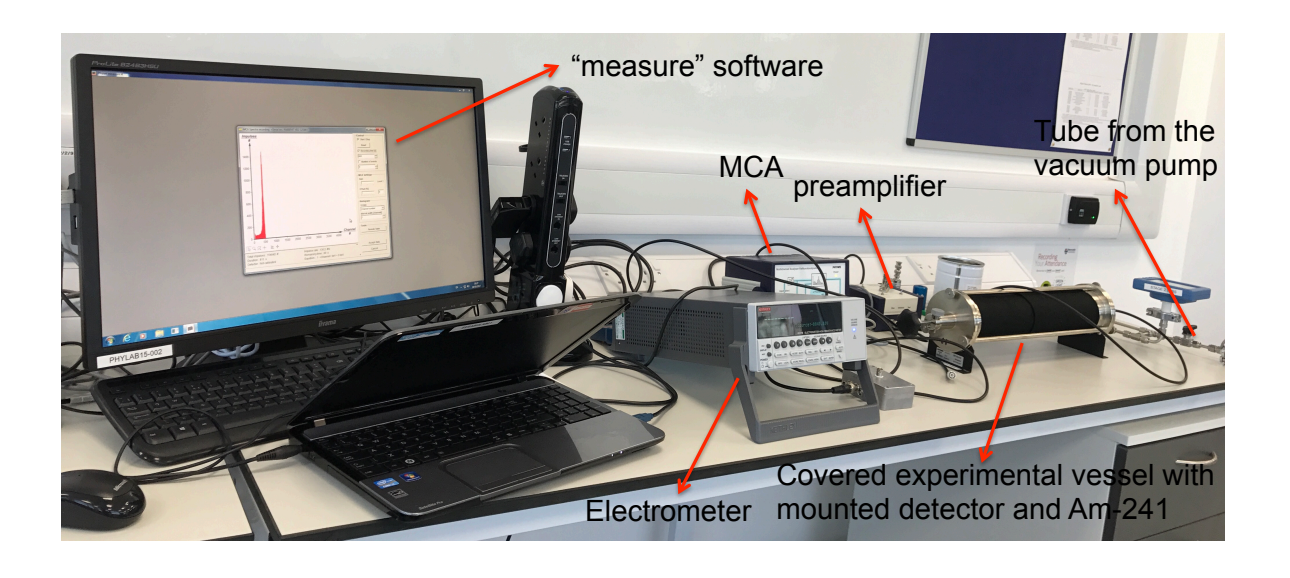


Figure 5.3: Experimental set up of the spectroscopy measurement on the fabricated detector.

al. [160], where increasing the bias voltage resulted in increasing noise and a peak build up at the lower energy can be seen. The pulse shape of peak from exposure to the ²⁴¹Am source demonstrated here is similar to the finding reported in [159], where the system noise prevented the identification of lower energy peaks. The origin of this system noise may be due to the silver paint that has been used to wire bond the diode to the PCB, which may absorb and filter the energy of the alpha source. The extracted and analysed properties of the detectors in terms of channel peak position, full–width at half maximum (FWHM), charge collection efficiency (CCE) and energy resolution of the main peak at 5.486 MeV have been fitted using Gaussian fitting using MagicPlot software.

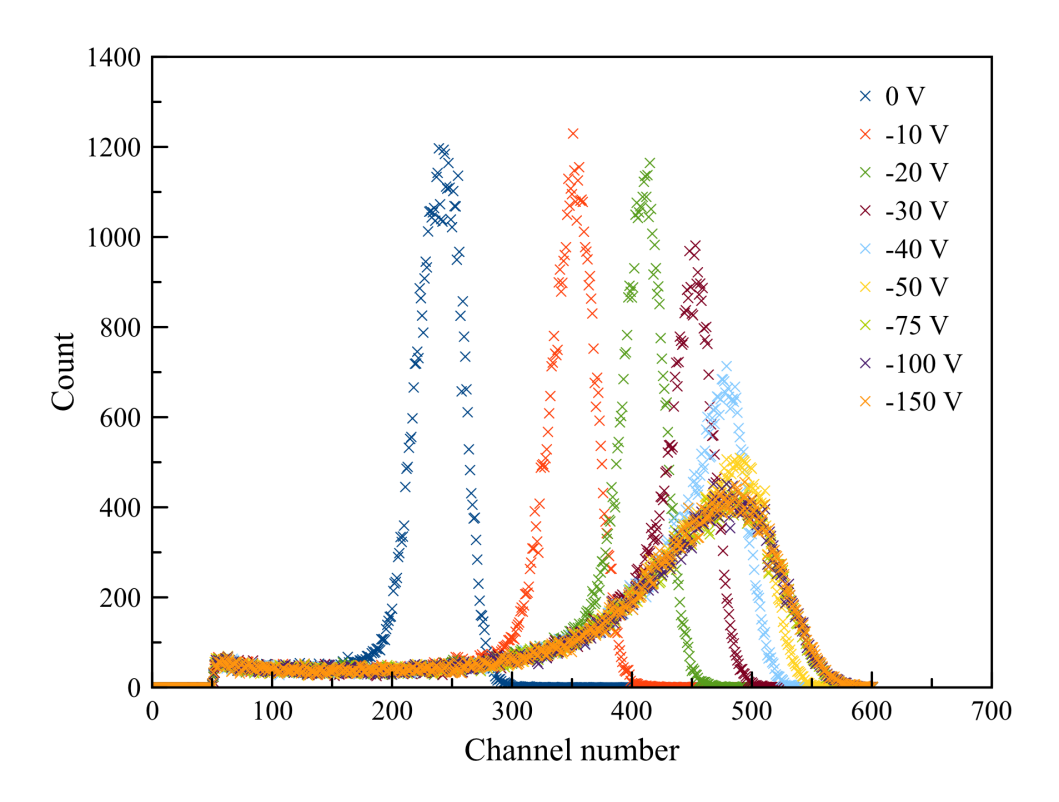


Figure 5.4: Spectra responses of detector D2 by exposure to 241 Am at different bias voltages before gaussian fitting.

5.2.2 Channel peak position

The channel peak position for fabricated detectors were analysed based on the spectra plotted in Figure 5.6. Increasing the bias voltage, shifted the peak position to a higher channel number and decreases the amplitude of the pulse height peak. This can be explained from the increasing width of the depletion region, with increasing bias voltage allowing the higher energy of the incoming radiation to be detected and recorded into higher channel. The high channel numbers corresponding to the high energies of the incoming radiation and the amplitude of the signal at preamplifier output is proportional to the number of generated electron—hole pairs [50]. However, the observed decrease in the pulse height peak amplitude may be related to the lower number of electron—hole pairs generated at the greater depth which corresponds to the higher channel or these carrier recombining at trapping states within the depletion region. Referring to the data in Figure 5.7, the saturated pulse height values occur at low applied bias voltages and can be observed to saturate at -50 V. This appears to contradict the estimated range that has been determined using SRIM software, which indicates that a bias voltage of -120 V is required to create a depletion region that will fully capture the energy of the incident alpha particles.

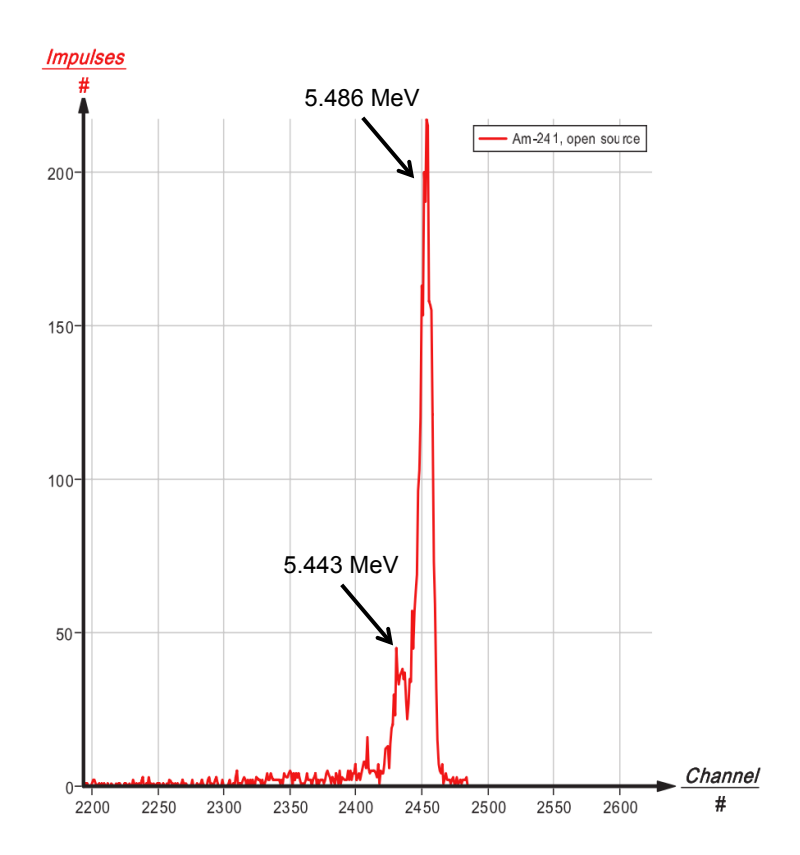


Figure 5.5: Typical spectra response from exposure to 241 Am which depicted two peaks from two energies of 5.486 MeV (84.8%) and 5.443 MeV (13.1%).

To observe the influence of the leakage current on the detector performance, a plot of peak position as a function of leakage current density is presented in Figure 5.8. From Equation 4.6, it can be observed that the leakage current density can be directly correlated with the width of the depletion region ($J_L \propto W_d$), resulting in the expected increase in the depletion region thickness with bias voltage. The data show that the leakage current is relatively constant for applied biases between 0 V and -50 V, with typical values below 0.37 nA/cm² and 2.55 nA/cm² for detectors D5 and D2 respectively. However, when the bias is increased beyond -50 V the leakage current density can be observed to increase significantly for detector D2, with a current of 14.6 nA/cm² observed at -150 V. Whilst, detector D5 shows only a minor increment. The increase in the leakage current density results in a significant effect on the detector performance, specifically in terms of the full—width at half maximum, energy resolution and charge detection efficiency, which will be discussed in detail in the subsequent subsection.

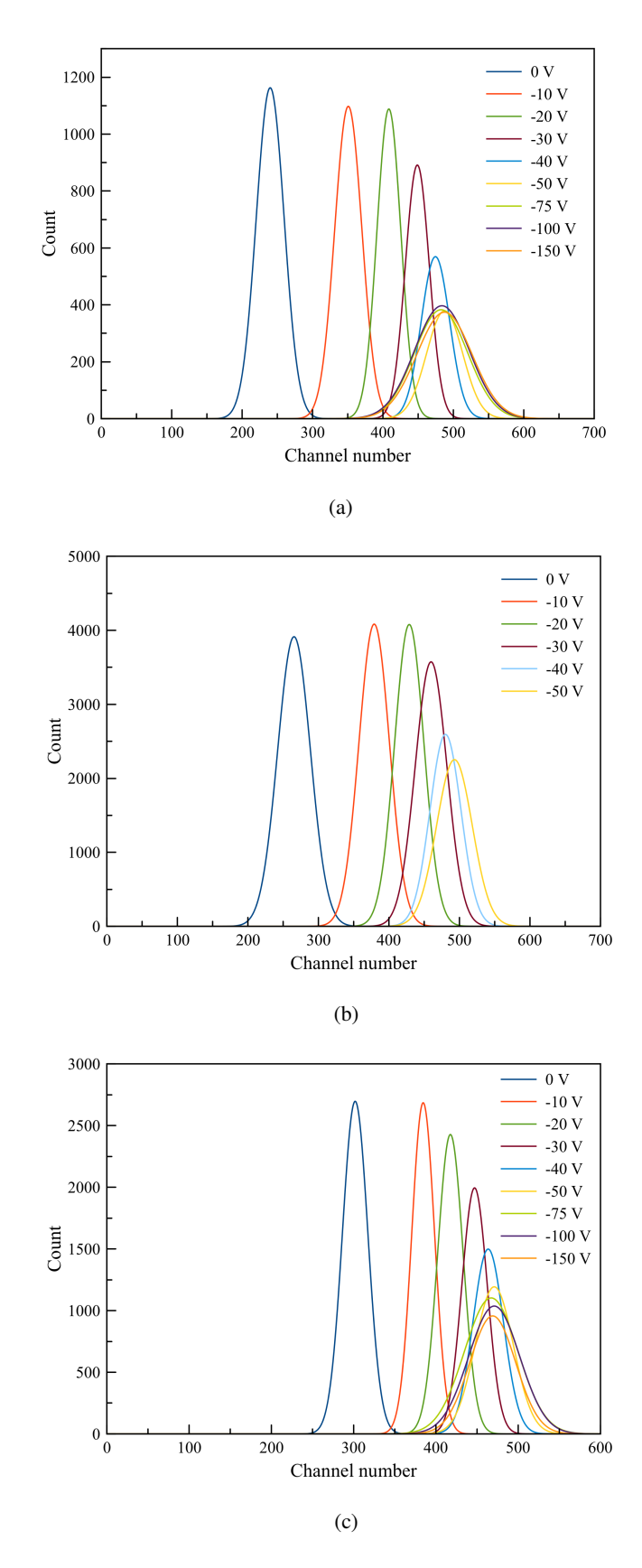


Figure 5.6: Pulse height spectra for (a) D2, (b) D4 and (c) D5 with increasing bias voltages after Gaussian fitting.

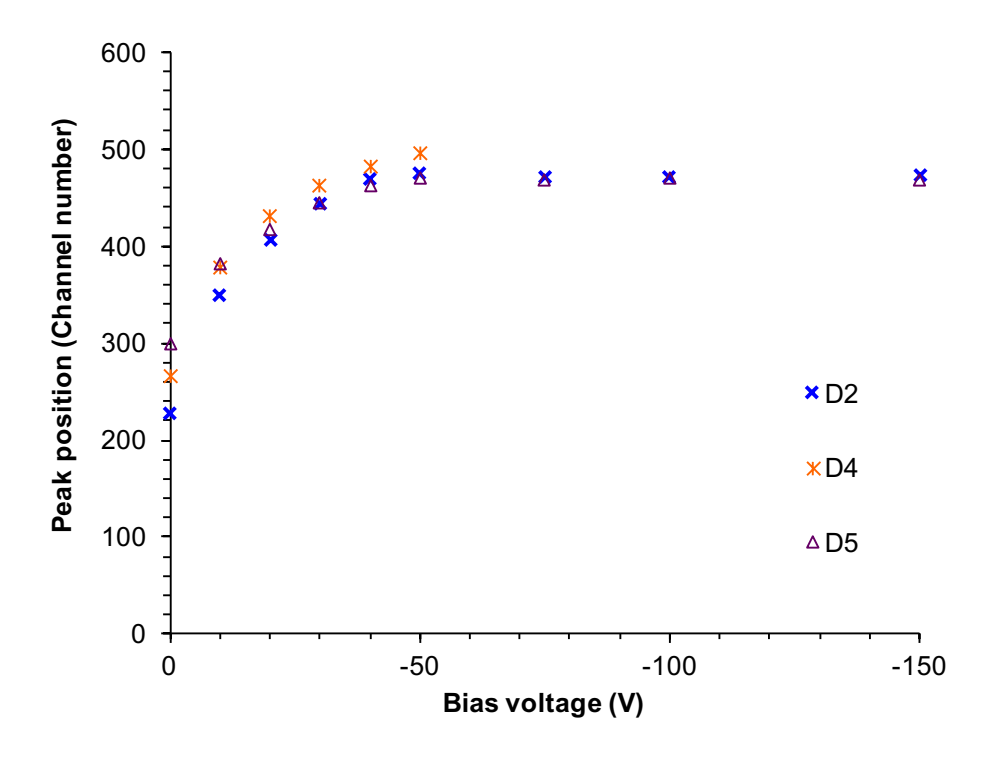


Figure 5.7: Channel peak position for detectors D2, D4 and D5 as a function of bias voltage applied.

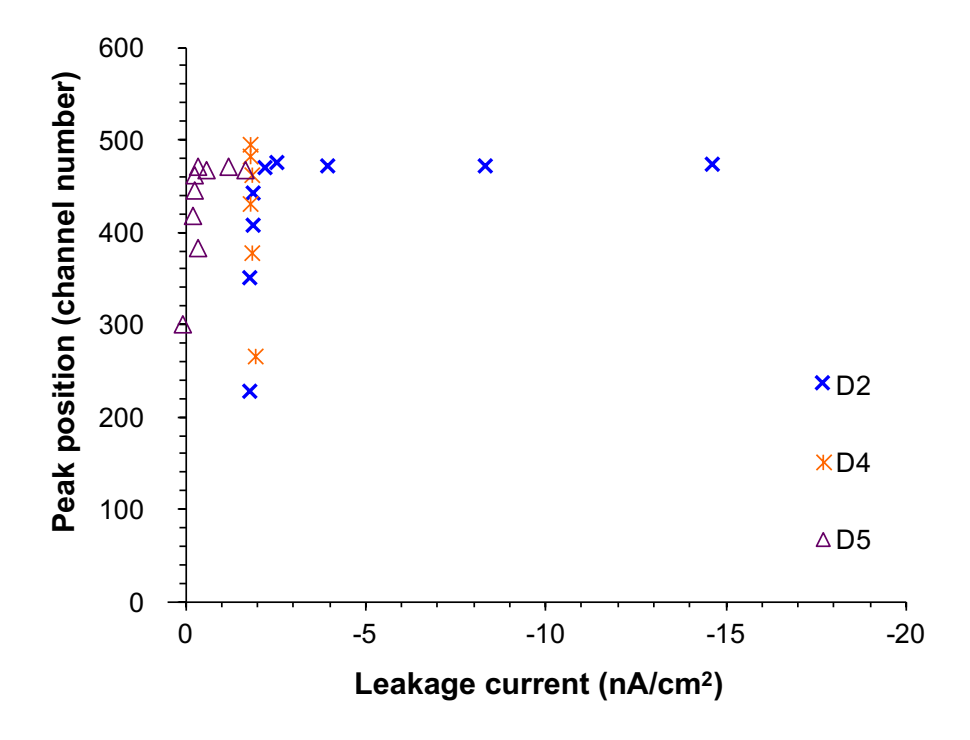


Figure 5.8: Channel peak position for detectors D2, D4 and D5 as a function of leakage current density at different applied bias voltages.

5.2.3 Full width at half maximum (FWHM) and energy resolution

The ability of a given measurement to resolve fine detail in the incident energy of radiation related to detector resolution is often described in terms of the full-width at half maximum (FWHM), which represent the width of the response function [46]. The FWHM can be defined as width of the distribution at a level that is half the maximum ordinate of the peak as shown in the Figure 5.9 [46]. Otherwise, the percentage energy resolution (R), which can be expressed as the FWHM divided by the peak centroid H_0 , $R = \frac{FWHM}{H_0}$ [46] can also be used to describe the energy resolution of the measurements. The resolution of the detector response function can be observed schematically from the illustration in Figure 5.10. Semiconductors diode detectors used in alpha spectroscopy should have an energy resolution below 1%, whereas scintillations detectors used in gamma spectroscopy normally has an energy resolution between 5 to 10% [46]. The better ability to distinguish between two different incident energies, which are close, requires a detector system with a higher energy resolution. A high energy resolution of a detector can be described by the smaller figure of the percentage resolution. The FWHM and energy resolution of detectors D2, D4 and D5 were extracted from the response function of the pulse peaks at different bias voltages, as shown by the data in Figure 5.6.

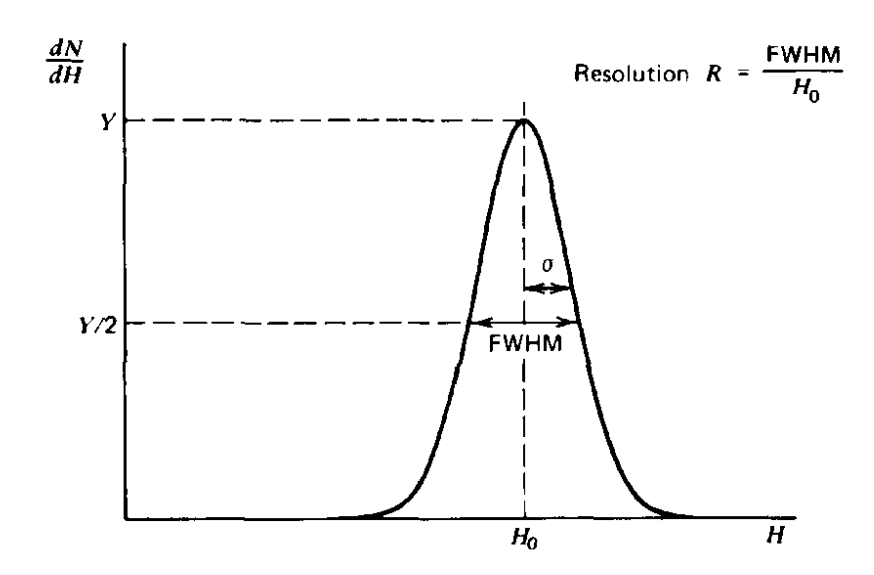


Figure 5.9: Definition of the full-width at half maximum (FWHM) and energy resolution. [46]

The FWHM in unit of channel peak position as well as energy (MeV) were plotted as a function of bias voltages for detectors D2, D4 and D5 in Figure 5.11. The FWHM in channel number were converted to the energy unit (eV) based on correlation with the data from the Si calibration. Detectors D2 and D5 both demonstrate FWHM values lower than 0.2 MeV (equivalent to 52 channel number) for bias voltages below -50 V. FWHM values at -10 V, -20 V and -30 V are consistent with

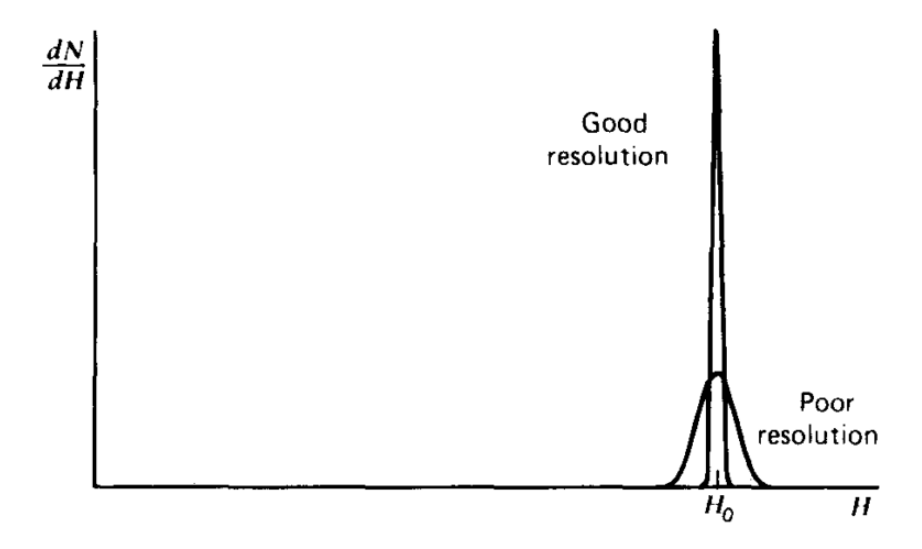


Figure 5.10: Illustration of the response functions for detectors with good and poor resolution. [46]

the data published previously [97] and FWHM values below -50 V are lower (signify better energy resolution) than that the data presented in [58] (FWHM are within 0.42 to 0.35 MeV), both for Ni₂Si 4H-SiC Schottky diode. However, for applied bias levels higher than this, the pulse peaks showed signs of saturation, which resulted in an increase in the observed values of FWHM. The spread of the response function width depicts a significant level of fluctuation in terms of the pulses recorded by the MCA, even though the energies of the incident photons were identical for each event [46]. From the FWHM data as a function of bias voltage, it can be observed that there are two different trends which correspond to the behaviour of the FWHM before and after the response peak has saturated. Similar trend of FWHM with increasing bias voltage can be observed in [107] for Au-SiC Schottky diode. The initial trend where the FWHM improves with the increasing bias voltage can be explained from the reduction in detector capacitance, which results in the lowering of the series noise [161]. On the other hand, the increasing spread of the pulse recorded after the peak saturation can be described in terms of the increase in leakage current with higher bias voltages as described in section 5.2.2. According to Mannan et al. [161] and Lioliou et al. [158], increasing the reverse bias during measurements results in increased leakage currents through the Schottky diode, which results in increased FWHM, which degrades the energy resolution of the detector.

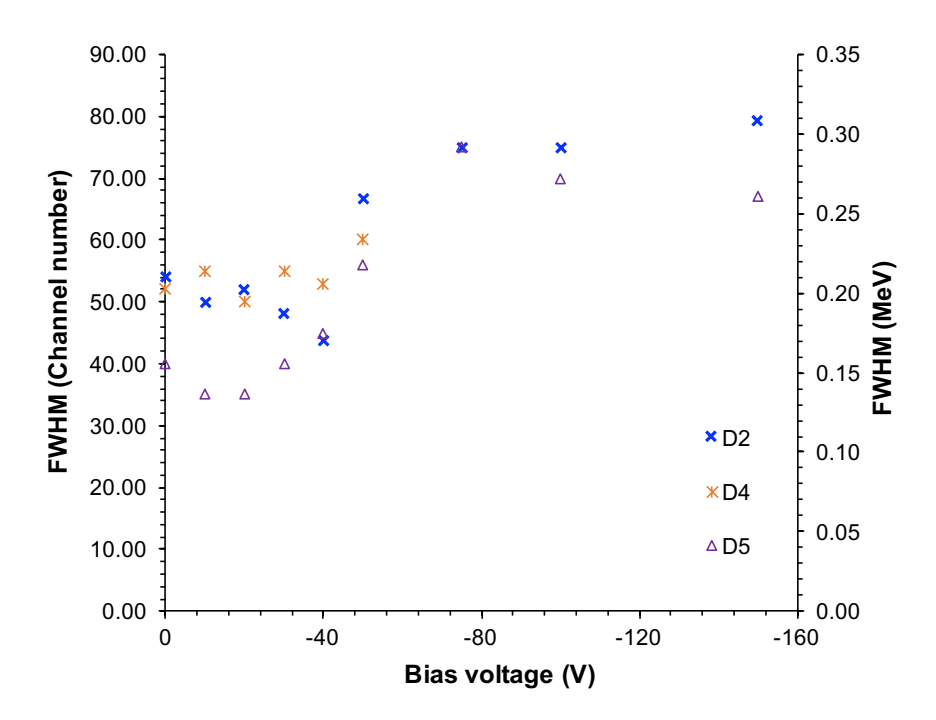


Figure 5.11: Full-width at half maximum (FWHM) for detectors D2, D4 and D5 as a function of bias voltage applied.

The energy resolution for three detectors with increasing bias voltages are shown in Figure 5.12. Before the peak response becomes saturated, it can be seen that the energy resolution decreases exponentially with increasing bias. However, as expected from the FWHM behaviour, the energy resolution increases after the spectral response started to saturate at -50 V, which is similar to the data presented in [161]. Detector D5 which has the lowest leakage current density in comparison to the other two detectors, gives the highest energy resolution, which is within the range of 0.084 % and 0.133 % for bias voltages between 0 and -40 V. In contrast, both D2 and D4 demonstrate slightly lower energy resolution which is between 0.093 % and 0.238 %. Mandal et al. relates the dependence of the energy resolution on the noise present in the detection system [162]. The high leakage current of the detector, that is typically observed at increased reverse bias is proportional to the overall electronic noise and in turn contributes to the lower energy resolution [162, 163]. This relationship between the energy resolution and the number of charge carriers generated during the radiation exposure was suggested by Knoll, where he proposed that the energy resolution is greatly improved with high number of generated charge carriers [46]. From the response of the pulses shown by the data in Figure 5.6, it can observed that the amplitude of the peak in the spectra at higher bias voltages is lower than those observed at low bias voltage. The reduction in the amplitude of the pulse response relates to the lower number of charge carriers generated by the radiation, resulting in a degraded energy resolution.

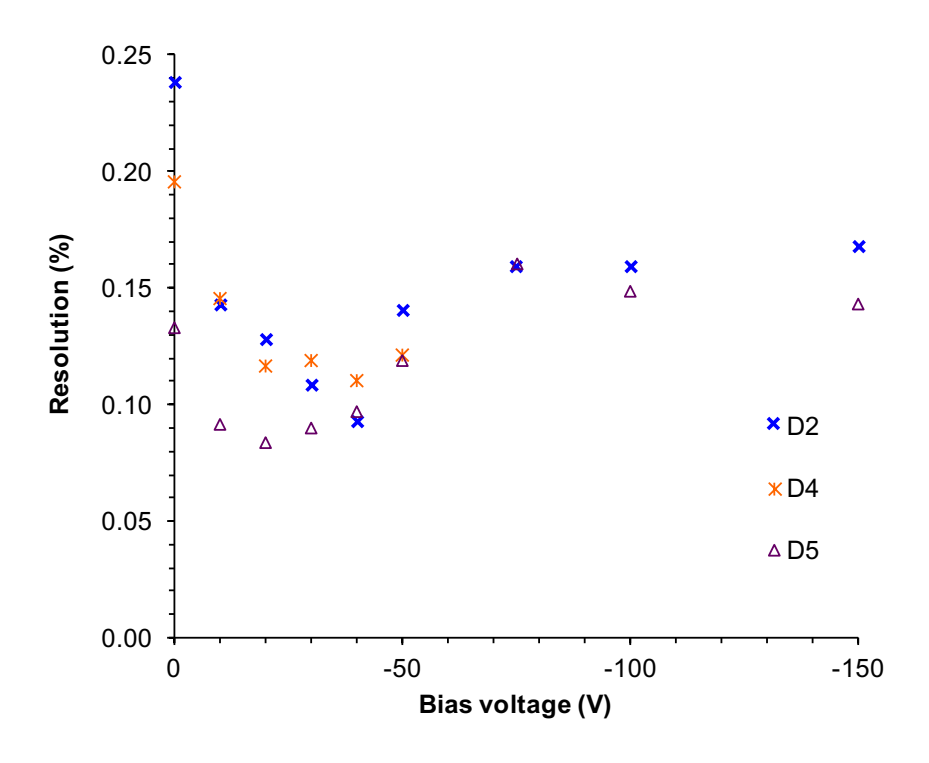


Figure 5.12: Energy resolution for detectors D2, D4 and D5 as a function of bias voltage applied.

5.2.4 Charge collection efficiency

Charge collection efficiency of the detectors can be determined from the ratio of the measured channel peak position to the saturated channel peak position. The data in Figure 5.13 show the variation of charge collection efficiency as a function of reverse bias for ²¹⁴Am measured using detectors D2, D4 and D5. As expected, the CCE increases with increasing bias voltage before becoming constant at the bias voltage where the response peak showed evidence of saturation. Prior to saturation, the increasing bias voltage resulted in higher CCE, due to the increasing depletion region width, as more energy is deposited within this region and the generated charge is collected efficiently [164]. Therefore, the wider depletion region results in a greater number of electron–hole pairs that are generated and subsequently collected at the detector terminals. From the data in Figure 5.13, it can be observed that detector D5 demonstrates a higher CCE, between 0.68 and 1.00 for bias voltages between 0 V and -50 V. However, after -50V CCE the characteristics of all the detectors is seen to saturate, which is due to the constant peak position at this range of bias voltage.

Any defect present within the depletion region will act to decrease the CCE, due to the enhanced recombination of the electron-hole pairs, which can also be considered as incomplete charge collection. To achieve maximum charge collection, it is important to maximize the separation of the electron-hole pairs once they are generated and minimize the recombination. Recombination of

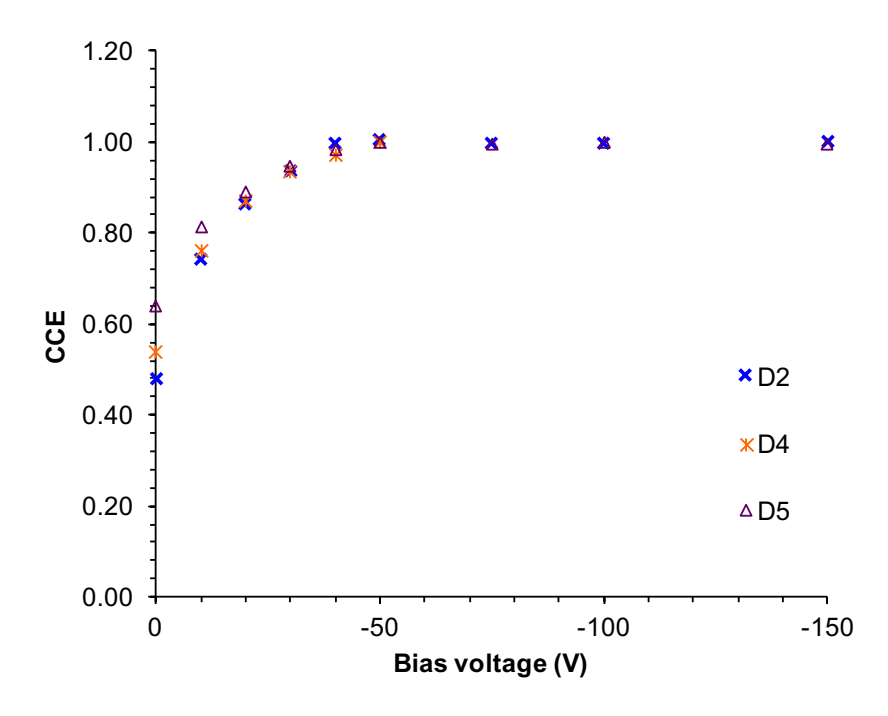


Figure 5.13: Charge collection efficiency (CCE) for detectors D2, D4 and D5 with increasing bias voltage applied.

the electron–hole pairs leads to incomplete charge collection, resulting in a reduction in the efficiency of the detector. Lu *et al.* suggested that the dependance of the charge collection efficiency on the drift length of the charge carrier, which is determined by the carrier mobility, electric field intensity, and carrier lifetime [69]. In addition, the separation mechanism of electron–hole pairs requires analysis in order to achieve maximum collection efficiency. The improvement in quality of semiconductor films by minimizing the dislocation density will also result in an increase the charge collection efficiency [51]. Alam *et al.* proposed that high quality crystalline semiconductor materials, coupled with high quality surface passivation are important in order to reduce recombination losses [51].

Increasing the reverse bias to increase the depletion width, results in the inclusion of a higher number of defects within the active volume of the detector, leading to poor performance [161]. The presence of defects in the semiconductor results in a significant degradation of the detector performance and can be observed by an enhancement in the leakage current as well as affecting extracted values for the dopant concentration, active volume, and charge collection efficiency [161]. This hypothesis was supported by the work of Cunningham *et al.*, who identified a correlation between the poor reverse characteristics and reduced CCE in detectors [165]. Therefore, detectors that show a high leakage current which is linked to a uncertainty in the energy resolution (which is often reported as a high FWHM) also show a poor CCE and this is likely to be as a consequence of defects and hence carrier trapping within the depletion region.

5.3 Low frequency noise (LFN) measurements

The characteristics of defects formed during crystal growth or subsequently created by irradiation have been studied using a range of different experimental techniques [166]. Low Frequency Noise (LFN) spectroscopy is widely recognized as a powerful tool to study the behaviour of impurities and defects in semiconducting materials and device structures. Whilst the technique has been used previously to study the properties of SiC Schottky diodes, Kozlovski et al. claim that it is not been used to study the generation of defects generated by exposure to ionising radiation [166]. In the presence of electrically active defect centers, the leakage current depends critically on the nature of the defects and these can be characterized depending on the concentration of the defects present in the detector [162]. Nava et al. suggested a correlation between the concentration of trapping states in the detector and the observed degradation of the extracted CCE, where the degradation in the most heavily irradiated samples was related to the creation of a high concentration of deep levels [58]. Hence, to investigate the possible correlation of the defect concentration with the detection properties and the performance for X-ray energy harvesting, LFN measurements were performed on the fabricated detectors. Measurements were performed using Model SR760 FFT spectrum analyser and Stanford research system SR570 low-noise current preamplifier, which was controlled using LabVIEW, as illustrated schematically in Figure 5.14.

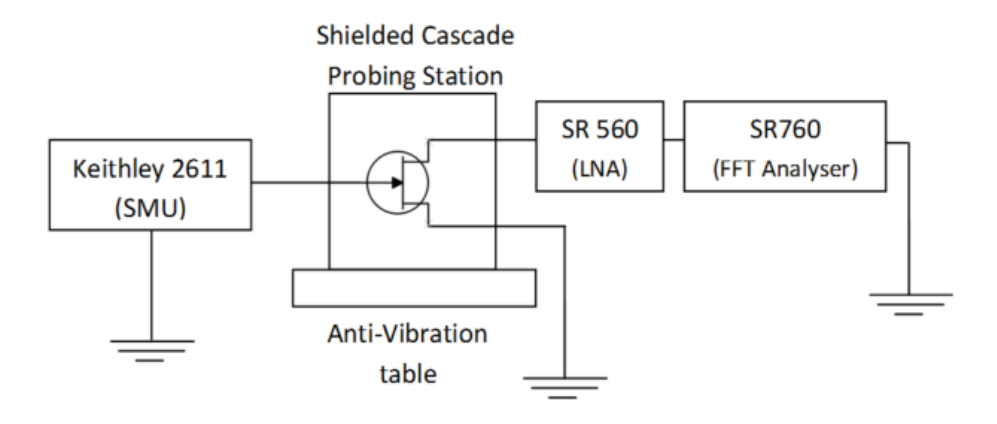


Figure 5.14: Schematic block diagram of the low frequency noise measurement system. [167]

The low frequency noise was measured in the frequency range from 1 Hz to 100 kHz at room temperature. The acquired noise data is post–processed to correct for the current gain settings in the preamplifier and to produce values in dB and A/Hz [167]. The acquired voltage noise power spectral density from the FFT analyser can be expressed as [167]

$$S_{VFFT-OUT} = S_{IDUT} * (V/A)^2, (V^2/Hz \text{ or } A^2/Hz)$$
 (5.1)

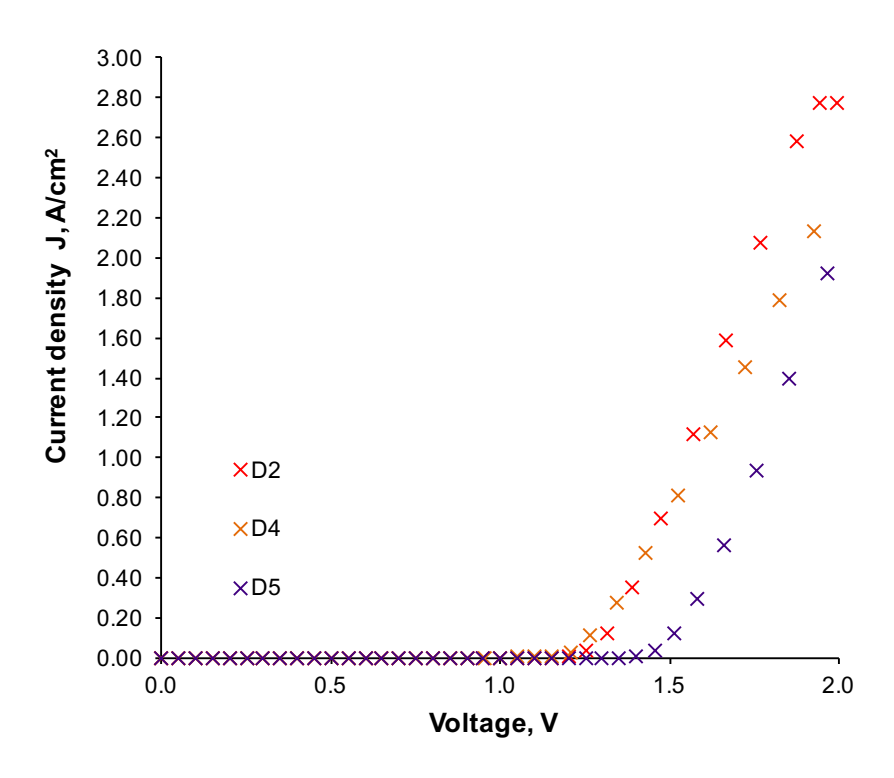


Figure 5.15: Current–voltage characteristics for detectors D2, D4 and D5 before measurement of low noise frequency.

where S_{IDUT} is the current noise power spectral density of the diode and A/V is the sensitivity of the LNA. The conversion of the dB and V²/Hz and A²/Hz can be calculated using [167]

$$S_{V/I-dB/Hz} = 10 \log(S_{V/I} - V^2/Hz \text{ or } A^2/Hz)$$
 (5.2)

$$S_{V/I-V^2/Hz \text{ or } A^2/Hz} = 10^{(S_{V/I-dB/Hz})/10}$$
 (5.3)

where $S_{V/I-dB/Hz}$ and $S_{V/I-V^2/Hz \text{ or } A^2/Hz}$ are the noise spectral density in decibel and voltage/current unit correspondingly.

5.3.1 Dependance of noise spectral density with frequency

The frequency dependance of the noise density for all detectors was extracted from the exponential part of the current–voltage characteristic in Figure 5.15 and are plotted in Figure 5.16 at currents typically between 2×10^{-09} to 2.5×10^{-04} A. From the I–V plot, detector D5 was observed to conduct at a higher forward bias than either D2 or D4 and this condition was taken into account in the determination of the bias voltage applied to the diodes during the noise measurements. This part

represents the thermionic emission regime, which is the most significant contribution to the current across the barrier of the Schottky diode detector. Figure 5.16 demonstrates that the contribution of the noise spectral density increases with increasing current for all fabricated detectors which leads to the appearance of the generation–recombination noise (100 Hz <f <1000 Hz) and it is more prominent in detectors D2 and D4. This condition may be attributed to the high barrier height of D5 ($\Phi_b = 1.673 \text{ eV}$) in comparison to other detectors D2 and D4, with barrier height of 1.660 eV and 1.540 eV, respectively. This hypothesis can be supported by Hsu's model, who proposed that the generation of low frequency noise in the diode is due to multistep tunnelling current flowing through the diode as a result of fluctuations in the occupancy of the trap states [76]. Therefore, the observed high barrier height of detector D5 causes a lower tunneling current that flows through the barrier.

5.3.2 Dependance of noise spectral density with current

To further compare the characteristics of noise density for all fabricated detectors, the dependance of noise density with current, S_I were analysed and extracted at f = 10 Hz, as shown by the data in Figure 5.17. In this frequency range, the main contribution to noise is dominated by the potential barrier formed by the Schottky contact, rather than the behaviour of the depletion region [166]. The data demonstrate that the current dependance of the noise spectral density at f = 10 Hz can be described using the mobility and diffusivity fluctuation model [168]. Therefore, the current dependance can be correlated with the noise spectral density as $S_I \sim I^{\beta}$, where $\beta = 3.16$ for D5, which is double the value for either D2 or D4; being $\beta = 1.62$ and 1.74, respectively. The frequency dependance of the LFN for detectors D2 and D4 are in agreement with the data presented in the literature [81], with a value of $\beta = 1.7$ and the majority of the semiconductor studies published previously, including those on Si, GaN, and 6H–SiC Schottky diodes which are in the range of $1 < \beta$ < 2 [81]. For the current range between 1×10^{-06} to 1×10^{-05} A, detector D5 demonstrates a noise spectral density that is approximately 40% lower than either detector D2 or D4, with a value in the range of 1×10^{-18} to 1×10^{-13} A²/Hz. The lower noise spectral density can be correlated with the higher spectroscopic performance of the detector in terms of both the FWHM and energy resolution. In addition, the lower leakage current density of D5 as shown by the data in Figure 5.8 is a significant factor that can minimize the loss of the created electron-hole pairs, through the existence of traps and defects. However, the noise spectral density for detector D5 approaches the same value as D2 and D4 at higher current value.

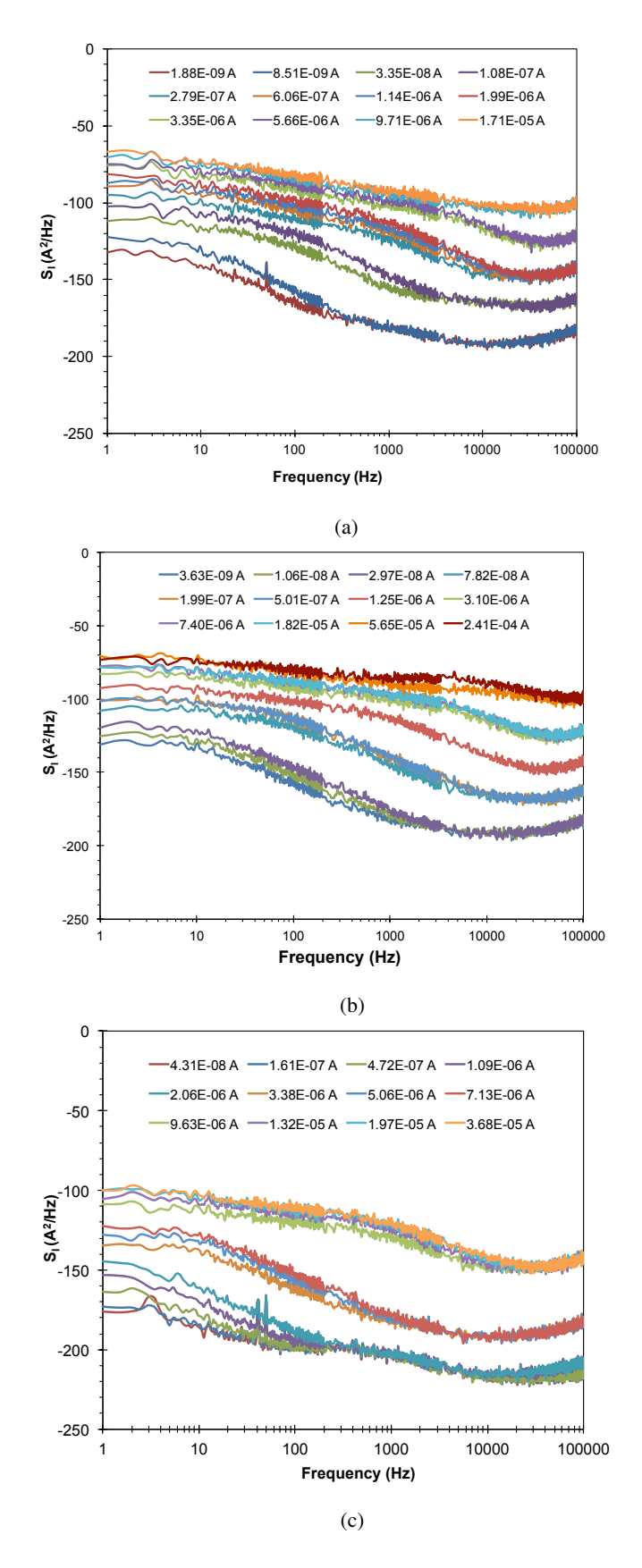


Figure 5.16: Frequency dependance of noise power spectral density, S_I at different currents for (a) D2 and (b) D4 (c) D5 detectors at room temperature.

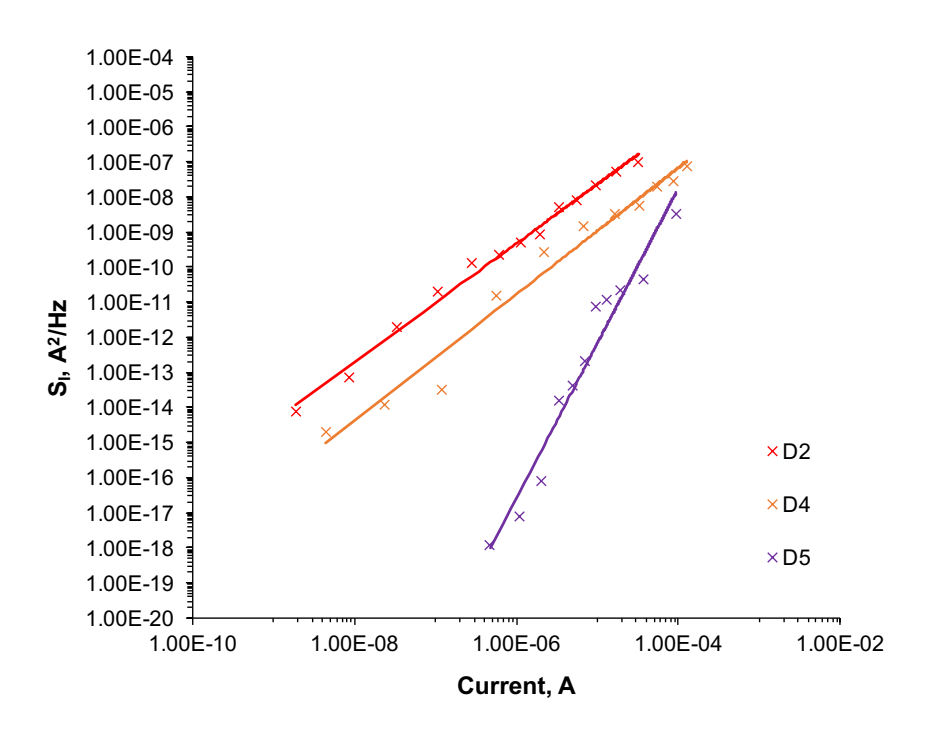


Figure 5.17: Noise power spectral density, S_I for detectors D2, D4 and D5 with increasing current at f = 10 Hz.

5.3.3 Normalised noise spectral density

In order to determine the dependance of the noise spectral density on the current, NPSD was normalised to I^2 , to give normalised noise spectral density (NNPSD), as shown by the data in Figure 5.18. Detectors D2 and D4 demonstrate almost constant values of the normalised noise spectral density with increasing current up to 1×10^{-05} A and then showed a minor decrease as the current is increased further. Meanwhile, the data for detector D5 demonstrated an abrupt decrease in the normalised noise spectral density for the currents between 1×10^{-08} to 1×10^{-06} A. However, the data shows a distinct minimum at a current of 1×10^{-06} A, the cause of which is still unknown at present.

5.4 Performance characteristics of 4H–SiC Schottky diode as X–ray photon energy harvester

The ability of the fabricated detectors to operate as X-ray photon energy harvesters has been evaluated in terms of the short circuit current density (J_{SC}) , open circuit voltage (V_{OC}) , peak power density (P_{OUT}) and fill factor (FF). Section 2.7.1 outlined the important to maximize the separation of the generated electron-hole pair in order to minimise the recombination of the electron-hole pair that will lead to a reduction of the maximum power generated by the energy harvester [51]. The

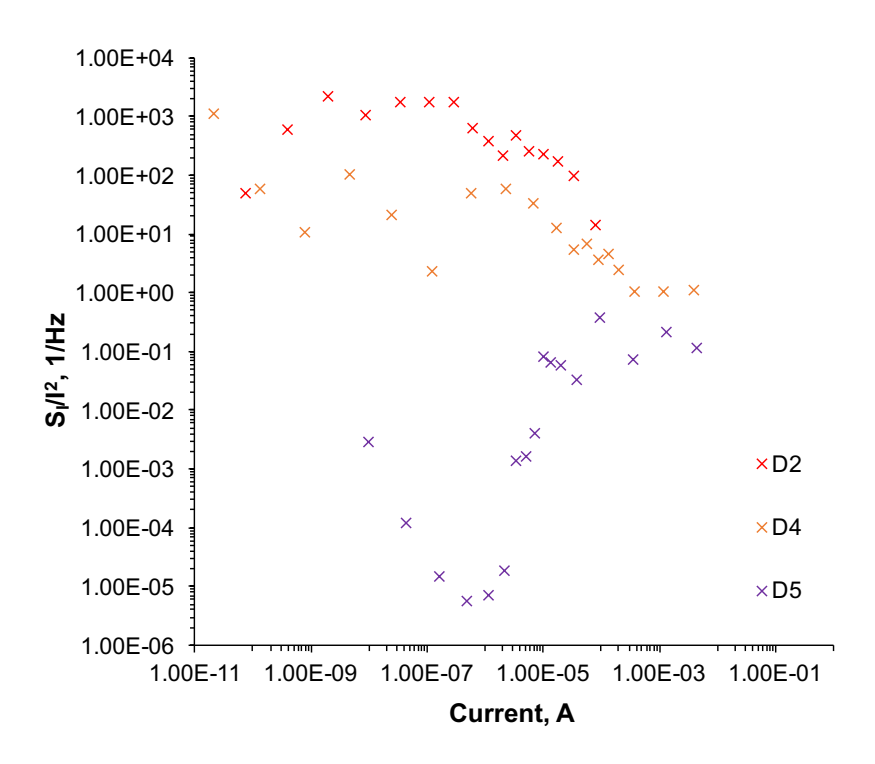


Figure 5.18: Normalised noise power spectral density, S_I/I^2 for detectors D2, D4 and D5 with increasing current at f = 10 Hz.

majority of the incident radiation needs to be absorbed within the depletion region in order to increase the collection efficiency of the electron–hole pairs created in the depletion region. However, the energy of the generated carriers may also lost due to collisions with other electrons or due to lattice vibrations resulting in a temperature increase [51]. Therefore, the main properties that govern good characteristics of energy harvesting detector need to be compromised. Further details of the important properties of a good energy harvesting detector has been discussed in previous section 2.7.2. The wide bandgap of SiC that has been used in this study resulted in good energy harvesting detector [51], which contribute to a low leakage current and a high barrier height detector in comparison to silicon and germanium detector. The lower leakage current of detector will contribute to a high collection of electron–hole pair, and therefore increasing the short circuit current. Whilst, detector with a wide bandgap material will have a higher barrier height that is important in producing high value of open circuit voltage and hence producing a high power output of energy harvester.

Energy scavenging in X-ray environment has been performed using a Phywe Xpert4 system with a tungsten (W) anode, operating at tube currents between 0.2 and 1.0 mA. The same experimental set up as described in section 4.2 was used for the energy harvesting measurements reported here. In order to study the performance characteristics of the detectors as X-ray photon energy harvesters, the forward I-V characteristics were determined whilst irradiated with an accelerating voltage of 35

kV and increasing tube current up to 1.0 mA. Previous characterisation of the X-ray generator using a BPW34 detector has shown that the dose rate increases linearly with the tube current, as described in section 4.4.1, with a maximum dose rate of 0.185 mGy/min for a tube current of 1 mA.

X–ray photovoltaic cell convert the kinetic energy of the incident X–rays into electrical energy, trough the formation of electron–hole pairs. The current generated in the device is negative as it supplies power to an external circuit as shown schematically in the current–voltage characteristics in Figure 5.19. The performance of the detectors were analysed and compared with the performance of a BPW34 Si photodiode detector when used as an X–ray photon energy harvester. The choice of a BPW34 for the comparison is due to these devices showing the highest sensitivity and response, coupled with the best repeatability and reproducibility in comparison to other commercially available photodiodes [148] as described in subsection 4.4.1. The performance of the detectors when exposed to the X–ray radiation is shown by the data plotted in Figure 5.20. Exposure to the radiation resulted in the observed shift in the current signal density to higher values, especially for detector D5. As described in section 4.2, all three detectors tested here have different Schottky characteristics, which give rise to different electrical behaviour as summarised in Table 5.1.

Detector	Schottky contact	Ideality factor	Barrier height	Current saturation density
			(eV)	$(A.cm^{-2})$
D2	Ni ₂ Si	1.077	1.660	4.00×10^{-18}
D4	Ni ₂ Si	1.160	1.540	2.13×10^{-11}
D5	Ni PVD	1.231	1.673	5.33×10^{-17}

Table 5.1: Table of material properties; Schottky contact, ideality factor, barrier height and current saturation density for detectors D2, D4, and D5.

From the plots in Figure 5.20, detector D5 demonstrates the highest short circuit current density (J_{SC}) , open circuit voltage (V_{OC}) and maximum power output (P_{OUT}) . The number of electronhole pairs created in the device due to the absorption of the incident radiation per second (N_e) is given in equation below [169]

$$N_e \left(\frac{\text{\# pairs}}{\text{s}} \right) = \frac{P_{total} \left(J/s \right) \cdot \eta_d}{\text{W (eV/ion pair)}} \cdot 6.25 \times 10^{18} \left(\frac{\text{eV}}{\text{J}} \right)$$
 (5.4)

where P_{total} is total power, η_d is fraction of power that is deposited in the depletion zone and $W(eV/ion\ pair)$ is the average amount of energy that it takes to make an electron-hole pair. The

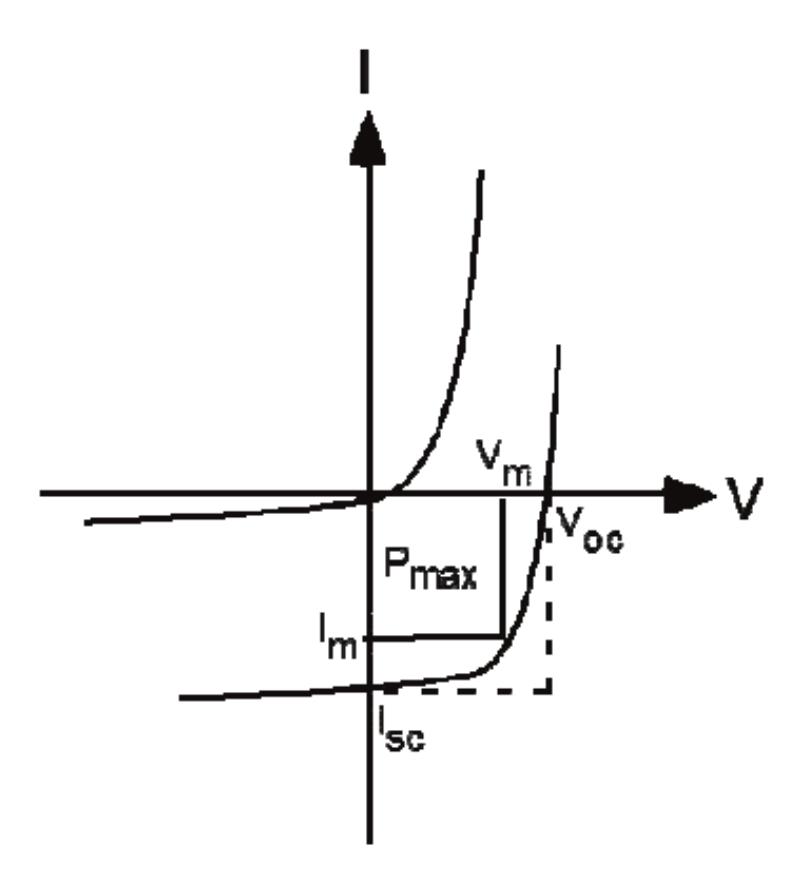


Figure 5.19: Typical trend of current–voltage characteristics of X–ray photon energy harvester depicting the maximum power (P_{max}) (described as peak power density (P_{OUT}) for the case in this section), short circuit current (I_{SC}) and open circuit voltage (V_{OC}).^[51]

electron-hole pair creation energy is linearly proportional to the value of energy bandgap [50]. Since all detectors were fabricated from the same polytype of silicon carbide (4H) they will all have an identical bandgap and hence an identical electron-hole pair creation energy of 7.8 eV [50]. However, BPW34 demonstrates a short circuit current density that is a factor of 10^3 higher than SiC fabricated detectors as shown by the plots in Figure 5.21. This condition is due to the lower electron-hole pair creation energy; 3.62 eV [50] for Si in comparison to SiC. Consequently, a prerequisite for high efficiency radiation to electricity conversion is a high mass attenuation coefficient, μ_m [153] because a material with a high μ_m will attenuate the radiation in a shorter distance and the majority of the energy is absorbed in the active part of the device [153].

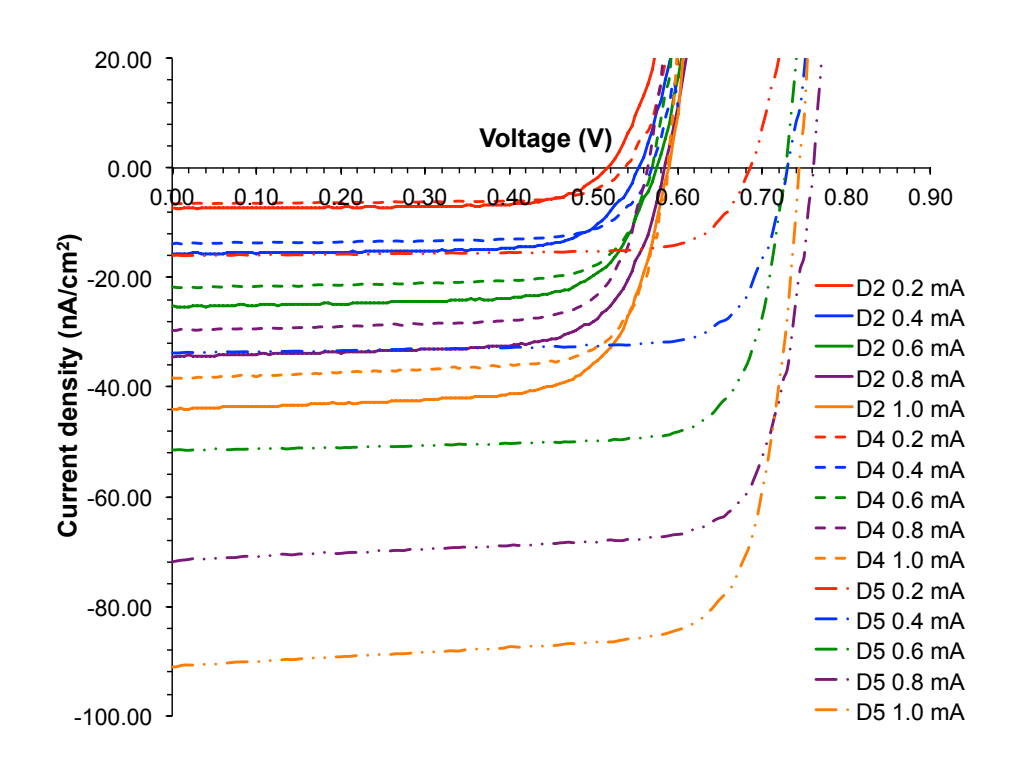


Figure 5.20: Current–voltage characteristics of detector D2, D4 and D5 after illumination with 35 kV X–ray and increasing tube current between 0.2 and 1 mA.

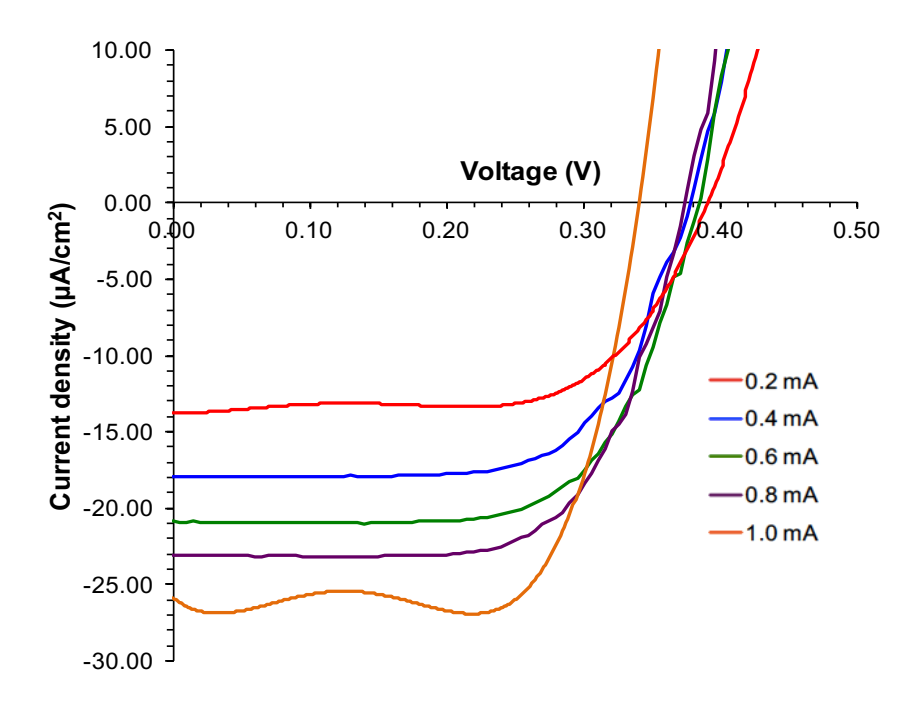


Figure 5.21: Current–voltage characteristics of BPW34 Si photodiode after illumination with 35 kV X–ray and increasing tube current between 0.2 and 1 mA.

5.4.1 Short circuit current density, J_{SC}

The short circuit current is the current that flows through the diode when the voltage across the terminals is zero and can be considered as the intercept of the I–V characteristics with the y-axis. The value of J_{SC} can be expressed as [169]

$$J_{SC} = N_e \left(\frac{\text{\# pairs}}{s}\right) \cdot 1.6 \times 10^{-19} \left(\frac{Coulumb}{pair}\right) \tag{5.5}$$

According to Equation 5.5, the short circuit current density, J_{SC} , is dependent on the number of electron–hole pairs created per second (N_e). Hence, any factors that decrease the production rate of electron–hole pairs will reduce the J_{SC} value. Therefore, semiconductors with high mass attenuation coefficients will produce high short circuit currents. As expected, the data show that the short circuit current has a linear dependance on the tube current in the X–ray generator. The data plotted in Figure 5.22 demonstrate that detector D5 produces almost double the short circuit current density of either detector D2 or D4, which are in the range of 16 to 91 nA/cm². This difference may attributed to the difference composition of the Schottky contact of D5 which is nickel, in comparison to the other two detectors, which have Ni_2Si Schottky contacts. The higher density of nickel, 8.908 g/cm³, results in a higher attenuation of the incident radiation in comparison to the lower density nickel silicide (7.4 g/cm³). The short circuit current values for detector D5 are higher than the values reported by Qiao *et al.* for SiC Schottky diode alpha–voltaic; 7.48 nA/cm² and beta–voltaic; 13.82 nA/cm² respectively using ^{142}Am (3.5 Ci g⁻¹) and ^{63}Ni (11.7 Ci g⁻¹) [68].

From the data it can be observed that the short circuit current density increases for all detectors with dose rate, as can be predicted using Equation 5.5, where the higher incident dose rate results in the generation of a larger number of electron-hole pairs. Devices with a low dopant concentration will result in the formation of a wider depletion region, which increases the active volume and hence the short circuit current by increasing the charge collection [51]. The stopping range of the X-ray radiation within the material also will affect the generation of electron-hole pairs. Low energy radiation with the combination of a high density semiconductor results in a shorter range of penetration, which in turn generates fewer electron-hole pairs. This results in a reduction in the short circuit current density. However, in the case of the detectors being characterised here, the short circuit current is compromised by the low dopant concentration in the epilayer. In addition, the existence of defects or trapping states (which may be linked to the observed higher leakage current) will result in a reduction of the number of electron-hole pairs created and hence lowers the observed values of J_{SC} . Hence, the maximum extracted power (P_{OUT}) is reduced, significantly diminishing the output

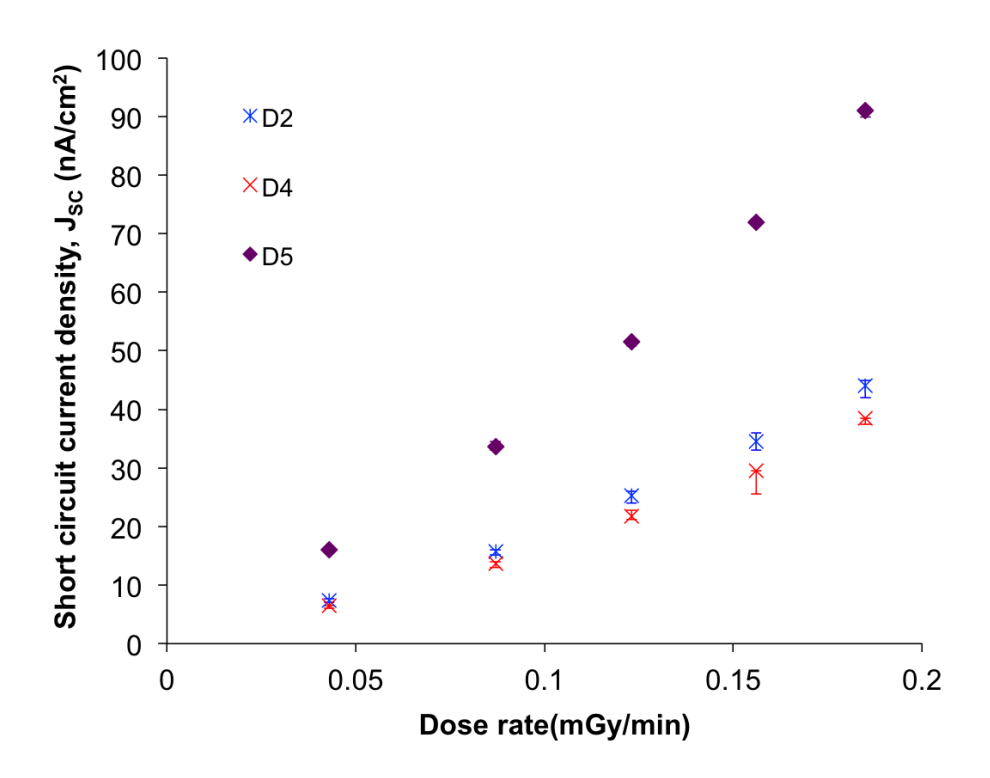


Figure 5.22: Short circuit current density (J_{SC}) for all detectors as a function of dose rate. The error bars represent the standard deviation of the data.

performance of the detector when used as a nuclear battery. This effect can be observed from the variation in the spectroscopic data in terms of the FWHM, CCE and resolution of the detector itself which was described in section 5.2.

5.4.2 Open circuit voltage, V_{OC}

The open circuit voltage (V_{OC}) is defined as the voltage across the device when the current is zero. It is determined from the point where the curves in Figure 5.20 intersect the horizontal axis. In contrast to the short circuit current, the open circuit voltage (V_{OC}) does not show a strong correlation with the incident dose rate, as can be observed from the characteristics in Figure 5.20. The open circuit voltage shown in Figure 5.23 demonstrate that detector D5 have the highest open circuit voltage (V_{OC}) of 0.74 ± 0.02 V, which is almost double that of the BPW34, which is 0.38 ± 0.02 V. Whilst, both detectors D2 and D4 were shown to have similar values of V_{OC} , which show only a slight variation with increasing dose rate, of 0.57 ± 0.02 V. For p-n diode based detectors, the open circuit voltage is typically close to the bandgap of the semiconductor. It is expected that the open circuit voltage for a Schottky detector should be close to the barrier height of the detector and Prelas $et\ al$. suggested that it should be less than or equal to the material bandgap [169]. For an ideal photovoltaic

cell, wide bandgap will resulted in lower saturation current density, and thus increasing the open circuit voltage [66].

High barrier typically leads to higher V_{OC} , where it result in lower leakage current and hence the saturation current density. From Equations 5.6 and 5.7, a very small reverse saturation current density (I_0) is required to improve the open circuit voltage (V_{OC}). Consequently, a high barrier height is required to have a low reverse saturation current (I_0) [157]. Referring to Table 5.1, detectors D2 and D5 provide lower values of the saturation current density of 4.00×10^{-18} A.cm⁻² and 5.33 $\times 10^{-17}$ A.cm⁻², respectively. The lower value of saturation current density for detector D5 lead to the higher values of open circuit voltage to that other fabricated detectors, as can be observed by the data in Figure 5.23. However, the lower value of saturation current density for detector D2 is unable to provide a high open circuit voltage, where the detector demonstrate almost identical open circuit voltage to detector D4. This can be explain from the relationship of the open circuit voltage with the short circuit current density as expressed in Equation 5.6. The low values of short circuit current density for detector D2, resulted in reduction of the open circuit voltage as can be observed by the data in Figure 5.22.

The low values of the open circuit voltage observed from the data indicate that the series resistance of the diode is significant, which is related to the thick epitaxial layer used in the fabrication. However, it is worth noting that the open circuit voltage is significantly higher than values reported for AlGaAs that have been published as potential gamma batteries [156] which is 0.05 V at room temperature. This suggests that silicon carbide is an ideal material for the realization of nuclear batteries for deployment in a range of applications, but particularly those that include extreme environments. Because of the low atomic number (silicon has Z = 14 and carbon Z = 6) and relatively low density (3.2 g/cm^3) of silicon carbide, the stopping power for X–ray photons is low, requiring a thick epitaxial layer to ensure sufficient charge generation. However, the resulting high resistance reduces the electrical power that can be extracted. This has been compromised with the using of the low doping concentration of the epitaxial layer during this study. As described in subsection 5.4.1, the low dopant concentration gives rise to an increased depletion region width and indirectly increases the generation of electron—hole pairs that can increase the charge collection efficiency in the detector.

The theoretical value of V_{OC} is governed by the ideality factor values and temperature of the detector as described by

$$V_{OC} = \frac{nkT}{q} \ln\left(\frac{I_{SC}}{I_0}\right) \tag{5.6}$$

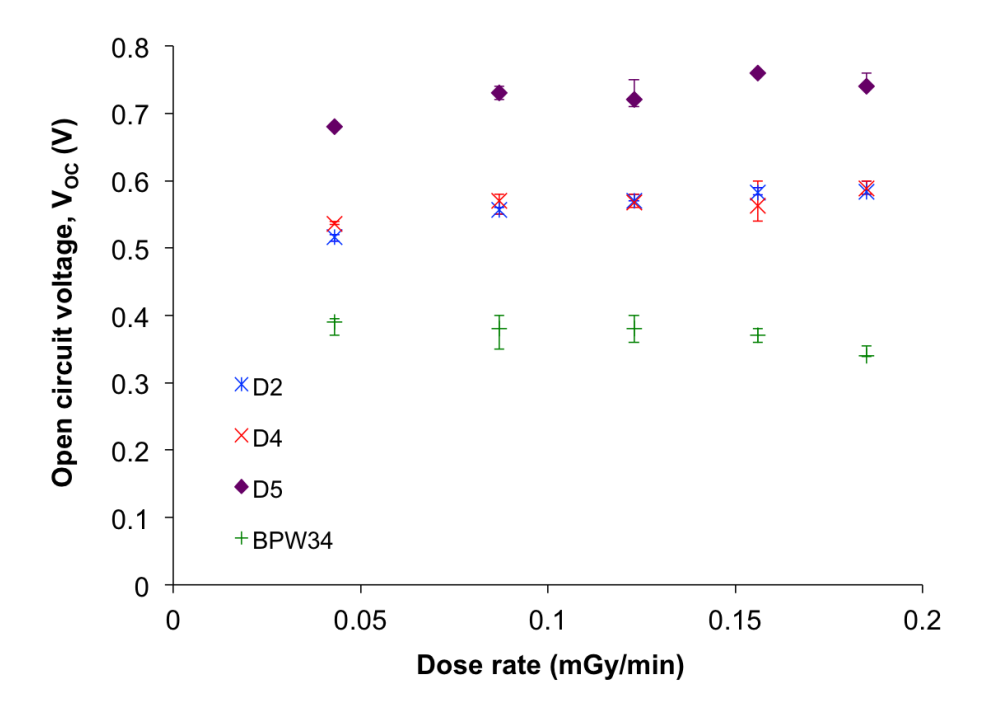


Figure 5.23: Open circuit voltage (V_{OC}) for all detectors as a function of dose rate. The error bars represent the standard deviation of the data.

and

$$I_0 = AA^*T^2 \exp\left(\frac{-q\Phi_B}{kT}\right) \tag{5.7}$$

where I_{SC} is the short circuit current, I_0 is the saturation current, T is the temperature, k is the Boltzmann's constant, q is the electronic charge and n is the ideality factor.

This indicates that detectors with high ideality factor are expected to show high V_{OC} . This can be observed from the data summarised in Table 5.1 and Figure 5.23, where the higher ideality factor of detector D5 (n = 1.231) can be correlated with the higher value of V_{OC} in comparison to detectors D2 and D4. The data obtained here is significantly higher than that published in the literature [68], which gave a value of V_{OC} for alpha–voltaic (using an 241 Am source) and beta–voltaic (using 63 Ni) was 0.25 V. As can be seen from Equation 5.6, the open circuit voltage has a logarithmic dependence on the leakage current, which in turn can be linked to the intrinsic carrier concentration, as described in section 4.4.3. The open circuit voltage decreases with increasing leakage current or intrinsic carrier concentration [51]. This supports the hypothesis that all the detectors investigated here comprise a high quality metal–semiconductor interface, which results in ideal characteristics, as described in detail in section 4.3.

5.4.3 Peak power density, P_{OUT}

The peak power density that can be extracted from the incident radiation can be determined from the product of the voltage and current density as shown by the plot in Figure 5.19. Increasing the bias voltage, increases the output power until a maximum, P_{max} is achieved (this is shown schematically in Figure 5.19) before decreasing at higher bias levels. The maximum power that can be extracted from the diode, determined from the data in Figures 5.22 and 5.23 is shown in Figure 5.24 as a function of the dose rate. As expected, the data show a linear behaviour which is related to the significant variation in the the short circuit current with dose rate because the short circuit current is the only parameter that shows a significant variation as the dose rate is varied. The high short circuit current density of detector D5 makes a significant contribution to the peak power density, as may be predicted using Equation 5.8. Here, it can be assumed that any factors affecting either J_{SC} or V_{OC} will affect the power output performance of the detector.

$$P_{OUT} = V_{OC}(V) \cdot J_{SC}(A) \cdot FF$$
(5.8)

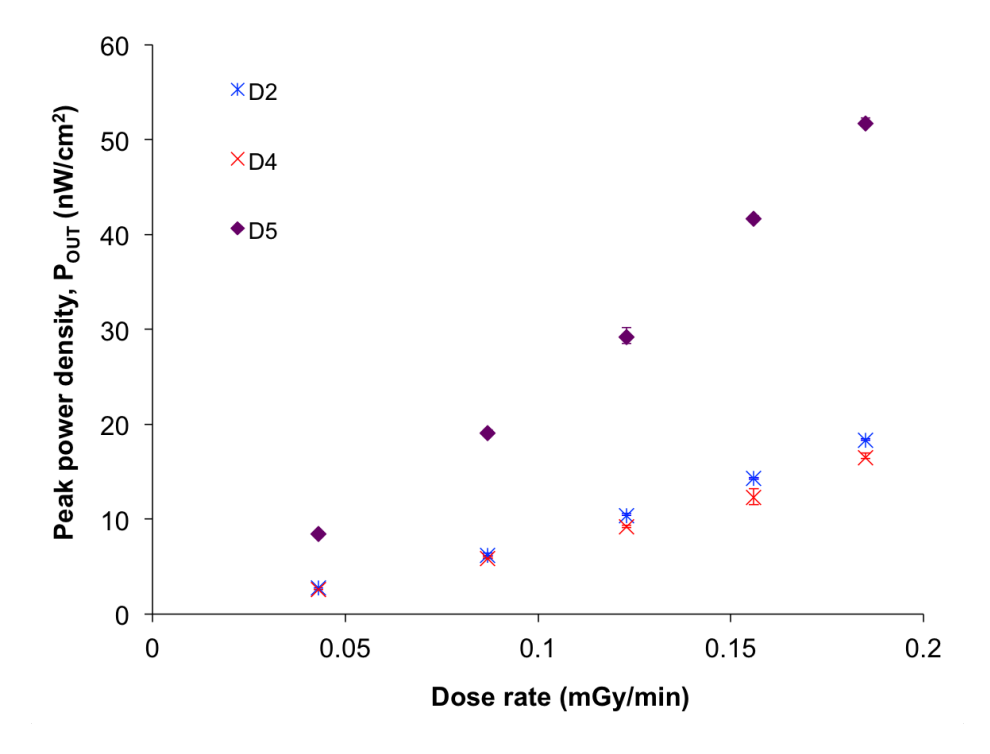


Figure 5.24: Peak power density (P_{OUT}) for all detectors as a function of dose rate. The error bars represent the standard deviation of the data.

The observed peak power value for detector D5 varies between 8.42 and 51.70 nW/cm² with increasing dose rate. These values are approximately three times higher than those observed for detectors D2 and D4 of 2.58 to 15.3 nW/cm². These values are significantly higher than those reported in the literature for other semiconductors, 5.96 pW/cm² (55 Fe X–ray, AlGaAs detector) [156] and 0.52 nW/cm² (63 Ni β –source, GaAs detector) [170]. Meanwhile, in comparison to SiC Schottky barrier diodes, the peak power density for D2 and D4 at 0.087 mGy/min are comparable to the beta–voltaic battery data reported in the literature evaluated using 63 Ni, which had a maximum output power density of 4.85 nW/cm² [68]. The carrier diffusion length and detector leakage current are directly related to the short circuit current and open circuit voltage of the device and the temperature dependence of these terms has a significant effect in determining the upper operating temperature of the energy harvester [51]. In addition, the leakage current has a strong dependence on the intrinsic carrier concentration as described in section 4.4.3 ($J_L \propto n_i$). An optimization of the dopant concentration by considering few parameters is necessary in order to obtain maximum power output as described in section 2.7.2.

5.4.4 Fill factor, FF

The fill factor is used as a figure of merit for photovoltaic cells and relates the maximum extractable power from the diode to the product of the short circuit current and open circuit voltage. The fill factor may be considered as a measure of the squareness of the current as a function of voltage in the characteristic presented in Figure 5.19. The fill factor for a practical diode has to be below 1, because the current has an exponential dependence on voltage, as an be predicted from Shockley's equation for a p-n diode. The closer the shape of the I-V characteristics to the rectangular, the higher the quality of the illuminated I-V characteristics [155]. The fill factor can be calculated using

$$FF = \frac{P_{OUT}}{V_{OC} \cdot J_{SC}}$$
 (5.9)

As presented by the data in the previous subsection for P_{OUT} , V_{OC} and J_{SC} , it is expected that the fill factor for detector D5 will be higher than those observed for detectors D2 and D4. The fill factor of detector D5 was extracted from the data shown in Figure 5.25, resulting in a constant value of 0.77 ± 0.02 for all the dose rates examined here. Both D2 and D4 demonstrate a minor reduction in fill factor, with values in range of 0.71 ± 0.005 and 0.74 ± 0.008 , respectively. However, despite the higher electron–hole pair creation energy in comparison to Si, these values are still higher than the fill factor of the commercial Si photodiode; BPW34 which is 0.67 ± 0.01 . This may contribute

from the high J_{SC} values of BPW34 as demonstrated in Figure 5.21 which resulted in a reduce of fill factor values.

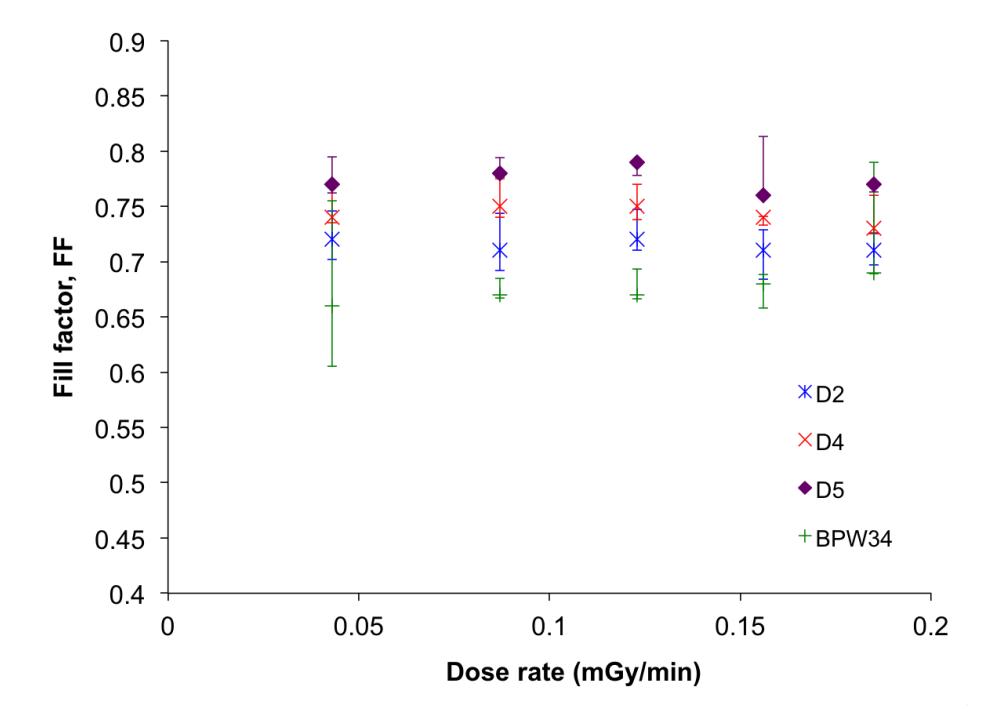


Figure 5.25: Fill factor (FF) for all detectors as a function of dose rate. The error bars represent the standard deviation of the data.

Furthermore, all detectors investigated here give higher values of fill factor than those published in [68] for SiC Schottky alpha–voltaic and beta–voltaic cells, which demonstrated fill factors of 0.68 and 0.57, respectively. The fill factor values presented in this section are in good agreement with the high grade solar cell proposed by Prelas *et al.* with a fill factor > 0.7 [169]. The design of the detector plays an important role in determining optimum output, because any layer between the radiation source and the depletion region will attenuate the energy of the incoming radiation and hence result the generation of a lower number of electron–hole pairs, decreasing the fill factor, as described in sections 2.7.2. It is worthy of note that the energy and type of the incident radiation needs to be carefully considered obtaining optimum performance of energy harvesters, because the different range of energy and type of radiation interacts with the detector through a range of different mechanisms.

5.5 Potential Applications

Based on the performance of the fabricated detectors, specifically detector D5, there is a possibility to power a sensor node using incident radiation with a dose rate comparable to that found in conventional medical systems. The proposed power electronic system, comprises a power converter, which along with signal conditioning and sensor circuits can be manufactured from silicon carbide, offering the potential for long term deployment in extreme environments. The ability to remotely monitor the radiation dose in environments where the radiation dose rate precludes the use of conventional technology offers a step change in capability and has potential application in a range of challenging environments from nuclear decommissioning to beam line monitoring in radiotherapy. The Internet of Everything approach to sensing, where small, self-powered sensor nodes can be easily deployed has revolutionised our understanding of the world around us. However, these nodes are typically based on silicon technology and so are precluded from deployment in a range of hostile environments, including those where the temperature exceeds 175 °C, contains chemically aggressive species or the radiation dose rate is high. Furthermore, photovoltaic cell that can withstand high radiation dose without efficiency loss is a prerequisite for economical astronautic applications [153]. The major challenge for conventional photovoltaic cells in the space environment is the radiation damage arising from from higher energy ions (particularly photons in the proximity of the earths magnetic field – where the dose rate can approach 10⁵ protons cm² s) in outer space; X-rays and γ -rays [153]. This restriction also limits their use in a range of scientific and industrial applications, including volcanic emission monitoring, closed loop control of combustion processes and long term nuclear installation monitoring.

In addition to the issues with the realisation of long term photovoltaic cells, one of the critical technologies in the development of the self-powered sensor nodes is the power conditioning circuitry that boosts the output voltage from the energy harvester to a level that makes it useful to power a circuit. The sensor node proposed here can be realised using silicon carbide technology and is suitable for long-term deployment in high temperature, high radiation environments.

5.5.1 Self-powered X-ray sensors for extreme environments

The proposed electronic circuits can be constructed from 4H–SiC Junction Field Effect Transistors, using the process described previously [171]. The JFETs can be used as the active devices that form the power conversion, signal conditioning and communications modules in the sensor node that is shown schematically in Figure 5.26. In this application, the diode structure described in this thesis can be used as both the sensor and the fundamental part of the energy harvesting module.

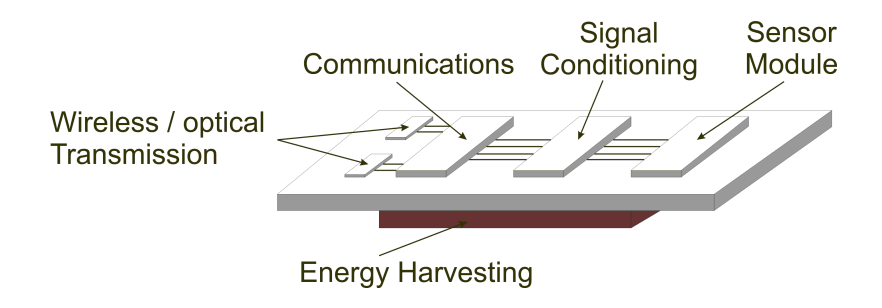


Figure 5.26: Schematic representation of a self–powered sensor node for deployment in extreme environments.^[171]

The maximum power that can be harvested from detector D5 to identify the possible harvested power for an incident dose rate of 100 mGy/min, which is comparable to the dose rate for a chest X-ray (quoted as 7 Gy in 5 seconds) can be extrapolated from the data shown in Figure 5.24. In the X-ray beam, the maximum harvestable power level from the plot for detector D5 at incident dose rate of 0.18 mGy/min is $28 \mu\text{W/cm}^2$. In order to operate the silicon carbide circuits for signal conditioning and communications, a voltage in excess of 12 V is required. A self-starting converter, based on oscillations in a tuned circuit has been shown to be an ideal candidate for this type of application [172]. The schematic of the circuit is shown in Figure 5.27. A second generation of the circuit, with an optimised inductor at the input, has demonstrated a voltage gain of 20, which would result in a potential output voltage of 14 V for detector D5 operating at the maximum power point. This voltage needs to be stored on a capacitor to enable intermittent operation of the high current (typically 5 mA) circuitry used for the other functions. This type of operation is typical for circuits that scavenge energy for the surroundings, where nodes harvest energy and store it in capacitors until sufficient to operate the node. Capacitor structures based on high-k dielectrics, such as HfO2, have been demonstrated that can operate at temperatures beyond 400 °C and in total ionising dose in excess of 1 Mrad [173], which would be ideally suited to this application.

In order to fully design the power system for the node, the dimensions of the power harvesting diode have to be matched to the requirements of the sensor. The majority of self-powered sensor nodes are used in locations where infrequent updates of the conditions are required, rather than in locations where real time data is critical. The power and duration required to perform a measurement and then transmit the data to a remote processing node can then be estimated as 14 mW for 0.5 s. Using the power determined for a system in a dose rate comparable to that found in a medical X-ray, the harvester is capable of transmitting the data once every 8 minutes, allowing for the power converter to be 55 % efficient. By increasing the diode area to that of a single silicon carbide wafer, by manufacturing pixellated diodes over the entire surface, it is possible to increase the harvested power

by a factor of 160 (allowing for the edge of the wafer to remain unprocessed), giving the possibility of data every three seconds using this technology.

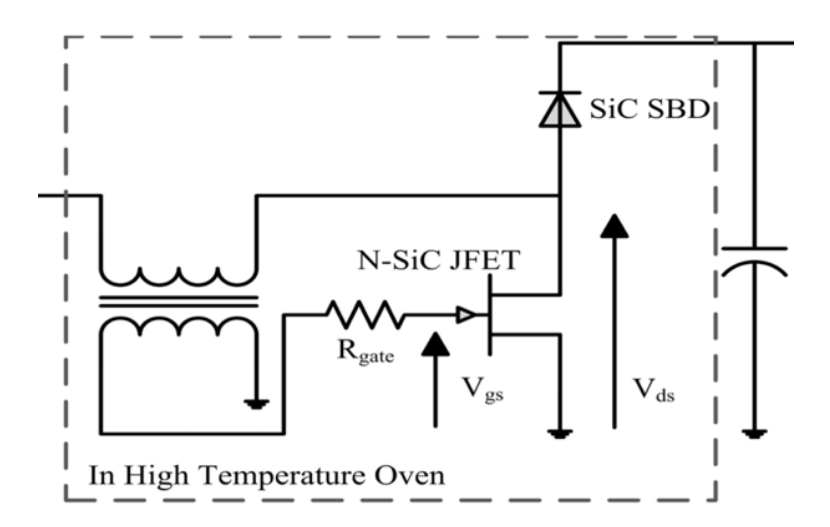


Figure 5.27: Circuit schematic for a self starting boost converter suitable for converting the 0.7 V output to 14 V.^[172]

Therefore, through the use of the fabricated 4H–SiC Schottky diode, it is possible to develop a self–powered system that harvests energy from the X–ray photon flux in the environment. Based on a silicon carbide diode detector, it is potential to fully integrate a power system that is capable of providing the voltage levels required to operate a sensor node in extreme environments. Whilst, silicon carbide technology has been used to demonstrate a range of nuclear battery applications previously, this is the first proposed self–powered X–ray photon energy harvester with a high performance capability in terms of maximum power density and fill factor. Additionally, it is a constructive structures that not only able to endure high radiation dose but also provide power in terms of electricity. This would also have far reaching consequences in converting waste X–ray and even γ –ray radiation in nuclear power plants [153].

5.6 Conclusion

Following characterisation of D1, D2, D3, D4 and D5 at elevated temperatures, the possibility of the fabricated detector as an energy harvester have been studied since one of the detector; D2 presented considerable response to lower energy radiation. The electrical and spectroscopic response based on the detection properties with ²⁴¹Am were performed prior to investigation on the capability of the 4H–SiC Schottky diode as an X–ray energy harvester. Alpha spectroscopy in terms of channel peak position, full–width at half maximum (FWHM), energy resolution and charge collection efficiency (CCE) were studied and analysed for detectors D2, D4 and D5. The data show that detector D5 demonstrate slightly better FWHM and energy resolution in comparison to the other detectors D2 and D4, while the channel peak position and CCE observed to be similar. Based on these measurement, there is interest to investigate the defect mechanism inside those detectors due to the distinct detection properties discovered.

Hence, the low noise frequency measurements have been determined to investigate the correlation of those detection properties with the defect and impurities present. Based on those measurements, it can be observed the current dependance of the noise spectral density where detector D2 and D4 demonstrate current dependance similar to other semiconductor detectors; $\beta = 1.6 - 1.7$. Whilst, detector D5 presented the lowest noise spectral density at moderate current values with $\beta = 3.16$, which is double than the other two detectors. The difference in the noise spectral density measurement between those detectors may exert a significance influence on their detection properties, and therefore the performance as X-ray energy harvester.

Subsequently, performance capability as X–ray photon energy harvester have been tested in term of short circuit current density, J_{SC} , open circuit voltage, V_{OC} , power output, P_{OUT} and fill factor, FF. Measured short circuit current density, J_{SC} and power output, P_{OUT} for all detectors observed to increase with increasing dose rate as more electron–hole pairs are generated. Otherwise, the open circuit voltage, V_{OC} , and fill factor, FF almost constant with dose rate applied and comparable to BPW34 silicon PIN photodiode. Detector D5 gave a high short circuit current density, J_{SC} and power output, P_{OUT} in comparison to the other two detectors which are within the range of 15 to 90 nA/cm² and 10 to 55 nW/cm², respectively. This can be explained based on the increased in barrier height (1.67 eV) and good spectroscopic properties in terms of full–width at half maximum (FWHM) and energy resolution measured with alpha source (241 Am). Furthermore, the low leakage current of detector D5, which is less than half to that observed in both of detectors D2 and D4 (<1 nA/cm²), may be one of the factor that can minimize the loss of electron–hole pairs created due to trapping and defect.

In summary, the correlation of the detection and defect properties with the capability of D2, D4 and D5 detectors as X-ray photon energy harvester has been made. Based on the exceptional detection and defect properties of D5 attributed to the considerable performance as X-ray photon energy harvester. Therefore, through the use of wide bandgap semiconductor materials, the data presented show that it is possible to develop a self-powered system that harvests energy from the X-ray photon flux in the environment. This opens up the possibility of developing a practical high power X-ray photon energy harvester, where the dose encountered by the power conversion electronics is beyond the limitations of silicon based systems.

Chapter 6

Radiation Tolerance of 4H–SiC Schottky Diode Radiation Detector in High–Energy Photon Environments

6.1 Introduction

Semiconductor detectors have been widely used in radiotherapy dosimetry applications since the beginning of the 20^{th} century. Silicon diodes are primarily used as on–line dosimeters in radiotherapy applications due to their high sensitivity to radiation in the absence of external bias, good mechanical stability and low active volume [21, 36]. However, the limited radiation hardness of silicon dosimeters in high radiation fields and a strong dependence of the sensitivity on the accumulated dose, which can be observed as an exponential decrease in the low dose range, coupled with a linear decay in sensitivity for high doses [21, 35, 36], presents a major drawback. This results in the need for pre-irradiation of the detector before each measurement and frequent recalibration [21, 35, 36, 95]. In addition, silicon can not be considered a tissue-equivalent material in clinical radiotherapy, due to its relatively high atomic number (Z = 14), which is higher than that of human tissue [21, 35]. Hence, their dosimetric response is strongly dependent on the energy of the incident radiation [35]. High radiation hardness and insensitivity to radiation damage results in high quality devices that show reduced charge trapping and polarization effects after radiation exposure. This is particularly true for beam monitors that are installed in treatment systems, where accurate and precise detection of the electrical signal that is produced by the incident radiation over long periods is essential. Radiation detectors that are prone to radiation damage show evidence of a decrease in dose sensitivity and increase in dark current [95] with continued exposure. Therefore, the development of radiation detectors with performance characteristics that are insensitive to radiation damage and high radiation hardness are required in order to offer long operational lifetimes and high detection efficiency.

6.1.1 Overview of the SiC as high dose rate radiation detector

Conventional radiation detectors are often fabricated from silicon and germanium, which in comparison to silicon carbide (SiC) have a lower radiation tolerance, related to the small bandgap and displacement threshold energy. Hence, the detectors are prone to radiation induced damage [95]. Tissue-equivalence and insensitivity of chemical vapour deposition (CVD) diamond to radiation damage has resulted in it being identified as a superior alternative to silicon and ionisation chambers for use as on-line dosimeters in radiotherapy applications [174, 175]. However, for particle detection purposes, the uniformity of the electrical quality of the device across the active area is limited and this affects the detector spatial resolution [149]. The spatial uniformity degradation observed in CVD diamond due to its micro-crystalline nature can be avoidable with the use of SiC epitaxial detectors [149]. Due to high bandgap and outstanding properties of SiC, it has been recently proposed as being suitable for the manufacture of radiation dosimeters operating in high radiation damage environments [108]. The suitability of SiC for standard on-line dosimeters in radiotherapy applications can be supported by the fundamental material properties that lie between those of diamond (Z = 6) and silicon (Z = 14) [36]. In dosimetry, detector with the atomic number that is equivalent to tissue or water is important to respectively mimicking human tissue and gave response comparable to the tissue or water equivalent dosimeters. This device will ensure an accurate estimation of dose response relative to water during calibration procedure, which use reference water equivalent dosimeters (usually ionization chamber) for treatment planning verification prior to radiotherapy treatment [176]. Referring to IAEA TRS-398 Code of Practice [177], a fluence scaling factor, h_{pl} need to be established in order to convert ionization chamber readings in a plastic phantom to the equivalent reading in a water phantom [176]. Finding from the study performed by Thwaites, who calculated the fluence scaling factors between water and plastic phantoms for electron beams showed that measured values of h_{pl} were dependent on the ionization chamber and beam energy [178]. Therefore, to be as a tissue or water equivalent material in in-vivo dosimetry, a detector-to-water conversion factor, $H_{pl,d}$, may need to be established to allow the derivation of the absorbed dose-to-water in a water phantom from detector readings.

Recently, a number of studies on the radiation hardness of epitaxial SiC have been performed. Several studies have been performed in high radiation fluence to observe the degradation in charge collection efficiency (CCE) and full-width half maximum of the devices. However, the detection properties; energy resolution and charge collection efficiency deteriorate significantly if there are radiation—induced defects within active volume of the detector. These defects, which are commonly have energy states in the bandgap [108] are often described as lifetime killing defects, because of the detrimental effect on carrier transport. Bertuccio *et al.* [21] reported the electrical and dosimetric

properties of SiC on exposure to photon beams and compared them with three commercial silicon dosimeters. The data showed that the leakage currents of SiC diodes are practically negligible at temperatures below 100 °C making them ideally suited for dosimetry in radiotherapy applications [21]. Whilst the performance degraded after irradiation to a 6 MV photon beam in the dose range of 50 to 1000 monitor units (MU) (at a constant dose rate of 200 MU/min), the characteristics were such that the detector was still suitable for spectroscopic measurements at room temperature [21]. In contrast, no significant increase in leakage current was observed after high energy proton irradiation of 10^{11} p/cm² on semi–transparent SiC Schottky diodes [25]. However, after a subsequent irradiation of 10^{13} p/cm², the full–width at half maximum of the spectral peak observed to be 31% broadened, resulting in a degradation of the spectral performance and increased low level (< 5 keV) noise [25].

Meanwhile, the effect of high energy irradiation on the performance of SiC dosimeters has been investigated. The suitability of SiC devices to act as radiation dosimeters in on-line configuration have been tested using a 60Co source, 20 MeV electron beam and a 6 MV photon beam from a linear accelerator in the dose range of 0.1–10 Gy [36]. The data showed that epitaxial 4H–SiC is an efficient dosimeter in radiation dosimetry applications due to the high quality of the epilayer which avoids the appearance of priming effects and leads to relatively high carrier diffusion lengths [36]. In addition, Bruzzi et al. characterised the response of epitaxial SiC detectors to electron and photon irradiation as on-line radiation dosimeters [149]. The detectors showed a response that exhibited a linear behaviour of the electron induced collected charge for electron doses in the range of 1-10 Gy and the sensitivity per volume of approximately a factor of 2 lower than that of standard silicon dosimeters. However, it is significantly higher than the best available commercial CVD diamond [149]. The radiation tolerance of 4H–SiC epitaxial layers grown by chemical vapour deposition (CVD) has been investigated after irradiation with 8.2 MeV electrons and gamma-rays from a 60Co source up to a dose of 40 Mrad and 24 GeV/c protons at a fluence of about 10^{14} p/cm² [108]. The proton and electron irradiation resulted in a decrease in the reverse leakage current and the net dopant concentration, $N_{\rm eff}$ in the epilayer with increasing dose, whilst gamma irradiation was observed to result in no significant effect on the reverse leakage current and slightly decrease in the $N_{\rm eff}$ with increasing dose [108]. This may due to the different average distance travelled and stopping power (rate of energy loss) produced from proton, electron and gamma radiation which lead to different level of damage occur during interaction in the detector active volume. The rate of energy loss caused by ionization interactions for charged particles is proportional to the square of the particle charge and inversely proportional to the square of its velocity [179]. In consequence, as the particle slows down, the rate of energy loss increases and so does the ionization or absorbed dose to the medium [179]. This condition causing more damage occur in comparison to the gamma irradiation.

6.1.2 Highlights of the chapter

The ability of the fabricated 4H–SiC detector to respond to low dose rate has been presented in Chapter 4. In this chapter, detector D2 which showed enhanced sensitivity at low dose rates has been tested with exposure to 6 MV photons in the range of 17.6 to 52.9 Gy/min. In order to study the radiation response and hardness of the fabricated detector, the responsivity to high–energy photon irradiation and the effect on the forward and reverse I–V and C–V characteristics were determined to a maximum cumulative dose of 1000 Gy. Based on the I–V characteristics, extracted values of the specific on resistance, ideality factor, barrier height and reverse leakage current were examined as a function of cumulative dose. The response to high–energy photons and dose rate linearity with increasing bias voltages were extracted and compared with those obtained for a commercial diode and data published in previous studies. Additionally, due to the high radiation tolerance and insensitivity to radiation induced damage of SiC, the effect on low frequency noise (LFN) and the performance capability as an X–ray photon energy harvester after irradiation to cumulative dose of 1000 Gy have been investigated.

6.2 Characterisation with high dose rate photon irradiation

During the radiation therapy procedure, the adverse effect from killing cancer cells with high radiation energy is a higher dose of radiation will be given to the tissues or organ in proximity to the tumour location. Consequently, in order to protect vital or radiosensitive organs neighbouring to deep seated tumours from high radiation energy, it is essential to accurately and constantly control the position, intensity and shape of the beams during radiation therapy treatment [5]. Detectors with high spatial resolution, sensitivity which is independent of dose rate, radiation energy and linear energy transfer (LET), fast response, high signal stability, good linearity with both dose and dose rate, and wide dynamic range are required for an accurate determination of the dose distribution delivered to the patient [95]. In addition, to ensure that the radiation dose is delivered to the patient with a high degree of accuracy, detectors with high radiation hardness, low temperature dependence and variation in the energy of incident radiation and a better match to tissue properties are crucial [21]. The use of detectors which offer high sensitivity to high dose irradiation with long-term stability, reproducibility and insensitivity to radiation damage will reduce time, cost and increase the effectiveness of treatment and instrumentation procedures. Semiconductors, primarily SiC are generating significant interest as alternative materials to silicon, due to their very small size, capability to be monolithically integrated with readout electronics, reusability and the possibility of real-time monitoring in a range of applications [21]. Good reproducibility, stability and enhanced sensitivity of detector D2 indicates the suitability of this detector to be evaluated as photon dosimeter in radiotherapy applications. Details of the fabrication process and initial electrical characterisation of detector D2 have been described in Chapters 3 and 4.

A maximum cumulative dose of 1000 Gy has been exposed to detector D2 to investigate the radiation tolerance of the fabricated 4H–SiC Schottky diode. For a cancer treatment in radiotherapy procedure, an average dose received by a patient using palliative treatment is approximately 2 Gy/fraction [180] and this value depend on the treatment planning and types of cancer. However, if this value is extrapolated per one radiotherapy treatment room and there are around 28 patients per day (estimated data from Northern Centre for Cancer Care, Freeman Hospital), the dose delivered in a one treatment room will be equivalent to 56 Gy/day. So, estimated dose delivered over a period of year in one treatment room is approximately around 12 320 Gy. The maximum cumulative dose that was used to study the radiation tolerance of the fabricated 4H–SiC detector is equivalent to approximately a dose delivered in one treatment room over a period of a month. Therefore, the maximum cumulative dose should be increase for about twelve times in order to estimate the radiation tolerance of a detector over a period of one year.

6.2.1 Experimental set up

The experimental procedure for high dose rate irradiation has been performed in Northern Centre for Cancer Care, located at Freeman Hospital in Newcastle using a 6 MV Varian TrueBeam STx linear accelerator (LINAC) machine. Prior to irradiation, the linear accelerator was calibrated using a NE2571 0.6cc Farmer chamber which was connected to a PTW dose electrometer whilst maintaining a source–to–surface distance of 68 cm and a radiation field size of 10 cm × 10 cm. The depth of the Farmer chamber in a tissue equivalent material from the surface was 3 cm and the tissue phantom ratio (TPR) was equivalent to 1.223. To simulate the set up that been used during treatment and evaluate the detector as a dosimeter, the detector was placed inside a plastic casing and embedded in a 1 cm slab of wax. The detector then was sandwiched between solid water phantoms (tissue equivalent materials). To vary the radiation dose rate between 8.8 to 52.9 Gy/min, the pulse repetition frequency (PRF) was changed whilst maintaining the distance from source to measuring point at 68 cm. A constant exposure time of 5.4 minutes for each of dose rate has been used in order to obtain a range of cumulative doses of 47.6, 142.9, 285.7, 476.2, 714.3, and 1000 Gy. Table 6.1 summarises the dose for the different measurements, expressed in monitor unit (MU), dose rate (Gy/min), dose (Gy) and cumulative dose (Gy).

No. of exposure	Monitor unit (MU)	Dose rate (Gy/min)	Dose (Gy)	Cumulative dose (Gy)
1	2160	8.8	47.6	47.6
2	4321	17.6	95.2	142.9
3	6481	26.4	142.9	285.7
4	8642	35.3	190.5	476.2
5	10802	44.1	238.1	714.3
6	12963	52.9	285.7	1000

Table 6.1: Table of different exposure performed during irradiation to 6 MV photon that expressed in monitor unit (MU), dose rate (Gy/min), dose (Gy) and cumulative dose (Gy); 1 MU is equivalent to 0.022 Gy.

A Keithley 6517B electrometer was connected to the detector to supply the external bias to the detector during the irradiation procedure. The applied reverse bias was swept to a maximum of - 150 V during irradiation. The experimental set up is shown in Figure 6.1. After each dose rate irradiation, the forward and reverse I–V characteristics were measured to investigate the radiation hardness of the detector by examining the parametric characteristics, particularly the specific on resistance (R_{on}), barrier height (Φ_b), ideality factor (n) and reverse bias leakage current determined from the data. Additionally, C–V measurements were performed to extract the dopant concentration (N_D) and allow the determination of the depletion width (W_d) after irradiation with the 6 MV photons to a maximum cumulative dose of 1000 Gy.

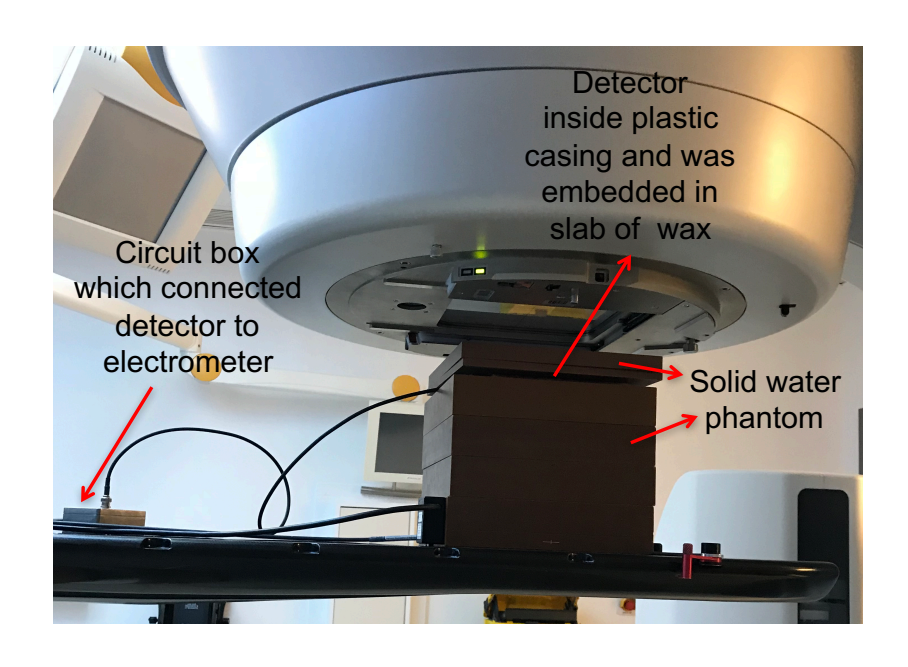


Figure 6.1: Experimental set up of the 6 MV photon irradiation.

6.2.2 High dose rate response

The current generated during exposure to dose rates ranging from 17.6 to 52.9 Gy/min are plotted in Figure 6.2 at different bias voltages. As expected from the low dose rate response data presented in section 4.4.2, the data show a linear correlation between the current density generated in the detector and the incident dose rate at all bias voltages. The current generated in the detector exhibits a high linearity with incident dose rate, where it varied between 1.50 to 3.08 nA/mm² and 9.22 to 15.00 nA/mm² for -10 V and -150 V, respectively. The current signal generated at -50 V and 17.6 Gy/min gave a value three times higher than value extrapolated from the slope of the fitted line of the current signal as a function of dose rate; 6.37×10^{-11} A.min/Gy.mm² (1.12 nA/mm²) which is reported in [149], for the same measurement conditions and epitaxial SiC detectors. Comparatively, the current signal generated at -150 V and 35.3 Gy/min photon beam is almost identical to the irradiated commercial diamond data for a dose rate of 7.5 Gy/min, with a typical value of 10 nA/mm² [175].

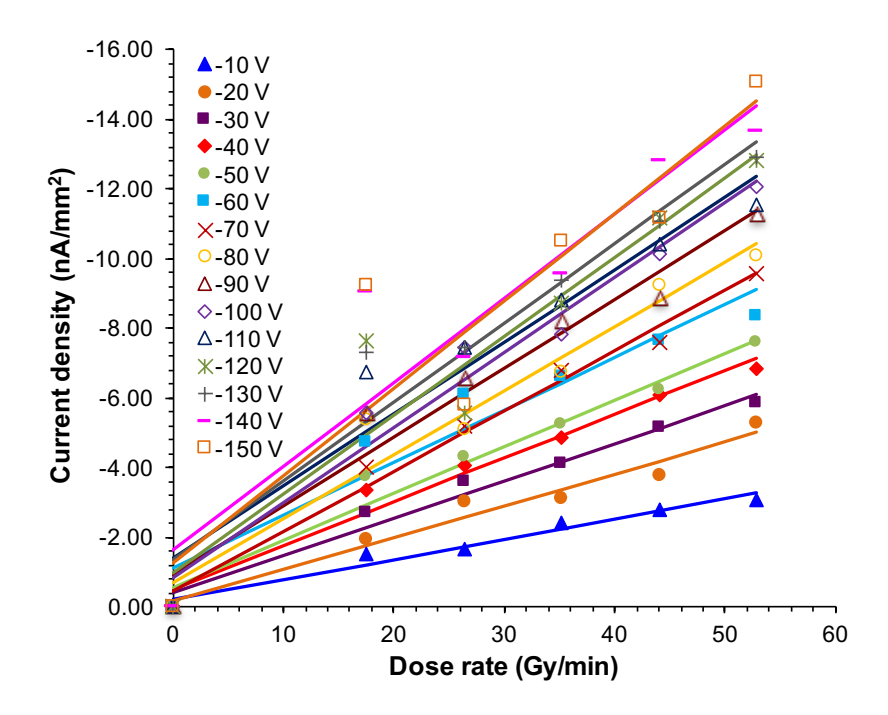


Figure 6.2: Current signal generated from irradiation between 17.6 to 52.9 Gy/min of 6 MV photons with increasing bias voltages.

The increase in the current generated at high bias voltages can be described by the increase in the depletion region width, as described in sections 3.2 and 4.4.2. The correlation of the current signal detected with the depletion width at different dose rates can be observed from the data plotted in Figure 6.3. With the exception of the data for dose rates of 17.6 and 26.4 Gy/min, the current generated shows the expected linear correlation between the current density and depletion width where linear regression fitting confirms that the generated current density falls to zero as the depletion

region width is reduced to zero. The abnormal behaviour of the 26.4 Gy/min data is related to the higher leakage current observed at high bias voltages for this measurement which was taken after irradiation to a cumulative dose of 142.9 Gy (refer Figure 6.4). Furthermore, the increase in the current signal generated is greater at low bias voltages (between 0 to -90 V) in comparison to higher bias voltage range (between -100 V to -150 V) as shown by the data in Figure 6.2. The current signal for a dose rate of 52.9 Gy/min increases from 3 to 11 nA/mm² for bias voltages between 0 to -90 V, whilst, a smaller increment can be observed for high bias voltages which is from 11 to 15 nA/mm². This can be explained from the influence of the leakage current which is more dominant when a high bias voltage is applied, since the current generated during the exposure to radiation is subtracted from the dark current (between 1.58 nA/mm² to 76.1 nA/mm² for bias voltages between -100 V to -200 V). When the high bias voltage is applied, the depletion region widens resulting in a higher leakage current density, where J_L is directly proportional to the depletion width, W_d ($J_L \propto W_d$) as described by Equation 4.6. This relationship can be supported by the data in Figure 6.4 where the leakage current density rises significantly for applied bias greater than -90 V, which leads to deterioration of the extracted current signal as shown by the data in Figure 6.2.

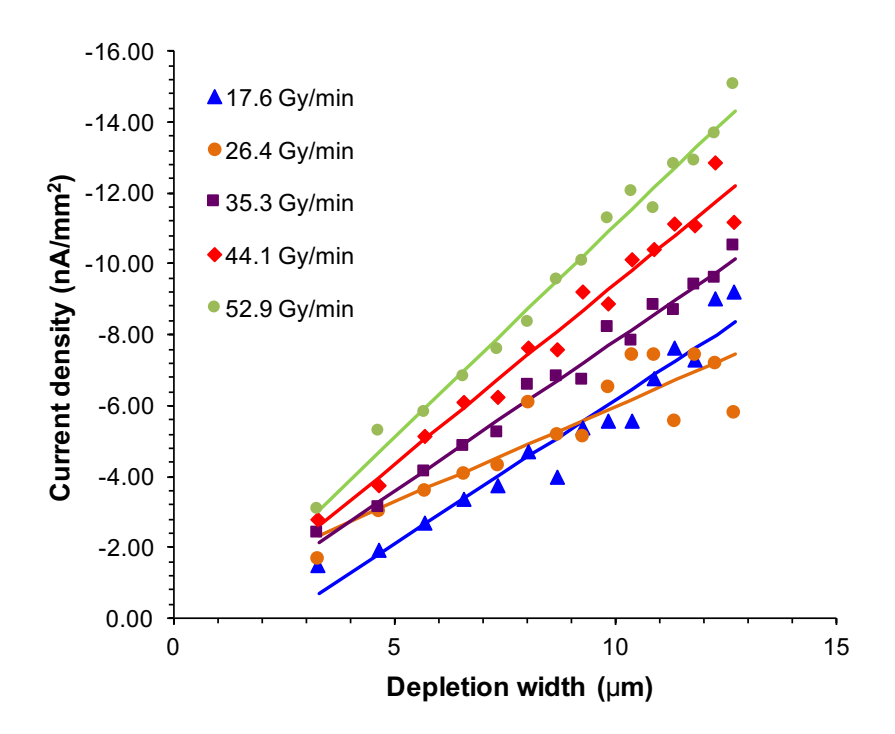


Figure 6.3: Current signal generated as a function of depletion width (W_d) from irradiation between 17.6 to 52.9 Gy/min of 6 MV photons.

As can be observed from the data in Figure 6.5, detector D2 exhibited low reverse leakage current densities, typically 1.66 nA/cm² for a reverse bias of -100 V after irradiation to 1000 Gy. This is a factor of 10⁴ lower than the results reported by Roccaforte et al. [181] and comparable to those reported in [108], respectively for Si^{+4} ion with different fluence between 1 \times 10⁹ and 1 \times 10¹² ions/cm² and 40 Mrad of gamma (⁶⁰Co source) irradiation. Additionally, the non-irradiated (0 Gy) data demonstrate higher leakage current densities (the highest being around 76.1 nA/cm² at -200 V) that are four times greater than the irradiated data. The leakage current density decreases after irradiation to different cumulative dose, in comparison to the initial leakage current density of the non-irradiated data. A slight decrease in the leakage current density data can be linked to an increase in the extracted barrier heights after irradiation to 285.7 Gy and slight increase in the specific on resistance after irradiation to 47.6 Gy, which will be discussed in the following subsection. Nonetheless, despite the slight decrease of the leakage current density after the first exposure to a cumulative dose of 47.6 Gy, the data demonstrate almost constant value of leakage current density after irradiation to 476.2 Gy up to a maximum of 1000 Gy, as can be observed by the plots in Figure 6.5 for -100 V, -150 V and -200 V. The decrease in the reverse leakage current after irradiation is not consistent with the study performed by Bertuccio et al. for moderate dose rate (0.5 to 10 Gy) measurements [21], however, it shows a similar trend to the data published by both Roccaforte et al. and Nava et al. for 1×10^9 to 1×10^{12} ions/cm² of Si $^{+4}$ ion irradiation [181], 20 and 40 Mrad of 8.2 MeV electron and 9.37×10^{13} of 24 GeV/c proton [108], respectively.

To investigate the sensitivity of the detector response to different dose rates, the slope of the fitted line from of the current generated as a function of dose rate was extracted from the data plotted in Figure 6.2. The extracted gradient are plotted as a function of bias voltage along with the low dose rate response to 35 kV X–ray as shown by the data in Figure 6.6. From the data, it can be observed that the dose rate linearity for both low and high dose rate increases linearly with increasing bias voltage. However, for 6 MV photon exposure, there is a slight reduction of the dose rate linearity with bias above -110 V that may be correlated with the higher leakage current, which results in a reduction of the current generated. This condition may be attributed to two different trends in the dose rate linearity, where the first is for bias voltage between -10 V to -100 V and the second is from -110 V to -150 V with dose rate linearity in the range of 0.051 to 0.215 nA.min/Gy.mm² and 0.207 to 0.25 nA.min/Gy.mm², respectively. The difference in the dose rate linearity data also show a small increase in the high bias voltage range (from -80 V to -150 V) in comparison to the low bias voltage data. This proves that the leakage current influences the performance and responsivity of detector, resulting in the deterioration of the sensitivity to radiation.

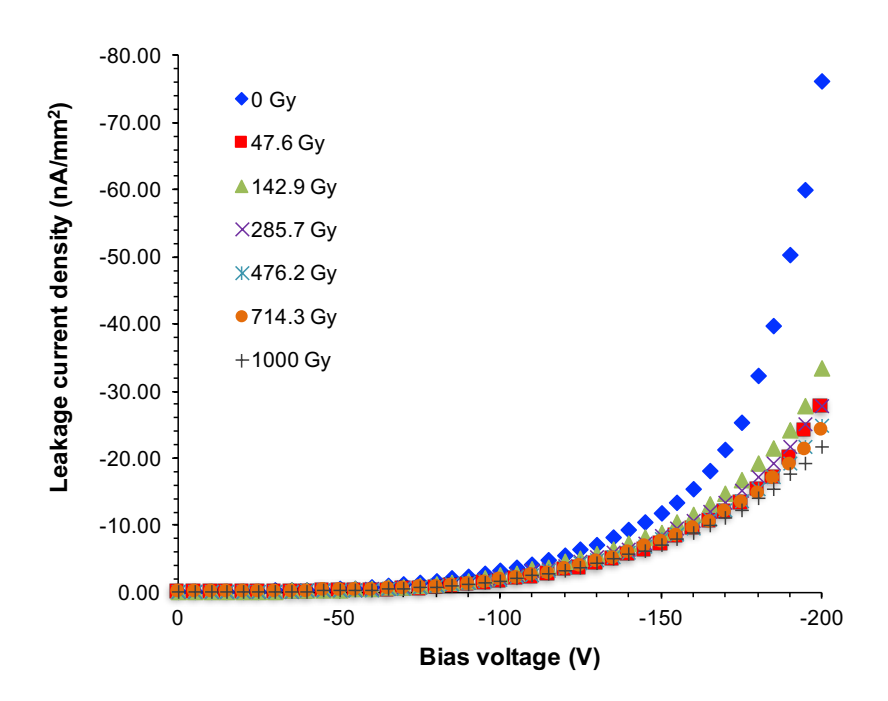


Figure 6.4: Leakage current density from irradiation between 47.6 to 1000 Gy cumulative dose of 6 MV photons with increasing bias voltages.

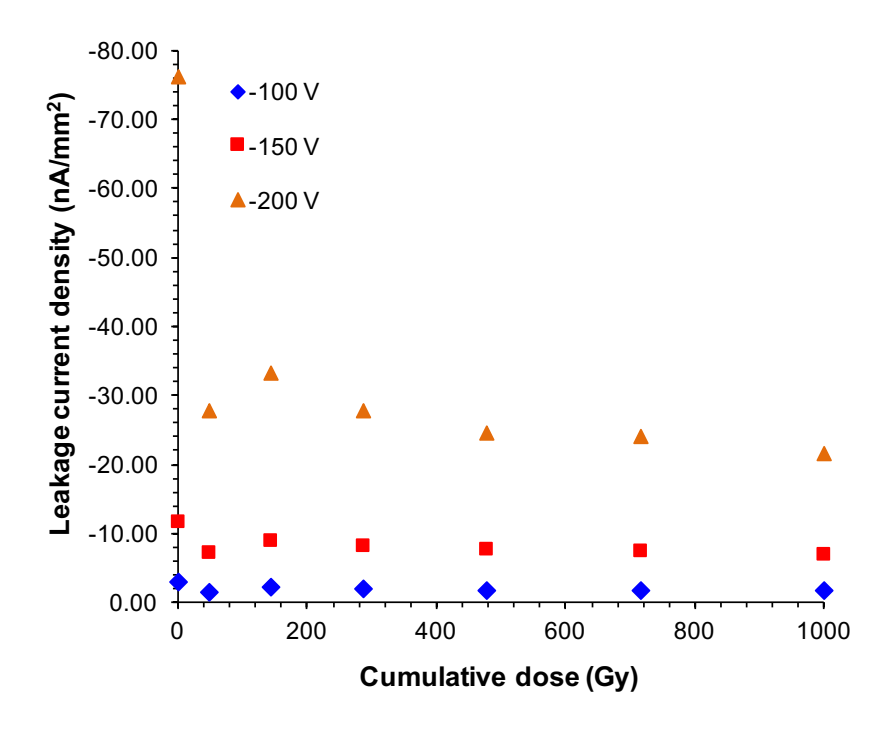


Figure 6.5: Leakage current density with increasing cumulative dose from 47.6 up to 1000 Gy of 6 MV photons at bias voltages between -100 V to -200 V.

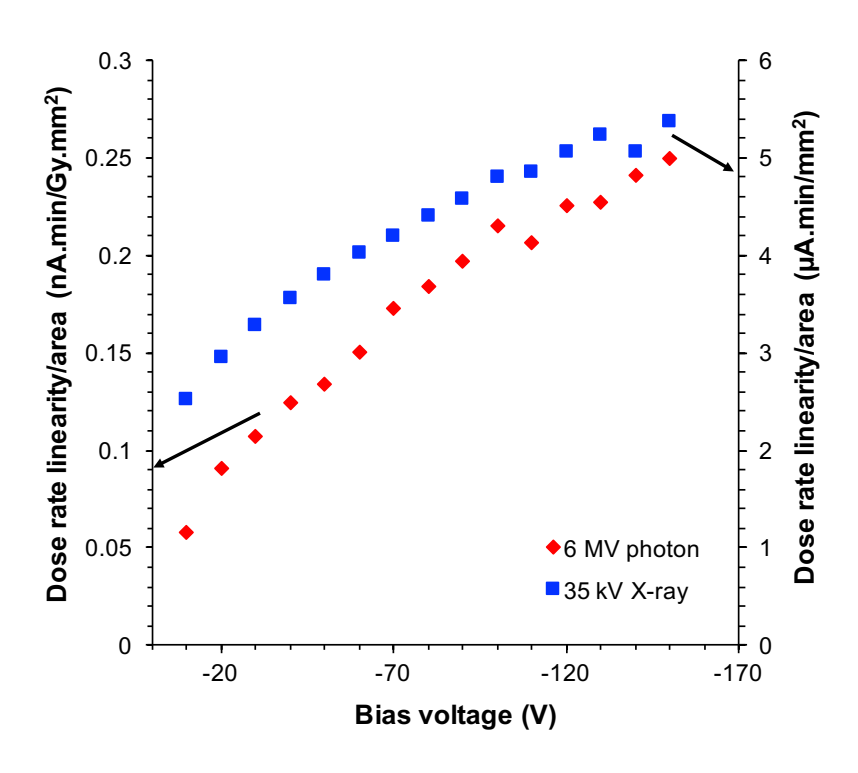


Figure 6.6: Dose rate linearity from low and high dose rate irradiation respectively between 0.020 to 0.185 mGy/min of 35 kV X-ray and 8.8 to 52.9 Gy/min of 6 MV photons at different bias voltages.

The data for high dose rate response produced by exposure to 6 MV photons demonstrates a linearity of 0.13 nA.min/Gy.mm² and 0.25 nA.min/Gy.mm² at respective applied bias of -50 V and -150 V, which are more than two times higher than the values reported in the literature previously, of 0.06 $nA.min/Gy.mm^2$ ($V_{SiC9} = -50 \text{ V}$) and 0.11 $nA.min/Gy.mm^2$ ($V_{SiC13} = -150 \text{ V}$) [149]. On the other hand, the dose rate linearity for high dose rate irradiation (6 MV photons) also exhibit a lower dose response in comparison to the 35 kV X-ray irradiation as can be observed by the data in Figure 6.6. This shows the ability of detector D2 to respond to very low dose rate exposure (in the range of 0.105 mGy/min to 0.185 mGy/min) with a higher sensitivity rather than high dose rate irradiation. This can be explained from the different energies of the radiation used (35 kV and 6 MV) and the dominant interaction takes place during irradiation, which contribute to different quantum detection efficiency and hence values of the generated current. Quantum efficiency can be define as the ratio of the number of carriers collected by the detector to the number of photons of a given energy incident on the detector as shown by the data published previously in Figure 6.7 [182]. The different energies of the incident radiation results in different penetrating depths and absorption mechanisms of the beam inside the active volume of the detector as described in details in section 2.4.1. The penetration depth can be defined as the depth required to stop a fraction of radiation passing through the object and it is inversely proportional to the quantum detection efficiency (refer to Figure 6.7). The penetration depth is governed by the energy of the individual photons, the atomic number, density and thickness of the object [47]. Increasing the photon energy increases the penetrating ability due to the decrease in the probability of interaction, and hence resulted in less photons detected in the detector active region.

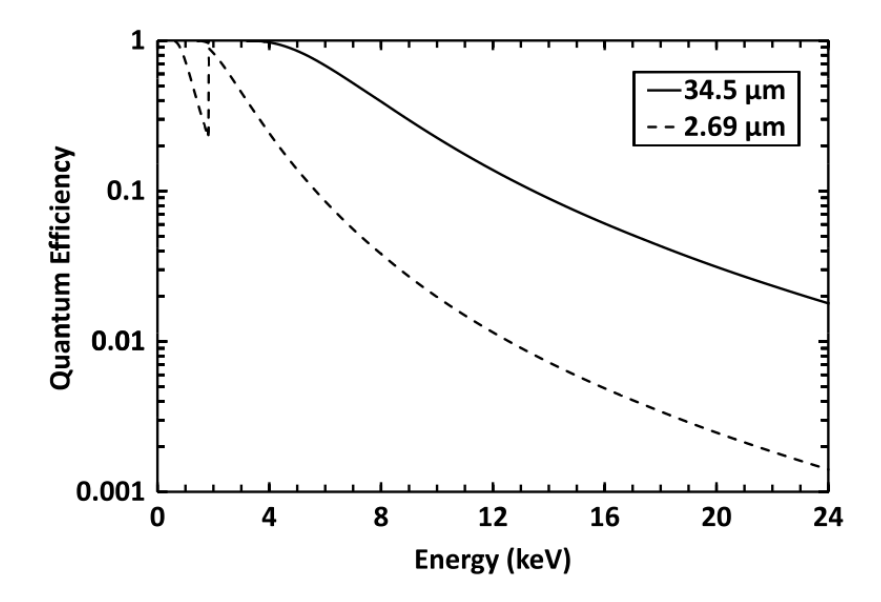


Figure 6.7: Plots of the calculated quantum detection efficiencies of the 0.06 mm² SiC photodiode based on two different thicknesses of active layer (2.69 μ m, dashed line; 34.5 μ m, solid line) as a function of X–ray energy. The discontinuity at 1.8 keV is the Si K absorption edge.^[182]

The low energy radiation (35 kV X–ray) that has been used to produce low dose rate, resulted in the dominant radiation attributed from the photoelectric effect, which is the dominant mechanism that contribute to the higher detection efficiency as described in sections 2.4 and 4.4. During photoelectric absorption interaction, the incident photon transfers all of its energy to the detection medium which resulted in the photon being completely absorbed in the active region of the detector, and therefore increasing the detection efficiency. Whilst, the dominant radiation interaction for the high dose rate (6 MV photons) is the Compton effect as can be observed from Figure 2.9 in section 2.4.2. Compton interaction is the scattering of incoming photons, which is deflected through an angle, θ with respect to its original direction. The incident photons will transfer part of its energy to the scattered electron, which results in a decrease in energy of the incident photon and contribute to a different value of number of photons being absorbed in the detector. Therefore, from these hypothesises, direct comparison between both measurements is not relevant. However, it can be suggested that the responsivity of the same detector (D2) to different dose rate ranges depend on modes of interaction and absorption mechanisms, that resulted in distinct values of dose rate linearity as can be observed from the data presented in Figure 6.6.

6.3 Effect of high-energy photon irradiation on the electrical characteristics

Knowledge of the effects of irradiation on the material properties of the detector and the resulting modifications to the electrical characteristics of Schottky barriers is imperative for gaining a full understanding of the radiation hardness [181]. Changes in the electrical characteristics of the detector were observed and compared with the non-irradiated data for each exposure in order to study the radiation hardness of the detector. The specific on resistance, ideality factor (n), and barrier height (Φ_h) were extracted from the I–V characteristics after each dose rate irradiation using Cheung's method. In addition, C-V measurements were performed to study the extracted doping concentration and depletion width before and after irradiation with a maximum cumulative dose of 1000 Gy. A high quality detector will show a minor shift after exposure to high energy radiation. Plots of the I–V characteristics shown in Figure 6.8 demonstrate high linear behaviour in the Ohmic region with no significant shift for all the cumulative doses investigated. The slope for the ideality factor can be observed to be independent on the irradiation, which indicate that the thermionic emission is the most significant contribution to the current across the barrier of the Schottky diode detector. This suggests that the high energy irradiation did not significantly change the material properties of the detector and the result found to be the same with the data published by Nava et al. for 20 and 40 Mrad electron and gamma-ray irradiation of 4H-SiC Schottky diode [108]. The extracted values of the specific on resistance, ideality factor and barrier height will be discussed in more detail in the following sections.

6.3.1 Specific on resistance, R_{on}

From the data plotted in Figure 6.8, it can be observed that there is no significant shift in the I–V characteristics in the high bias range, where series resistance is dominates. This indicates that exposure to high energy radiation did not significantly affect the specific on resistance of the detector. The data in Figure 6.9 show the calculated specific on resistances (R_1 and R_2) extracted from the I–V characteristics expose to different cumulative doses between 47.6 to 1000 Gy. The values of R_{on} extracted from the two different steps in Cheung's method demonstrate an increase of 5 % with cumulative dose, from (2.22 ± 0.13) $\times 10^{-2}$ to (2.41 ± 0.50) $\times 10^{-2}$ Ω .cm² for R_1 and (2.60 ± 0.03) $\times 10^{-2}$ to (3.29 ± 0.21) $\times 10^{-2}$ Ω .cm² for R_2 . The small increment in the specific on resistances can be observed after first exposure to 47.6 Gy cumulative dose. However, after that first exposure, the variation in the specific on resistances are almost insignificant with increasing cumulative dose for both R_1 and R_2 .

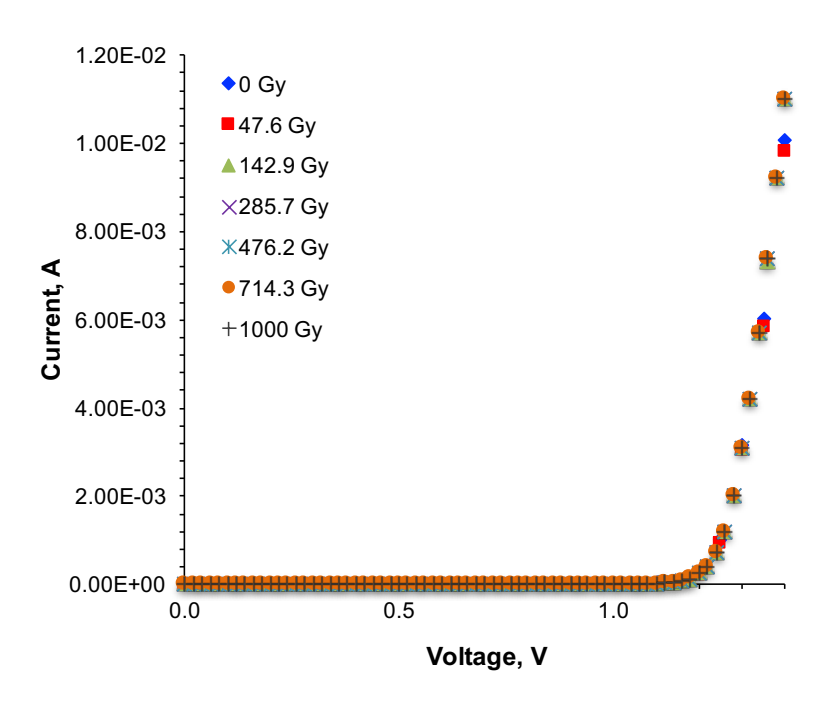


Figure 6.8: Current–voltage (I–V) characteristics of detector D2 before and after each irradiation of cumulative dose between 47.6 to 1000 Gy.

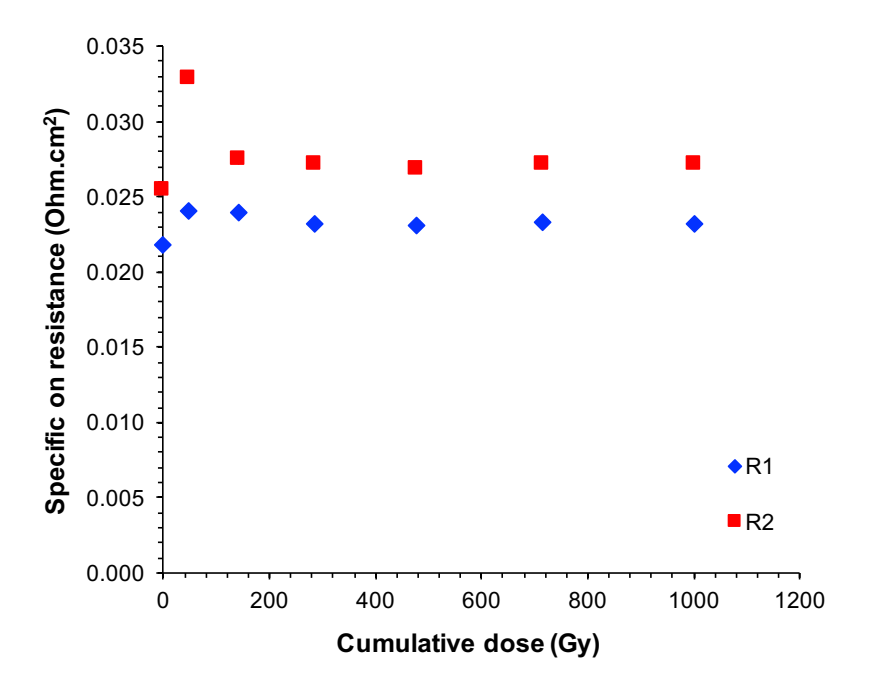


Figure 6.9: Specific on resistances (Ω .cm²); R_1 and R_2 for detector D2 before and after exposure to cumulative dose between 47.6 to 1000 Gy. The error bars which represent the standard deviation of the data are smaller than the bullet points.

The observed increase in the specific on resistance, R_{on} (after the first exposure) is similar to that observed by Roccaforte *et al.* for Si⁺⁴ ion irradiation in Ti/4H–SiC [181]. They suggested that the increase in the semiconductor resistivity arises from the ion–irradiation–induced damage, that leads to a decrease of the dopant concentration (N_D) and/or to a decrease in the carrier mobility, μ [181]. The lower carrier mobility is thought to be linked to the degradation of charge collection efficiency, which is governed by the $\mu\tau$ product as described in section 3.2. Despite, there is difficulty in measuring the lifetime from the open–circuit voltage decay technique in order to extract the mobility, due to the technical problem of the circuit system that produced very small resistance value. Deep level impurities can be linked to a formation of recombination centers located under the Schottky contact, which led to the increase in resistivity and decrease in the conductivity [42, 108]. However, the insignificant increase that can be observed in the specific on resistance after irradiation between 142.9 Gy to a maximum cumulative dose of 1000 Gy, predicted that there is negligible amount of deep level impurities formed from the exposure to high energy photon in the active region of the detector. This signifies a valuable insights on the considerable radiation tolerance of the fabricated detector.

6.3.2 Ideality factor, n and Schottky barrier height, Φ_b

As described in section 3.3.3, the ideality factor of a diode should be in the range between 1 and 2, depending on the dominant current mechanism and it will be more than 1 if the current is influenced by generation recombination mechanisms [127]. A high barrier height is necessary to minimise the current under reverse bias conditions and hence increase the signal–to–noise ratio when operated as a radiation detector. This suggests that the Schottky barrier height value plays an important role in determining the leakage current density. In this section, the extracted values of ideality factor and barrier height were plotted as a function of cumulative dose (Gy) as shown by the data in Figure 6.10. The data show that the ideality factor values demonstrate almost insignificant variation with increasing cumulative dose up to a maximum cumulative dose of 1000 Gy, which is between 1.070 \pm 0.004 to 1.040 \pm 0.014. Whilst, barrier height values increase slightly with increasing cumulative dose, which is in the range of 1.670 \pm 0.001 eV to 1.720 \pm 0.003 eV. The deviation of the ideality factor and barrier height of detector D2 are exceptionally noticeable at 47.6 Gy cumulative dose, which act as outliers to the presented data. This can be correlated with the significant increase of both specific on resistance values (R₁ and R₂) after the first exposure, which is described previously. The high specific on resistance of the diode attributed to the deviation of forward bias I–V characteristics

of the Schottky diode from that predicted by the thermionic emission model [121], that resulted in less accuracy of the extracted barrier height and ideality factor [122].

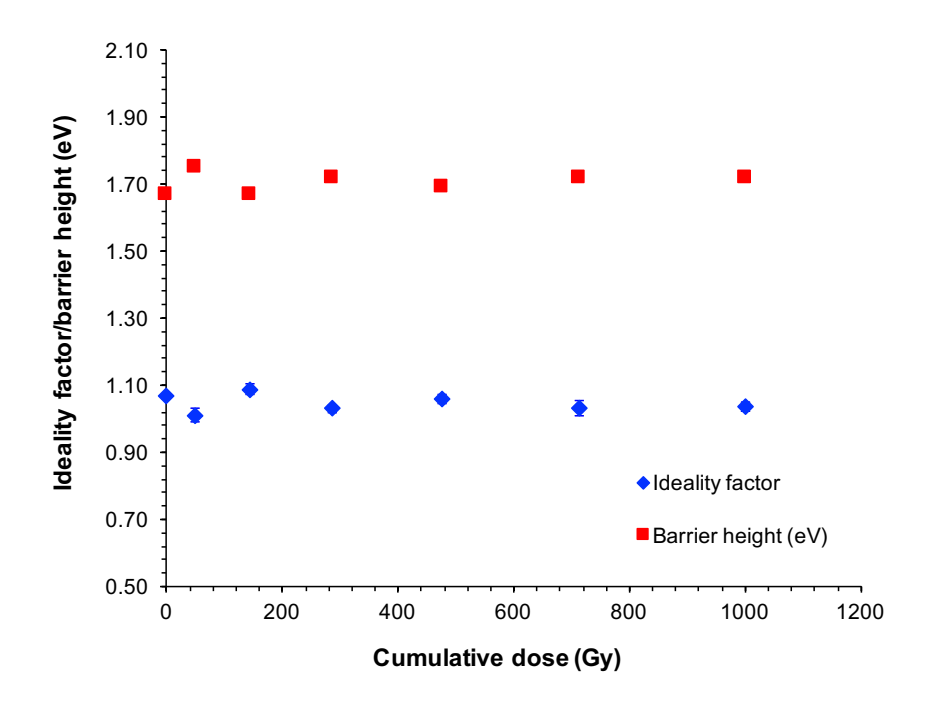


Figure 6.10: Ideality factor and barrier height (eV) for detector D2 before and after each exposure to cumulative dose between 47.6 to 1000 Gy. The error bars which represent the standard deviation of the data are smaller than the bullet points.

As discussed in section 3.3.5, any defects formed inside the detector are expected to behave as recombination centers or as intermediate states for trap–assisted tunnel currents, which lead to an increase in the ideality factor [42]. However, for the case here, it is observed to contradict this hypothesis, suggesting that the presence of donor–like traps leads to the degradation of electrical performance in terms of the ideality factor and barrier height in SiC Schottky diodes [42, 116]. Nonetheless, the insignificant variation in the ideality factor and slight increase in the barrier height values after irradiation, can supported an argument that there is improvement in the electrical characteristics. The data presented here also in good agreement with the findings published in [108], after irradiation of 4H–SiC Schottky diode with 8.2 MeV electron and 24 GeV/c protons. The increase of barrier height results in significant decrease in the leakage current [181], as can be clearly observed from the data in Figure 6.4. This also can be supported by Equations 3.13 and 3.14, where increasing the barrier height is linked to a decrease in the magnitude of image force lowering, which can be explained by the observed decrease in the reverse leakage current density. Additionally, the slight increase in the barrier height of the irradiated data is consistent with data published previously [181, 183]. This is linked to the Schottky interface modification after Si⁺⁴ ion [181] and proton

irradiation [183]. The observation from those reports also are in good agreement with the hypothesis from Tung who correlated the increase in the barrier height with the presence of charged deep levels in the energy gap [184]. However, the assumption of almost negligible concentration of defect presents as stated in section 6.3.1 previously, can be strongly supported by the presented data in this section, where there are almost constant values of the ideality factor and barrier height with increasing cumulative dose.

6.3.3 *C–V measurements at room temperature*

To extract the dopant concentration (N_D) and depletion width (W_d) of detector D2, C-V measurements have been performed at 100 kHz before and after irradiation to a maximum cumulative dose of 1000 Gy. Figure 6.11 shows a linear trend between the reciprocal of the squared capacitance and bias voltage, along with the fitted line of best fit over the voltage range 0 – -30 V. The non-irradiated and irradiated data demonstrate the expected reciprocal relationship between the capacitance and bias voltage, where the capacitance decreases with increasing reverse bias voltage. The dopant concentration value before irradiation to 6 MV photons was extracted from the plot in Figure 6.11 and directly compared with the extracted dopant concentration value after irradiation. The gradient from both plots at typically low bias voltage (less than -10 V) give a dopant concentration of $N_D(W) = 1.12 \times 10^{15}$ cm⁻³ and 1.24×10^{15} cm⁻³, respectively for non-irradiated and irradiated data. Almost consistent values of extracted dopant concentration for the non-irradiated and irradiated is though to be linked to the insignificant variation of the specific on resistance with increasing cumulative dose as described in section 6.3.1.

However, a significant shift in the capacitance and hence X-intercept is observed between these plots at high bias voltage (-10 V - -30 V), which relate to a dopant concentration of 1.40×10^{15} cm⁻³ for the irradiated data. The discrepancies in the extracted dopant concentration before and after irradiation within these range, may be attributed to the non-uniform of the dopant concentration across the vertical structure in the detector active region. The difference in the dopant concentration can be assumed that those different regions governed by the dopant concentration which are the active region close to the surface (immediately under the Schottky contact) and region generates by the built–in potential. The electrically active defects can behave as acceptor or donor levels, which regulate the effective doping concentration, and therefore the depletion width [161]. Traprecombination which also known as generation–recombination as described in section 2.9.2 can be related to this defect. The increase in the doping concentration after high dose irradiation was contradict with the data found by Nava *et al.* [108] and Roccaforte *et al.* [181], which believed that

the defect centres can reduce the effective doping by the compensation of the nitrogen donors and consequently the base conductivity at room temperature.

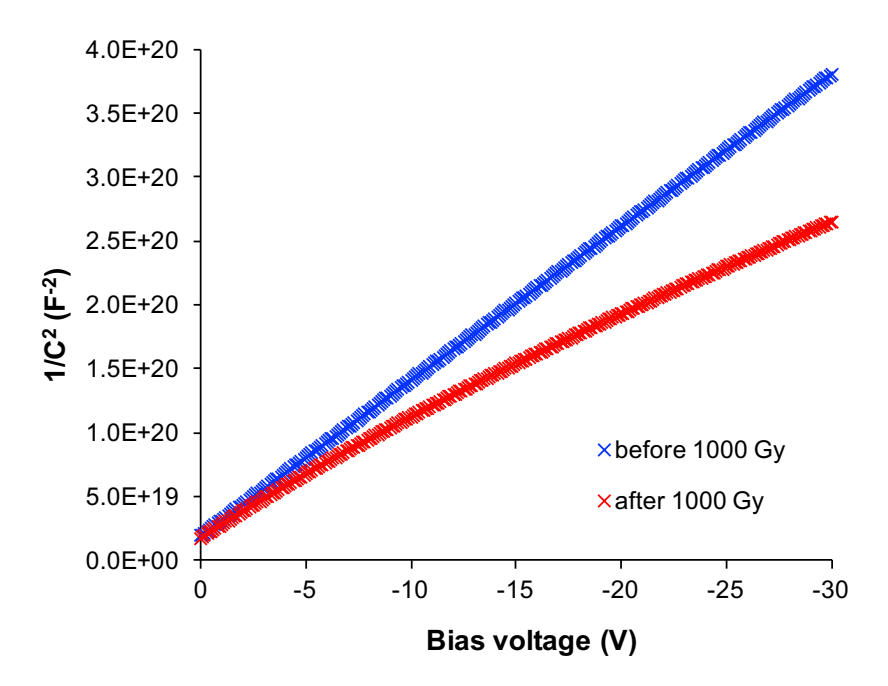


Figure 6.11: $1/C^2$ plotted against bias voltage for detector D2, slope from the graph was used to extracted doping concentration, N_D values before and after irradiation to 6 MV photons with 1000 Gy maximum cumulative dose.

Other than the calculated depletion width explained in section 6.2.2, measurement of the capacitance value allows the extraction of the depletion width. The extracted depletion width of detector D2 for non-irradiated and irradiated were determined using Equation 3.15 in section 3.4.1 and are plotted as a function of bias voltage in Figure 6.12. Based on the calculated dopant concentration, the depletion width for non-irradiated and irradiated were almost comparable at bias voltages less than -5 V, which are within the range of 1.33 to 2.77 μ m. The decrease in the $d(1/C^2)/dV$ value and hence, dopant concentration N_D for irradiated data at bias voltages more than -5 V, resulted in 17 % decrease in the depletion width. This result found not to be consistent with the increase in the barrier height presented in section 6.3.2, since barrier thickness depends on the electrical active doping N_D through the depletion width [181]. The decrease in the depletion width would lead to deterioration of the detection efficiency of a radiation detector due to the lower volume of space region for the radiation to interact and then detected. Therefore, other than leakage current as described in previous section 6.2.2, decrease in the depletion width will resulted in degradation of the current signal generated as can be observed by the data in Figures 6.2 and 6.3. In order to achieve a high quantum efficiency, the detector needs a wide depletion region where 100% of the incident

energy is stopped, which depends on the number of electron hole–pairs generated per incident photon [44].

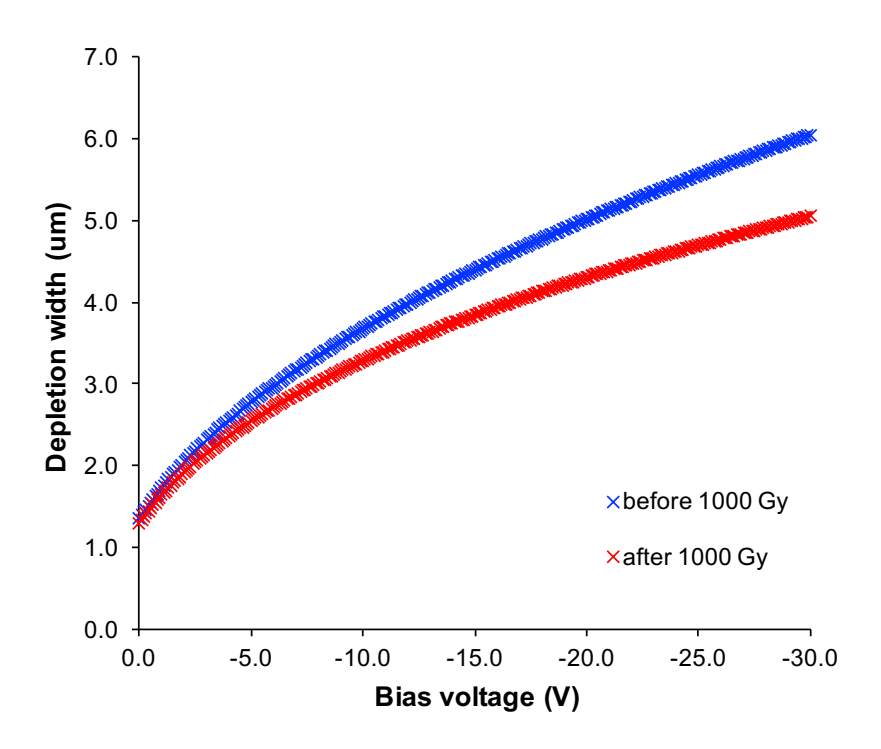


Figure 6.12: Depletion width, W_d plotted against bias voltage before and after irradiation to 6 MV photons with 1000 Gy maximum cumulative dose.

6.4 Radiation tolerance of X-ray photon energy harvester in high radiation dose environments

Detectors that are able to sustain radiation damage arising from higher energy ions and scavenge the radiation energy into electricity would be very beneficial [153]. This includes application in the nuclear power plants waste storage that converting the waste from X-ray and γ -ray radiation, volcanic emission monitoring, closed loop control of combustion processes and long term nuclear installation monitoring, which needs a system that able to remotely monitor the radiation dose in extreme environments [185]. Therefore, designing and fabricating devices which take into account the degradation effect due to radiation induced damage is an important factor to prolong the life of the batteries and electronic circuits that is connected to it [186]. Liu *et al.* had reported the radiation-damage resistance property of silicon Schottky diodes for use as beta-voltaic batteries [186]. However, there is no reported data related to the radiation tolerance of SiC Schottky diodes for energy scavenging in X-ray environments. The capability of the fabricated 4H–SiC Schottky diode

detector to be self-powered in extreme environments was presented in section 5.5. In this section, the effect of high energy photon irradiation on the characteristic parameters of detector D2 as an X-ray photon energy harvester has been investigated. The same experimental procedure as described in section 5.4 has been followed. The characteristic parameters and current generated before and after irradiation to a maximum cumulative dose of 1000 Gy were compared and presented by the plots in Figure 6.13. Both plots show similar current generated at low voltages, however, the open circuit voltage was lower after irradiation by approximately 0.1 V.

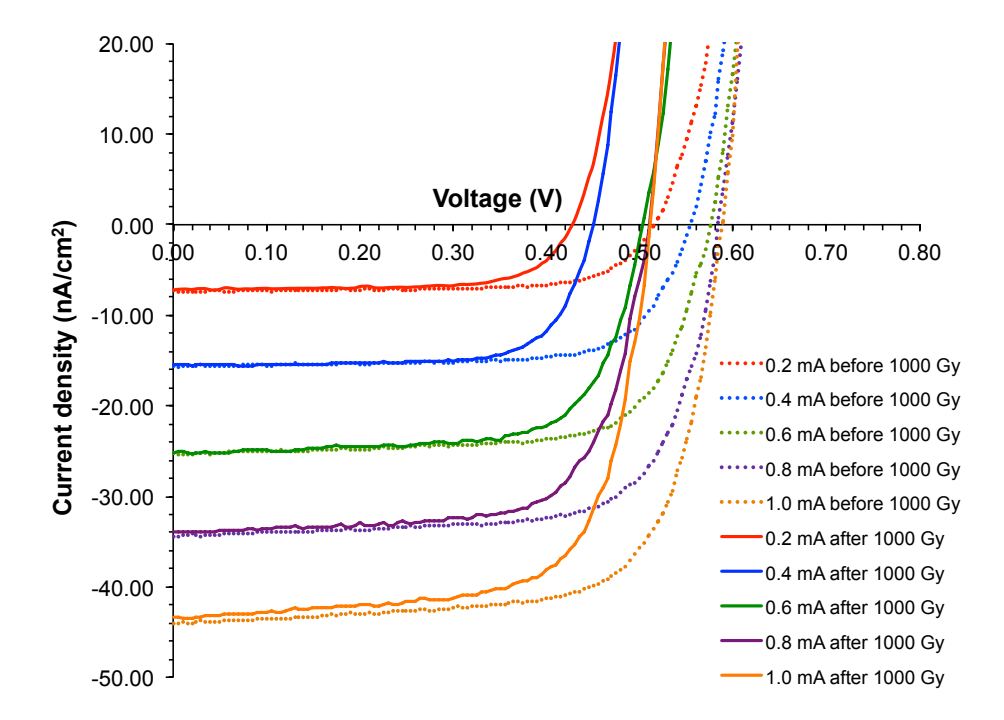


Figure 6.13: Current–voltage characteristics of detector D2 after illumination with 35 kV X–ray and increasing dose rate between 0.043 and 0.185 mGy/min for before and after irradiation to 1000 Gy cumulative dose.

6.4.1 Short circuit current density, J_{SC}

From the curves plotted in the Figure 6.13, it can be observed that there is no degradation of the short circuit current density after irradiation in comparison to the non-irradiated data. The comparison of both short circuit current density before and after irradiation are presented by the data in Figure 6.14. As expected from the Equations 5.4 and 5.5, extracted values of J_{SC} that are governed by the production rate of electron-hole pair, N_e are unchanged after irradiation to high dose rate of 52.9 Gy/min, with values between 7.15 to 43.4 nA/cm². This finding proved that the production rate of electron-hole pair inside the detector D2 depletion region is unaffected by exposure to the 6 MV

photon beam. This also indicates that there is no recombination losses produced due to the high energy radiation that will lead to a reduction in the number of electron–hole pairs created. This condition can be correlated with the hypothesis made for the electrical characteristics data, which are described in sections 6.3.1 and 6.3.2, where the assumption of insignificance variation in the specific on resistance, ideality factor and barrier height leads to a negligible concentration of defects present due to trapping site, and hence constant amount of charge carriers generated from the interaction with incident radiation.

The results presented here are consistent with the finding for Si Schottky diode beta–voltaic battery after irradiation to a maximum total fluence of a 1.9×10^{11} α/cm^2 alpha particles from ²⁴¹Am [186]. Their finding proved the higher radiation resistance of Schottky diodes in comparison to p-n junction structures with minimal degradation in the short circuit current density, is due to the large intrinsic I_0 of the Schottky diode in comparison to the p-n junction [186].

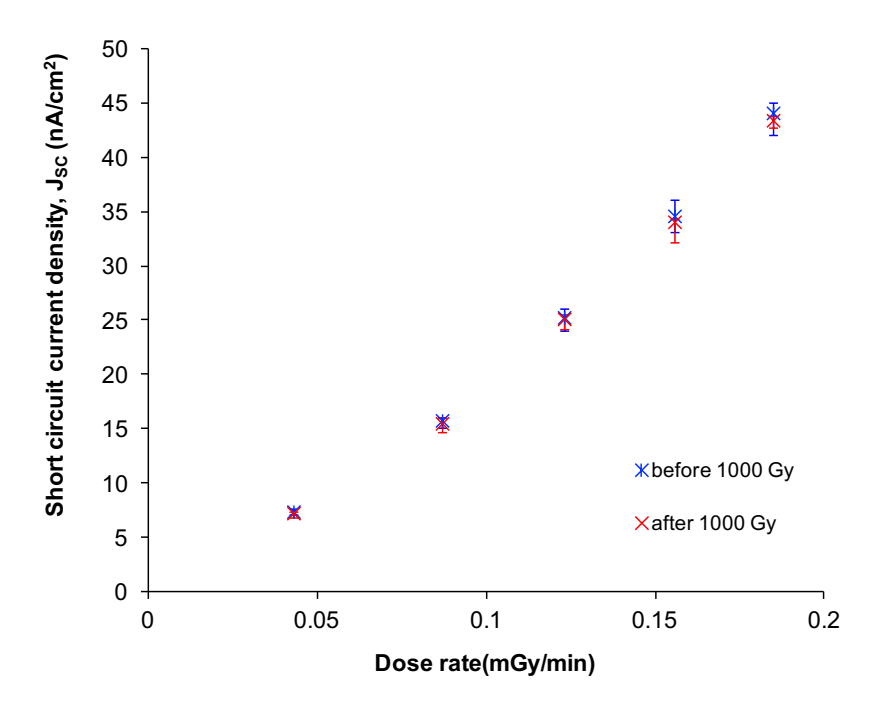


Figure 6.14: Short circuit current density (J_{SC}) for detector D2 as a function of dose rate before and after irradiation to 6 MV photon. The error bars represent the standard deviation of the data.

6.4.2 Open circuit voltage, V_{OC}

As shown by the data in Figure 6.13, it can be observed that the open circuit voltage (V_{OC}) after irradiation is slightly reduced in comparison to the data for non-irradiated data. The % difference between the open circuit voltage values as demonstrated by the data in Figure 6.15 have decreased by

less than 20% after irradiation to 1000 Gy cumulative dose. The decrease in the open circuit voltage can be correlated with the changes in the electrical properties presented previously in section 6.3. Reduction in the ideality factor as presented in section 6.3.2 may be one of the factor that contributes to the lower value of the open circuit voltage. This can be proved from the correlation of the open circuit voltage with the ideality factor as expressed in Equation 5.6 in section 5.4.2. Other than that, the increase in the saturation current density from 4×10^{-18} A.cm⁻² to 2×10^{-16} A.cm⁻² after irradiation resulted in lower open circuit voltage, due to the dependance of the open circuit voltage on the saturation current as predicted by Equation 5.6.

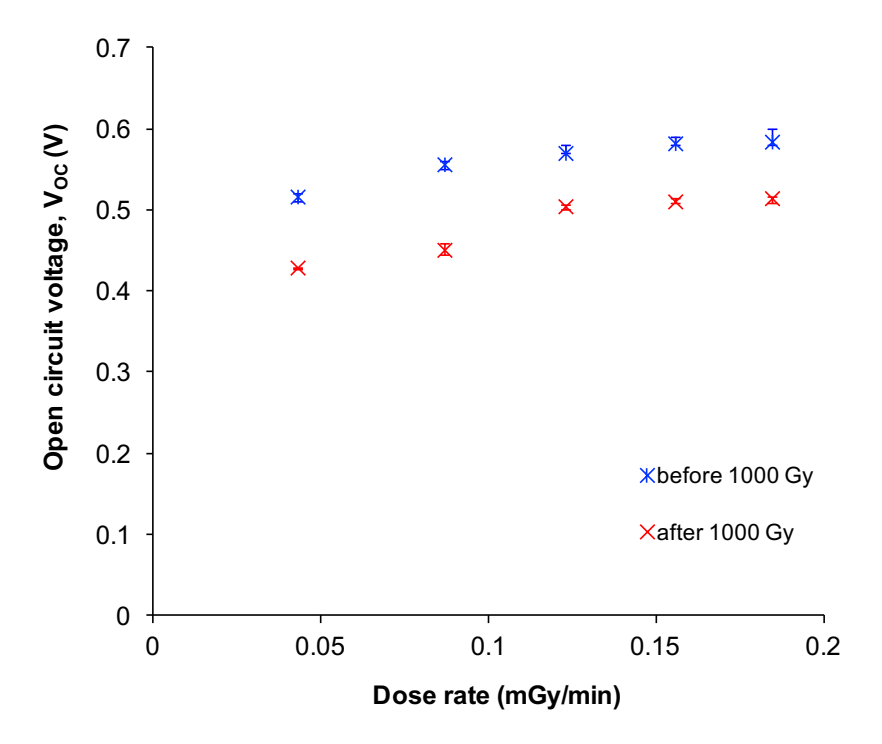


Figure 6.15: Open circuit voltage (V_{OC}) for detector D2 as a function of dose rate before and after irradiation to 6 MV photon. The error bars represent the standard deviation of the data.

This finding is identical to the previously published data of p-n and Schottky barrier diode beta voltaic battery after exposure to 241 Am alpha source of $1.95 \times 10^{11} \ \alpha/\text{cm}^2$ [186]. They suggested that irradiation to low energy particle and heavy ions of 241 Am contribute to the generation of defects on the surface and interface, which increases the recombination of electron-hole pairs, and resulted in an increased of the saturation current, I_0 [186]. However, this argument contradict to our case here as there is increment in the dopant concentration, N_D . The observed increase in the saturation current is not in agreement with the increase in the barrier height, which is linked to a decrease in the magnitude of image force lowering, and hence an expected decrease in the reverse leakage current after irradiation as described respectively in sections 6.3.2 and 6.2.2. The degradation in the open

circuit voltage still remains under the threshold value, where the threshold for noticeable degradation is defined as the amount of fluence that lead to 75% reduction in the open circuit voltage of the battery to that of the original value [186].

6.4.3 Peak power density, P_{OUT}

As expected from the short circuit current and open circuit voltage data presented in sections 6.5.1 and 6.5.2, the peak power density decreases slightly after irradiation, due to the decrease in the open circuit voltage. This can be explained from the dependance of the peak power density on short circuit current and open circuit voltage than can be extracted from the forward bias I–V plot. The peak power density was observed to decrease approximately 21% after irradiation. However, the irradiated data present similar trend of the peak power density with the non–irradiated data where it increases with increasing dose rate which are within the range of 2.15 to 15.4 nW/cm² as shown in Figure 6.16. This demonstrates that high energy irradiation did not cause a significant detrimental effect on the power output of the detector as minimal degradation observed. Liu *et al.* suggested that the radiation–induced damage in the detector including the displacement defects is the main factor affecting the output performance in energy conversion device of a battery [186]. The minimal degradation of the peak power density of the detector to high energy photon irradiation found to be consistent with SiC p–i–n junction beta–voltaic that is irradiated over a period of four half–lives (over a 3+ month) of 8.5 GBq 33 P [154].

6.4.4 Fill factor, FF

The fill factor is related to the maximum extractable power from the diode to the product of the short circuit current and open circuit voltage, hence the decrease in peak power density and open circuit voltage will affect the extracted fill factor values. Data shown in Figure 6.17 are the fill factor values for non–irradiated and irradiated data. The data show that the fill factor demonstrate almost constant values of fill factor for the irradiated data to that of non–irradiated data with only a 2.8% difference. However, the extracted fill factor values after irradiation to a maximum cumulative dose of 1000 Gy are still > 0.7, which is within 0.690 ± 0.001 to 0.730 ± 0.007 , to be a high grade photon energy harvester [66]. The minimal degradation in the efficiency which convert X–ray into electrical current indicates that there is possible application of the detector to scavenge energy in radiation–rich environments such as in outer space or nuclear power plants as proposed previously [185]. This

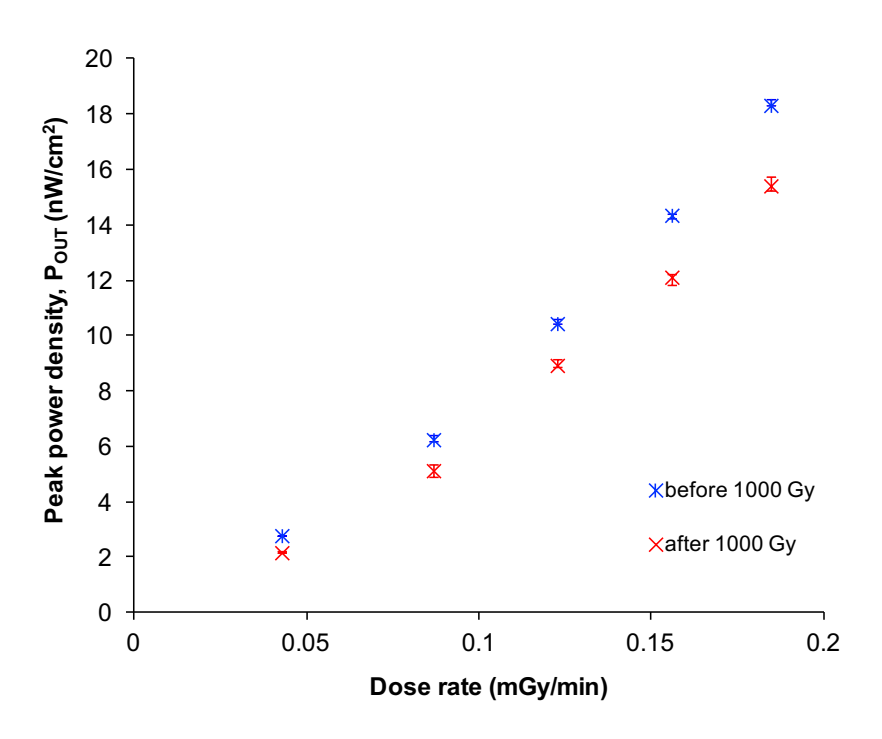


Figure 6.16: Peak power density (P_{OUT}) for detector D2 as a function of dose rate before and after irradiation to 6 MV photon. The error bars represent the standard deviation of the data.

finding propose the ability to sustain high radiation dose without significant performance loss with high stability in a range of challenging environments from nuclear decommissioning to beam line monitoring in radiotherapy.

6.5 Low frequency noise (LFN) before and after irradiation at elevated temperatures up to 100 $^{\circ}\text{C}$

To study the behaviour of impurities and the generation of defects generated resulting from exposure to the 6 MV photon beam, low frequency noise was measured after irradiation of the detector to a maximum cumulative dose of 1000 Gy. The same experimental set up as described in section 5.3 was used. In this section, the behaviour of current dependance of noise spectral density, S_I before and after irradiation at room temperature up to 100 °C has been investigated. The dependance of noise density with current, S_I at different measurement temperatures before and after irradiation can be shown by the data in Figure 6.18. Figure 6.18 (a) demonstrates the dependance of noise density for non–irradiated data on the current through the detector, and this decreases with increasing measurement temperature. A similar trend showing a decrease in the dependance of noise density as a function of temperature has been observed in studies published previously for 4H–SiC [81] and Ni/n–GaN Schottky barrier diodes [82]. Güttler and Werner related this behaviour to the existence

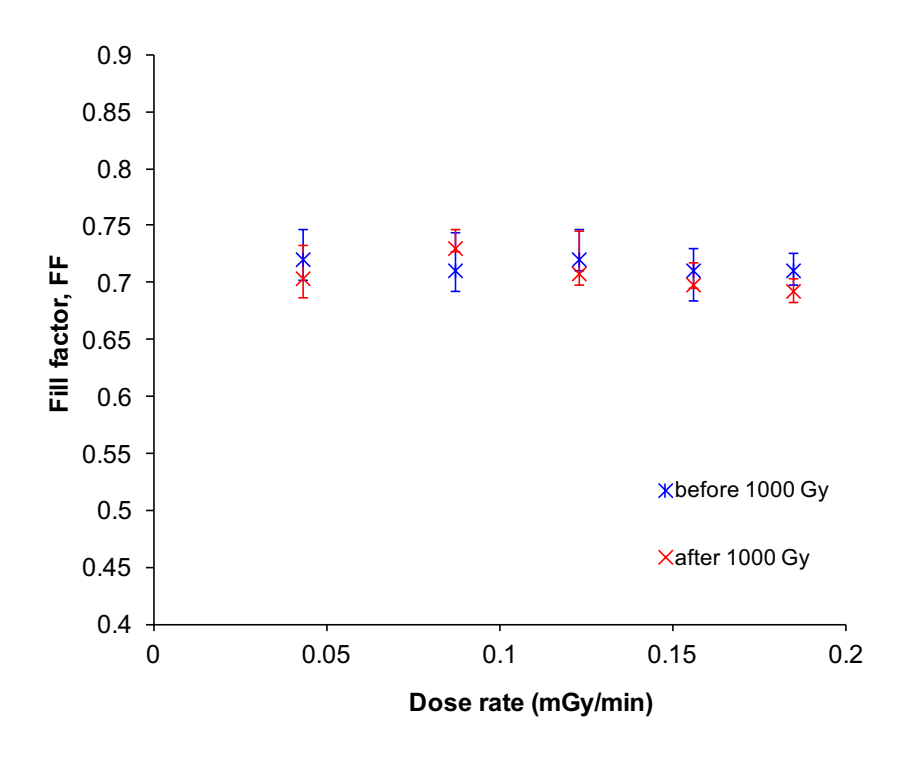


Figure 6.17: Fill factor (FF) for detector D2 as a function of dose rate before and after irradiation to 6 MV photon. The error bars represent the standard deviation of the data.

of spatial inhomogeneities at the metal–semiconductor interface [79]. However, the data after irradiation demonstrates almost negligible temperature dependance. This finding will be discussed further in the following section.

6.5.1 Dependance of noise spectral density with frequency

Since, the I–V characteristics of the non-irradiated and irradiated demonstrate an identical trend as plotted in Figure 6.8, the frequency dependance of noise density for both data are plotted in Figure 6.19 at different current values. This current range fall in the regime within the exponential part of I–V characteristics that represents the thermionic emission part, which is the most significant contribution to the current across the barrier of the Schottky diode detector. Low noise frequency provides an important information on the location and nature of noise sources, which can be obtained from the noise properties of forward biased Schottky diodes that may contributed to the spatial inhomogeneities or fluctuations in the occupancy of the trap states or mobility of the free carriers [75–77]. The noise density with frequency dependance at all measured currents (typically between 2×10^{-09} to 2×10^{-05} A) was observed to be higher in the non–irradiated data. The contribution of the noise spectral density increases with increasing current which leads to the appearance of the

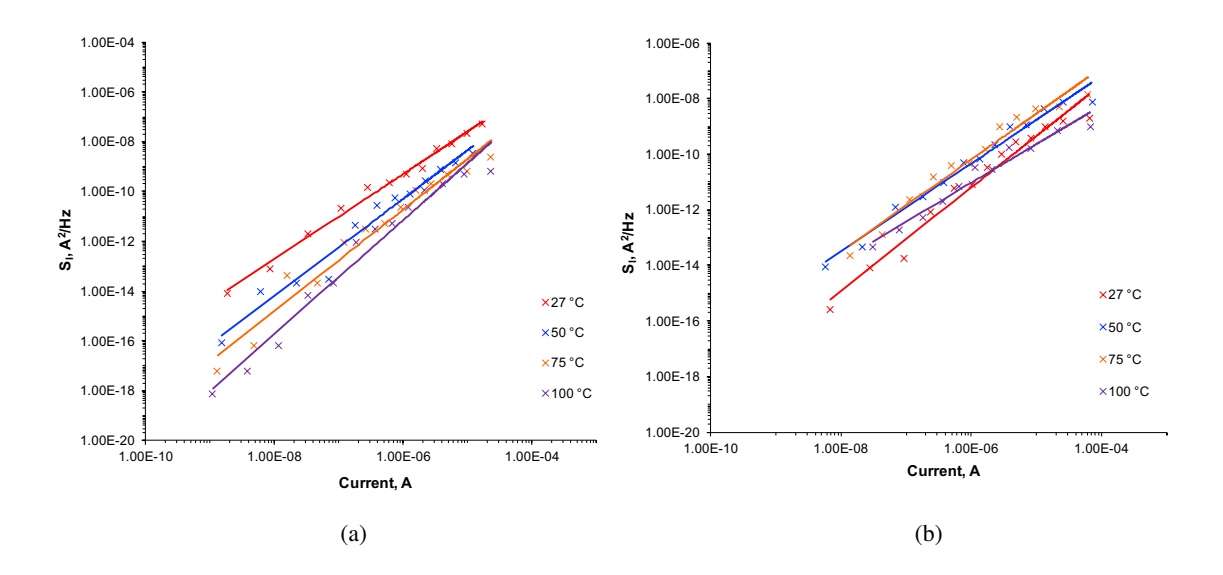


Figure 6.18: Current dependance of noise spectral density, S_I at f = 10 Hz for (a) before and (b) after irradiation with 6 MV photon.

generation—recombination noise (100 Hz < f < 1000 Hz) and it is more prominent in non-irradiated data. This finding appears to contradict the data published in [166], where electron irradiation resulted in an increase in the noise spectral density, which is due to the increased generation—recombination. However, the decrease in the current dependance of noise density for the case here, may be related to the increase in the doping concentration and barrier height as discussed in the previous section.

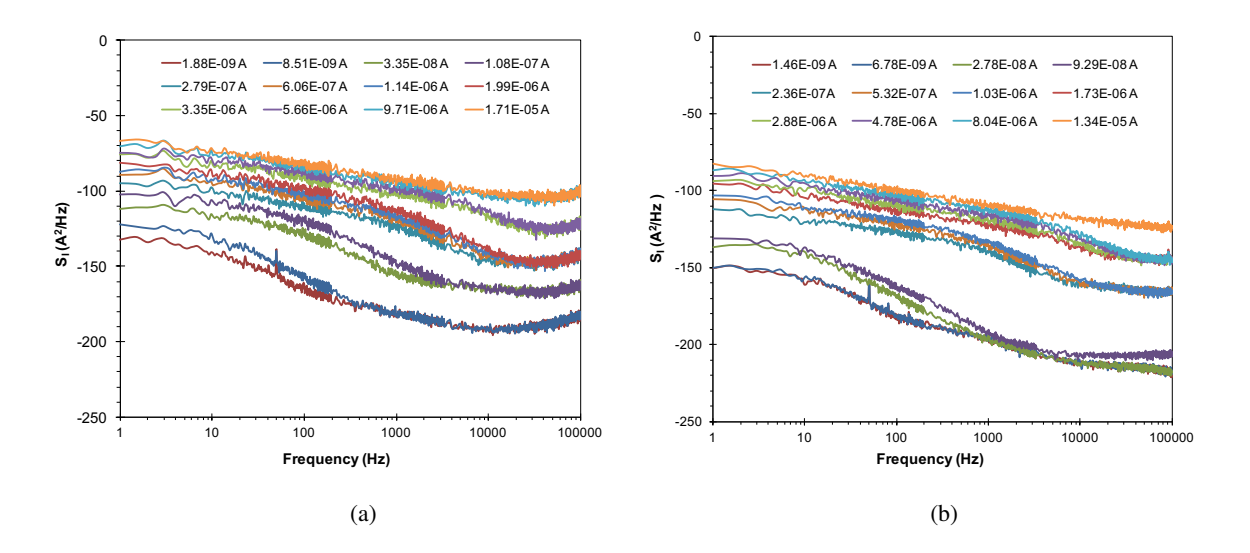


Figure 6.19: Frequency dependance of noise power spectral density, S_I at different currents for (a) before and (b) after irradiation with 6 MV photon at room temperature.

6.5.2 Dependance of noise spectral density with current

In addition, a comparison of the noise density before and after irradiation for each of the measurement temperatures involved; 27 °C, 50 °C, 75 °C and 100 °C are plotted in Figure 6.20. Increasing the measurement temperature is observed to shorten the linear part of the current dependance of the noise density as can be observed by the data in Figures 6.20 (a), (b), (c) and (d). At room temperature (Figure 6.20 (a)), the non–irradiated noise density is higher than that after irradiation. However, after increasing the temperature to 75 °C, the current dependance of noise density for non–irradiated and irradiated become almost identical. Unexpectedly, at 100 °C, the current dependance of noise density for higher current range (between 1×10^{-06} to 1×10^{-04} A) of the irradiated data become lower than the non–irradiated data. This condition may be attributed from the different behaviour of the current dependance of noise density as a function of temperatures for the non-irradiated and irradiated data.

The current dependance, β of the noise spectral density is extracted from the gradient of the linear line in Figure 6.20 and is plotted in Figure 6.21 as a function of temperature. Different trends of the current dependance of noise density (β) as a function of temperature can be observed from the non–irradiated and irradiated data. There is increase in the current dependance for non–irradiated and decrease for irradiated data as a function of measurement temperature. However, the current dependance for both non–irradiated and irradiated data are within the same range which are between 1.53 to 1.90. Those values are still in agreement with the data presented in the literature [81], which give $\beta = 1.7$ and the majority of the semiconductor studies published previously, including Si, GaN, and 6H–SiC Schottky diodes which are in the range of $1 < \beta < 2$ [81].

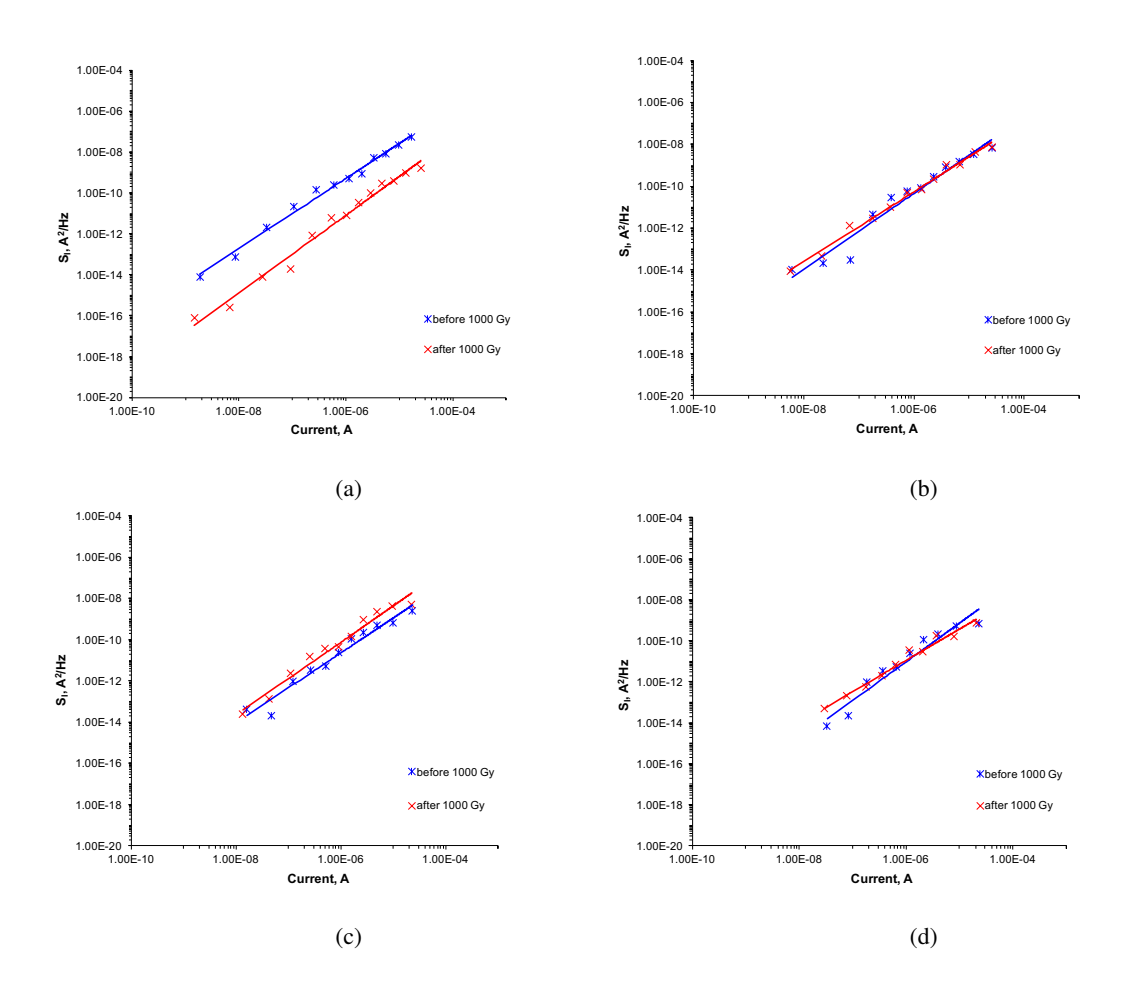


Figure 6.20: Current dependance of noise spectral density, S_I at f = 10 Hz and (a) 27 °C, (b) 50 °C, (c) 75 °C and (d) 100 °C measurement temperatures for before and after irradiation with 6 MV photons.

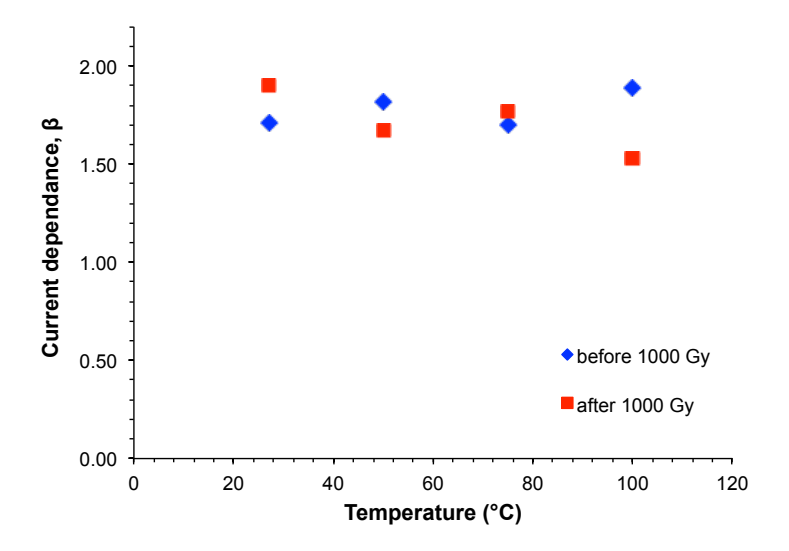


Figure 6.21: Current dependance of noise spectral density, S_I as a function of measurement temperatures for before and after irradiation with 6 MV photons.

6.6 Conclusion

The radiation response and tolerance of the 4H–SiC Schottky diode in high energy photon environments has been determined. The first part of the chapter involves discussion on the radiation response of fabricated detector to high dose rate of 6 MV photon within the range of 17.6 to 52.9 Gy/min. The data show that the detected current originates within the depletion region of the detector and the response is linearly dependent on the volume of the space charge region. The influence of the high leakage current density which is controlled by the bias voltage applied degrades the detected current signal of the detector. High linear correlation of the current response as a function of dose rate has been observed for low dose data (35 kV), which is in the range of 2.52 to 5.37 μ A.min/Gy.mm² in comparison to high dose rate data with dose rate linearity between 0.058 to 0.250 nA.min/Gy.mm². This is due to the different energy used and types of radiation interactions take place that plays a major role in those extracted values.

Subsequently, the effect of high energy photon irradiation on the electrical characteristics in terms of I–V, C–V, low frequency noise and as an X–ray photon energy harvester have been presented to study radiation hardness of the detector. There is slight increase in the extracted values of specific on resistance with 5% difference after the first exposure and 2% for barrier height values (Φ_b = 1.670 \pm 0.001 eV to 1.72 \pm 0.003 eV) over a range of cumulative dose from 47.6 to a maximum of 1000 Gy. The slight increase in the barrier height values can be related to the increase in the specific on resistance after the first exposure, which resulted in the deviation of forward bias I–V characteristics of the Schottky diode from that predicted by the thermionic emission model. The ideality factor demonstrates almost constant values as a function of dose rate with n = 1.05 \pm 0.03. The irradiation with high energy photons led to the generation of two different regions of dopant concentration. The first region, which is for applied bias below -10 V demonstrates a minor change in the dopant concentration with only 11% difference. The increase in the capacitance value from -10 V to -30 V led to rise in the dopant concentration and reduce the depletion width. The decrease in the depletion width from -10 V to -30 V observed to be inconsistent with the increase in the barrier height value from the I–V characteristics.

High energy irradiation did not result in significant effects on the performance of the detector as a X-ray photon energy harvester. A constant value of the short circuit current density and fill factor along with a 20% degradation in the open circuit voltage and peak power density proved a high grade X-ray photon converter has been realised. Unexpectedly, the LFN measurement at room temperature for the non-irradiated data is higher than the irradiated data. The decrease in the current dependance of noise as a function of measurement temperature for the irradiated data can be related to the increase in the dopant concentration and barrier height values. Nevertheless, the noise spectral density showed

negligible dependance on the temperature over a range of 27 °C to 100 °C, with the β values between 1.53 to 1.90. This indicates that there is only minor defects present due to generation–recombination after irradiation to high energy photon.

In summary, detector D2 presented good response to high energy photon irradiation with comparable current signal generated to previous studies. In addition, high radiation tolerance to high energy photon of a maximum cumulative dose of 1000 Gy, demonstrate the capability of the detector which offers significant opportunities as radiation dosimeters and X–ray photon energy harvester in radiation—rich environments.

Chapter 7

Conclusions and Future works

7.1 Summary

This thesis presents an investigation on the capability of fabricated 4H–SiC Schottky diode for the realisation of radiation detectors with high dose rate response by exposure to low and high dose rate irradiation and investigated for the first time the possibility of scavenging X-ray energy in extreme environments. These aims have been achieved through the optimisation on the parameters that influence condition during fabrication process and based on electrical characterisation measurements including I-V and C-V characteristics. Additionally, initial irradiation of 4H-SiC Schottky diodes to low dose rate were performed in order to observe their response to increasing X-ray radiation dose between 0.105 to 0.185 mGy/min. The outstanding response from this characterisation has initiated further study of the spectroscopic properties and low frequency noise prior to exposure to 6 MV high energy photon irradiation. Changes in the electrical characteristics demonstrate the ability of SiC to be radiation tolerant in high radiation flux, which generally results in damage due to trapping defects. By taking advantage of the high radiation hardness and insensitivity to radiation damage of SiC, evaluation of the ability of the fabricated detectors to operate as X-ray photon energy harvesters in radiation environment has been performed. The final phase of this study investigated the radiation response and tolerance to high energy photon irradiation. Detectors with ideal electrical characteristics in terms of ideality factor and barrier height, were tested to identify the response to increasing radiation flux. The detailed outcomes of the capability of fabricated 4H-SiC Schottky diodes as radiation detector and for X-ray photon energy harvesting are summarised as follow.

The I–V characteristics of selected 4H–SiC Schottky diodes were tested at room and elevated temperatures up to 100 °C, to compare with the measurements performed at the wafer level, prior to wire–bonding. All detectors revealed unchangeable barrier heights and ideality factors, indicating that the wire bonding did not produce any significant effect on the characteristics. The ideality factor

and barrier height of detectors D1, D2, D3, D4 and D5 exhibited insignificant variation over the range of measurement temperatures up to $100\,^{\circ}$ C, which are in the range of $(1.00-1.10)\pm0.04$ and 1.54-1.74 eV, respectively. Therefore, the suitability of detectors D1, D2 and D3 as radiation detectors for use in low energy and low dose rate applications was determined for bias voltages up to -180 V and operating temperatures up to $100\,^{\circ}$ C. The high linearity showed a correlation of the current response as a function of dose rate, where it increases with increasing bias voltage. This is due to the dependance of the current response on the volume of the space charge region, which controlled by the bias voltage applied. The observed increase in the collected charge and hence dose sensitivity of the detectors at higher applied bias is observed to be identical to the enhancement in the detected current, where detector D2 demonstrated a factor of 1.5 times increase in collected charge in comparison to that of detector D1. The linearity and sensitivity for measurements performed below 75 °C were observed to be independent of temperature, indicating a highly stable performance of detectors D1 and D2.

Due to considerable response of the fabricated detectors to lower dose rate irradiation, the possibility of the detectors D2, D4 and D5 as an energy harvester have been studied. The performance characteristics of a X-ray energy harvester were then correlated with the electrical and spectroscopic response based on the alpha spectroscopy detection properties using ²⁴¹Am. Channel peak position, full-width at half maximum (FWHM), energy resolution and charge collection efficiency (CCE) were analysed at a range of bias voltage from 0 V to -150 V. The channel peak position and CCE observed to be similar for all detectors, whilst D5 demonstrate slightly better FWHM and energy resolution in comparison to the others. Due to the distinct detection properties discovered, low noise frequency measurements have been determined to investigate the defect mechanism inside those detectors. Detector D5 presented the lowest noise spectral density at moderate current values with β = 3.16, which is double than detectors D2 and D4 with β = 1.6 – 1.7. The difference in the noise spectral density measurement between detectors resulted in a significant influence on their detection properties, and therefore the performance as X-ray energy harvester. The performance capability as X-ray photon energy harvester have been tested in term of short circuit current density, J_{SC} , open circuit voltage, V_{OC}, power output, P_{OUT} and fill factor, FF. Increasing the dose rate of the Xray irradiation, was observed to increase the measured short circuit current density, J_{SC} and power output, P_{OUT} for all detectors. Otherwise, comparable values of open circuit voltage, V_{OC} , and fill factor, FF with BPW34 silicon PIN photodiode were discovered, where they were almost constant as a function of dose. The higher barrier height ($\Phi_b = 1.67 \text{ eV}$) and superior detection properties for detector D5 resulted in a high short circuit current density, J_{SC} and power output, P_{OUT}, which are within 15 to 90 nA/cm² and 10 to 55 nW/cm², respectively. This may be attributed to the low leakage current density of D5 that is less than half (<1 nA/cm²) of that observed in the other detectors, which led to minimization of the loss in electron–hole pairs created due to trapping and defects. Notable finding in this section is the considerable performance as X–ray photon energy harvester of detector D5 may due to the exceptional detection and defect properties measured. This opens up the possibility of developing high power X–ray photon energy harvester in the X–ray photon flux environment.

The radiation tolerance of detector D2 has been evaluated by exposure to a maximum cumulative dose of 1000 Gy photon energy. The current generated by exposure to 6 MV photon in the range of 17.6 to 52.9 Gy/min show linear dependance on the volume of the space charge region. However, degradation in the detected current signal density has been observed at high bias voltage due to the dominant leakage current density. Comparison of the current response as a function of dose rate between low dose rate (35 kV) and high dose rate (6 MV) measurements were observed to be influence by the different of radiation interactions take place in the detection medium. Low dose rate data demonstrated a dose rate linearity in the range of 2.52 to 5.37 μ A.min/Gy.mm², in comparison to the high dose rate data with the values between 0.058 to 0.250 nA.min/Gy.mm². To study the radiation hardness of detector D2, the electrical characteristics in terms of I-V, C-V, low frequency noise and performance as an X-ray photon energy harvester have been investigated. The slight increase in barrier height values (2%) over a range of cumulative dose from 47.6 to a maximum of 1000 Gy can be related to the increase in the specific on resistance (2%) after the first exposure. This can be predicted by the thermionic emission model, which resulted in the deviation of forward bias I-V characteristics of the detector. Nonetheless, detector D2 demonstrates almost constant values of ideality factor as a function of dose rate, with $n = 1.05 \pm 0.03$. C-V measurements after irradiation to high energy photon irradiation generate two different regions of dopant concentration, which was 11% increment in the first region (below -10 V) and gave further increase in dopant concentration with $N_D = 1.4 \times 10^{15}$ cm⁻³ for bias voltages between -10 V to -30 V. Otherwise, a constant value of short circuit current density and fill factor along with only 20% degradation in open circuit voltage and peak power density proved that high energy irradiation did not exert a significant effect on the performance of the detector as a X-ray photon energy harvester. The decrease in the noise spectral density with current at room temperature for the irradiated data can be related to the increase in the dopant concentration and barrier height values. The current dependance of the noise spectral density for both non-irradiated and irradiated data present negligible dependance on the temperature over a range temperatures between 27 °C to 100 °C, with the β values between 1.53 and 1.90. Therefore, it can be proposed that detector D2 has a high radiation tolerance to high energy photon of a maximum cumulative dose of 1000 Gy with only minor defects present due to generationrecombination. This offers significant opportunities on the capability of the detector to be realised as as radiation dosimeters and energy scavenging in radiation—rich environments.

7.2 Future work

In this part, few possible further measurements, which can be considered for future work are proposed. It is beneficial if the carrier lifetime and mobility of all the fabricated device can be extracted to support the measurements in Chapters 4 and 5. In Chapter 4, measurement of the carrier lifetime will allow the extraction of the diffusion length, L that is required to express the actual active depth (L + W) of the detector. The active depth enables the determination of the sensitivity per unit volume to be extracted and hence a comparison between commercial diodes or other fabricated detectors in previously published studies can be made. Whilst, in Chapter 5 the extraction of the diffusion length values allow the determination of theoretical charge collection efficiency. This imperative to compare with the experimental charge collection efficiency values published in the literature, since few parameters influence the experimental methods and hence contribute to possible error.

The performance of the detector as an X-ray battery presented in Chapter 5 can be expanded to the ability of the fabricated detectors in harvesting different radioisotopes such as α and β -particles. Few trial and error procedures have been measured using 241 Am and 14 C sources, however, due to the very low activity of these sources, the current generation on the detector did not produce a significant value of the short circuit current density. Therefore, it can be suggested that measurement on the capability of the fabricated detector as nuclear battery can be investigated using different radioisotopes with higher activity such as 63 Ni or 55 Fe.

The other interesting areas that are important in discovering the radiation tolerance of the fabricated Schottky diode to high energy irradiation are the deep level transient spectroscopy measurement (DLTS) that are enable identification of defect related parameters including energy level, concentration, capture cross—section, and spatial profile in semiconductors. Through DLTS measurement, comparison of the defect level in terms of these parameters can be made between non—irradiated and irradiated data. Unfortunately, during this study, the facility to measure these parameters is under construction and it was replaced with the measurement of the defect mechanism using the low noise frequency method.

Bibliography

- [1] ICRP, 1977. Recommendations of the ICRP. ICRP Publication 26. Ann. ICRP 1 (3).
- [2] K. P. Nesteruk, Reports of Practical Oncology & Radiotherapy, 2014, 19, S32–S36.
- [3] A. La Rosa, M. Garella, F. Bourhaleb, R. Cirio, M. Donetti, S. Giordanengo, N. Givehchi, F. Marchetto, F. Martin, S. Meyroneinc, C. Peroni and G. Pittà, *Nuclear Instruments and Methods in Physics Research Section A: Accelerators, Spectrometers, Detectors and Associated Equipment*, 2006, **565**, 833–840.
- [4] International Atomic Energy Agency, Technical Reports Series No. 469 Calibration of Reference Dosimeters for External Beam Radiotherapy, 469, 2009.
- [5] S. Braccini, A. Ereditato, F. Giacoppo, I. Kreslo, K. P. Nesteruk, M. Nirkko, M. Weber, P. Scampoli, M. Neff, S. Pilz and V. Romano, *Journal of Instrumentation*, 2012, 7, T02001– T02001.
- [6] F. Nava, G. Bertuccio, A. Cavallini and E. Vittone, *Measurement Science and Technology*, 2008, 19, 102001.
- [7] A. Barry, B. Lehmann, D. Fritsch and D. Braunig, *IEEE Transactions on Nuclear Science*, 1991, **38**, 1111–1115.
- [8] F. Ruddy, A. Dulloo, J. Seidel, S. Seshadri and L. Rowland, *IEEE Transactions on Nuclear Science*, 1998, **45**, 536–541.
- [9] R. S. Goldberg Yu., Levinshtein M.E., *Properties of Advanced Semiconductor Materials GaN*, *AlN*, *InN*, *BN*, *SiC*, *SiGe*, John Wiley & Sons, Inc., 2001, pp. 93–148.
- [10] N. G. Wright and A. B. Horsfall, *Material Matters*, 2009, 4, 1–5.
- [11] Acheson E.G., J. Franklin Inst., 1893, **136**, 279.

- [12] A.R. Verma and P. Krishna, *Polymorphism and Polytypism in Crystals*, John Wiley & Sons Inc, 1966, pp. 1 362.
- [13] H. Morkoç, S. Strite, G. B. Gao, M. E. Lin, B. Sverdlov and M. Burns, *Journal of Applied Physics*, 1994, 76, 1363–1398.
- [14] T. Kimoto and J. A. Cooper, Fundamentals of Silicon Carbide Technology: Growth, Characterization, Devices and Applications, Wiley, 2014.
- [15] H. Ou, Y. Ou, *PhD Thesis*, Technical University of Denmark (DTU), Kgs. Lyngby., 2012.
- [16] K. Kawahara, PhD Thesis, Kyoto University, 2013.
- [17] N. G. Wright, A. B. Horsfall and K. Vassilevski, Materials Today, 2008, 11, 16–21.
- [18] C. M. Zetterling and M. Ostling, Materials Research Society Symposium Proceedings, 1994.
- [19] J. Palmour and R. Singh, IEEE International Symposium on Power Semiconductor Devices and IC's, 1997, 1997, pp. 25–32.
- [20] S. Seshadri, A. Dulloo, F. Ruddy, J. Seidel and L. Rowland, *IEEE Transactions on Electron Devices*, 1999, 46, 567–571.
- [21] G. Bertuccio, D. Puglisi, D. Macera, R. Di Liberto, M. Lamborizio and L. Mantovani, *IEEE Transactions on Nuclear Science*, 2014, **61**, 961–966.
- [22] C.M. Johnson, N. Wright, M. Uren, K. Hilton, M. Rahimo, D. A. Hinchley, P. A. Knights, D. J. Morrison, A. B. Horsfall, S. Ortolland and A. G. O'Neill, IEEE Circuits, Devices and Syst., 2001, pp. 101–108.
- [23] J. Lees, D. Bassford, E. Bunce, M. Sims and A. B. Horsfall, Nuclear Instruments and Methods in Physics Research Section A: Accelerators, Spectrometers, Detectors and Associated Equipment, 2009, 604, 174–176.
- [24] N. G. Wright and A. B. Horsfall, Journal of Physics D: Applied Physics, 2007, 40, 6345–6354.
- [25] J. E. Lees, A. M. Barnett, D. J. Bassford, R. C. Stevens and A. B. Horsfall, *Journal of Instrumentation*, 2011, 6, C01032–C01032.
- [26] Q. Wahab, T. Kimoto, A. Ellison, C. Hallin, M. Tuominen, R. Yakimova, A. Henry, J. P. Bergman and E. Janzén, *Applied Physics Letters*, 1998, 72, 445–447.
- [27] R. Singh and M. Pecht, IEEE Industrial Electronics Magazine, 2008, 19–31.

- [28] N. V. Dyakonova, P. A. Ivanov, V. A. Kozlov, M. E. Levinshtein, J. W. Palmour, S. L. Rumyantsev and R. Singh, *IEEE Transactions on Electron Devices*, 1999, **46**, 2188–2194.
- [29] G. Bertuccio, R. Casiraghi, A. Cetronio, C. Lanzieri and F. Nava, *Nuclear Instruments and Methods in Physics Research Section A: Accelerators, Spectrometers, Detectors and Associated Equipment*, 2004, **518**, 433–435.
- [30] G. Bertuccio, S. Caccia, D. Puglisi and D. Macera, Nuclear Instruments and Methods in Physics Research Section A: Accelerators, Spectrometers, Detectors and Associated Equipment, 2011, 652, 193–196.
- [31] A. Owens, Compound Semiconductor Radiation Detectors, CRC Press, 2016.
- [32] C. Romei, A. Di Fulvio, C. A. Traino, R. Ciolini and F. D'Errico, *Physica Medica*, 2015, **31**, 112–116.
- [33] P. J. Sellin and J. Vaitkus, Nuclear Instruments and Methods in Physics Research, Section A: Accelerators, Spectrometers, Detectors and Associated Equipment, 2006, 557, 479–489.
- [34] P. J. Sellin, Nuclear Instruments and Methods in Physics Research, Section A: Accelerators, Spectrometers, Detectors and Associated Equipment, 2003, 513, 332–339.
- [35] S. Pini, M. Bruzzi, M. Bucciolini, E. Borchi, S. Lagomarsino, D. Menichelli, S. Miglio, F. Nava and S. Sciortino, Nuclear Instruments and Methods in Physics Research, Section A: Accelerators, Spectrometers, Detectors and Associated Equipment, 2003, 514, 135–140.
- [36] M. Bruzzi, M. Bucciolini, F. Nava, S. Pini and S. Russo, Nuclear Instruments and Methods in Physics Research, Section A: Accelerators, Spectrometers, Detectors and Associated Equipment, 2002, 485, 172–177.
- [37] J. Susini, R. Barrett, J. Chavanne, P. Fajardo, A. Götz, J.-L. Revol and L. Zhang, *Journal of Synchrotron Radiation*, 2014, 21, 986–995.
- [38] F. H. Ruddy, J. G. Seidel, H. Chen, A. R. Dulloo and S. H. Ryu, *IEEE Transactions on Nuclear Science*, 2006, **53**, 1713–1718.
- [39] F. Ruddy, A. Dulloo, J. Seidel, M. Das, S.-H. Ryu and A. Agarwal, *IEEE Symposium Conference Record Nuclear Science* 2004., 2004, 7, 4575–4579.
- [40] Y. M. Abubakar, A. Lohstroh and P. J. Sellin, *IEEE Transactions on Nuclear Science*, 2015, 62, 2360–2366.

- [41] K. C. Mandal, P. G. Muzykov, S. K. Chaudhuri and J. R. Terry, *IEEE Transactions on Nuclear Science*, 2013, 60, 2888–2893.
- [42] D. K. Schroder, *Semiconductor Material and Device Characterization*, John Wiley & Sons, 3rd edn., 2006.
- [43] S. N. Ahmed, *Physics and Engineering of Radiation Detection*, Elsevier Science, 2014.
- [44] S. M. Sze and K. K. Ng, Physics of Semiconductor Devices, Wiley, 2006.
- [45] H. A. Bethe, *Theory of the Boundary Layer of Crystal Rectifiers*, Radiation Laboratory, Massachusetts Institute of Technology, 1942.
- [46] G. F. Knoll, Radiation Detection and Measurement, John Wiley & Sons, 2010.
- [47] P. Sprawls, *Physical Principles of Medical Imaging*, Medical Physics Publishing Corporation, 2nd edn., 1995.
- [48] P. Andreo, M. Evans, J. Hendry, J. Horton, J. Izewska, B. Mijnheer, J. Mills, M. Olivares, P. Ortiz López, W. Parker, H. Patrocinio, E. Podgorsak, M. Podgorsak, G. Rajan, J. Seuntjens, K. Shortt, W. Strydom, N. Suntharalingam, D. Thwaites and H. Tolli, *Radiation Oncology Physics: A Handbook for Teachers and Students*, International Atomic Energy Agency (IAEA), Vienna, 2005, pp. 1–657.
- [49] B. G. Lowe and R. A. Sareen, Semiconductor X-Ray Detectors, CRC Press, 2013.
- [50] G. Bertuccio and R. Casiraghi, *IEEE Transactions on Nuclear Science*, 2003, **50**, 175–185.
- [51] T. R. Alam and M. A. Pierson, Journal of Energy and Power Sources, 2016, 3, 11–41.
- [52] T. R. Garcia, A. Kumar, B. Reinke, T. E. Blue and W. Windl, *Applied Physics Letters*, 2013, 103, 152108–1 – 152108–4.
- [53] B. Zat'ko, F. Dubecký, A. Šagátová, K. Sedlačová and L. Ryć, *Journal of Instrumentation*, 2015, 10, C04009–C04009.
- [54] S. Sciortino, S. Lagomarsino and F. Nava, *IEEE Transactions on Nuclear Science*, 2009, **56**, 2538–2542.
- [55] S. Sciortino, F. Hartjes, S. Lagomarsino, F. Nava, M. Brianzi, V. Cindro, C. Lanzieri, M. Moll and P. Vanni, Nuclear Instruments and Methods in Physics Research Section A: Accelerators, Spectrometers, Detectors and Associated Equipment, 2005, 552, 138–145.

- [56] S. Nigam, J. Kim, F. Ren, G. Y. Chung, M. F. MacMillan, R. Dwivedi, T. N. Fogarty, R. Wilkins, K. K. Allums, C. R. Abernathy, S. J. Pearton and J. R. Williams, *Applied Physics Letters*, 2002, 81, 2385.
- [57] J. Wu, M. Li, Y. Jiang, J. Li, Y. Zhang, H. Gao, X. Liu, J. Du, D. Zou, X. Fan, L. Gan, C. Peng, Y. Lu and J. Lei, Nuclear Instruments and Methods in Physics Research Section A: Accelerators, Spectrometers, Detectors and Associated Equipment, 2015, 771, 17–20.
- [58] F. Nava, A. Castaldini, A. Cavallini, P. Errani and V. Cindro, *IEEE Transactions on Nuclear Science*, 2006, **53**, 2977–2982.
- [59] S. del Sordo, L. Abbene, E. Caroli, A. M. Mancini, A. Zappettini and P. Ubertini, *Sensors*, 2009, **9**, 3491–3526.
- [60] G. Bertuccio, R. Casiraghi, A. Cetronio, C. Lanzieri and F. Nava, *Nuclear Instruments and Methods in Physics Research Section A: Accelerators, Spectrometers, Detectors and Associated Equipment*, 2004, **522**, 413–419.
- [61] K. V. Vassilevski, I. P. Nikitina, N. G. Wright, A. B. Horsfall, A. G. O'Neill and C. M. Johnson, Microelectronic Engineering, 2006, 83, 150–154.
- [62] R. R. Ferber and G. N. Hamilton, *Nuclear Technology*, **2**, 246–251.
- [63] J. Lees, D. Bassford, G. Fraser, A. Horsfall, K. Vassilevski, N. Wright and A. Owens, Nuclear Instruments and Methods in Physics Research Section A: Accelerators, Spectrometers, Detectors and Associated Equipment, 2007, 578, 226–234.
- [64] J. Lees, Nuclear Instruments and Methods in Physics Research Section A: Accelerators, Spectrometers, Detectors and Associated Equipment, 2010, 613, 98–105.
- [65] H. Spieler, Semiconductor Detector Systems, Oxford University Press, 2005.
- [66] M. A. Prelas, C. L. Weaver, M. L. Watermann, E. D. Lukosi, R. J. Schott and D. A. Wisniewski, Progress in Nuclear Energy, 2014, 75, 117–148.
- [67] J. F. Ziegler, M. D. Ziegler and J. P. Biersack, *Nuclear Instruments and Methods in Physics Research, Section B: Beam Interactions with Materials and Atoms*, 2010, **268**, 1818–1823.
- [68] D. Y. Qiao, X. J. Chen, Y. Ren and W. Z. Yuan, Journal of Microelectromechanical Systems, 2011, 20, 685–690.
- [69] M. Lu, G. G. Zhang, K. Fu, G. H. Yu, D. Su and J. F. Hu, Energy Conversion and Management, 2011, 52, 1955–1958.

- [70] X. Tang, Y. Liu, D. Ding and D. Chen, *Science China Technological Sciences*, 2012, **55**, 659–664.
- [71] M. Lu, G. Wang and C. S. Yao, Advanced Materials Research, 2011, 343-344, 56-61.
- [72] A. Henry, X. Li, S. Leone, O. Kordina and E. Janzén, *Materials Science Forum*, 2012, **711**, 16–21.
- [73] G. Wang, R. Hu, H. Wei, H. Zhang, Y. Yang, X. Xiong, G. Liu and S. Luo, *Applied Radiation and Isotopes*, 2010, **68**, 2214–2217.
- [74] L. Anghel, T. Ouisse, T. Billon, P. Lassagne and C. Jaussaud, *Diamond and Related Materials*, 1997, **6**, 1494–1496.
- [75] S. L. Rumyantsev, N. Pala, M. S. Shur, R. Gaska, M. E. Levinshtein, V. Adivarahan, J. Yang, G. Simin and M. A. Khan, *Applied Physics Letters*, 2001, 79, 866–868.
- [76] S. Hsu, IEEE Transactions on Electron Devices, 1971, 18, 882.
- [77] T. G. M. Kleinpenning, Solid State Electronics, 1978, 22, 121–128.
- [78] M.-Y. Luo, G. Bosman, A. Van Der Ziel and L. Hench, *IEEE Transactions on Electron Devices*, 1988, **35**, 1351–1356.
- [79] H. H. Güttler and J. H. Werner, Applied Physics Letters, 1990, **56**, 1113–1115.
- [80] O. Jäntsch, IEEE Transactions on Electron Devices, 1987, 34, 1100–1115.
- [81] E. I. Shabunina, M. E. Levinshtein, N. M. Shmidt, P. A. Ivanov and J. W. Palmour, *Solid-State Electronics*, 2014, **96**, 44–47.
- [82] A. Kumar, K. Asokan, V. Kumar and R. Singh, *Journal of Applied Physics*, 2012, **112**, 024507 1–7.
- [83] H. Ouacha, M. Mamor and M. Willander, Journal of Applied Physics, 2000, 87, 3858–3863.
- [84] H. Ouacha, O. Nur, M. Willander, Y. Fu and A. Ouacha, *Applied Physics Letters*, 1996, **69**, 2382–2384.
- [85] R. Singh and D. Kanjilal, Journal of Applied Physics, 2002, 91, 411–413.
- [86] M. Bouterfa, K. Aouadi, D. Bertrand, B. Olbrechts, R. Delamare and E. C. Gil, 2011 2nd International Conference on Advancements in Nuclear Instrumentation, Measurement Methods and their Applications, 2011, pp. 1–6.

- [87] C. S. Porumb, A. H. Aldosari, I. Fuduli, D. Cutajar, M. Newall, P. Metcalfe, M. Carolan, M. L. F. Lerch, V. L. Perevertaylo, A. B. Rosenfeld and M. Petasecca, *IEEE Transactions on Nuclear Science*, 2016, 63, 1808–1817.
- [88] M. Bouterfa, K. Aouadi, D. Flandre and E. C. Gil, 2013 IEEE International Instrumentation and Measurement Technology Conference (I2MTC), 2013, 1088–1091.
- [89] M. G. Bisogni, G. A. P. Cirrone, G. Cuttone, A. D. el Guerra, P. Lojacono, M. A. Piliero, F. Romano, V. Rosso, V. Sipala, A. Stefanini and S. Vecchio, 2008 IEEE Nuclear Science Symposium Conference Record, 2008, 362–365.
- [90] International Commission On Radiation Units and Measurements (ICRU)., 2, 1989.
- [91] T. Ohshima, S. Onoda, N. Iwamoto, T. Makino, M. Arai and Y. Tanak, *Physics and Technology of Silicon Carbide Devices*, 2012.
- [92] R. Schulte, V. Bashkirov, K. Mueller, J. Heimann, L. Johnson, B. Keeney, H.-W. Sadrozinski, A. Seiden, D. Williams, S. Peggs, T. Satogata and C. Woody, *IEEE Transactions on Nuclear Science*, 2004, 51, 866–872.
- [93] N. S. Mohamed, N. G. Wright and A. B. Horsfall, *IEEE Transactions on Nuclear Science*, 2017, 64, 1912–1919.
- [94] S. Metzger, H. Henschel, O. Kohn and W. Lennartz, *IEEE Transactions on Nuclear Science*, 2002, **49**, 1351–1355.
- [95] M. Bruzzi, M. Bucciolini, M. Casati, D. Menichelli, C. Talamonti, C. Piemonte and B. G. Svensson, *Applied Physics Letters*, 2007, 90, 172109–1–172109–3.
- [96] M. Bruzzi, S. Lagomarsino, F. Nava and S. Sciortino, *Diamond and Related Materials*, 2003, 12, 1205–1208.
- [97] F. Nava, P. Vanni, M. Bruzzi, S. Lagomarsino, S. Sciortino, G. Wagner and C. Lanzieri, *IEEE Trans. Nucl. Sci.*, 2004, **51**, 238–244.
- [98] S. Barker, B. Miao, D. Brennan, N. G. Wright and A. B. Horsfall, IEEE Sensors 2009 Conference, 2009, pp. 777–780.
- [99] K. J. Schoen, J. M. Woodall, J. A. Cooper and M. R. Melloch, *IEEE Transactions on Electron Devices*, 1998, **45**, 1595–1604.
- [100] B. J. Baliga, *Power Semiconductor Devices*, PWS Publishing Company, 1996.

- [101] J. Bardeen, *Physical Review*, 1947, **71**, 717–727.
- [102] L. M. Porter and R. F. Davis, Materials Science and Engineering B, 1995, 34, 83–105.
- [103] W. M. Haynes, CRC Handbook of Chemistry and Physics, 97th Edition, CRC Press, 2016.
- [104] T. Ayalew, Ph.D. thesis, Vienna Univ. Technology, 2004.
- [105] Akira Itoh, Tsunenobu Kimoto and H. Matsunami, *IEEE Electron Device Letters*, 1995, **16**, 280–282.
- [106] I. A. Amatalo, N. E. Makori, J. Maera, D. Wamwangi and P. M. Karimi, *Microelectronics and Solid State Electronics*, 2014, **3**, 11–14.
- [107] F. Nava, P. Vanni, C. Lanzieri and C. Canali, Nuclear Instruments and Methods in Physics Research Section A: Accelerators, Spectrometers, Detectors and Associated Equipment, 1999, 437, 354–358.
- [108] F. Nava, E. Vittone, P. Vanni, G. Verzellesi, P. Fuochi, C. Lanzieri and M. Glaser, Nuclear Instruments and Methods in Physics Research Section A: Accelerators, Spectrometers, Detectors and Associated Equipment, 2003, 505, 645–655.
- [109] F. H. Ruddy, A. R. Dulloo, J. G. Seidel, J. W. Palmour and R. Singh, *Nuclear Instruments and Methods in Physics Research Section A: Accelerators, Spectrometers, Detectors and Associated Equipment*, 2003, **505**, 159–162.
- [110] S. U. Omar, T. S. Sudarshan, T. A. Rana, H. Song and M. V. S. Chandrashekhar, *Journal of Physics D: Applied Physics*, 2014, **47**, 295102.
- [111] K. In-Ho, K. Sang-Cheol, J. Sung-Jae, B. Wook, K. Nam-Kyun, P. Byung-Jae and Y. Geon-Young, *Journal of the Korean Physical Society*, 2009, **55**, 1036.
- [112] A. Mahajan and B. Skromme, Solid-State Electronics, 2005, 49, 945–955.
- [113] I. P. Nikitina, K. V. Vassilevski, A. B. Horsfall, N. G. Wright, A. G. O'Neill, C. M. Johnson, T. Yamamoto and R. K. Malhan, *Semiconductor Science and Technology*, 2006, **21**, 898–905.
- [114] I. P. Nikitina, K. V. Vassilevski, A. B. Horsfall, N. G. Wright, A. G. O'Neill, S. K. Ray, K. Zekentes and C. M. Johnson, Semiconductor Science and Technology, 2009, 24, 055006.
- [115] M. Lazar, H. Vang, P. Brosselard, C. Raynaud, P. Cremillieu, J. L. Leclercq, A. Descamps, S. Scharnholz and D. Planson, *Superlattices and Microstructures*, 2006, 40, 388–392.

- [116] V. Khemka, T. P. Chow and R. J. Gutmann, Journal of Electronic Materials, 1998, 27, 1128.
- [117] E. H. Rhoderick and R. H. Williams, Metal-semiconductor Contacts, Clarendon Press, 1988.
- [118] G. Güler, Ö. Güllü, . Karata and Ö. F. Bakkalolu, *Journal of Physics: Conference Series*, 2009, **153**, 012054.
- [119] S. K. Cheung and N. W. Cheung, *Applied Physics Letters*, 1986, **49**, 85–87.
- [120] N. Kwietniewski, M. Sochacki, J. Szmidt, M. Guziewicz, E. Kaminska and A. Piotrowska, Applied Surface Science, 2008, 254, 8106–8110.
- [121] K. Çinar, C. Cokun, . Aydoan, H. Asil and E. Gür, *Nuclear Instruments and Methods in Physics Research, Section B: Beam Interactions with Materials and Atoms*, 2010, **268**, 616–621.
- [122] Z. Tekeli, . Altndal, M. Çakmak, S. Özçelik, D. Çalikan and E. Özbay, *Journal of Applied Physics*, 2007, **102**, 1–8.
- [123] S. Gholami and M. Khakbaz, World Academy of Science, Engineering and Technology, 2011, 57, 1001–1004.
- [124] T. Kimoto, T. Urushidani, S. Kobayashi and H. Matsunami, *IEEE Electron Device Letters*, 1993, **14**, 548–550.
- [125] F. La Via, F. Roccaforte, A. Makhtari, V. Raineri, P. Musumeci and L. Calcagno, *Microelectronic Engineering*, 2002, **60**, 269–282.
- [126] S. Cicho, B. Barda and P. Machác, *Radioengineering*, 2011, **20**, 209–213.
- [127] S. Moloi and M. McPherson, *Physica B: Condensed Matter*, 2009, **404**, 2251–2258.
- [128] C. R. Crowell, Solid-State Electronics, 1965, **8**, 395–399.
- [129] I. P. Nikitina, K. V. Vassilevski, N. G. Wright, A. B. Horsfall, A. G. O'Neill and C. M. Johnson, *Journal of Applied Physics*, 2005, **97**, 083709.
- [130] M. Badila, G. Brezeanu, J. Millan, P. Godignon and V. Banu, *Diamond and Related Materials*, 2002, **11**, 1258–1262.
- [131] K. V. Nguyen, M. A. Mannan and K. C. Mandal, *IEEE Trans. Nucl. Sci.*, 2015, **62**, 3199–3206.
- [132] B. Kinaci, T. Asar, Y. Özen and S. Özçelk, *Optoelectronics and Advance Material Rapid Communications*, 2011, **5**, 434–437.

- [133] A. Owens and A. Peacock, Nuclear Instruments and Methods in Physics Research Section A: Accelerators, Spectrometers, Detectors and Associated Equipment, 2004, **531**, 18–37.
- [134] X. Ma, P. Sadagopan and T. S. Sudarshan, *Physica Status Solidi (A) Applications and Materials Science*, 2006, **203**, 643–650.
- [135] G. Bertuccio, R. Casiraghi and F. Nava, IEEE Trans. Nucl. Sci., 2001, 48, 232–233.
- [136] K. V. Vassilevski, A. B. Horsfall, C. M. Johnson, N. G. Wright and A. G. O'Neill, *IEEE Transactions on Electron Devices*, 2002, 49, 947–949.
- [137] I. Dökme, . Altindal and M. M. Bülbül, Applied Surface Science, 2006, 252, 7749–7754.
- [138] M. E. Aydin, N. Yildirim and A. Türüt, *Journal of Applied Physics*, 2007, **102**, 043701–1 043701–7.
- [139] Y. P. Song, R. L. Van Meirhaeghe, W. H. Laflère and F. Cardon, *Solid State Electronics*, 1986, 29, 633–638.
- [140] M. Bruzzi, F. Nava, S. Pini and S. Russo, *Applied Surface Science*, 2001, **184**, 425–430.
- [141] J. D. Wrbanek, S. Y. Wrbanek and G. C. Fralick, ISA 59th International Instrumentation Symposium, 2013, pp. 1–14.
- [142] V. Saxena, J. Nong and A. J. Steckl, *IEEE Transactions on Electron Devices*, 1999, **46**, 456–464.
- [143] R. F. Schmitsdorf, Journal of Vacuum Science & Technology B: Microelectronics and Nanometer Structures, 1997, 15, 1221.
- [144] R. T. Tung, *Physical Review B*, 1992, **45**, 13509–13523.
- [145] R. D. Evans, *The Atomic Nucleus*, McGraw-Hill, 1955.
- [146] Vishay Semiconductors, (2002). Silicon PIN Photodiode [Online]. Available: http://www.farnell.com/datasheets/2046123.pdf.
- [147] The JCS RMS30 Intelligent radiation monitor system | John Caunt Scientific Ltd. [Online]. Available: http://www.johncaunt.com/rms30/.
- [148] C. N. Oliveira, H. J. Khoury and E. J. Santos, *Physica Medica*, 2016, **32**, 1495–1501.
- [149] M. Bruzzi, F. Nava, S. Russo, S. Sciortino and P. Vanni, *Diamond and Related Materials*, 2001, **10**, 657–661.

- [150] L. Storasta and H. Tsuchida, *Materials Science Forum*, 2007, **556-557**, 603–606.
- [151] A. Shrivastava, P. B. Klein, E. R. Glaser, J. D. Caldwell, A. V. Bolotnikov and T. S. Sudarshan, Materials Science Forum, 2009, 615-617, 291–294.
- [152] K. J. Schoen, J. P. Henning, J. M. Woodall, J. A. Cooper and M. R. Melloch, *IEEE Electron Device Letters*, 1998, **19**, 97–99.
- [153] B. Náfrádi, G. Náfrádi, L. Forró and E. Horváth, Journal of Physical Chemistry C, 2015, 119, 25204–25208.
- [154] C. J. Eiting, V. Krishnamoorthy, S. Rodgers, T. George, J. D. Robertson and J. Brockman, *Applied Physics Letters*, 2006, **88**, 064101 1–3.
- [155] K. E. Bower, Y. A. Barbanel, Y. G. Shreter and G. W. Bohnert, *Polymers, Phosphors, and Voltaics for Radioisotope Microbatteries*, CRC Press, 2002.
- [156] S. Butera, M. D. C. Whitaker, G. Lioliou and A. M. Barnett, Scientific Reports, 2016, 6, 38409.
- [157] X. Y. Li, Y. Ren, X. J. Chen, D. Y. Qiao and W. Z. Yuan, *Journal of Radioanalytical and Nuclear Chemistry*, 2011, **287**, 173–176.
- [158] G. Lioliou, H. Chan, T. Gohil, K. Vassilevski, N. Wright, A. Horsfall and A. Barnett, Nuclear Instruments and Methods in Physics Research Section A: Accelerators, Spectrometers, Detectors and Associated Equipment, 2016, 840, 145–152.
- [159] F. Dubecký, E. Gombia, C. Ferrari, B. Zat'ko, G. Vanko, M. Baldini, J. Kováč, D. Baček, P. Kováč, P. Hrkút and V. Nečas, *Journal of Instrumentation*, 2012, 7, P09005–P09005.
- [160] M. De Napoli, G. Raciti, E. Rapisarda and C. Sfienti, Nuclear Instruments and Methods in Physics Research, Section A: Accelerators, Spectrometers, Detectors and Associated Equipment, 2007, 572, 831–838.
- [161] M. A. Mannan, S. K. Chaudhuri, K. V. Nguyen and K. C. Mandal, *Journal of Applied Physics*, 2014, 115, 224504–1 – 224504–6.
- [162] K. C. Mandal, S. K. Chaudhuri and K. Nguyen, *IEEE Nuclear Science Symposium Conference Record*, 2013, 1 6.
- [163] G. Bertuccio, A. Pullia and I. Introduction, *Review of Scientific Instruments*, 1993, **64**, 3294–3299.

- [164] G. Verzellesi, P. Vanni, F. Nava and C. Canali, *Nuclear Instruments and Methods in Physics Research, Section A: Accelerators, Spectrometers, Detectors and Associated Equipment*, 2002, **476**, 717–721.
- [165] W. Cunningham, A. Gouldwell, G. Lamb, J. Scott, K. Mathieson, P. Roy, R. Bates, P. Thornton, K. M. Smith, R. Cusco, M. Glaser and M. Rahman, *Nuclear Instruments and Methods in Physics Research, Section A: Accelerators, Spectrometers, Detectors and Associated Equipment*, 2002, 487, 33–39.
- [166] V. V. Kozlovski, A. A. Lebedev, M. E. Levinshtein, S. L. Rumyantsev and J. W. Palmour, *Applied Physics Letters*, 2017, **110**, 1–4.
- [167] H. K. Chan, *PhD thesis*, University of Newcastle, UK, 2014.
- [168] J. I. Lee, J. Brini, A. Chovet and C. A. Dimitriadis, *Solid-State Electronics*, 1999, **43**, 2185–2189.
- [169] M. Prelas, M. Boraas, F. D. La, T. Aguilar, J.-d. S. Modeste, T. Tchouaso and D. Wisniewski, *Lecture Notes in Energy 56: Nuclear Batteries and Radioisotopes*, Springer International publishing Switzerland 2016, 2016, pp. 1–355.
- [170] S. Butera, G. Lioliou and A. Barnett, Applied Radiation and Isotopes, 2017, 125, 42-47.
- [171] P. Bhatnagar, A. B. Horsfall, N. G. Wright, C. M. Johnson, K. V. Vassilevski and A. G. O'Neill, *Solid-State Electronics*, 2005, **49**, 453–458.
- [172] D. R. Brennan, O. Mostaghimi, K. V. Vassilevski, N. G. Wright and A. B. Horsfall, *Proceedings of IEEE Sensors*, 2012.
- [173] B. Miao, R. Mahapatra, R. Jenkins, J. Silvie, N. G. Wright and A. B. Horsfall, *IEEE Transactions on Nuclear Science*, 2009, **56**, 2916–2924.
- [174] M. Bruzzi, M. Bucciolini, G. A. Cirrone, G. Cuttone, A. Guasti, S. Mazzocchi, S. Pirollo, M. G. Sabini and S. Sciortino, *IEEE Transactions on Nuclear Science*, 2000, 47, 1430–1433.
- [175] M. Bruzzi, M. Bucciolini, G. A. Cirrone, G. Cuttone, S. Mazzocchi, S. Pirollo and S. Sciortino, *Nuclear Instruments and Methods in Physics Research, Section A: Accelerators, Spectrometers, Detectors and Associated Equipment*, 2000, **454**, 142–146.
- [176] A. Lourenço, N. Wellock, R. Thomas, M. Homer, H. Bouchard, T. Kanai, N. Macdougall, G. Royle and H. Palmans, *Physics in Medicine and Biology*, 2016, **61**, 7623–7638.

- [177] S. Andreo, P., Burns, D.T., Hohlfield, K., Huq, M.S., Kanai, T., Laitano, F., Smyth, V., and Vynckier, *Absorbed Dose Determination in External Beam Radiotherapy*, 2000.
- [178] D. I. Thwaites, *Physics in Medicine and Biology*, 1985, **30**, 41–53.
- [179] F. M. Khan, *The Physics of Radiation Therapy*, Lippincott Williams & Wilkins, 2010.
- [180] The Royal College of Radiologists, *Radiotherapy dose fractionation*, *second edition*, December, 2016.
- [181] F. Roccaforte, S. Libertino, F. Giannazzo, C. Bongiorno, F. La Via and V. Raineri, *Journal of Applied Physics*, 2005, **97**, 123501–1 123502–9.
- [182] S. Zhao, G. Lioliou and A. Barnett, Nuclear Instruments and Methods in Physics Research Section A: Accelerators, Spectrometers, Detectors and Associated Equipment, 2018, 887, 138–143.
- [183] P. Godignon, X. Jorda, M. Vellvehi, X. Perpina, V. Banu, D. Lopez, J. Barbero, P. Brosselard and S. Massetti, *IEEE Transactions on Industrial Electronics*, 2011, **58**, 2582–2589.
- [184] R. T. Tung, *Materials Science and Engineering R*, 2001, **35**, 1–138.
- [185] N. Mohamed, N. Wright and A. Horsfall, Conference Proceedings IEEE SENSORS 2017, 2017, pp. 1–3.
- [186] Y. Liu, R. Hu, Y. Yang, G. Wang, S. Luo and N. Liu, Applied Radiation and Isotopes, 2012, 70, 438–441.